UTS UNIVERSITY OF TECHNOLOGY SYDNEY

Design and Properties of Sustainable Geopolymeric Recycled Aggregate Concrete

by Zhuo TANG

Thesis submitted in fulfilment of the requirements for the degree of

Doctor of Philosophy

under the supervision of
Dr Wengui Li (Principal supervisor)
A/Prof Xinqun Zhu (Co-supervisor)
Prof Vivian Tam (Co-supervisor)

University of Technology Sydney
Faculty of Engineering and Information Technology

March 2021

CERTIFICATE OF ORIGINAL AUTHORSHIP

I, Zhuo Tang declare that this thesis is submitted in fulfillment of the requirements for the award of Doctor of Philosophy, in the Faculty of Engineering and Information Technology at the University of Technology Sydney.

This thesis is wholly my own work unless otherwise reference or acknowledged. In addition, I certify that all information sources and literature used are indicated in the thesis.

This document has not been submitted for qualifications at any other academic institution.

This research is supported by the Australian Government Research Training Program.

Signature: Production Note:
Signature removed prior to publication.

Date: 31/03/2021

ACKNOWLEDGEMENTS

I would like to take this chance to express my sincere gratitude to my principal supervisor, Dr. Wengui Li, for his invaluable guidance, constructive suggestion, strong support, and meticulous care throughout my Ph.D. study. The practices I got have significantly promoted my professional growth, and meantime awarded me with the abilities, skills, and characteristics that are essential for an independent and mature academic researcher. Hearty thanks also go to my co-supervisors, Prof. Vivian Tam and A/Prof. Xinqun Zhu. Their invaluable advice and support greatly smooth the path to accomplishing this project.

The foremost part of this project, experimental research, was conducted in the laboratory of the Centre for Infrastructure Engineering, West Sydney University, and Tech Lab, University of Technology Sydney. The staff in these laboratories were of great assistance to me, which was indispensable to the completement of this project. Besides, I was greatly benefited from and impressed by their professionalism, sense of responsibility, and enthusiasm. Thus, my heartfelt thanks to all staff in these laboratories.

Moreover, I would like to convey my thanks to many of my colleagues and friends. They indeed improve the quality of my life, boost happiness and reduce stress, as well as help me cope with dilemmas. All these make this period fulfilling and unforgettable. It is my fortune to have them in my life.

Finally, I would like to extend my love and gratitude to my parents. They spare no effort to love and support me. Getting parents like them by my side makes me what I am today– love and hugs to my parents.

Once again, I offer my best regards and grateful thanks to all of those who supported me in any respect during the completion of this study.

Zhuo Tang

March 2021

LIST OF PUBLICATIONS

Journal Papers

Tang, Z., Hu, Y., Li, W. & Tam, V.W.Y. 2019, Uniaxial compressive behaviors of fly ash/slag-based geopolymeric concrete with RAs, *Cement and Concrete Composites*, 104, p. 103375.

Tang, Z., Li, W., Hu, Y., Zhou, J.L. & Tam, V.W.Y. 2019, Review on designs and properties of multifunctional alkali-activated materials (AAMs), Construction and Building Materials, 200, pp. 474-489.

Hu, Y., **Tang, Z.**, Li, W., Li, Y. & Tam, V.W.Y. 2019, Physical-mechanical properties of fly ash/GGBFS geopolymeric composites with RAs, *Construction and Building Materials*, 226, pp. 139-151.

Tang, Z., Li, W., Tam, V.W.Y. & Luo, Z. 2020, Investigation on dynamic mechanical properties of fly ash/slag-based geopolymeric RA concrete, *Composites Part B: Engineering*, 185.

Tang, Z., Li, W., Tam, V.W.Y. & Xue, C. 2020, Advanced progress in recycling municipal and construction solid wastes for manufacturing sustainable construction materials, *Resources, Conservation & Recycling: X*, 6.

Tang, Z., Li, W., Tam, V.W.Y. & Yan, L. 2020, Mechanical behaviors of CFRP-confined sustainable geopolymeric RA concrete under both static and cyclic compressions, *Composite Structures*, 252.

Tang, Z., Li, W., Tam, V.W.Y. & Yan, L. 2020, Mechanical performance of CFRP-confined sustainable geopolymeric recycled concrete under axial compression, *Engineering Structures*, 224.

Tang, Z., Li, W., Peng, Q., Tam, V. W. Y. and Wang, K. 2021, Study on the failure mechanism of geopolymeric recycled concrete using digital image correlation method, *Journal of Sustainable Cement-Based Materials*, 1-20.

Conference Papers

Tang, Z., Li, W., Li P. & Shah S.P., 2018, Durability of Sustainable Construction Materials with Solid Wastes. *The 25th Australasian Conference on Mechanics of Structures and Materials*, ACMSM25, Brisbane, Australia, 4-7 December.

Tang, Z. & Li, W., 2018, Mechanical properties of fly ash/GGBFS based geopolymer concrete incorporating RAs. *The 1st International Conference on Construction Project Management and Construction Engineering*, iCCPMCE 2018, Sydney, Australia, 3-6 December.

Tang, Z. & Li, W., 2019, Rate-dependent behaviors of fly ash-slag geopolymer concrete containing RA. *The 13th Shock & Impact Loads on Structures*, Guangzhou, China, 13-15 December.

TABLE OF CONTENTS

LIST OF ACRONYMS

CAC	Calcium aluminate cement
CFA	Coal-derived fly ash
CFRP	Carbon fiber-reinforced polymer
CG	Coal gangue
CSW	Construction solid waste
CWP	Ceramic waste powder
DCP	Dolomite-concrete powder
DIC	Digital image correlation
DIF	Dynamic increase factor
FRP	Fiber-reinforced polymer
GGBFS	Ground granulated blast furnace slag
GNAC	Geopolymeric natural aggregate concrete
GRAC	Geopolymeric recycled aggregate concrete
ITZ	Interfacial transition zone
LSCT	Linear strain conversion transducers
LOI	Loss on ignition
MIBA	Municipal solid waste incineration bottom ash
MIFA	Municipal solid waste incineration fly ash
MK	Metakaolin
MSW	Municipal solid waste
NA	Natural aggregate
NP	Natural pozzolana
nS	Nano-SiO_2
OPC	Ordinary Portland cement
RA	Recycled aggregate
RAC	Recycled aggregate concrete
RT	Room temperature
SEM	Scanning electron microscopic

SHPB	Splitting Hopkinson pressure bar
SSD	Saturated surface dry
S/S	Stabilization/solidification
SiMn	Silico-manganese
TMWM	Tungsten mining waste mud
WCB	Waste clay brick
WCP	Waste concrete powder
WGP	Waste glass powder
WPSA	Waste paper sludge ash

LIST OF NOTATIONS

Chapter 7

AAE	Average absolute error
c	Constant in the proposed strain enhancement expression
c_1	Constant in the strength enhancement expression
c_2	Constant in the strain enhancement expression
D	Diameter of concrete core (mm)
E_c	Elastic modulus of unconfined concrete (MPa)
E_l	Lateral confinement stiffness
f'_{co}	Peak axial compressive stress of unconfined concrete (MPa)
f^*_{cc}	Peak axial compressive stress of actively confined concrete (MPa)
f'_{cc}	Ultimate axial compressive stress of FRP-confined concrete (MPa)
f_{frp}	Ultimate tensile strength of FRP material
f^*_l	Lateral confining pressure of actively confined concrete (MPa)
f_{lo}	Threshold confining pressure (MPa) in the model proposed by Ozbakkaloglu & Lim (2013)
$f_{lu,a}$	Actual lateral confining pressure at ultimate (MPa)
k_1	Axial strength enhancement coefficient in the proposed model
k_2	Axial strain enhancement coefficient in the proposed model
LTS	Linear trend slope
MSE	Mean square error
n	Constant in proposed strength enhancement model
N	Number of data in the sample
SD	Standard deviation
t_{frp}	Total thickness of FRP jackets
ε^*_{cc}	Axial strain of actively confined concrete at f^*_{cc}

ε_c Axial strain of concrete

ε_{co} Axial strain of unconfined concrete at f'_{co}

ε_{cu} Ultimate axial strain of FRP-confined concrete

ε_{frp} Ultimate tensile strain of FRP material

$\varepsilon_{h,rup}$ Hoop rupture strain of CFRP jackets

ε_l Lateral strain of concrete

ε_o Intercept strain of the axial strain axis of axial strain-lateral strain curve in model proposed by Xiao & Wu (2000)

ε_{vol} Volumetric strain of concrete

ε_θ Circumferential strain of concrete

μ_{tu} Average tangent dilation rate of confined-concrete at ε_{cu} in model proposed by Xiao & Wu (2000)

α Parameter in the proposed strain enhancement expression

β Parameter in the proposed strain enhancement expression

Chapter 8

AAE Average absolute error

a Parameter in the model proposed by Lim & Ozbakkaloglu (2014)

c_1 Parameter in the model proposed by Ozbakkaloglu & Lim (2013)

c_2 Parameter in the model proposed by Ozbakkaloglu & Lim (2013)

D Diameter of concrete core

E_1 Slope of the initial branch of axial stress-strain curve

E_2 Slope of the second branch of axial stress-strain curve

E_c Elastic modulus of unconfined concrete

E_{frp} Elastic modulus of FRP material

E_l Lateral confinement stiffness

E_{re}	Reloading modulus
$E_{\sec u}$	Unloading secant modulus
$E_{un,0}$	Residual modulus
$f_{co}^{'}$	Peak axial compressive stress of unconfined concrete
f_{cc}^{*}	Peak axial compressive stress of actively confined concrete
$f_{cc}^{'}$	Ultimate axial compressive stress of FRP-confined concrete
f_{frp}	Ultimate tensile strength of FRP material
f_{l}^{*}	Lateral confining pressure of actively confined concrete
f_{lo}	Threshold confining pressure in the model proposed by Ozbakkaloglu & Lim (2013)
$f_{lu,a}$	Actual lateral confining pressure at ultimate condition
f_{new}	New stress
f_{un}	Unloading stress
k_1	Axial strength enhancement coefficient
k_2	Axial strain enhancement coefficient
MSE	Mean square error
N	Number of data in sample
SD	Standard deviation
t_{frp}	Thickness of FRP jackets
ε_{cc}^{*}	Axial strain of actively confined concrete at f_{cc}^{*}
ε_{c}	Axial strain of concrete
ε_{co}	Axial strain of unconfined concrete at $f_{co}^{'}$
ε_{cu}	Ultimate axial strain of FRP-confined concrete
ε_{frp}	Ultimate tensile strain of FRP material
$\varepsilon_{h,rup}$	Hoop rupture strain of CFRP jackets

ε_l	Lateral strain of concrete
ε_{new}	Strain of reloading curve at stress f_{new}
ε_{un}	Unloading strain
ε_o	Intercept strain of the axial strain axis of axial strain-lateral strain curve in the model proposed by Xiao & Wu (2000)
ε_{pl}	Plastic strain
μ_{tu}	Average tangent dilation rate of confined-concrete at ε_{cu} in model proposed by Xiao & Wu (2000)
ρ	Confinement stiffness ratio
ϕ_1	Stress deterioration ratio

LIST OF FIGURES

LIST OF TABLES

ABSTRACT

Geopolymeric recycled aggregate concrete (GRAC) is a type of geopolymeric concrete that recycled aggregate (RA) was utilized to replace the virgin aggregate. Thus, GRAC can provide the environmental benefits of both geopolymeric concrete and recycled aggregate concrete (RAC). Specifically, geopolymeric concrete offers a valuable method for recycling industrial by-products and reducing greenhouse gas emissions associated with the production of ordinary Portland cement. As for the RAC, the merits consist of, but not limited to, the avoidance of natural resource extraction, reduced landfills of construction and demolition waste (C&DW), and diminished transportation of wastes. Accordingly, GRAC suggests a route with a high degree of environmental friendliness for concrete materials.

In this study, fly ash and ground granulated blast furnace slag combination based geopolymeric concrete incorporating C&DW based RA was developed and evaluated. Firstly, the engineering properties of GRAC were studied. Subsequently, quasi-static and dynamic compressive tests were conducted on GRAC, respectively, by using a high-force servo-hydraulic test system and a Ø80-mm split Hopkinson pressure bar apparatus. Special attention was devoted to the failure patterns, stress-strain curves, and energy absorption capacity. Moreover, the failure process and mechanism of GRAC under compression was investigated with the help of a digital image correlation system.

Existing studies have validated that external confinement by confining materials is an effective strategy to enhance the mechanical and long-term performance of RAC or even to qualify RAC with structural purposes. Therefore, carbon fiber-reinforced polymer (CFRP) material was utilized in this study to provide external confinement for GRAC. Experimental studies on the mechanical behaviors of CFRP-confined GRAC under monotonic and cyclic compression were carried out. The failure model, stress-strain relationship, and axial-lateral strain relationship were investigated. Further, the results were compared with the predictions by existing models to evaluate these models' applicability to CFRP-confined GRAC.

Overall, this study could support the producers of C&DW to gain considerable interest by applying the C&DW-based RA into geopolymeric concrete and can benefit the stakeholders of geopolymeric material industries who seek more sustainability in their products.

CHAPTER 1: INTRODUCTION

1.1 Background

1.1.1 Geopolymeric recycled aggregate concrete

Stimulated by the booming economy, population growth, and rapid urbanization, the construction sector worldwide is fueled at a sheer growth rate. However, construction, by nature, is not an environmentally friendly process. For instance, 25–40% of the world's carbon emissions are attributed to construction. Besides, construction consumes substantial natural resources and produces a lot of waste that ends up in landfills. Those issues have aroused stinging concerns from the nations, municipalities, and individuals. As a result, the concept of adopting green chemistry and technologies has been increasingly recognized and included in the construction sector.

Concrete is the most widely used construction material, owing to its inherent advantages, such as the cost of cheapness, extended service life, and availability of raw materials. It has been estimated that approximately 4.5 billion tons/year of concrete are produced globally, and this number is also growing at lightning speed, with a rate of 2.5% per year (Kaliyavaradhan & Ling 2017; Meng et al. 2019). However, the production of ordinary Portland cement (OPC), the main binder in concrete, consumes over 3% of the world's energy and contributes to almost 8% of the anthropogenic greenhouse gas emission (Nidheesh & Kumar 2019; van Oss & Padovani 2002). Thus, seeking an alternative to OPC concrete has attracted considerable attention from both industry and academia.

Among many attempts, geopolymeric concrete is treated as a viable alternative to OPC concrete. Geopolymeric concrete is a type of concrete, which is developed by synthesizing aluminosilicate materials with alkaline solutions to form the slurry to bind aggregate particles in the production of concrete (Duxson et al. 2006). In addition to low energy consumption and carbon footprint, geopolymeric concrete demonstrates good performance, such as high mechanical properties, excellent creep resistance, low drying shrinkage, and good stability under acid environment (Bernal et al. 2014b; Ding et al. 2016; Provis 2014; Reddy et al. 2016; Zhang et al. 2017).

Even though, it should be noted that aggregates account for the major constituent of geopolymeric concrete as the nature of concrete. With the increasing demand for concrete arising from the growing infrastructure construction, the scarcity of natural aggregate (NA) is becoming more serious. Meanwhile, excessive construction and demolition waste (C&DW) has aroused great concern from the society, economy, and environment. Reusing C&DW into new engineering construction, for example, as a constituent in new concrete, is considered as an integral part of reversing this trend. Tremendous efforts have been made to use recycled aggregate (RA) derived from C&DW for producing concrete (Silva et al. 2014). The utilization of C&DW waste as aggregate in new concrete would potentially reduce the aggregate costs. Additionally, it would also promote the sustainability in the construction of infrastructure by reducing construction debris being placed in landfills and minimizing greenhouse-gas emissions associated with aggregate disposal and transportation (Behera et al. 2014; del Rio Merino et al. 2010; Siad et al. 2017). Till now, the research related to recycled aggregate concrete (RAC) has been going on for nearly 70 years (Guo et al. 2018; Xiao et al. 2012b). It has been established that its use is both commercially and technically viable (Shi et al. 2016; Tam & Tam 2006), and nowadays, it has been used for non-structural or even structural applications (Li 2009; Poon & Chan 2007; Tam et al. 2018). To follow this trend, the investigation on the geopolymeric concrete incorporated with RA, namely geopolymeric recycled aggregate concrete (GRAC), is gaining momentum and significance.

There have been only a few relevant studies on GRAC so far. Shi et al. (2012) first applied RA in geopolymeric concrete and studied the influences of using RA as the coarse aggregate on the mechanical and microstructural behavior of geopolymeric concrete. After that, several researchers carried out investigations on GRAC in terms of physical, mechanical, and durability properties (Liu et al. 2016; Nuaklong et al. 2016; Nuaklong et al. 2018a; Shaikh 2016). Generally, the adverse effect of the RA replacement on geopolymeric concrete is similar to that on OPC concrete. However, due to the different matrix formation processes, the geopolymeric paste is composed of more homogeneous and denser substances than OPC paste. This, therefore, leads to comparatively higher strength in GRAC (Shi et al. 2012). Moreover, it has been reported that the refined

microstructure of geopolymeric paste contributes to GRAC with better durability properties than OPC-based RAC (Nuaklong et al. 2016; Shaikh 2016). Liu et al. (2016) observed that no interfacial transition zone (ITZ) could be identified around the interface between the old cement paste of RA and the new geopolymeric paste. Recently, Khedmati et al. (2019) found that geopolymeric material could fill the pre-existing incomplete interphase within the RA. Besides, it has been demonstrated the feasibility of using RA for making lightweight geopolymeric concrete and pervious geopolymeric composites (Posi et al. 2013; Sata et al. 2013). Although these results reveal the excellent prospects of GRAC, the current knowledge for GRAC is far from supporting its safe and reliable application and design. Therefore, it is necessary to fully characterize the properties of GRAC before future promotion and application.

1.1.2 FRP-confined GRAC

External confinement by confining materials has been treated as an effective strategy to enhance the mechanical and long-term performance of RAC or even to qualify RAC with structural purposes (Gao et al. 2019; Nour & Güneyisi 2019; Tang et al. 2018; Xu et al. 2019a). Moreover, using fiber-reinforced polymer (FRP) composites as confining materials has attracted increasing attention because of the superiority, such as high strength-to-weight ratio, commendable thermo-mechanical performance, and excellent corrosion resistance. In the literature, studies of FRP-confined RAC have been documented well (Chen et al. 2016a; Gao et al. 2016; Jiang et al. 2019; Teng et al. 2016; Xiao et al. 2012a; Xie & Ozbakkaloglu 2016; Yan et al. 2017; Zeng et al. 2018; Zhao et al. 2014). For instance, Xiao et al. (2012a) were the first who suggested using FRP composites to enhance RAC performance, in which RAC with different RA replacement percentages was confined by glass FRP tubes. Afterward, Zhao et al. (2014) and Chen et al. (2016a) investigated the effects of the RA replacement ratio and FRP thickness on the compressive behavior of RAC confined by glass FRP and carbon FRP (CFRP), respectively. Xie & Ozbakkaloglu (2016) recently compared the performance of FRP-confined RAC with circular cross-section and square cross-section. It was concluded that, under similar confinement levels, the circular specimens showed higher compressive strength but lower ultimate axial strain, in comparison with the square ones.

Analogously, FRP confinement might also be able to provide beneficial effects to the performance of GRAC. However, it should be pointed out here that, to the best of the authors' knowledge, no study has been reported on the behavior of FRP-confined GRAC. The only existing studies related were conducted by Ozbakkaloglu & Xie (2016) and Lokuge & Karunasena (2015), who studied the behavior of FRP-confined geopolymeric concrete. Based on the test results, it was found that under a given confinement ratio, FRP-confined geopolymeric concrete exhibited a similar strength enhancement to, but a lower axial strain enhancement than the counterpart of FRP-confined conventional concrete (Ozbakkaloglu & Xie 2016). Similar results have also been observed when comparing the behaviors of FRP-confined RAC and FRP-confined conventional concrete: specifically, the existing models for FRP-confined conventional concrete exhibited some discrepancies in predicting the behavior of FRP-confined RAC (Gao et al. 2016; Teng et al. 2016; Xie & Ozbakkaloglu 2016; Yan et al. 2017; Zhou et al. 2016). Therefore, it is evident that the behavior of FRP-confined GRAC needs to be properly understood.

On the other hand, as the porous nature of RA and the old cement mortar adhered to the aggregate surface, the RA replacement usually causes a reduction in the compressive strength and stiffness (Tam et al. 2018; Xiao et al. 2012b). Moreover, this effect has been reported to be additionally pronounced when the concrete is subjected to cyclic loading, resulting in the rapid degradation in the stiffness and strength (Hu et al. 2018; Liu et al. 2019a; Ma et al. 2013; Xiao et al. 2013a). Also, the current practice for evaluating the seismic performance is mainly based on the response under cyclic loading. Hence, the mechanical behavior of concrete under cyclic axial compression is of particular importance for the accurate modeling of the corresponding structure members under seismic loading. Accordingly, for the safe and reliable design of FRP-confined GRAC, it is necessary to comprehend its mechanical behavior under cyclic loading.

1.2 Research objectives and scope

The main objective of this work is to evaluate the properties of GRAC, in which the combination of fly ash and ground granulated blast furnace slag (GGBFS) is used as the precursor, and RA is utilized as coarse aggregate. Firstly, the engineering properties of

GRAC were studied. Subsequently, the focuses are concentrated on the quasi-static and dynamic compressive behaviors of GRAC. Afterward, the failure process and mechanism of GRAC under compression are investigated. Furthermore, the mechanical behaviors of CFRP-confined GRAC under both monotonic and cyclic compressive loading are studied.

The specific objectives are listed as follows:

- To review the progress in recycling solid waste materials into the manufacture of geopolymeric composites;
- To develop sustainable GRAC by using the fly ash and GGBFS combination as the precursor and utilizing RA as coarse aggregate;
- To characterize the engineering properties of the developed GRAC;
- To investigate and compare the static and dynamic compressive behaviors of GRAC;
- To propose an empirical model to describe the static stress-strain curve of GRAC;
- To explore the failure process and mechanism of GRAC under compression;
- To study the mechanical behaviors of CFRP-confined GRAC under monotonic and cyclic compression;
- To examine the applicability of existing models in predicting the behavior of CFRP-confined GRAC under monotonic and cyclic compression.

1.3 Research methodology

1.3.1 Advanced progress in recycling municipal and construction solid wastes for geopolymeric composites

A literature review is carried out to deals with the anthology and analyses of the achievements previously obtained when municipal and construction solid waste was employed in the manufacture of geopolymeric composites. Furthermore, the benefits and limitations of these resulted geopolymeric composites incorporating municipal and construction solid waste are summarized.

1.3.2 Engineering properties of sustainable GRAC

This work is attempted to utilize fly ash/GGBFS combination as the precursor and RA as coarse aggregate to develop the sustainable GRAC. The physical (i.e., workability, setting time, density, water absorption, sorptivity, and volume of voids) and mechanical (i.e., compressive strength, flexural strength, and splitting tensile strength) properties of the developed GRAC are evaluated. Moreover, the scanning electron microscopic (SEM) is conducted to characterize the microstructure of GRAC.

1.3.3 Static compressive behavior of sustainable GRAC

The static compressive stress-strain behavior of GRAC is studied by using a high-force servo-hydraulic test system. Special attention is devoted to the failure behaviors and patterns, stress-strain characteristics (i.e., the peak stress, elastic modulus, peak strain, and ultimate strain), and energy absorption capacity. Furthermore, a stress-strain model is developed by modifying the parameters of existing models to describe the uniaxial stress-strain behavior of GRAC.

1.3.4 Dynamic compressive behavior of sustainable GRAC

A Ø80-mm split Hopkinson pressure bar apparatus is employed in this study. The stress-strain behavior of GRAC under dynamic compression is investigated and then compared with that under quasi-static compression. The effects of the strain rate on compressive behaviors of GRAC are studied, including the failure patterns, stress-strain behavior, and energy dissipation.

1.3.5 Failure process and mechanism of sustainable GRAC

In this work, sliced GRAC specimens with a dimension of 100×100×10 mm are subjected to static compression. The crack evolution and failure mode of specimens are observed during the test. Then, the displacement field and strain distribution over the specimen surfaces are obtained and analyzed by using the digital image correlation (DIC) technique. Based on the results, the failure process and mechanism of GRAC under compression are further investigated.

1.3.6 Mechanical performance of CFRP-confined sustainable GRAC under monotonic compression

In this work, GRAC is confined by CFRP jackets. The major test parameters include (1) coarse aggregate type, (2) number of CFRP layers, and (3) slag content. Special attention is devoted to the stress-strain relationship, dilation behavior, and ultimate condition. The test results are also compared with the predictions by existing stress-strain models proposed for FRP-confined concrete to examine their applicability to CFRP-confined GRAC. Empirical models are developed to predict the ultimate condition of CFRP-confined GRAC.

1.3.7 Mechanical performance of CFRP-confined sustainable GRAC under cyclic compression

This work experimentally studies the static and cyclic compression behaviors of CFRP-confined GRAC. The parameters considered in this study include (1) aggregate replacement ratio, (2) thickness of CFRP jackets, and (3) loading scheme (i.e., monotonic compression and cyclic compression). Special attention is devoted to the failure model, compressive stress-strain behavior, and axial-lateral strain relationship. Subsequently, detailed discussions are provided regarding the key shape factors that govern the cyclic stress-strain curves. Meanwhile, the results are compared with the predictions by existing models for evaluating the applicability of these models to CFRP-confined GRAC.

1.4 Layout of the thesis

This thesis is presented in nine chapters, and the contents of each chapter are as follows.

Chapter 1: This chapter introduces the background, research objectives and scope, and research methodology for this project.

Chapter 2: This chapter contains a literature review on the recycling municipal and construction solid waste materials into the manufacture of geopolymeric composites.

Chapter 3: This chapter presents the development of the sustainable GRAC. Additionally, the engineering properties of GRAC are experimentally investigated and informed in this chapter.

Chapter 4: This chapter provides an experimental study on the mechanical behavior of GRAC under static compression. The failure behaviors, stress-strain characteristics, and energy absorption capacity are obtained and then discussed. Moreover, an empirical model is developed to describe the stress-strain curves of GRAC.

Chapter 5: This chapter shows an experimental study on the mechanical behavior of GRAC under dynamic compression. The failure patterns, stress-strain behavior, and energy dissipation of GRAC under different strain rates are discussed and compared.

Chapter 6: This chapter establishes an experimental investigation to understand the failure process and mechanism of GRAC under static compression by using a DIC system. The crack evaluation and failure mode of the specimens are observed. Meanwhile, the displacement field and strain distribution over the surface of the specimen are analyzed.

Chapter 7: This chapter presents experimental work on the mechanical behavior of CFRP-confined GRAC under monotonic compression. The stress-strain relationship, dilation behavior, and ultimate condition are examined and discussed. This chapter also examines the applicability of the existing empirical models in predicting the behavior of mechanical behavior of CFRP-confined GRAC.

Chapter 8: This chapter provides experimental research on the mechanical behavior of CFRP-confined GRAC under cyclic compression. The failure model, compressive stress-strain behavior, and axial-lateral strain relationship are examined and discussed. The key shape factors that govern the cyclic stress-strain curves are further analyzed and then compared with the predictions by the existing empirical models.

Chapter 9: This chapter highlights the main contributions of this work and the recommendations for future research.

CHAPTER 2: LITERATURE REVIEW

In recent years, the concept of adopting green chemistry and technologies for environmental sustainability has been increasingly recognized and included. Most notably, the traditional concept, in which waste is regarded as pollution, has been progressively shifting towards the new perspective that waste is treated as a resource. Against this scenario, some attractive achievements have been made in recycling solid waste materials for the manufacture of geopolymeric composites.

This chapter, therefore, deals with the anthology and analyses of the achievements previously attained when municipal and construction solid waste was employed in geopolymeric composite manufacturing. In addition, the benefits and limitations of these resulted geopolymeric composites incorporating municipal and construction solid waste are evaluated. Overall, this work examines the potential of using solid waste materials as a component in geopolymeric composites, including municipal and construction solid wastes.

2.1 Municipal solid waste

Municipal solid waste (MSW) generally refers to domestic and commercial waste generated within the jurisdiction of a municipal authority. In most cases, MSW mainly consists of organic material, waste paper, waste glass, plastic waste, tin cans, textiles, etc. As the world hurtling toward the urban future, the growth rate of MSW has exceeded the speed of urbanization (Sun et al. 2018). It has been reported that the global MSW per annum is expected to reach 2.2 billion by 2025, which is tripled of 0.68 billion in 2002 (Hoornweg & Bhada-Tata 2012). Figure 2.1 presents the annual MSW generation from the selected countries (Waste Atlas 2019). Consequently, researchers have attempted to employ this waste for the preparation of geopolymeric composites. Surprisingly, they have encountered exciting and impressive discoveries in this regard. Therefore, the following part deals with the emerging research studies on recycling MSW into geopolymeric composites, including municipal solid waste incinerator ash, waste paper, rubber waste, plastic waste, and others.

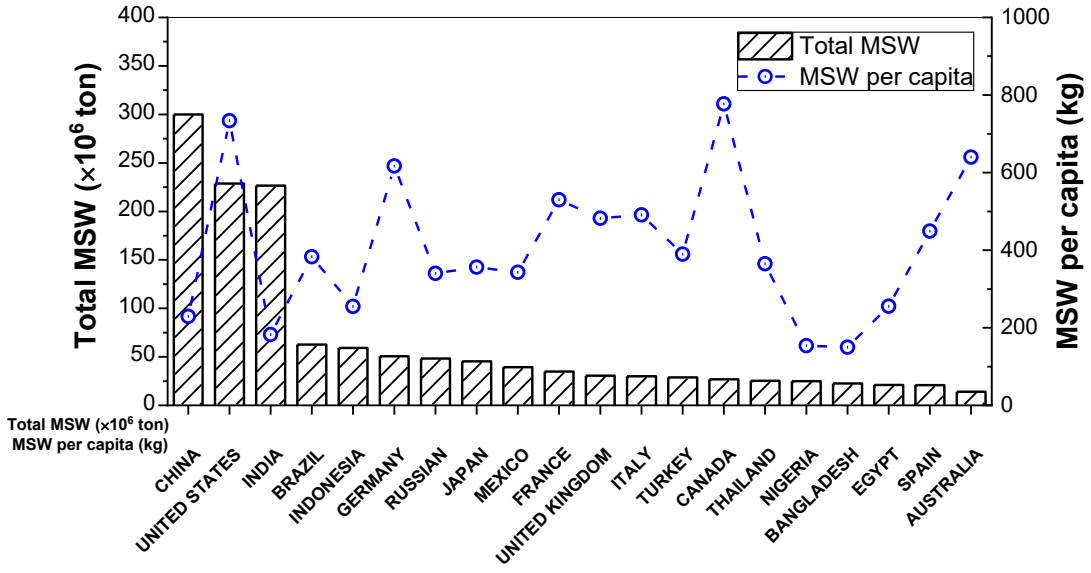

Figure 2.1. Annual MSW generation from selected countries (Waste Atlas 2019)

2.1.1 Municipal solid waste incineration ash

Currently, incineration is a commonly used practice against the context of substantial MSW. Incineration can reduce waste volume and mass by up to 90% and 70%, respectively (Silva et al. 2014). Additionally, incineration allows for producing energy from waste. While after the incineration process, two types of ashes are generated, namely municipal solid waste incineration bottom ash (MIBA) and municipal solid waste incineration fly ash (MIFA). MIBA is the residue with large particles, which is found at the bed of the incinerator, whereas MIFA corresponds to the very fine particles collected by the air pollution control system (Sarmiento et al. 2019). As different characteristics of MIBA and MIFA, their utilization in geopolymeric composites is discussed below separately.

MIBA

MIBA accounts for about 80% of the waste combustion residues and contains much less toxic organic substances in comparison with MIFA. Thus, there is great potential of the utilization of MIBA rather than sending it to a landfill. Although there have been considerable efforts to valorize this waste by using it as raw material for cement

production or as filler for road construction, several significant drawbacks limit the wide applications of MIBA, especially the leach of heavy metals (Siddique 2010a).

The chemical composition of the MIBA from the select studies is presented in Figure 2.2(a), including the average value as well as the minimum and maximum values. Also, the mineralogy of MIBA is provided in Figure 2.2(b). Obviously, MIBA can potentially be utilized as a geopolymeric precursor due to the presence of both amorphous fraction and high content silica and aluminum oxide. Initially, MIBA was used as a partial replacement for the precursors during the synthesis of geopolymeric composites (Lancellotti et al. 2013). Lancellotti et al. (2013) demonstrated that MIBA was suitable source material for producing metakaolin blended geopolymers, with the contents up to 70% of the precursor.

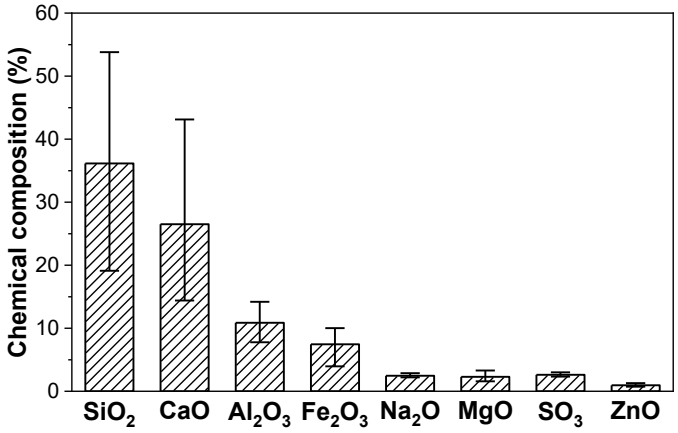

(a) Chemical composition of MIBA from the selected studies. Data from Chen et al. (2016b); Gao et al. (2017); Huang et al. (2018b); Huang et al. (2019a); Xuan et al. (2019); Zhu et al. (2018)

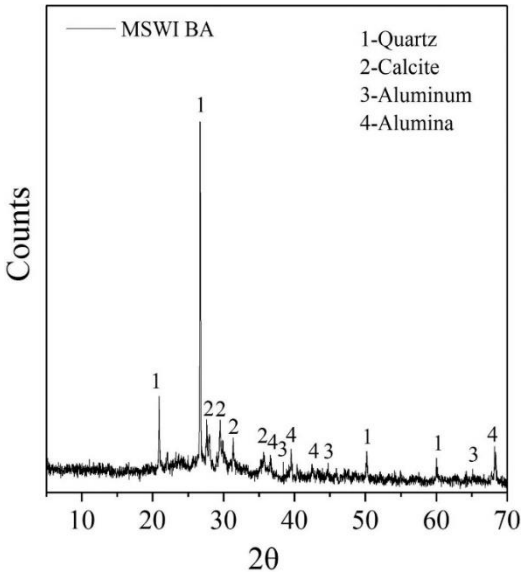

(b) XRD pattern of MIFA (1, CaClOH; 2, NaCl; 3, KCl; 4, SiO_2; 5, $CaCO_3$) (Li et al. 2019b)

Figure 2.2. Chemical composition and mineralogy of MIBA

The follow-up studies then examined the feasibility of using MIBA as the only geopolymeric precursor (Chen et al. 2016b; Lancellotti et al. 2015; Zhu et al. 2019a). For instance, through microstructure analysis and composition characterization, Chen et al. (2016b) have identified the successful geopolymerization of MIBA, and the formation of a new crystal phase consisting of silica, aluminum, and sodium, as shown in Figure 2.3.

Similar results have also been observed in the studies by Lancellotti et al. (2015) and Zhu et al. (2019a). Furthermore, numerous studies have investigated the heavy metal binding effect of MIBA-based geopolymeric composites. It is consistently believed that geopolymerization is able to immobilize the majority of hazardous elements in MIBA effectively, and the produced geopolymeric composites can be characterized as non-hazardous materials (Chen et al. 2016b; Gao et al. 2017; Zhu et al. 2019b).

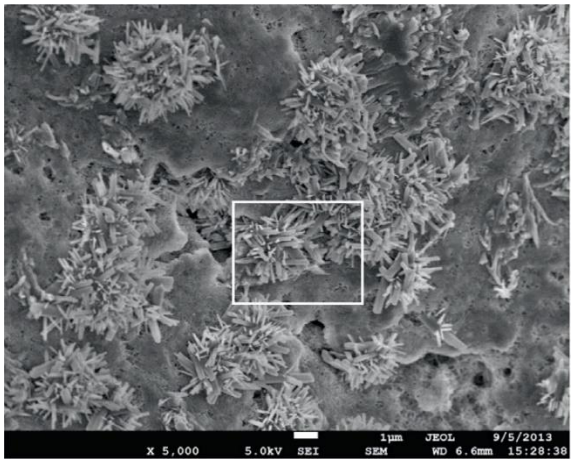

(a) SEM image

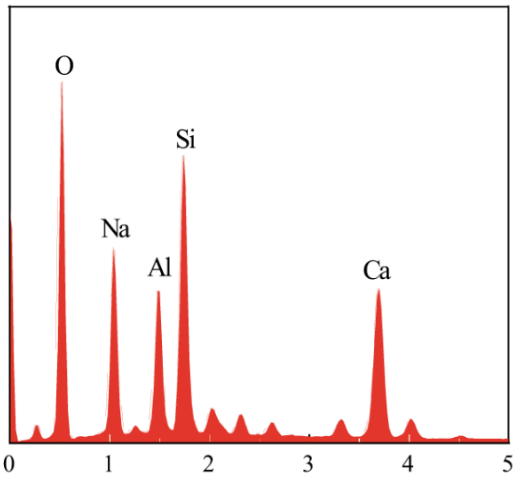

(b) EDX spectrum

Figure 2.3. SEM/EDX of Na–Si–Al system crystal in MIBA geopolymer (Chen et al. 2016b)

It should, however, be noted that the resulting MIBA-based geopolymeric composites usually possess low mechanical performance and highly porous structures (Lancellotti et al. 2015). This is mainly attributed to that the metallic aluminum presented in MIBA can react with alkaline solution and then generate hydrogen gas (Chen et al. 2016b). Consequently, MIBA has been employed as the precursor partially or fully to synthesize aerated geopolymeric composites (Chen et al. 2016b; Xuan et al. 2019). Chen et al. (2016b) produced the MIBA aerated geopolymeric pastes with the dry density ranging from 600 kg/m^3 to 1000 kg/m^3. The test results also showed that the alkaline concentration, the ratio of liquid to solid, and mixing duration were the important factors in controlling the physical and mechanical properties of the produced MIBA aerated geopolymer. Likewise, in the study of Xuan et al. (2019), the aerated geopolymeric pastes synthesized by the utilization of MIBA and waste glass powder exhibited low density values ranging from 494 kg/m^{3}to 1295 kg/m^3, and low thermal conductivities ranging from 0.14 W/m·K to 0.38 W/m·K. Besides, in comparison with the traditional aerated concrete, the prepared aerated geopolymeric concrete had less spherical air voids and wider air-void size distribution (Xuan et al. 2019).

Additionally, researchers adopted MIBA as a gas-forming additive to aerate geopolymeric composites (Zhu et al. 2018; Zhu et al. 2019b). For instance, Zhu et al. (2018) compared the effects of MIBA and commercial aluminate powder on lightweight aerated geopolymers. The results showed that MIBA had a comparable reaction rate and gas generation capacity to the commercial aluminate powder. Moreover, the resulting MIBA aerated geopolymers had a density of as low as 860 kg/m^3 and thermal conductivity of 0.33 W/m-K, which was comparable to the reference aerated geopolymers based on commercial aluminate powder.

On the other hand, several studies have been conducted to use pre-treatments such as alkaline treatment, vitrification, and wet grinding to eliminate the foaming and expansion effects by metallic aluminate presented in MIBA (Zhu et al. 2019b). In the series of studies by Huang et al. (2019a), the alkaline treatment was employed. Specifically, MIBA was mixed with sodium hydroxide solution to form slurry and to age this slurry for 4 hr,

prior to preparing MIBA-based geopolymeric composites. Meanwhile, several additives were incorporated during the geopolymeric composite preparation for further improving the performance (Huang et al. 2018b; Huang et al. 2019a; Huang et al. 2019b). The test results showed that the resulted geopolymeric composites possessed satisfactory compressive strength and durability due to the high degree of geopolymerization and dense microstructure (Huang et al. 2018b; Huang et al. 2019b).

More to the point of utilizing MIBA as a precursor or gas-forming additive, researchers have evaluated the feasibility of the application of MIBA to substitute the aggregate in geopolymeric composites. The study of Gao et al. (2017) was on this aspect. Here, MIBA was employed as a substitute for a maximum of 50% fine aggregate (by volume) in geopolymeric mortar. Although MIBA negatively affected the strength for its porous and fragile structure, no expansion and cracking was observed caused by the metallic aluminate from MIBA. Eventually, the compressive strength of 35–56 MPa was achieved, suggesting wide application potentials and high reuse rates of MIBA in geopolymeric composites. Furthermore, the leaching behavior of formed products met the relevant legislation, confirming the advantages of using geopolymeric composites again.

MIFA

MIFA is a fine powder extracted from the combustion gas by the air pollution control devices. Although the weight of MIFA is only 2-5 wt.% of the original MSW before incineration, global MIFA generation is huge and growing up with the increased urbanization and population (Siddique 2010b). For instance, the quantity of MIFA is estimated to reach 1.0×10^7 tons/year by 2020 in China (Xu et al. 2019b). Furthermore, MIFA contains high amounts of heavy metals such as chromium, cadmium, lead, and zinc, etc., and, therefore, is considered as hazardous waste (Ashraf et al. 2019). In addition to the heavy metals, several types of soluble salts are the other cause of concern (Siddique 2010b). Therefore, a method that can attenuate this harm and effectively utilize MIFA is urgently needed.

As geopolymeric composites could serve as waste immobilizing agents in the stabilization/solidification (S/S) system of hazardous waste (Ji & Pei 2019), numerous studies have evaluated the effectiveness of utilizing geopolymers composites for the S/S of MIFA. As shown in Table 2.1, special attention has been given to the role of synthesis parameters, such as precursor type and content, alkaline activator type and dosage, and curing process, on the S/S efficiency. Overall, geopolymeric composites have been proved to be a high-efficiency material for the S/S of MIFA, thus contributing to the reduction in the leachability of toxic elements to the environment. For instance, Lancellotti et al. (2010) incorporated MIFA into the geopolymeric matrix based on coal-derived fly ash (CFA). The test results showed that the release of heavy metals from geopolymeric composite was much lower than the value of the as-received MIFA, such as the leachable chromium was reduced from 1.57 down to 0.02 mg/L, copper from 3.80 down to 0.04 mg/L, and lead from 11.5 down to 0.1 mg/L. Besides, a recent study demonstrated the excellent long-term S/S efficiency of MIFA-containing geopolymeric composites even exposed to the aggressive environment (Jin et al. 2016). Specifically, the leaching concentration of heavy metals (e.g., chromium, copper, lead, zinc, mercury, and cadmium) still remained relatively low after being immersed in aqueous alkali or leached by acid rain. Furthermore, the mechanism of the heavy metal immobilization mechanisms of geopolymeric composites containing MIFA has been elucidated by several researchers (Shiota et al. 2017). The mechanism of heavy metals immobilization is believed to perform through both physical and chemical ways, involving the physical encapsulation by the geopolymeric matrix, ion exchange of Friedel's salt, and geopolymer adsorption (Liu et al. 2019b; Shiota et al. 2017).

Table 2.1 Recent research on the applications of MIFA in geopolymeric composites

Precursor[1]	Activator	Curing condition[2]	MIFA content	Leachate analysis[3]	Compressive strength	Reference
Blend with aluminosilicate-rich precursors						
Uncalcined coal gangue	NaOH+ Na_2SiO_3	30, 45, 60, 75 or 90 °C for 24 hrs	10–60%	Cu, Zn, Pb, and Cd	1.7-28.7 MPa (7 days) 2.1-31.4 MPa (28 days)	Zhao et al. (2019)
GGBFS and CFA	NaOH+Na_2SiO_3	RT	20–40%	Cu, Zn, Pb, Cr, Ba, Se	Grate-firing bed MIFA: 11.7-20.2 MPa (28 days) Fluidized bed MIFA: 28.7-36.7 MPa (28 days)	Xu et al. (2019b)
Granulated lead smelting slag	NaOH+Na_2SiO_3	RT	20–80 %	Zn, Pb, As, Cd, Ni, Cr, Ba, and Cu	5.1-12.5 MPa (7 days) 5.4-15.3 MPa (28 days)	Liu et al. (2019b)
Red mud	NaOH+Na_2SiO_3	RT	20–50%	Zn, Pb, As, Cd, Ni, Cr, Ba, Be, Cu, Se, Sb, Co, and V	–	Li et al. (2019b)
Volcanic ash	NaOH+Na_2SiO_3	RT	50–100%	Pb, Cr, Hg, Zn, Ba, Se, Ag, and Cd	1.1-7.2 MPa (7 days) 1.4-10.5 MPa (28 days)	Tome et al. (2018)
Dehydrated pyrophyllite	NaOH+Na_2SiO_3	60, 80, and 105 °C for 34 hrs	50%	Cs		Shiota et al. (2017)
Bayer red mud	NaOH	RT	40–60%	Cu, Zn, Pb, and Cr	1.4-3.9 MPa (7 days) 1.2-1.7 MPa (28 days)	Ye et al. (2016)

MK	$NaOH+Na_2SiO_3$	RT	40%	Pb, Zn, Cu, Cr, Cd, and Hg	36.1 MPa (28 days)	Jin et al. (2016)
CFA	$NaOH+Na_2SiO_3$	100 °C for 7 days	20–100%	Pb, As, Cd, Cr, Ba, Se, Ag, and Hg	10.1-34.3 MPa (7 days)	Diaz-Loya et al. (2012)
CFA, GGBFS, kaolin, and MK	$NaOH+Na_2SiO_3$; $KOH+K_2SiO_3$	RT, and 60 °C for 7 days	23–26%	Pb, Cd, Cr, Zn, and Ba	1-3 MPa (7days) 1-9 MPa (7days)	Luna Galiano et al. (2011)
MK	$NaOH+Na_2SiO_3$	50 °C for 24 hrs	17%	Cr, Cd, Ni, Cu, and Pb	–	Lancellotti et al. (2010)
Use as a neat precursor						
MIFA	NaOH; $NaAlO_2$; Na_2SiO_3	RT	100%	Cu, Zn, Pb, and Cd	7.1-18.8 MPa (14 days)	Zheng et al. (2016)
MIFA	$NaOH+Na_2SiO_3$	RT	100%	Cr, Cu, and Zn	Unwashed MIFA: 15.9 MPa (28 days) Water-washed MIFA: 22.7 MPa (28 days)	Zheng et al. (2011)

Note: 1. GGBFS, CFA, and MK denote ground granulated blast furnace slag, coal-derived fly ash, and metakaolin, respectively; 2. RT represents room temperature; 3. Ag–silver, As–arsenic, Ba–barium, Be–beryllium, Cd–cadmium, Co–cobalt, Cr–chromium, Cs–cesium, Cu–copper, Hg–mercury, Ni–nickel, Pb–lead, Se–selenium, Sb–antimony, V–vanadium, Zn–zinc

The feasibility of MIFA as a precursor in the production of geopolymeric composites has also been assessed. Figure 2.4 presents the chemical composition of MIFA from the select studies, which includes the average, minimum, and maximum values, and the XRD pattern of MIFA. In most cases, the low amounts of reactive SiO_2- and Al_2O_3-containing phases presented in MIFA do not allow the formation of chemically stable geopolymeric composites without any addition (Tome et al. 2018). Alternatively, the partial replacement of aluminosilicate-rich precursors by MIFA usually resulted in a decrease in mechanical strength (Diaz-Loya et al. 2012; Liu et al. 2019b). Even though the relatively low strength, most resulting products still meet the landfill waste acceptance criteria, further demonstrating the viability of the S/S of MIFA using geopolymeric composites before the landfill disposal (Luna Galiano et al. 2011; Ye et al. 2016). However, there also exist studies demonstrating that MIFA exhibited good reactivity in alkaline medium, and thus good mechanical strength for construction purposes (Diaz-Loya et al. 2012; Zhao et al. 2019; Zheng et al. 2016). For instance, compressive strength up to 18.8 MPa at 14 days was obtained in geopolymeric pastes based on neat MIFA by Zheng et al. (2016). Diaz-Loya et al. (2012) synthesized geopolymeric concrete by the gradual introduction of MIFA to CFA from 20% to 100%. The achieved compressive strength and flexural strength varied from 10.1 MPa to 34.3 MPa and from 1.0 MPa to 3.5 MPa, respectively, after curing for 7 days at 100 °C.

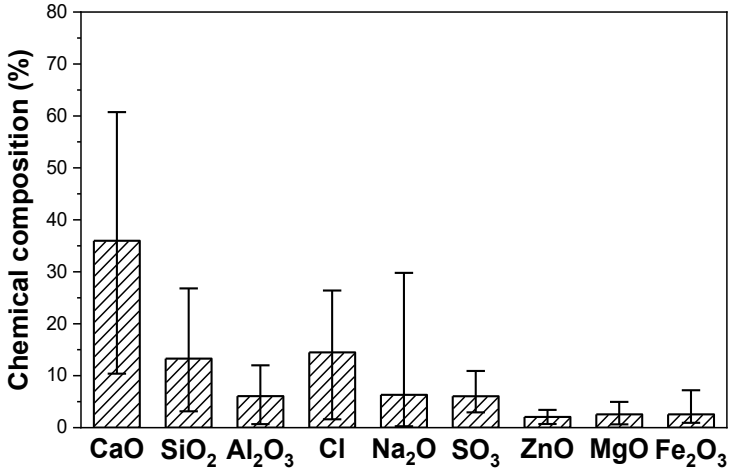

(a) Chemical composition of MIFA from the selected studies. Data from Diaz-Loya et al. (2012); Jin et al. (2016); Lancellotti et al. (2010); Li et al. (2019b); Liu et al. (2019b); Luna Galiano et al. (2011); Tome et al. (2018); Xu et al. (2019b); Ye et al. (2016); Zhao et al. (2019); Zheng et al. (2011); Zheng et al. (2016)

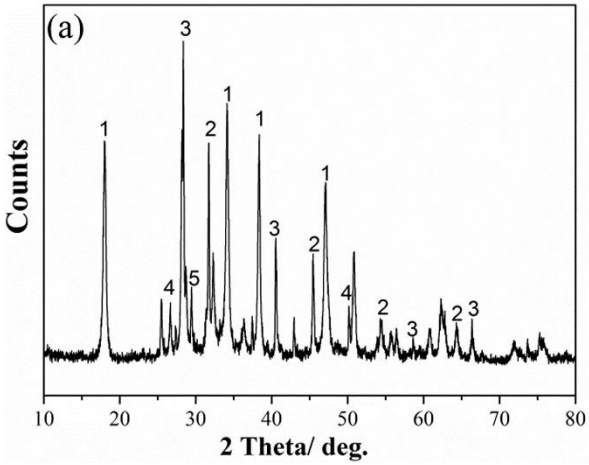

(b) XRD pattern of MIFA (1, CaClOH; 2, NaCl; 3, KCl; 4, SiO2; 5, CaCO3) (Li et al. 2019b)

Figure 2.4. Chemical composition and mineralogy of MIFA

As the contents of chlorides and sulfates are commonly high in MIFA (as shown in Figure 2.4), the negative effects of these compounds on geopolymerization kinetic cannot be ignored. Zheng et al. (2011) utilized the water-wash pre-treatment to eliminate the inorganic slat from MIFA and then investigated the geopolymerization of MIFA to determine the efficacy of water-wash pre-treatment. It was found that water-wash pre-

treatment considerably promoted the early strength and also resulted in a higher ultimate strength (22.7 MPa at 28 days) in comparison with the counterpart without water-wash pre-treatment. Meanwhile, a better immobilization efficiency of heavy metal was identified in the geopolymeric composites based on water-washed MIFA. Therefore, a viable and practical pre-treatment is essential for the use of MIFA as the raw material for geopolymeric composites in civil construction applications as well as a more effective stabilization process.

2.1.2 Waste paper sludge

By far, the application of raw waste paper in construction materials is not very common. Instead, a large quantity of waste paper has been recycled into new paper products, which could conserve wood and other forest resources and make less environmental impacts. However, the processing of recycled paper into usable fiber for papermaking often generates a secondary stream typically termed as waste paper sludge. This sludge has a high content of water ranging from 50% to 70% and therefore is usually dried before processing for ease handling, incineration, and any potential applications. Besides, waste paper sludge contains approximately equal amounts of organics (mainly residual cellulose fiber) and inorganic fillers (such as kaolin clay and calcium carbonate) (Kinuthia 2018). Previous studies mainly focused on employing waste paper sludge in the construction materials based on OPC, while the utilization of waste paper sludge in geopolymeric composites is a relatively advanced development (Yan & Sagoe-Crentsil 2012).

In general, the previous studies reported two main approaches for the utilization of waste paper sludge in geopolymeric composites. Chemical analysis has indicated that waste paper sludge appears compatible with geopolymer chemistry and could serve as a potential supplementary additive to geopolymeric composites. Thus, the first approach adopts this material in its raw form. Yan & Sagoe-Crentsil (2012) evaluated both fresh and hardened properties for the geopolymeric mortar incorporating 2.5–10% dry waste paper sludge by weight of total precursor. Results demonstrated that the incorporation of waste paper sludge into geopolymeric mortar reduced the workability by 11–33% and

decreased compressive strength by 8–42%. However, the compressive strength still maintained over 31.2 MPa. It was also reported that, with increasing waste paper sludge addition, the drying shrinkage was decreased by up to 64%, which was contrary to the trend of increasing drying shrinkage observed for the OPC matrix after the inclusion of waste paper sludge.

More recently, Adesanya et al. (2018) utilized waste paper sludge as a waste-based source of calcium carbonate in the one-part ("just add water") geopolymer. Specifically, waste paper sludge was pre-treated by mixing with sodium hydroxide and then dried in the oven, in which waste paper sludge acted as activator and also as filler. The test results showed that the generated geopolymeric mortar possessed the compressive strength up to 48 MPa at 50 days. In addition, the prepared sample exhibited low drying shrinkage, with the highest shrinkage of 0.39% and the lowest of 0.14% at 90 days.

The other approach to recycling waste paper sludge in geopolymeric composites is the use of waste paper sludge ash (WPSA), which derives from thermal processes such as the combustion of waste paper sludge. During the thermal process, the latent energy of the organic component can be recovered. At the same time, the highly reactive metakaolin-type phases and calcined limestone are produced (Antunes Boca Santa et al. 2013). The chemical composition and mineralogy of WPSA from the selected studies are presented in Figure 2.5. It was found that WPSA can be utilized as a precursor substitution in geopolymeric composites (Antunes Boca Santa et al. 2013; Mamat et al. 2018; Yan & Sagoe-Crentsil 2016). Figure 2.6 presents the relationship between the inclusion percentage of WPSA and the relative compressive strength. Although the inclusion of WPSA has varied effects in different studies owing to the different raw materials and curing conditions, these results consistently indicated that the inclusion of WPSA in geopolymeric composites presented a positive effect on the degree of geopolymerization and therefore resulted in better mechanical performance. Moreover, some researchers investigated the geopolymeric composites based on WPSA only (Bernal et al. 2014a; Gluth et al. 2014; Ridzuan et al. 2014a). It was elucidated that WPSA was a suitable precursor for producing geopolymeric composites (Gluth et al. 2014), and also the

formulation parameters, especially the concentration of alkaline activators, need to be optimized to manufacture a desirable product (Bernal et al. 2014a; Ridzuan et al. 2014b).

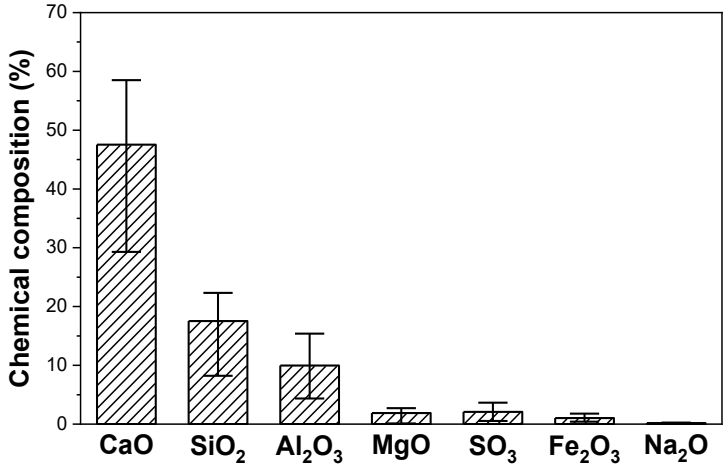

(a) Chemical composition of WPSA from the selected studies. Data from Bernal et al. (2014a); Gluth et al. (2014); Mamat et al. (2018); Ridzuan et al. (2014b); Yan & Sagoe-Crentsil (2016)

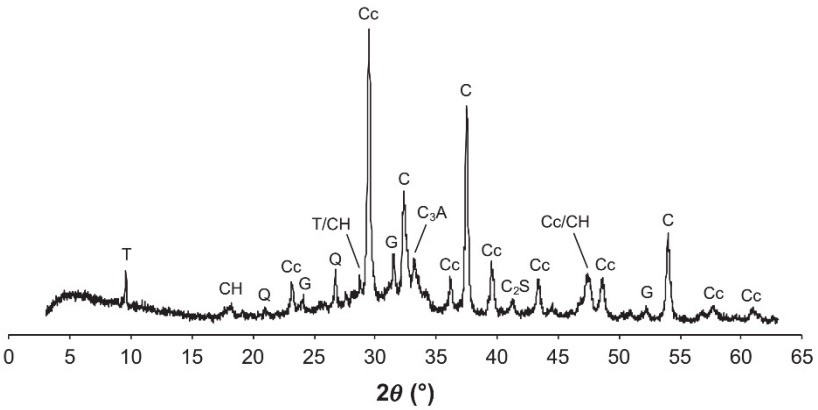

(b) XRD pattern of WPSA (CH: portlandite, Q: quartz, Cc: calcite, G: gehlenite, C: lime, C3A: tricalcium aluminate, C2S: belite) (Gluth et al. 2014)

Figure 2.5. Chemical composition and mineralogy of WPAS

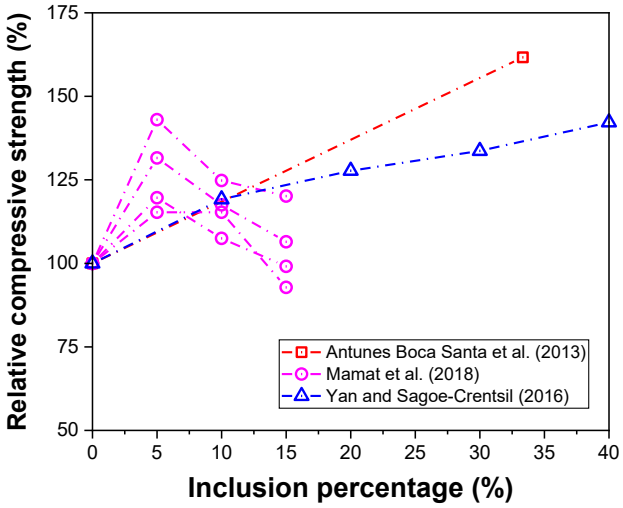

Figure 2.6. Relationship between the inclusion percentage of WPSA and relative compressive strength. Data from Antunes Boca Santa et al. (2013); Mamat et al. (2018); Yan & Sagoe-Crentsil (2016)

2.1.3 Rubber waste

Enormous disposal of rubber waste has become a challenging task, as rubber, featured with a three-dimensional network structure, takes a very long time to decompose. The waste tire is by far the predominant source of rubber waste, and it is estimated to exceed 1,200 million annually by 2030 (Thomas & Gupta 2016). The traditional method of waste tire management includes stockpiling or dumping, and landfilling, all of which are a short-term solution. Moreover, stockpiled tires could provide favorable breeding grounds for insects and mosquitoes. It would also cause an environmental impact as the toxins in tires can easily leach out and then cause contamination to the soil and groundwater. Henceforth, recycling waste tires is an urgent environmental task worldwide.

The use of rubber waste, recycled from automotive and truck scrap tires, in geopolymeric composites was introduced in recent years (Gandoman & Kokabi 2015). Table 2.2 summarized the existing studies.

Table 2.2 Recent research on the applications of rubber waste in geopolymeric composites

Composites	Form	Substitution	Content[1]	Precursor	Activator	Curing condition	Mechanical properties[2]	Reference
Concrete	Rubber fiber (width: 2-4 mm; length: 22 mm)	Fine aggregate	0, 10, 20, and 30 wt.%	CFA	$NaOH+Na_2SiO_3$	90°C for 48 hrs	30.0–48.3 MPa (28-day compressive strength) 8.4–8.8 MPa (28-day flexural strength) 5.1–5.3 MPa (28-day indirect tensile strength)	Luhar et al. (2018, 2019a)
	Crumb rubber	Fine aggregate	0, 5, 10, 15, and 20 wt.%	CFA	$NaOH+Na_2SiO_3$	RT	11.3–33.2 MPa (28-day compressive strength)	Azmi et al. (2019)
	Crumb rubber (0-4 mm)	Fine and coarse aggregates	0, 10, 20, and 30 vol%	GGBFS	$NaOH+Na_2SiO_3$	RT	24.6–40.0 MPa (28-day compressive strength) 1.8–2.0 MPa (60-day flexural strength) 2.3–2.8 MPa (60-day indirect tensile strength)	Aly et al. (2019)
	Crumb rubber (5-10 mm)	Coarse aggregate	0, 5, 10, 15, and 20 wt.%	CFA	$NaOH+Na_2SiO_3$	Seawater	14.1–40.0 MPa (28-day compressive strength)	Yahya et al. (2018)
	Crumb rubber (0-3.75 mm)	Fine aggregate	0, 5, 10, 15, 20 wt.%	CFA	$NaOH+Na_2SiO_3$	RT	15.8–48.0 MPa (28-day compressive strength)	Azmi et al. (2016)

	Crumb rubber (0-4.75 mm)	Fine aggregate	0, 5, 10, 15, and 20 vol%	CFA	$NaOH+Na_2SiO_3$	46°C for 7 days (stream-curing)	17.5–40.6 MPa (7-day compressive strength)	Park et al. (2016)
	Crumb rubber (0-1 mm)	Fine aggregate	0, 2, 6, 10, and 14 wt.%	MK	$NaOH+Na_2SiO_3$	65°C for 48 hrs	9.0–42.9 MPa (28-day compressive strength)	Gandoman & Kokabi (2015)
Mortar	Crumb rubber (0-6 mm)	Fine aggregate	0, 5, 10, and 15 wt.%	CFA+GGBFS	$NaOH+Na_2SiO_3$	RT	30.9–35.6 MPa (28-day compressive strength) 3.6–3.9 MPa (28-day flexural strength)	Zhong et al. (2019)
	Crumb rubber (0-4 mm)	Fine aggregate	0 and 100 vol%	CFA	$NaOH+Na_2SiO_3$	25, 60, 90°C for 48 hrs	2.7 MPa (28-day compressive strength) 1.0 MPa (28-day flexural strength)	Wongsa et al. (2018a)
	Crumb rubber	Fine aggregate	100 vol%	CFA	$NaOH+Na_2SiO_3$	RT	2.8–4.3 MPa (28-day compressive strength)	S Mohammed et al. (2018)
	Crumb rubber (0-4.25 mm)	Fine aggregate	0, 20, 40, and 60% vol%	GGBFS	$NaOH+Na_2SiO_3$	RT	14.6–31.3 MPa (28-day compressive strength) 8.6–14.7 MPa (28-day flexural strength)	Long et al. (2018)

Note: 1. wt.% and vol% denote the replacement percentages by weight and volume, respectively; 2. The mechanical properties exclude the results of control specimens (the specimens without rubber waste)

The most preferred method for the recycling of tire rubber is grinding shredded tire pieces into granules with desired sizes, namely, crumb rubber. When used in geopolymeric composites, the crumb rubber replaces coarse or fine aggregates partially or even fully. There is a consensus among the existing studies that the addition of crumb rubber into geopolymeric composites remarkably alters the properties of geopolymeric composites. As illustrated in Figure 2.7, the compressive strength showed a systematic reduction with the increment of the crumb rubber replacement ratio. Also, the loss of strength due to the crumb rubber substitution by mass is greater than that by volume under a certain percentage. The loss of strength can be explained from several aspects. One of the main reasons is the hydrophobic nature of rubber, which causes the weak bond between the rubber and geopolymeric matrix. Long et al. (2018) performed a microstructure test and confirmed the imperfect adhesion between the rubber aggregates and the geopolymeric matrix, which was indicated by the deep cracks and voids at the interface. Another cause of the strength loss is the significantly low modulus of rubber, which could result in the premature cracking near the joint of the rubber and geopolymeric matrix.

However, when the rubber replacement ratio within an appropriate amount, an acceptable reduction in the mechanical strength can be obtained, which would be suitable for structural purposes (Park et al. 2016; Wongsa et al. 2018a; Yahya et al. 2018). Otherwise, geopolymeric composites with high replacement ratios are limited to secondary or non-critical structures. For instance, in the study of S Mohammed et al. (2018), the non-load bearing brick was developed by utilizing crumb rubber as the sole fine aggregate in the geopolymeric mortar. Analogously, degradation by the crumb rubber incorporation was also observed in other mechanical performance, physical properties, and durability. Recently, the study of Zhong et al. (2019) disclosed that the comparable compressive (as shown in Figure 2.7(a)) and superior flexural strength could be achieved in waste rubber geopolymeric composites by introducing steel fibers. That is, the addition of steel fibers into geopolymeric composites compensates for the strength loss caused by the crumb rubber incorporation, while maintains the positive impact of the crumb rubber incorporation. As a result, the usage of rubber waste in geopolymeric composites can be increased.

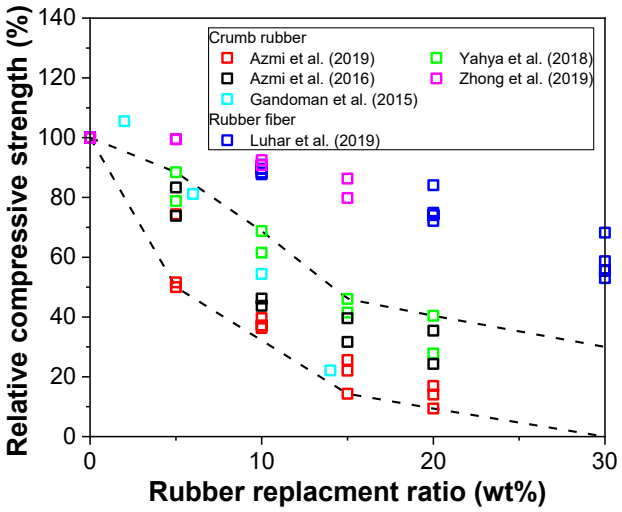

(a) Replacement by mass

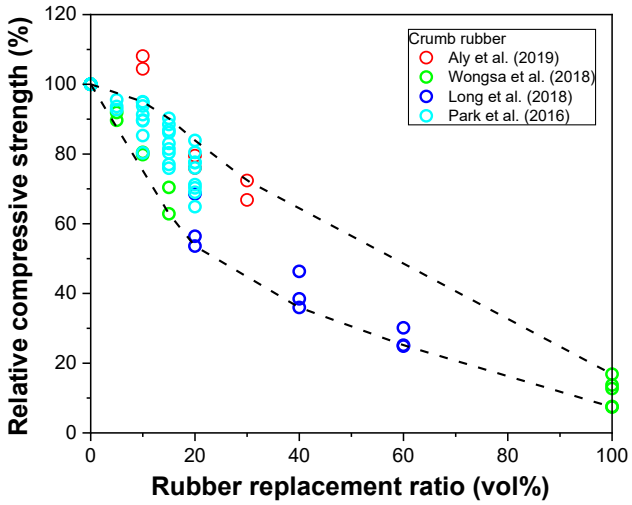

(b) Replacement by volume

Figure 2.7. Relationship between the replacement ratio of waste rubber and relative compressive strength

Figure 2.7 also demonstrates that the replacement of rubber waste in the form of rubber fiber has less effect on the compressive strength than that in the form of crumb rubber (Luhar et al. 2019a). Additionally, rubber fiber was found to improve the tension properties of geopolymeric concrete, such as flexural strength and splitting tensile strength. For example, Luhar et al. (2019a) reported that, at 28 days, the splitting tensile strength and flexural strength were improved from 5.0 MPa to 5.3 MPa, and from 6.4

MPa to 6.8 MPa, respectively, after 30% replacement of fine aggregate by rubber fibers. This improvement was associated with that the fibers could provide a bridge between propagated cracks.

On the other hand, Aly et al. (2019) investigated the impact resistance of geopolymeric composites with three different levels of aggregate replacement by crumb rubber under drop weight test. Based on the test results, improved impact energy absorption was observed in geopolymeric composites with higher contents of crumb rubber. It can be explained by that rubber possesses good elastic behavior, especially at large deformation, and thus good energy absorbing capacity. In other words, rubber can absorb sudden shock, which cannot be achieved by NA due to the brittle nature. The inclusion of crumb rubber was also found to enhance the viscoelasticity and the damping properties of the geopolymeric mortars. The study by Long et al. (2018) reported that the damping ratio of geopolymeric mortar increased dramatically after the inclusion of crumb rubber.

In addition, enhanced insulation properties, including acoustic and thermal impedance, have been observed for geopolymeric composites after the incorporation of crumb rubber (Gandoman & Kokabi 2015; Wongsa et al. 2018a). As reported, the thermal conductivity of geopolymeric concrete was greatly lowered by the incorporation of crumb rubber, decreasing from 1.284 W/mK to 0.237 W/mK (Wongsa et al. 2018a). It is due to that rubber has lower thermal conductivity, ranging from 0.1 W/mK to 0.25 W/mK, in comparison with the thermal conductivity of normal aggregate, approximately 1.5 W/mK. Gandoman & Kokabi (2015) compared the sound transmission loss and sound absorption of geopolymeric concretes with varied waste rubber contents. Test results validated the pronounced improvement in noise reduction coefficient and sound absorption property for geopolymeric concrete after the inclusion of crumb rubber.

2.1.4 Plastic waste

Plastic waste has become one of the most pressing environmental issues, as the rapidly increasing production of plastic products overwhelms the world's ability to deal with them. It is well known that plastic is a non-biodegradable material that takes a long time

to break down when it is landfilled, and thus landfilling plastic products places a heavy burden on the environment. In addition, since plastic production involves the use of some harmful chemicals, land-filling plastic waste would result in the release of harmful chemicals. One of the best solutions to reduce these negative effects is to recycle plastic waste to produce new materials (Saikia & de Brito 2012).

Several studies have been carried out to evaluate the properties of geopolymeric composites containing plastic waste as aggregate. In the study by Wongkvanklom et al. (2019), the plastic waste was melted to form lumps and then ground into particles with a diameter of about 2.1 mm to act as fine aggregate for the geopolymeric composite preparation. Akçaözoğlu & Ulu (2014) substituted the waste PET bottles granules, having particle sizes less than 4 mm, for the fine aggregates in geopolymeric mortar at different levels (20–100%). Besides, Posi et al. (2015) incorporated the polystyrene foam particles with a size between 2.36 mm and 4.75 mm into geopolymeric concrete, which was sourced from the discarded packaging foam. Generally, the density of geopolymeric composites decreased with the increase of replacement ratios of waste plastic aggregate, mainly attributing to the low density of plastic material. The increasing of waste plastic aggregate replacing ratios also resulted in the decreases in mechanical properties, including compressive strength and flexural strength, as shown in Figure 2.8. However, the waste plastic aggregate replacement under an appropriate ratio could produce geopolymeric concrete with acceptable strength and density to serve as an alternative to lightweight structural concrete (Posi et al. 2015). In addition, the reduction in the surface abrasion resistance and increase in the porosity and water absorption were also observed as the amount of waste plastic aggregate increased (Wongkvanklom et al. 2019). Due to the low thermal conductivity coefficient of plastic, the inclusion of plastic waste also equips geopolymeric composites with lower thermal conductivity and better thermal insulation properties (Posi et al. 2015).

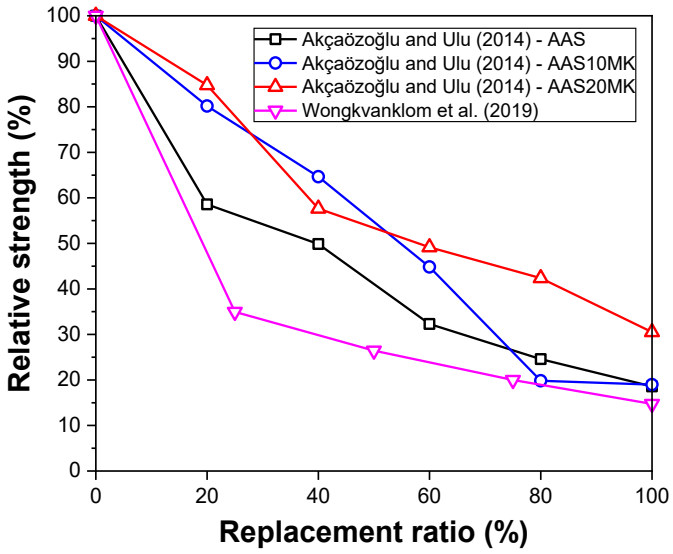

(a) Compressive strength

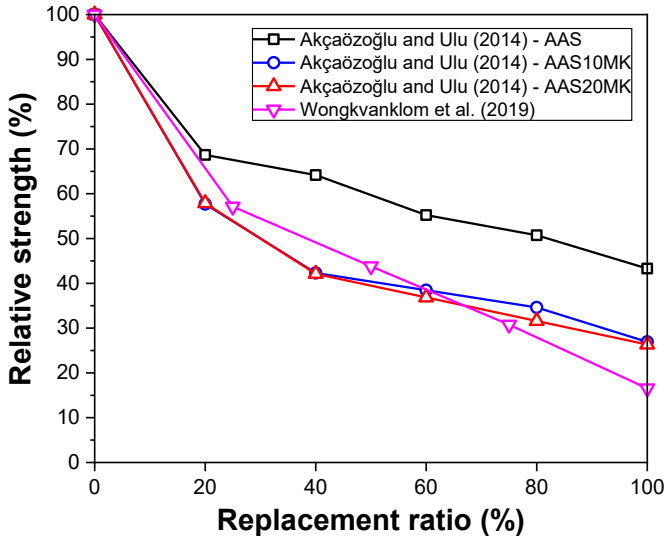

(b) Flexural strength

Figure 2.8. Relationship between the replacement ratio of waste plastic and relative strength

In another study, Dave et al. (2017) replaced the virgin coarse aggregate with waste plastic granules having diameters of between 7 mm and 9 mm in geopolymeric concrete, and then investigated the impact resistance of geopolymeric concrete by performing drop hammer tests. The test results revealed that the 10% inclusion of waste plastic aggregate greatly improved the impact resistance from 179.77 kJ to 193.02 kJ. It has been explained

that the plastic aggregate possessed excellent ductile properties that could well absorb sudden impact energy, and thus arrested the cracks propagation.

Inspired by the successful employment of plastic waste fiber as one constituent in OPC-based concrete, researchers examined its feasibility in geopolymeric composites (Bhogayata & Arora 2019; Patel et al. 2013). As expected, plastic waste could be successfully utilized as reinforcement fibers in the formulation of geopolymeric composites. For instance, Bhogayata & Arora (2019) mixed the plastic waste fiber (with an average size of 20 mm length and 1 mm width) in geopolymeric concrete under varying proportions from 0% to 2% by volume. The plastic waste fiber was obtained from shredding the metalized plastic films, which was the polypropylene-based metalized thin film with a layer of aluminum on one side surface and usually used as a food package. It was identified that the addition of plastic waste fiber reduced the workability, density, and compressive strength of geopolymeric concrete. While as for the splitting tensile strength, it was increased by about 8%, 18%, 16%, and 12% with the 0.5% increment of the plastic waste fiber dosage from 0.5% to 2%. Furthermore, the enhancement was also observed in the strength and deformation capacity under flexural loading, as well as the energy absorption under impact (Bhogayata & Arora 2019; Patel et al. 2013).

2.1.5 Other wastes

Waste glass

In addition to the above-discussed MSW, varied progress in the re-utilization for geopolymeric composites has been made for other types of MSW. One of the predominant achievements is glass waste recycling. The global annual generation of glass waste is about 65 million tons, accounting for about 5% of the MSW composition (Hoornweg & Bhada-Tata 2012). Nevertheless, waste glass has not been fully recycled or efficiently reused. In the United States, only 28% of waste glass is recycled from 11.54 million tons. In Mainland China, 40 million tons of waste glass is produced annually, but with only 13% of it being recycled (Liu et al. 2019c). The chemical composition and mineralogy of glass are given in Figure 2.9. Obviously, waste glass contains abundant amorphous silicon and calcium, and also has higher reactivity. The suitability of

employing waste glass in manufacturing geopolymeric composites has been verified by numerous researchers. Overall, glass waste could be re-utilized as aggregates (Hajimohammadi et al. 2018; Lu & Poon 2018), precursors (Si et al. 2020; Xuan et al. 2019), and alkali activators (Vinai & Soutsos 2019), in the context of geopolymer. Since there are several studies that have reviewed the reuse of glass waste in geopolymeric composites, researchers attempting to valorize the glass waste through the development of geopolymeric composites can consult these fruits (Liu et al. 2019c; Luhar et al. 2019b, 2019c; Moghadam et al. 2019).

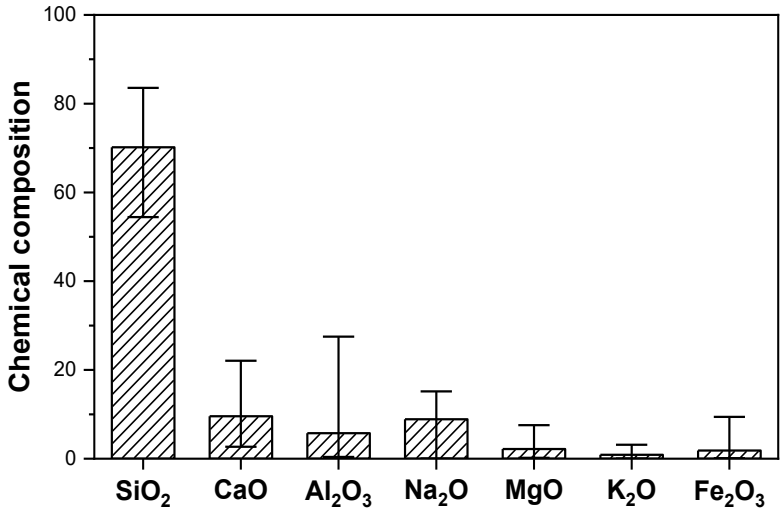

(a) Chemical composition of waste glass (Liu et al. 2019c)

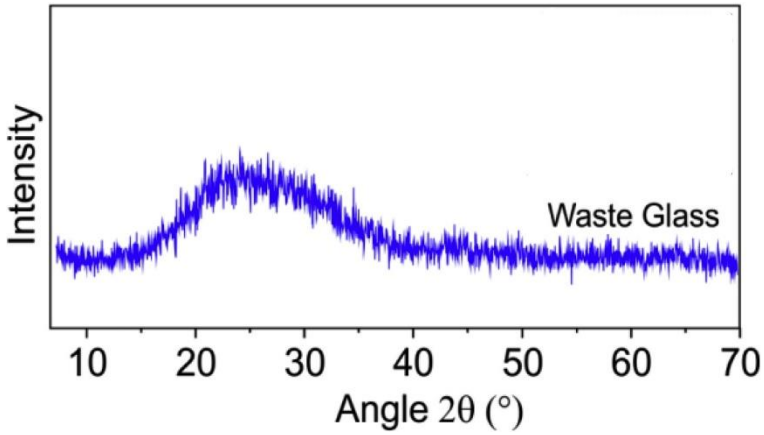

(b) XRD pattern of waste glass (Q: Quartz) (Burciaga-Díaz et al. 2020)

Figure 2.9. Chemical composition and mineralogy of waste glass

Tire steel and textile fiber

During the process of grinding tires into granules, steel and textile waste materials are also obtained. The possibility of using these materials as fiber reinforcement for geopolymeric composites has been examined (Łach et al. 2018; Onuaguluchi et al. 2017; Zhong et al. 2019). It has been demonstrated that although the incorporation of tire steel fiber might impair the compressive strength, a remarkable enhancement in flexural performance was observed for geopolymeric composites reinforced with tire steel fiber. For example, Onuaguluchi et al. (2017) reported that the addition of 1% and 2% tire steel fiber increased the flexural peak strength by 71.5% and 45.1%, respectively; and increased the toughness from 0.14 J to 1.70 J and 2.18 J, respectively. Similar results have also been identified in the geopolymeric composites reinforced with tire textile fiber (Łach et al. 2018). Specifically, the introduction of tire textile fiber altered the failure mode from brittle to ductile, and the flexural strength was improved by up to 10% due to the inclusion of tire textile fiber.

Spent coffee grounds

Spent coffee grounds are the solid granular residue of the ground beans during the final liquid coffee making, and are primarily disposed to landfills. A series of studies have been conducted to assess the feasibility of combining coffee grounds with conventional geopolymeric precursors into sustainable subgrade construction materials (Arulrajah et al. 2017; Kua et al. 2017; Kua et al. 2018; Suksiripattanapong et al. 2017). Specifically, coffee grounds, used as the fill materials, were blended with conventional geopolymeric precursors (e.g., CFA, slag, or even glass waste), and then were activated with an alkali solution. The performance of the produced materials was evaluated in terms of compressive strength, elastic modulus, microstructure properties, and contaminants leaching. On the whole, the test results revealed that geopolymers could be employed to stabilize coffee grounds into a subgrade material in fulfillment of the strength, stiffness, and environmental requirements.

Waste cork

In the investigation by Novais et al. (2019), the pyrolyzed waste cork was, for the first time, used to synthesize the cork-geopolymeric composites. Recycled corks, sourced from wine stopper, were heated to 900 ºC under nitrogen in a graphite furnace, followed by being ground into powder below 75 μm. The addition of 2.5% and 3.75% pyrolyzed cork was directly added to the geopolymeric composites. Due to the high carbon content (90.74 wt.%), pyrolyzed cork could act as a carbon source to enhance geopolymeric composites' electromagnetic interference shielding properties. Results exhibited that all cork-geopolymeric composites presented enhanced specific shielding effectiveness in comparison with the normal geopolymeric matrix. Taking the samples with 3 mm thickness as an example, the specific shielding effectiveness was increased from 4.7–6.0 -dB g^{-1} cm^3 to 8.8–10.8 and 11.7–13.5 -dB g^{-1} cm^3, respectively, after the addition of 2.5% and 3.75% pyrolyzed cork. Overall, the incorporation of pyrolyzed cork into geopolymeric composites provided an environmentally friendly strategy for electromagnetic interference shielding applications.

2.2 Construction solid waste

Construction solid waste (CSW), an inescapable by-product of the construction, renovation, or demolition activities, comprises a wide array of materials, including concrete, metals, bricks, timber, ceramics, asphalt, soil, plaster, and polymers. This waste accounts for the largest source of the solid waste stream in most countries around the world. Figure 2.10 gives the annual CSW generation from the selected countries in 2014 (Menegaki & Damigos 2018). As a result, how to address the CSW problem has raised great concerns from economic, environmental, and societal perspectives. In recent decades, numerous studies have been devoted to increasing the recycling rate and reducing the landfill rate of CSW. This section provides a thorough review of the achievement in recycling CSW in geopolymeric composites, including waste clay brick, ceramic waste, and waste asphalt pavement, along with some others.

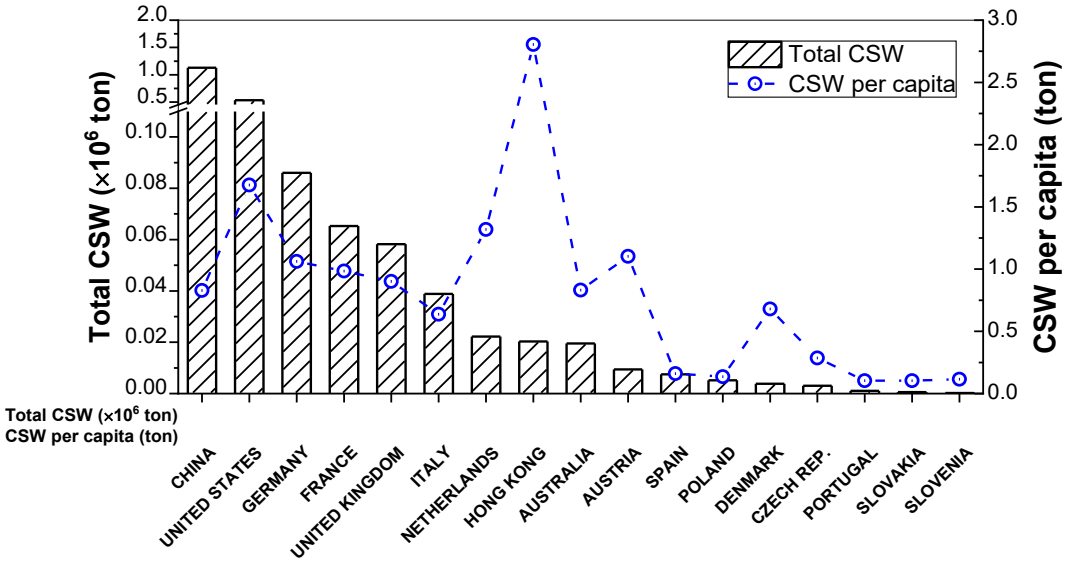

Figure 2.10. Annual CSW generation from selected countries (Menegaki & Damigos 2018)

2.2.1 Waste clay brick

The waste clay brick (WCB) originates not only from demolition activities, but also from the rejected bricks during the manufacturing, transporting, and construction processes. Clay bricks are produced by mixing ground clay with water, forming the clay into the desired shape, and then drying and firing. Figure 2.11(a) shows the average, maximum, and minimum values for the chemical composition of WCB collected from the selected studies. In particular, clay brick contains high levels of SiO_2 and Al_2O_3 and therefore is considered to have great potential as a geopolymeric precursor.

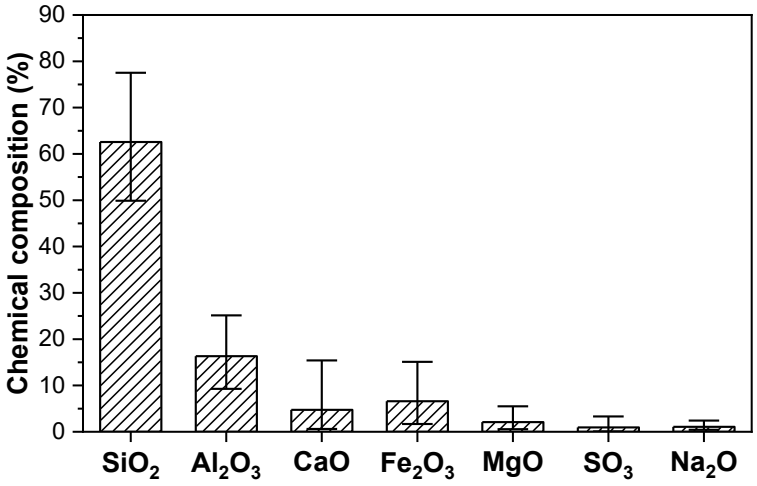

(a) Chemical composition of WCB from the selected studies. Data from Fořt et al. (2018); Hwang et al. (2019a); Keppert et al. (2018); Komnitsas et al. (2015); Ouda & Gharieb (2020); Rakhimova & Rakhimov (2015); Reig et al. (2016); Robayo et al. (2016); Rovnaník et al. (2018); Sedira et al. (2018); Silva et al. (2019); Tuyan et al. (2018); Wongsa et al. (2018b); Zawrah et al. (2016)

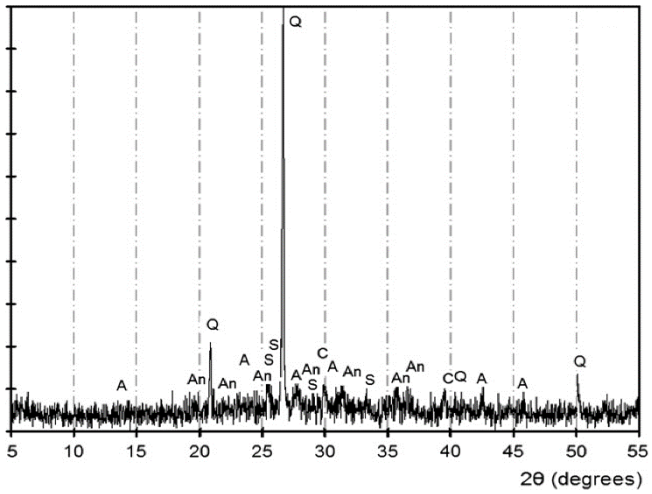

(b) XRD pattern of WCB (Q: Quartz; A: Albite; An: Anortite; S: Sanidine ; C: Calcite) (Reig et al. 2013a)

Figure 2.11. Chemical composition and mineralogy of WCB

Table 2.3 summarizes the previous research studies assessing the feasibility of WCB as the precursor of geopolymeric composites. It is concluded that WCB could provide a valid alternative to the precursor material for geopolymeric composites (Peyne et al.

2017). Also, in order to achieve better performance, a number of researchers optimized the formation of WCB-based geopolymers by varying the alkaline solution parameters such as the alkaline type, silica modulus, alkaline concentration, and curing condition (Fořt et al. 2018; Keppert et al. 2018; Komnitsas et al. 2015; Reig et al. 2013a). For instance, Tuyan et al. (2018) investigated the effect of alkali concentration (4–10%), silica modulus (0–2.2), curing temperature (50–90 ºC), and curing duration (1–7 days) on the consistency and strength of WCB-based geopolymeric mortar. Test results demonstrated that the optimum activator composition had an alkali concentration of 10% and a silica modulus of 1.6, and the maximum compressive strength was obtained upon curing at 90 °C for 5 days.

Nevertheless, it should be noted that in order to attain sufficient mechanical strengths, the WCB-based geopolymeric composites were mostly synthesized under the curing condition with high temperatures (usually above 60 °C) and a long period. This is mainly attributed to that the high content of crystalline mineral and the low concentration of amorphous matter in WCB (as shown in Figure 2.11(b)) usually result in a relatively low geopolymerization reaction with low/no strength development at the early age (Keppert et al. 2018; Tuyan et al. 2018). Such kind of curing condition apparently increases the cost of production and energy demand, and also hinders its application in cast-in-suit construction (Hwang et al. 2019b). For this reason, it is preferable to use WCB in a blend with other reactive material, such as metakaolin, fly ash, and OPC, to achieve an effective geopolymerization process without high temperature curing. In the study of Hwang et al. (2019b), high-strength geopolymeric pastes using a high volume of WCB as precursor materials were developed under ambient temperature curing. In these mixtures, WCB composed 60% of the total mass of the precursor materials, while CFA and GGBFS with different portions composed the remaining 40%. The resulted samples could achieve the compressive strength ranging from 36 to 70 MPa, whereas the control mixture based on sole WCP did not set even after 24 hr of casting. Robayo et al. (2016) also indicated that the inclusion of 20% OPC could yield WCB-based geopolymeric pastes with a compressive strength of 102.6 MPa after 28-day ambient curing, which was twice the strength obtained in the mixture without OPC.

Table 2.3 Recent research of the geopolymeric composites made from waste clay brick

Composites	Precursor[1]	WCB content (wt.%)	Activator	Curing condition		Compressive strength (MPa)	Reference
				Temperature	Duration		
Mortar	WCB	100	$NaOH+Na_2SiO_3$	65 ºC	3 or 7 days	7.1–50.0 (7 days)	Reig et al. (2013a)
	WCB+GGBFS	20, 40, 60, 80, 100	$NaOH+Na_2SiO_3$; NaOH	95 ºC, RT	12 hrs	26–112.3 (28 days)	Rakhimova & Rakhimov (2015)
	WCB	100	$NaOH+Na_2SiO_3$, SH	50, 60, 70, 80, 90, 100 °C, RT	1, 3, or 7 days	4.0–36.2 (7 days)	Tuyan et al. (2018)
	WCB+GGBFS	50, 60, 70, 80, 90, 100	$NaOH+Na_2SiO_3$, NaOH	RT	–	23.1–91.3 (28 days)	Hwang et al. (2019b)
Paste	WCB	100	$NaOH+Na_2SiO_3$	60, 80, or 90 ºC	7 days	4.7–49.5 (7 days)	Komnitsas et al. (2015)
	WCB+CAC	50, 60, 70, 80, 90, 100	$NaOH+Na_2SiO_3$	65 ºC, RT	3 or 7 days	4.1–93.7 (7 days)	Reig et al. (2016)
	WCB+OPC	80, 90, 95, 100	$NaOH+Na_2SiO_3$; NaOH	70 ºC, RT	1 or 2 days	7.5–102.6 (28 days)	Robayo et al. (2016)
	WCB+GGBFS	20, 40, 60, 80, 100	$NaOH+Na_2SiO_3$	RT	–	11.7–79.2 (28 days)	Zawrah et al. (2016)
	WCB+OPC	70, 80, 90, 100	Na_2SiO_3; NaOH; Na_2SO_3	RT	–	10.2–102.7 (28 days)	Robayo et al. (2016)
	WCB	100	$NaOH+Na_2SiO_3$	RT	–	10.3–41.9 (28 days)	Fořt et al. (2018)

WCB	100	$NaOH+Na_2SiO_3$	RT	–	27.5–38.8 (28 days)	Keppert et al. (2018)
WCB+MK	25, 50, 75, 100	$NaOH+Na_2SiO_3$	40 ºC	20 hrs	6.6–26.5 (14 days)	Rovnaník et al. (2018)
WCB+TMWM	10, 20, 30, 40, 50	$NaOH+Na_2SiO_3$	RT	–	25–59 (28 days)	Sedira et al. (2018)
WCB+GGBFS+CFA	60, 100	$NaOH+Na_2SiO_3$	RT	–	38.2–68.2 (28 days)	Hwang et al. (2019a)
WCB+DCP	70, 80, 85, 90, 95, 100	NaOH	80 ºC	1 day	3.0–51.4 (28 days)	Ouda & Gharieb (2020)
WCB+NP	100	$NaOH+Na_2SiO_3$	65, 80, 95 ºC	1, 3, or 7 days	0.7–37.0 (28 days)	Silva et al. (2019)

Note: 1. CAC, TMWM, DCP, and NP denote calcium aluminate cement, tungsten mining waste mud, dolomite-concrete powder, and natural pozzolana, respectively

There also exist other studies on the use of crushed clay brick as coarse or fine aggregates in geopolymer products (Reig et al. 2017; Sata et al. 2013; Wongsa et al. 2018b). As brick aggregate is comparatively weaker and more porous than virgin aggregate, a significant reduction in the mechanical strength has been observed when the recycled brick was used as an aggregate substitute in geopolymeric concrete and mortar (Reig et al. 2017; Sata et al. 2013; Wongsa et al. 2018b). However, by harnessing the low density feature of clay brick, Wongsa et al. (2018b) employed clay brick aggregate to produce lightweight geopolymeric concrete, with densities ranging from 1685 kg/m^3 to 1749 kg/m^3. The test results also demonstrated that the use of crushed clay brick as coarse aggregate could equip geopolymeric concrete with excellent thermal insulation, and thermal resistance under the temperatures of 400–800 °C. In another study, pervious geopolymeric concrete was successfully developed using crush clay brick aggregate, which contained continuous voids and possessed high water permeability (Sata et al. 2013).

2.2.2 Ceramic waste

Ceramic materials and products are often applied in building decoration projects, such as floor-wall tiles, garden ceramic, terracotta products, and sanitary ceramic. The production of ceramics is similar to that of clay brick: normally starts from raw material, mixing, molding, burning, polishing, and glazing. While ceramic materials are usually fired at a higher temperature than bricks so that the silica re-crystallizes to form a glassy material, having greater density, strength, hardness, resistance to chemicals and frost, and greater dimensional stability. Figure 2.12 presents the average, maximum, and minimum values for the chemical composition of ceramic waste powder (CWP) from the selected studies, as well as the XRD pattern. The chemical composition of ceramic, along with highly amorphous aluminosilicate, makes it possible to manufacture geopolymeric composites. Therefore, utilizing CWP as the precursor materials in geopolymer formulation has gained great academic interest. Table 2.4 summarizes the recent studies on CWP-based geopolymeric composites.

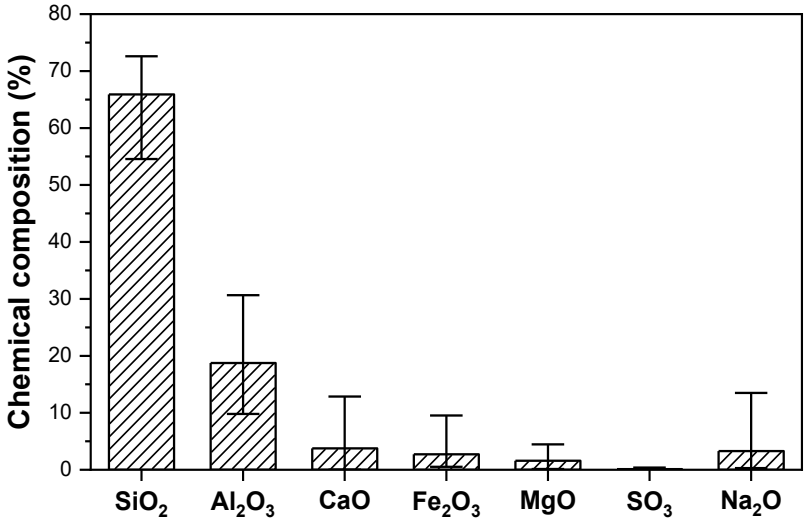

(a) Chemical composition of CWP from the selected studies. Data from Abdollahnejad et al. (2019); Aly et al. (2018); Amin et al. (2017); Huseien et al. (2019b); Hwang et al. (2019a); Komnitsas et al. (2015); Ramos et al. (2018); Reig et al. (2013b); Shoaei et al. (2019); Sun et al. (2013); Usha et al. (2016)

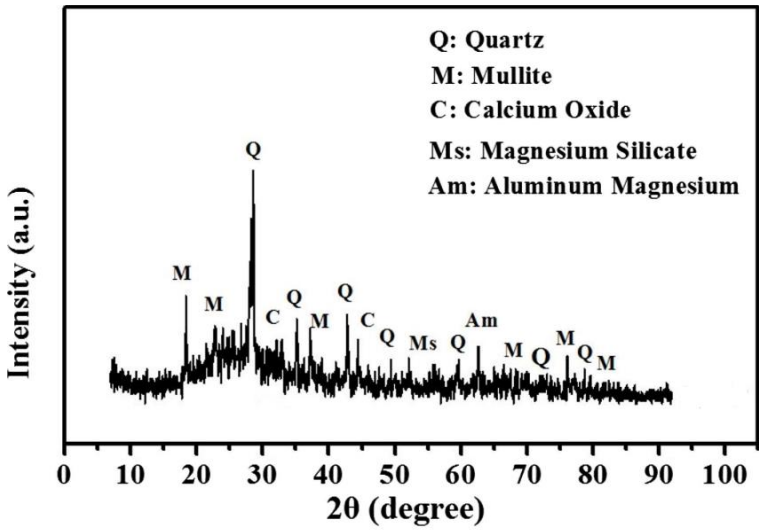

(b) XRD pattern of CWP (Huseien et al. 2020)

Figure 2.12. Chemical composition and mineralogy of CWP

Table 2.4 Recent research of the geopolymeric composites made from ceramic waste powder

Composite type	Precursor	WCT content (wt.%)	Activator	Curing condition		Compressive strength (MPa)	Reference
				Temperature	Duration		
Mortar	CWP	100	$NaOH+Na_2SiO_3$	60, 75, 90, 105 ºC	24 hrs	22.2–27.9 (28 days)	Shoaei et al. (2019)
	CWP+GGBFS+CFA	50	$NaOH+Na_2SiO_3$	RT	–	45.9–66.2 (28 days)	Huseien et al. (2019b)
	CWP+GGBFS+CFA	50, 60, 70	$NaOH+Na_2SiO_3$	RT	–	22.2–70.1 (28 days)	Huseien et al. (2018b); Huseien et al. (2019a)
	CWP+GGBFS	10, 20, 30	$NaOH+Na_2SiO_3$	60 ºC, RT	3 hrs	10.3–17.9 (28 days)	Abdollahnejad et al. (2019)
	CWP+GP+GGBFS+CFA	15	$NaOH+Na_2SiO_3$	RT	–	30.1–54.0 (28 days)	Huseien et al. (2018a)
	CWP+GGBFS	60, 80, 90, 100	NaOH, KOH	60 ºC, RT	24 hrs	6.2–32.8 (7 days)	Aly et al. (2018)
	CWP	100	$NaOH+Na_2SiO_3$	65 ºC	3 days	9.4–32.3 (3 days)	Reig et al. (2017)
	CWP	100	$NaOH+Na_2SiO_3$	35, 45, 55, 65, 75 ºC	24 hrs	7.1–26.5 (28 days)	Usha et al. (2016)
	CWP	100	$NaOH+Na_2SiO_3$	65 ºC	7 days	25.6–29.5 (7 days)	Reig et al. (2013b)

Paste	CWP+GGBFS+CFA	60, 100	$NaOH+Na_2SiO_3$	RT	–	34.6–58.0 (28 days)	Hwang et al. (2019a)
	CWP+MK	15, 30, 45	$NaOH+Na_2SiO_3$	RT	–	20.5–71.6 (28 days)	Ramos et al. (2018)
	CWP	100	$NaOH+Ca(OH)_2$	RT	–	2.3–8.0 (28 days)	Amin et al. (2017)
	CWP	100	$NaOH+Na_2SiO_3$	60, 80, 90 ºC	7 days	1.5–57.8 (7 days)	Komnitsas et al. (2015)
	CWP	100	$NaOH+Na_2SiO_3$; $KOH+Na_2SiO_3$; NaOH+KOH; NaOH	60 ºC	27 days	30.5–71.2 (28 days)	Sun et al. (2013)

Among these, part of the studies investigated the properties of geopolymeric composites completely based on CWP. Reig et al. (2013b) first formulated geopolymeric mortars based on CWP, and also analyzed the impact of the alkali activator concentration on the mechanical strength and microstructure of the mortars formed. It was manifested that at a constant water-to-binder ratio, increasing the alkali concentration from 6.0% to 9.0% increased the compressive strength of CWP-based geopolymeric mortar from 25 MPa to 29 MPa. Afterward, further research has been conducted aiming to understand the geopolymerization process of CWP, and to enrich the technical data on the effects of particle size, curing condition, and alkaline solution properties on the performance of final products (Amin et al. 2017; Komnitsas et al. 2015; Shoaei et al. 2019; Usha et al. 2016). In short, CWP exhibits high geopolymerization potential, which is even better compared with waste bricks and concrete (Komnitsas et al. 2015). Moreover, by optimizing the initial reacting system and the alkaline activating solution, a well geopolymerization process and better performance of final products could be obtained.

Furthermore, a number of studies have evaluated the performance of geopolymeric composites based on the combination of CWP and other aluminosilicate precursors. The group of Huseien conducted a series of investigations on the workability, strength, and durability properties of multi-blend geopolymeric pastes and mortars containing CWP (Huseien et al. 2018b; Huseien et al. 2019a; Huseien et al. 2019b). Specifically, the majority of the starting material was CWP, and the remaining consisted of CFA and GGBFS. The findings suggested that high volume CWP could produce geopolymeric composites with compressive strength over 70 MPa. Also, the developed geopolymeric composites exhibited enhanced resistance to elevated temperature with the increase of CWP content, which also has been verified by Sun et al. (2013). Similarly, researchers blended CWP with metakaolin and even waste glass powder to synthesize geopolymeric composites, and the resulted products also exhibited satisfactory performance (Huseien et al. 2018a; Ramos et al. 2018).

In addition to utilizing ceramic waste as the precursor materials, the other possible application of ceramic waste is using as the aggregate replacement in geopolymeric

mortar and concrete (Abdollahnejad et al. 2019; Hwang et al. 2019b; Reig et al. 2017). Particularly, in the studies by Abdollahnejad et al. (2019) and Reig et al. (2017), ceramic waste was used as both the precursor and RA. It has been observed that after immersion in the activating solution, the original rounded pores of ceramic waste aggregates could not be distinguished clearly, and crystalline particles accumulated into the pore network (as seen in Figure 2.13). These changes denoted the dissolution of the ceramic waste aggregates by the activating solution, which created a good ITZ (Hwang et al. 2019b). As a result, the strength of geopolymeric mortar was improved by adding ceramic waste aggregates, up to 43 MPa (under the optimum percentage of 50 wt.%) (Abdollahnejad et al. 2019).

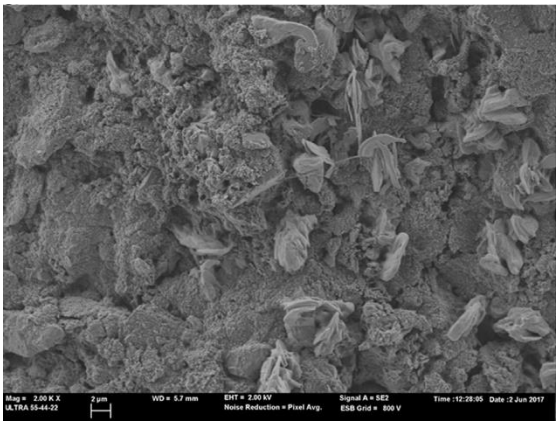

(a) General view

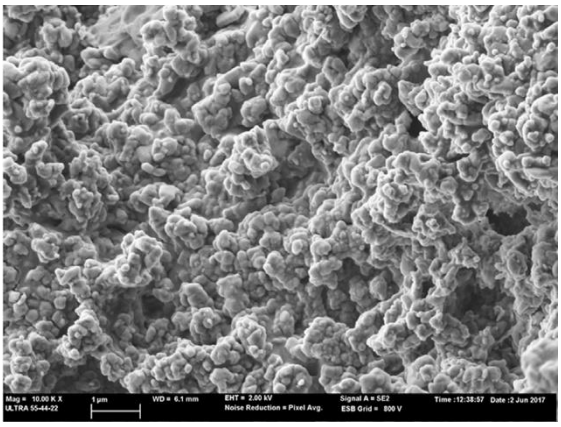

(b) Solid-phase magnification

Figure 2.13. SEM micrographs of the ceramic waste aggregates after immersion in the alkali-activating solution (Reig et al. 2017)

2.2.3 Waste asphalt pavement

Waste asphalt pavement (WAP) is generated when existing asphalt pavements are removed for reconstruction, resurfacing, or gaining access to buried utilities. When properly crushed and screened, WAP consists of high-quality and well-graded aggregates coated by aged asphalt. The recycling of WAP rates relatively high (such as 47% in Europe and 84% in the US), which is mainly through hot and warm mix asphalt processes. However, a large quantity of WAP materials remains unutilized yet (Zaumanis et al. 2014). Recent investigations have shown that the problem of WAP can be solved by using WAP as base or subbase aggregate materials. Several researchers have successfully adopted geopolymers to stabilized WAP material as pavement base or subbase applications.

It have been demonstrated that the CFA and/or slag-based geopolymeric stabilization considerably enhanced the mechanical properties (e.g., unconfined compressive strength and elastic modulus) of WAP (Mohammadinia et al. 2016a; Mohammadinia et al. 2016b). It was additionally proved that the mechanical strength of stabilized WAP materials increased with the increase of geopolymeric binder content. This result was also in agreement with that obtained by Saride et al. (2016), who investigated the performance of specimens prepared at various proportions of WAP and NA, stabilized by CFA-based geopolymer. In addition, it has been found that the amount of exposed aggregate surface of WAP particles played a major role in the strength characteristics (Saride et al. 2016). It is attributed to that the WAP particles are coated with the amorphous asphalt layer, which will reduce the strength of the cementitious bond created by geopolymeric binders. Besides that, Hoy's research team evaluated the strength development and microstructural of geopolymer-stabilized WAP (Hoy et al. 2016a; Hoy et al. 2018). In the studies, CFA or slag was activated with a combination of sodium hydroxide solution and sodium silicate solution and then was used to stabilize the WAP. The test results confirmed that these products met the related specification, as shown in Figure 2.14, and therefore could be used as a base course material in road work. Figure 2.14 also reveals that the increased NaOH content contributes to the superior performance, which is due to the more steady three-dimensional formation of the aluminosilicate geopolymer structure

(Hoy et al. 2017). Furthermore, the existing studies on permanency in terms of wet-dry cycles and toxic leaching showed that geopolymer stabilized WAP also performed satisfactorily (Avirneni et al. 2016; Hoy et al. 2016b; Hoy et al. 2017).

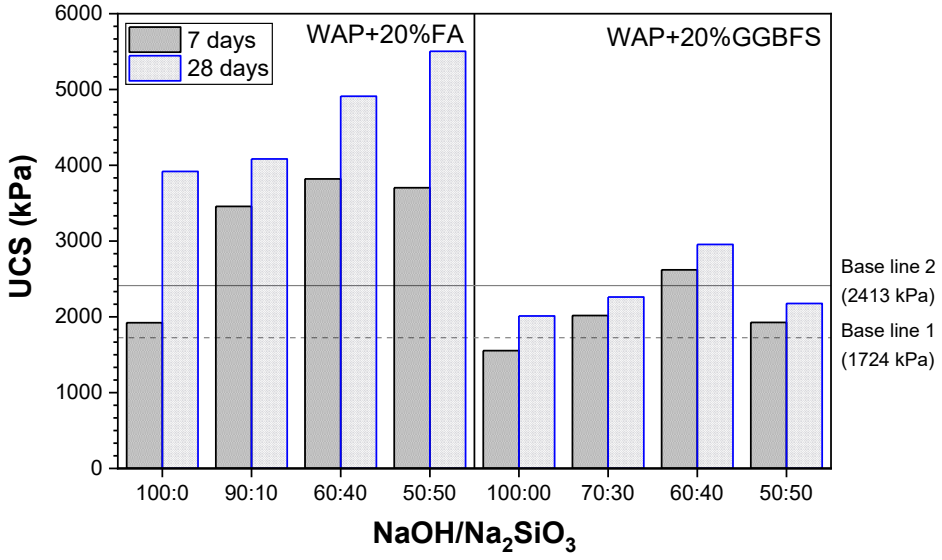

Figure 2.14. Unconfined compressive strength (UCS) of WAO-CFA blends and WAO-GGBFS blends at 7 and 28 days. Data from Hoy et al. (2016a); Hoy et al. (2018)

2.2.4 Other wastes

Asbestos

Asbestos-containing materials have been used for insulation in buildings and in various products such as roofing materials, water supply lines, and wall cladding, owing to the excellent tensile strength, poor heat conduction, and high resistance to chemical attack. However, asbestos is considered to be extremely carcinogenic, and the mining and use of asbestos have been banned in most countries since the beginning of the 80s. Nevertheless, challenges remain in the disposal of asbestos-contaminated waste materials. Physical, thermal, chemical, and biological treatments have been proposed to transform asbestos-contaminated materials into non-hazardous materials (Spasiano & Pirozzi 2017). But for the end-products, a suitable or even attractive recycling solution is being sought. Gualtieri et al. (2012) successfully employed the product of asbestos-cement after thermal

treatment for the formulation of geopolymers. The treated asbestos-cement contained Al-, Ca-, Mg-rich silicates (SiO_2: 30.8%, Al_2O_3: 5.4%, CaO: 48.5%, MgO: 7.5%). The test results indicated that the addition of treated asbestos-cement could promote the geopolymerization reaction, and meantime increase the physical and mechanical characteristics of the geopolymers. It therefore demonstrates the potential of recycling treated asbestos waste in geopolymeric composites.

Mineral wool

Mineral wool is the fibrous material formed by spinning or drawing molten mineral or rock materials. The applications of mineral wool mainly include thermal insulation (such as structural insulation and pipe insulation) and soundproofing. In literature, the study on recycling mineral wool waste remains low. Yliniemi et al. (2019) investigated the suitability of mineral wool waste for geopolymeric precursor material. In the study, mineral wool waste (stone wool and glass wool) collected from building demolition and construction sites was milled into powder and then used as a geopolymeric precursor. A range of 25–45 MPa was reported for the compressive strength of the resulted geopolymeric pastes at 28 days. Furthermore, excellent durability under the aggressive freeze-thaw cycles was observed for the prepared geopolymeric pastes. This study provided valuable information for promoting the utilization of mineral wool waste as a geopolymeric precursor.

2.3 Summary

Table 2.5 presents the general view of the characteristics of solid waste studied, as well as their usages and the corresponding performance of the resulted geopolymeric composites. It could be observed that recycling these solid waste materials in geopolymeric composites shares some commons, and therefore the experiences achieved can be shared with each other.

Table 2.5 General view of waste materials characteristic, usages, and respective performance of resulted geopolymeric composites

Waste materials	Characteristics	Solid waste usage	Inclusion content	Performance of resulted geopolymeric composites
Municipal solid waste				
Municipal solid waste incinerator bottom ash	Contains metallic aluminum, contains heavy metals, porous structure	Precursor	Up to 100% can be used (after the alkaline pre-treatment)	- Decreased compressive strength - Highly porous structure - Immobilized hazardous elements
		Additive	Up to 50% can be used	- Highly porous structure
		Fine aggregate	A maximum of 50 vol.% is recommend	- Decreased compressive strength
Municipal solid waste incinerator fly ash	High content of heavy metal, chlorides and sulfates, low reactivity	Precursor	Only 20 wt.% or lower percentage is recommended, or 100% can be used after water-wash pre-treatment	- Decreased compressive strength - Controlled hazardous elements leaching
Waste paper sludge	Contains organic matter and cellulose fiber	Precursor	A maximum of 10 wt.% can be used	- Decreased workability - Decreased drying shrinkage
Waste paper sludge ash	High reactivity, high calcium content	Precursor	Up to 100% can be used	- Decreased workability - Increased setting time - Increased compressive strength - Increased drying shrinkage
Rubber waste	Low density, hydrophobic nature, low stiffness, high deformability, good sound and thermal insulation, high toughness and impact resistance	Aggregate	A maximum of 10 wt.% or 20 vol.% is recommended	- Decreased density - Decreased mechanical properties (e.g., compressive, splitting tensile and flexural strength, elastic modulus)
		Fiber reinforcement	Up to 30 wt.% can be used	

Plastic waste	Low density, low stiffness, high deformability, good sound and thermal insulation, not easily biodegradable	Fine aggregate Fiber reinforcement	A maximum of 20 vol.% is recommended A maximum of 2 wt.% can be used	- Increased thermal and sound insulation - Increased ductility - Increased impact resistance and damping property - Decreased surface abrasion resistance - Increased tension strength (only as fiber reinforcement)
Tire steel and textile fiber	Tire steel fiber: High tensile strength, high density, potential corrosion Tire textile fiber: High tensile strength, low density	Fiber reinforcement	Tire steel fiber: a maximum of 2 vol.% can be used Tire textile fiber: a maximum of 20 vol.% is recommended	- Decreased compressive strength - Increased flexural strength - Increased toughness - More ductile behavior
Spent coffee grounds	Highly organic material, Low shear strength, high compressibility,	Filling material	A maximum of 70 wt.% is recommended	- Suitable mechanical properties for subgrade material (e.g., compressive strength and stiffness)
Waste cork	High carbon content (after thermal treatment)	Additive	A maximum of 3.75 wt.% can be used	- Increased electromagnetic interference shielding properties - Decreased compressive strength
Construction solid waste				
Waste clay brick	Low density, poor strength, high porosity, good fire resistance, relatively low reactivity	Precursor Aggregate	Up to 100% can be used	As aggregate usage: - Decreased density and increased porosity - Decreased mechanical properties (e.g., compressive, splitting tensile

Ceramic waste	Low density, poor strength, high porosity, good fire resistance, high reactivity			and flexural strength, elastic modulus) - Decreased durability properties (e.g., chemical attack, abrasion resistance) - Increased thermal insulation and thermal resistance (waste clay brick and ceramic waste) As precursor usage: - Decreased mechanical properties (e.g., compressive, splitting tensile, and flexural strength) - Increased thermal resistance (ceramic waste)
Waste asphalt pavement	High porosity, contain heavy metal, aged asphalt coating	Filling material	A maximum of 80 wt.% is recommended	- Suitable mechanical properties for base/subbase applications (e.g., compressive strength and stiffness) - Decreased cementitious bond
Asbestos-containing cement	Chemically comparable to an Mg-rich clinker, high reactivity (after thermal treatment)	Additive	A maximum of 2.5 wt.% is recommended	- Decreased porosity - Increased flexural strength
Mineral wool	High reactivity	Precursor	Up to 100% can be used	- Increased freeze-thaw durability

In general, both the municipal and construction solid waste materials can be potentially recycled, as the forms of precursor, aggregate, additive, reinforcement fiber, and filling materials, to fabricate the sustainable green concept geopolymeric composites. However, precaution must be taken to the possible detrimental effects caused by the use of waste, which can be achieved by carefully selecting the inclusion content. Therefore, it is crucial to conduct a systematic study on the effect of solid waste on the various properties of geopolymeric products. Also, if considering the use of municipal and construction solid waste for the mass production of geopolymeric composites, there is a need to assess the consistency and availability of materials supply in the waste streams as well as the distance to the geopolymeric product manufacturers.

Moreover, suitable treatments, such as the water-wash treatment, proper incineration course, and mechanical grinding, are well recognized to boost the behavior of solid waste-containing geopolymeric products. Another way to say, the usage of waste materials in geopolymeric composites could be greatly maximized without compromise in the performance of final geopolymeric products. However, there are some barriers to be overcome. Mostly, high costs and energy consumption demanded, especially by physical and thermal treatments, will drive down the environmental friendliness of the products from a global point of view (Gualtieri et al. 2012). Besides, as for the processes of chemical treatment, in addition to a large number of reagents necessary, the fate of the post-treatment reagents remains an issue of considerable concern (Spasiano & Pirozzi 2017). As a consequence, it is greatly advised to compile and examine the impacts associated with energy and material inputs and environmental releases for each treatment scenario. For this purpose, life cycle assessment is an effective tool, which can support decision-makers on waste treatment options and provide information on the attendant risks (Chen et al. 2019; Khandelwal et al. 2019; Kurda et al. 2018). Furthermore, advanced new technical methods are in high demand to overcome the defects of conventional treatment methods. For instance, Shi et al. (2016) recommended the carbonation treatment for RA, which is not only an efficient way for enhancing the properties of RA but also an environmentally friendly approach.

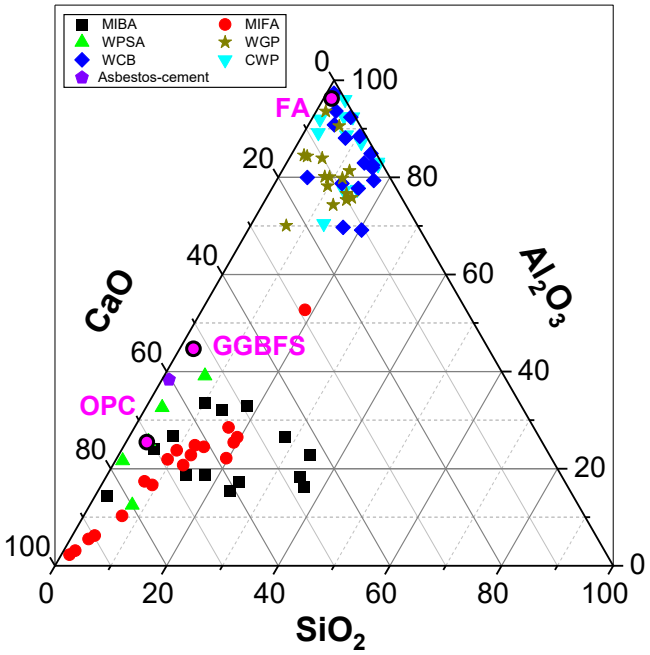

Figure 2.15. The ternary diagram of silica, alumina, and calcium oxide content in municipal and construction solid waste. Data from the results of Figs 2, 4, 5, 9, 12, 14, and 15, and the study of Gualtieri et al. (2012) for asbestos-cement

Figure 2.15 compares the main chemical compositions (i.e., calcium, silica, and alumina oxides) of different solid waste materials. Apparently, a wide variation in the main chemical compositions occurs due to the differences in their types and sources. Besides, the contents of other chemical compounds also vary according to the sources of solid waste, which can be seen from the previous sections. Furthermore, different solid waste materials also have various physical properties and mineralogical composites (Provis 2014; Reddy et al. 2016). All these diversities contribute to the disparate behaviors between synthesized geopolymeric composites (Provis et al. 2015). This, therefore, highlights the significance of the elucidation and modeling for geopolymerization reaction kinetics and mechanisms based on different source materials. It is because that high understanding could serve as a guideline for the researchers in identifying the crucial parameters during the design and fabrication stage, and also linking the performance of

resulted geopolymeric composites with the properties of source materials and formulation conditions. Thus, the true value of solid waste materials can be unlocked. Additionally, since the solid waste materials are often mineralogically heterogeneous and complex and often span a broad range of particle shapes and sizes, it also emphasizes the importance of the advanced characterization techniques for precursor materials (Provis et al. 2015).

To promote recycling solid waste materials into geopolymeric composites, the necessity of effective solid waste management plans and strategies is also evident. Especially, waste sorting is the key step in waste management to ensure a higher recycling rate (Ajayi et al. 2015). It is because that municipal and construction solid waste often contains a wide variety of materials, and mixed and contaminated waste is not suitable for recycling. Sorting could separate the waste into different groups in line with its components. Through waste sorting, more valuable components can be picked up for recycling. Against this scenario, more effective separation and sorting techniques, as well as the corresponding machinery, should be implemented to the waste stream, regardless of on-site or off-site operations (Gundupalli et al. 2017). In addition, the increasing awareness and participation of the public and relevant stakeholders are the critical components in the management program of municipal and construction waste. Finally, yet importantly, intervention and support from the government should be enhanced. It could include providing tax refunds for contractors who recycle waste materials, establishing recycling markets, setting up incentive-based market support, and granting no-interest loans for small companies to begin and expand their recycling projects (Huang et al. 2018a; Sun et al. 2018).

CHAPTER 3: ENGINEERING PROPERTIES OF SUSTAINABLE GRAC

This chapter mainly describes the development of sustainable GRAC, specifically the source materials, mix proportions, and preparing method are introduced. Afterward, the engineering properties of the developed GRAC under fresh and harden conditions are evaluated. Additionally, a detailed SEM study is conducted to characterize the microstructure.

3.1 Experimental program

3.1.1 Raw materials

Aggregate

The used coarse aggregates consisted of NA and RA. Both NA and RA were the mixtures of aggregates with 9.5 and 19 mm in nominal maximum size. The NA was crushed basalt aggregate from a local quarry. The RA was supplied by a local C&DW recycling plant in Sydney, which accepts and processes the C&DW. Then, the RA was washed in the laboratory to remove the floating particles. As shown in Figure 3.1, the NA exhibits an irregular morphology with sharp edges, while the RA has relatively round sides.

Locally available river sand with a fineness modulus of 2.76, a specific gravity of 2.61, and water absorption of 0.8% was adopted as fine aggregate. As shown in Figure 3.2, the particle size distribution of fine aggregate could meet the requirement stipulated in ASTM C33-16 (Standard Specification for Concrete Aggregates).

(a) NA (maximum size of 9.5 mm)

(b) NA (maximum size of 19 mm)

(c) RA (maximum size of 9.5 mm)

(d) RA (maximum size of 19 mm)

Figure 3.1.Comparison of the morphology of coarse aggregates

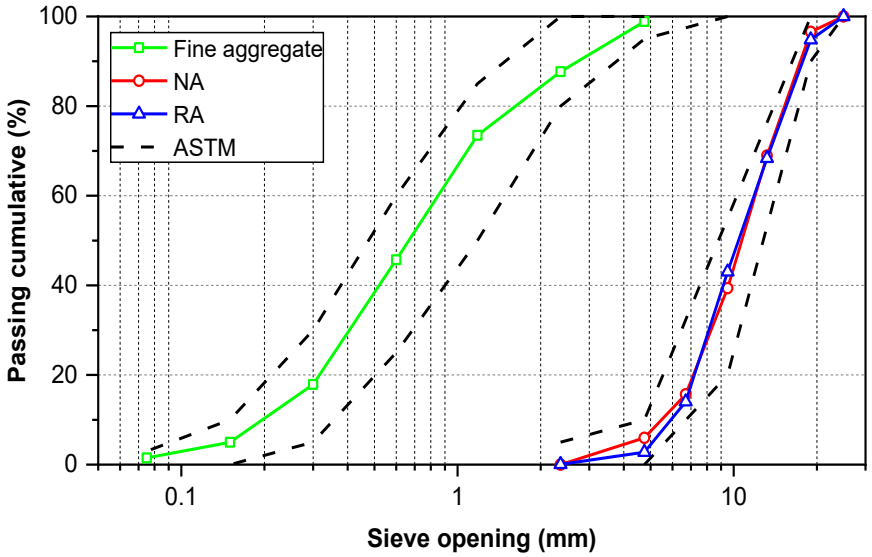

Figure 3.2. Particle size distribution curves for aggregates

Fly ash

Commercially available 'Class F' fly ash was used as the main binder. Fly ash was sourced from Eraring power plant in Australia. The percentage of retained particles on the 45-μm sieve was 1.2%. The chemical composition and loss on ignition (LOI) of fly ash are presented in Table 3.1.

Slag

GGBFS was used as the slag and a partial replacement of fly ash in this study. The percentage of retained particles on the 45-μm sieve was 2.0%. Table 3.1 presents the chemical composition and LOI of GGBFS.

Table 3.1 Chemical compositions of fly ash and GGBFS

Oxide composition	Fly ash (wt. %)	GGBFS (wt. %)
SiO_2	65.90	36.00
Al_2O_3	24.00	13.80
Fe_2O_3	2.87	0.30
CaO	1.59	42.60
MgO	0.42	5.80
MnO	0.06	0.40
K_2O	1.44	0.27
Na_2O	0.49	0.21
P_2O_5	0.19	0.10
TiO_2	0.92	0.80
SO_3	–	0.56
LOI	1.53	-1.00

Alkali activator

The mixture of sodium hydroxide (NaOH) solution and sodium silicate (Na_2SiO_3) solution was used as the alkaline activator. Sodium hydroxide solution of 12 M concentration was prepared by mixing 97-98% pure pallets with tap water, one day prior to the concrete mixing. The commercially available D-grade sodium silicate solution with a specific gravity of 1.53 and modulus ratio (Ms) (SiO_2/Na_2O) of 2.0 (SiO_2=29.4%, Na_2O=14.7%, and water=55.9%) was obtained from PQ Australia Ltd.

3.1.2 Characterization of coarse aggregates

The RA was examined for the purpose of identifying and estimating the relative proportions of constituent materials as specified in BS EN 933-11:2009 (Tests for Geometrical Properties of Aggregates. Classification Test for the Constituents of Coarse RA). The physical properties of the NA and RA, including density and water absorption, particle size distribution, and particle shape, were determined according to ASTM C127-15 (Standard Test Method for Relative Density and Absorption of Coarse Aggregate), ASTM C136-14 (Standard Test Method for Sieve Analysis of Fine and Coarse Aggregates), and BS EN 933-3:2012 (Tests for Geometrical Properties of Aggregates. Determination of Particle Shape, Flakiness Index), respectively. The mechanical properties (aggregate crushing value) of the NA and RA were also measured according to BS 812-110:1990 (Tests for Geometrical Properties of Aggregates. Methods for Determination of Aggregate Crushing Value).

3.1.3 Mix proportions and specimen preparation

In this study, twelve mixtures of geopolymeric concrete were designed. Three different RA replacement levels and four different contents of slag in the binder were considered. In detail, the RA was used as 0%, 50%, and 100% by weight replacement of the NA, while slag was used as 0%, 10%, 20%, and 30% by weight substitution of fly ash. The activator solution content in the mixture was taken as 55% of the total binder mass, and the mass of Na_2SiO_3 solution used was 2.0 times that of NaOH solution. The mix proportions of geopolymeric concrete studied are presented in Table 3.2.

Table 3.2 Mix proportions of geopolymeric concrete

Mixes	Components (kg/m^3)						
	FA	GGBFS	Na_2SiO_3	NaOH	Sand	NA	RA
S00	420	0	165	66	550	1220	0
S10	378	42	165	66	550	1220	0
S20	336	84	165	66	550	1220	0
S30	294	126	165	66	550	1220	0
S00R50	420	0	165	66	550	610	610
S10R50	378	42	165	66	550	610	610
S20R50	336	84	165	66	550	610	610
S30R50	294	126	165	66	550	610	610
S00R100	420	0	165	66	550	0	1220
S10R100	378	42	165	66	550	0	1220
S20R100	336	84	165	66	550	0	1220
S30R100	294	126	165	66	550	0	1220

The mixing was performed in a laboratory tilting drum mixer. Coarse and fine aggregates in saturated surface dry (SSD) condition and the binders (fly ash and slag) were dry mixed thoroughly in the mixer for 2 min. After that, the premixed alkaline activator solution was added slowly and evenly into the mixer over a period of 1 min. Then mixing was continued for further 3-5 min to ensure a uniform mixing and no dry residuals left in the mixer. The fresh mixture was cast into moulds and put on a vibration table to ensure compaction. Subsequently, the specimens were covered with plastic films to prevent the evaporation of the free water in the mixture during cure. Then the specimens were stored at room temperature of approximately 20 °C for 1 h, followed by heat-cured at 75 °C for 1 day. Next, the specimens were demoulded and wrapped with plastic films, and were stored in ambient temperature ranging from 15 to 20 °C until the ages of testing.

3.1.4 Properties of fresh concrete

The slump value was measured immediately after mixing to determine the workability of the fresh mixture as recommended in ASTM C143-15 (Standard Test Method for Slump of Hydraulic Cement Concrete). Meanwhile, setting times were determined by the means of the penetration resistance measurements on mortar sieved from the concrete mixture,

as described in ASTM C403-16 (Standard Test Method for Time of Setting of Concrete Mixtures by Penetration Resistance).

3.1.5 Physical characterization of hardened concrete

The density, absorption, and permeable voids of concrete were measured after 28 days of curing, by using cylindrical specimens with 100 mm diameter and 100 mm height as per ASTM C642-13 (Standard Test Method for Density, Absorption, and Voids in Hardened Concrete). The capillary sorptivity was assessed after 28 days of curing, by using cylindrical discs with 100 mm diameter and 50 mm height following ASTM C1585-13 (Standard Test Method for Measurement of Rate of Absorption of Water by Hydraulic-Cement Concretes). Specifically, the rate of sorptivity of water was determined by measuring the increase in the mass of a specimen resulting from absorption of water as a function of time when only one surface of the specimen is exposed to water. The specimen is conditioned in an environment at a standard relative humidity to induce a consistent moisture condition in the capillary pore system. The exposed surface of the specimen is immersed in water and water ingress of unsaturated concrete is dominated by capillary suction during initial contact with water.

3.1.6 Mechanical characterization of hardened concrete

Compressive strength was determined at 3, 7, and 28 days' age, while the splitting tensile strength and flexural strength were measured at 28 days' age. Compressive strength test was conducted using cylindrical specimens with 100 mm diameter and 200 mm height at a loading rate of 0.25 MPa/s in accordance with ASTM C39-18 (Standard Test Method for Compressive Strength of Cylindrical Concrete Specimens). Tensile splitting strength test was conducted at the loading rate of 1.0 MPa/min using cylindrical specimens with 100 mm diameter and 200 mm height in accordance with ASTM C496-17 (Standard Test Method for Splitting Tensile Strength of Cylindrical Concrete Specimens). The flexural strength was determined at the loading rate of 1.0 MPa/min using prismatic specimens of size 100 × 100 × 400 mm under third-point loading as per ASTM C78-18 (Standard Test Method for Flexural Strength of Concrete, Using Simple Beam with Third-Point Loading). The average result of three samples was reported for each test.

3.1.7 Microstructural characterization

SEM images were used to characterize the microstructure, including the morphology of the geopolymer matrix and the ITZ between the matrix and aggregate. After the compression tests, selected samples containing geopolymeric matrix and coarse aggregate were immersed into isopropanol alcohol for 24 hours to stop the geopolymerization process and then stored in the vacuum environment until tests. The sample was coated with gold prior to test staring, and then was examined with a Zeiss FEG-SEM at an accelerating voltage of 15 kV.

3.2 Coarse aggregate properties

3.2.1 Compositional characterization

The constituents of RA are presented in Table 3.3, as well as the proportion, density, and absorption of each constituent. The constituent based on concrete products was the major part of RA, accounting for 80% and 64% of the RA with nominal maximum sizes of 9.5 and 19 mm respectively. The secondary was brick masonry, which constituted 10% and 33% for 9.5 and 19 mm RA, respectively. The rest included tile, natural stone, and glass (less than 10%). According to the classification suggested by Silva et al. (2014), the used RA can be categorized into mixed RA.

Table 3.3 Details of RA constituents

Constituents	Nominal maximum diameter					
	9.5 mm			19 mm		
	Amount (wt. %)	Relative density (SSD)	Absorption (wt. %)	Amount (wt. %)	Relative density (SSD)	Absorption (wt. %)
Concrete products	79.52	2.34	7.74	64.44	2.41	6.33
Brick	9.73	2.22	10.60	33.42	2.23	8.55
Tile	5.40	2.30	8.51	1.23	2.35	6.93
Natural stone	2.93	2.55	3.62	0.91	2.53	3.77
Glass	2.42	2.49	0.92	–	–	–

The relative densities of RA constituents ranged from 2.22 to 2.55, depending on the material type. In terms of absorption, the brick masonry based aggregates exhibited the highest value, followed by the aggregates based on tile, concrete products, natural stone, and glass.

3.2.2 Physical properties

Based on the results of aggregate particle size distributions and the grading requirement, the NA and the RA were composed of the corresponding aggregates with nominal maximum sizes of 9.5 and 19 mm in ratios of 1:2 and 2:1, respectively. The particle size distributions of the final combined NA and RA are shown in Figure 3.2. It can be seen that the particle size distribution of RA is very close to that of NA, and they both fall within the upper and lower limit bounds stipulated in ASTM C33-16 (Standard Specification for Concrete Aggregates).

Table 3.4 compares the physical properties of the final combined NA and RA. The results show that the RA was less dense than the NA by about 20%. In addition, the RA absorbed 3.5 times higher amounts of water than the NA. This observation is to be expected as the high porosity and low density of the RA components, as shown in Table 3.3. As for particle shape, the NA had a higher flakiness index than the RA. This is because the recycling process consists typically of two crushing stages (i.e., primary crushing stage and secondary crushing stage), which would result in a rounder and less sharp particles.

Table 3.4 Physical and mechanical properties of coarse aggregates

	Relative density (SSD)	Relative density (Oven-dry)	Absorption (wt. %)	Flakiness index (%)	Aggregate crushing value (wt. %)
NA	2.88	2.83	1.57	11.46	16.65
RA	2.34	2.18	6.78	9.99	24.54

3.2.3 Mechanical properties

As shown in Table 3.4, a crushing value of 24.54% is found for the RA, which is 47% higher than the crushing value of 16.65% for the NA. This is because of the presence of

adhered mortar and clay masonry units in the RA, which are prone to disintegrate during the test. Similar values were observed by Medina et al. (2014), which values of 16% and 20% for NA and RA, respectively.

3.3 Fresh properties

3.3.1 Workability

In the absence of additional water and superplasticizer, the fresh mixtures of geopolymeric concrete exhibited highly cohesive and viscous feature, which made it relatively hard to handle. The slump values of the geopolymeric concrete mixtures are plotted in Figure 3.3. It can be observed that the slump value decreased with the increase of slag content in the binder, and this effect appeared to be more pronounced at the higher content of slag. The lower workability of mixtures containing slag was attributed to the high content of calcium ions dissolved from slag and its rapid reaction with the alkali activator to precipitate as calcium silicate hydrate (Bernal et al. 2011). Moreover, the smooth surface and the spherical shape of fly ash particles help to lubricate the mixture, as opposed to the irregular shape of slag particles with rougher surfaces (Şahmaran et al. 2008).

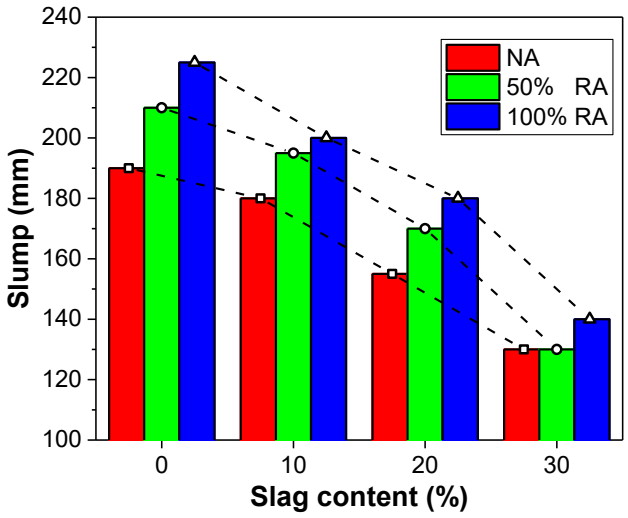

Figure 3.3. Slump values of geopolymeric concrete

At the same content of slag, the workability of the geopolymeric concrete mixtures exhibited a slightly increasing trend with the increase in RA content. The studies conducted by Nuaklong et al. (2016) and Poon et al. (2004) also showed that the use of RA at SSD condition improved the workability of concrete. This was due to the RA contained a larger volume of free water at SSD condition than the NA. The larger amount of initial free water inside RA was available and therefore improved the workability of the mixture (Behera et al. 2014). On the other hand, the RA had a more rounded and spherical shape, which allowed the mortar to flow better around the aggregate.

3.3.2 Setting time

The setting time test was carried out at a controlled temperature of 18-20 °C. As shown in Figure 3.4, the setting time of geopolymeric concrete was mainly influenced by the content slag. Mixtures without slag took significantly long time to set. However, both the initial and final setting time of geopolymeric concrete decreased considerably after the incorporation of slag in the binder. Moreover, the setting time (both initial and final setting time) exhibited a continuous downtrend with the increase of slag content. Besides that, the difference between the initial and final setting time also reduced with the increase of slag content in the binder. This was in agreement with the result observed by other researchers that the higher slag content in the binder, the quicker was the rate of setting (Lee & Lee 2013; Nath & Sarker 2014). It has been reported that as the slag contained a reasonably high CaO content, the incorporation of slag resulted in an increase in calcium content in the geopolymeric system. The addition of calcium significantly accelerated the hydration reaction of the mixture (Nath & Sarker 2014). Additionally, Puligilla & Mondal (2013) revealed that in the presence of free calcium, the rate and the extent of fly ash dissolution would be improved due to the precipitated calcium silicate hydrate acts as nucleation sites.

Although the test for the setting time was conducted on the mortar obtained from sieving concrete mixtures, it could be observed that the replacement of NA by RA resulted in a slight increase in the setting time, which can be explained by a large amount of initial free water inside the RA. Also, it has been reported that RA consists of soluble sugars or

other organic substances. Some of these have inhibiting effects on the setting and hardening of geopolymeric concrete (Lee et al. 2016). However, the effect of the inclusion of RA on the setting time was insignificant when compared with that of adding slag.

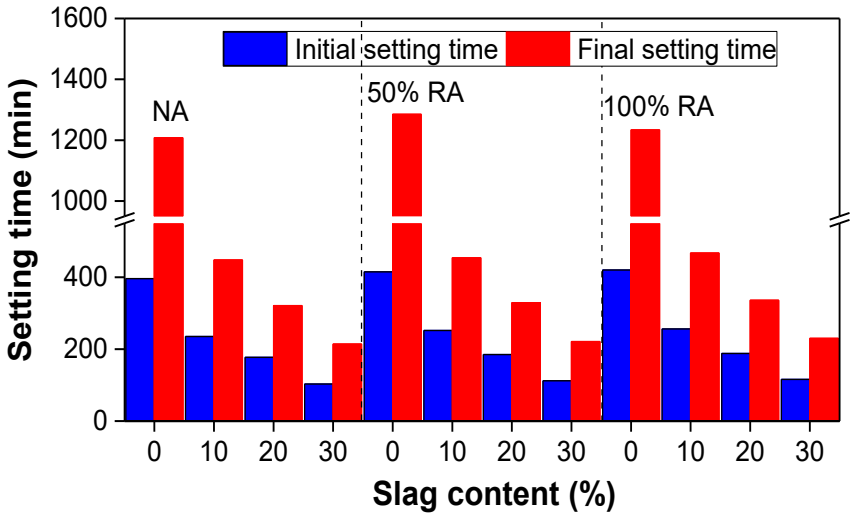

Figure 3.4. Setting time of geopolymeric concrete

3.3.3 Segregation and bleeding

Previous research stated that the liquid content played an important role in the workability of geopolymeric concrete. The inclusion of liquid beyond a certain limit would cause segregation or bleeding of fresh geopolymeric concrete (Posi et al. 2015). In this study, no bleeding or segregation occurred in the mixtures during the specimen preparation.

3.4 Physical properties

3.4.1 Density

Table 3.5 presents the density of the test mixtures in saturated condition at 28 days. The density varied from 2165 to 2432 kg/m^3 depending on the slag content and the RA replacement ratio. Specifically, the substitution of fly ash by slag increased the density. On the other hand, the use of RA decreased the density by 4-8% due to the lower density of the RA. The density values as a function of the RA replacement ratio under the

different slag content are presented in Figure 3.5. As shown in Figure 3.5, linear relationships can be observed between the density and the RA replacement ratio, which is consistent with the results reported by Medina et al. (2014).

Table 3.5 Physical properties of geopolymeric concrete at 28 days of age

Mixes	Bulk density (kg/m^3)	Water absorption (%)	Volume of permeable void (%)	Sorptivity ($10^{-3}\times$ $mm/s^{1/2}$)
S00	2383	6.20	14.87	13.87 ± 0.48
S10	2402	5.76	14.35	7.54 ± 0.48
S20	2415	5.65	14.01	5.98 ± 0.43
S30	2432	5.48	13.70	5.27 ± 0.41
S00R50	2284	8.04	17.98	23.49 ± 1.02
S10R50	2317	7.63	16.82	13.55 ± 0.36
S20R50	2323	7.35	16.74	11.96 ± 0.73
S30R50	2334	6.95	16.60	11.02 ± 0.55
S00R100	2165	10.18	20.01	27.21 ± 0.59
S10R100	2210	9.41	19.01	14.77 ± 0.99
S20R100	2219	9.20	18.70	14.00 ± 0.79
S30R100	2224	8.40	18.15	13.88 ± 0.64

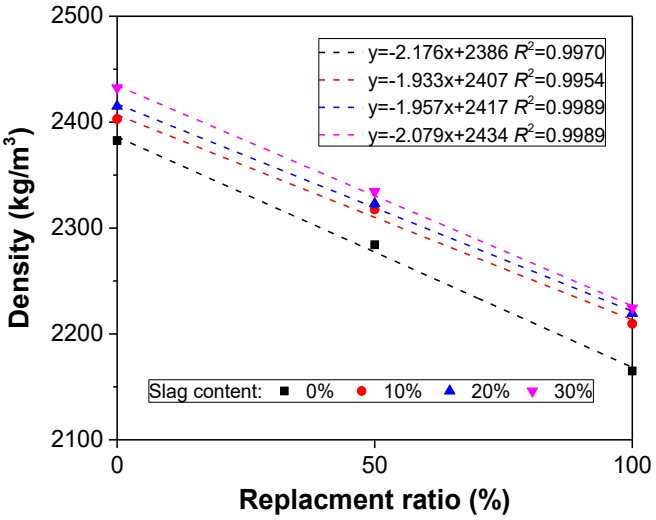

Figure 3.5. Density of geopolymeric concrete at 28 days of age

3.4.2 Water absorption

Figure 3.6 presents the water absorption results of the test mixtures. The water absorption increased significantly with the increasing content of RA. This increase is mainly due to the higher absorption value of RA compared to NA. The results also show that the substitution of fly ash by slag led to lower water absorption. Such a decrease in water

absorption can be explained by consideration of the binder chemistry. The slag inclusion resulted in the formation of calcium alumino-silicate hydrate (C-A-S-H) binding type gels, which are denser than geopolymer type gels (Provis et al. 2012).

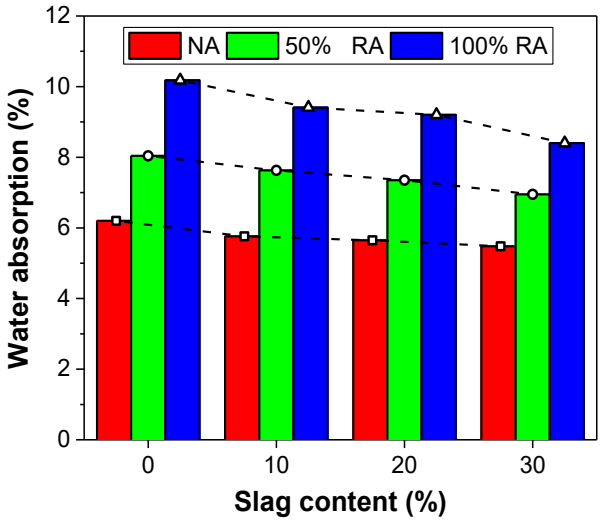

Figure 3.6. Water absorption of geopolymeric concrete at 28 days of age

3.4.3 Volume of permeable void

Figure 3.7 presents the volume of permeable voids of the test mixtures. A similar trend to water absorption can be observed in the result of the volume of permeable voids: specifically, the value increases with the increase of RA replacement ratio while decreases with the increase of slag content. As shown in Figure 3.8, a good correlation could be observed between the volume of permeable void and water absorption. As the water absorption increased, the volume of permeable void also increased correspondingly.

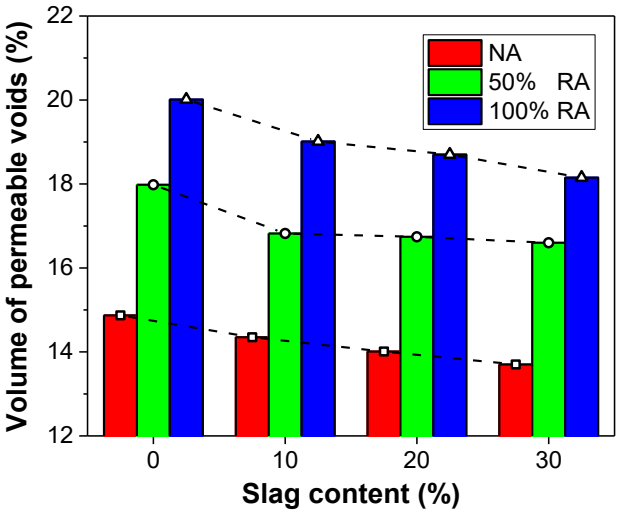

Figure 3.7. Volume of permeable voids of geopolymeric concrete at 28 days of age

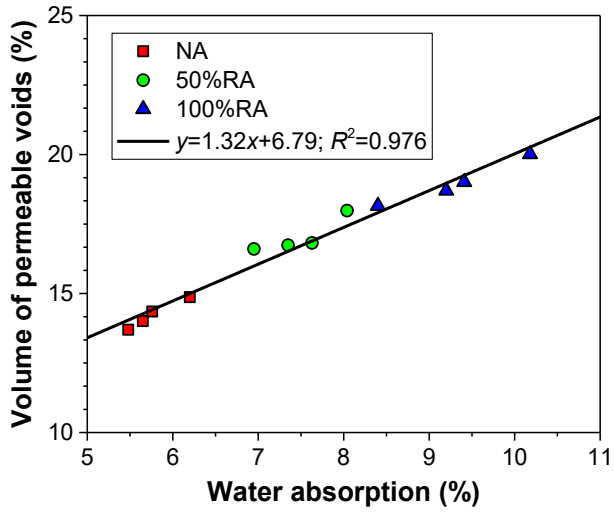

Figure 3.8. Relationship between water absorption and volume of permeable voids for geopolymeric concrete at 28 days of age

3.4.4 Water sorptivity

Figure 3.9 shows the rate of water absorption (sorptivity) of test mixtures for the first six hours, namely initial sorptivity. It can be seen that the rate of water absorption increases as the content of RA increases. The increased sorptivity was expected and was attributed to the porous components of RA, such as the attached mortars and the masonry products. Furthermore, given the manufacturing process of the RA, it tends to form cracks and

fissures in the aggregate, which would further increase the sorptivity of concrete (Shaikh et al. 2015). The result furthermore shows that the inclusion of slag could significantly lower the sorptivity of geopolymeric concrete, which coincides with the more porous microstructure in fly ash based geopolymer in comparison with geopolymer with slag inclusion. (Fernández-Jiménez et al. 2005; Ismail et al. 2013). However, the improvements on the sorptivity due to the addition of slag were relatively unvarying at different slag contents.

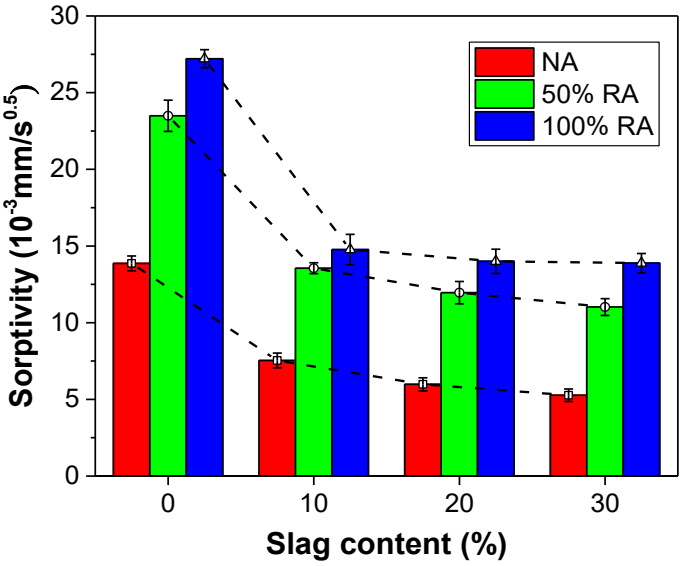

Figure 3.9. Sorptivity results of geopolymeric concrete at 28 days of age

Figure 3.10 presents the relationship between sorptivity and volume of permeable voids of the test mixtures. In general, an excellent correlation can be observed between the sorptivity and the volume of permeable voids: specifically, sorptivity increases with the volume of permeable voids. Moreover, the inclusion of slag resulted in a shift as to the relationship between the sorptivity and volume of permeable voids. This is mainly attributed to that, in addition to the volume of permeable voids, the capillary sorption is also linked to the tortuosity of the pore network. It has been reported that the inclusion of slag resulted in an increase in pore network tortuosity due to the formation of C-A-S-H having high tortuosity characteristics (Provis et al. 2012).

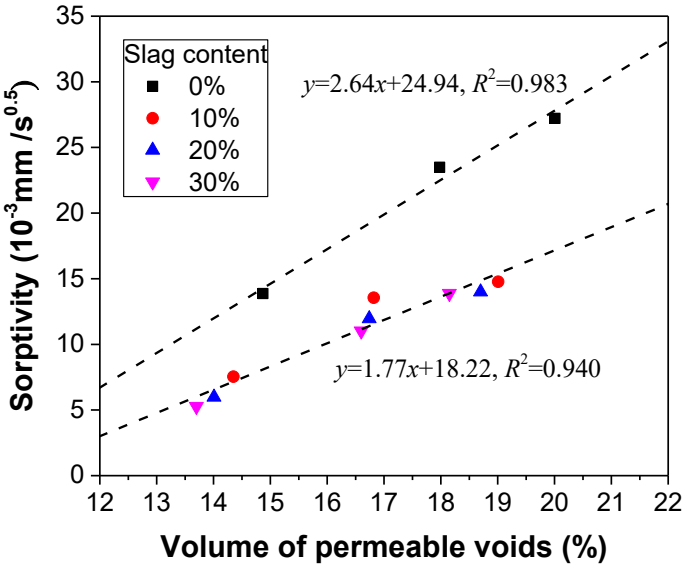

Figure 3.10. Relationship between sorptivity and permeable void of the geopolymeric concrete at 28 days of age

3.5 Mechanical properties

3.5.1 Compressive strength

The results of compressive strength for the test mixtures at 3, 7, and 28 days are listed in Table 3.6. The heat treatment can accelerate the formation of hard structures of geopolymers. As expected, the elevated temperature cure led to the high-strength gain at the early age. As shown in Figure 3.11, the 3-day and 7-day compressive strengths were observed to be more than 77% and 90% of the corresponding 28-day strength, respectively. This demonstrates the feasibility of heat-cured geopolymeric concrete for manufacturing precast concrete elements.

Table 3.6 Mechanical properties of geopolymeric concrete

Mixes	Compressive strength (MPa)			Flexural strength (28-day) (MPa)	Splitting tensile strength (28-day) (MPa)
	3-day	7-day	28-day		
S00	20.2 ± 1.37	23.7 ± 0.54	26.1 ± 1.23	3.50 ± 0.34	2.76 ± 0.02
S10	36.6 ± 2.89	41.7 ± 3.16	43.5 ± 1.90	4.56 ± 0.14	3.97 ± 0.08
S20	41.0 ± 2.21	45.3 ± 1.57	47.0 ± 2.43	4.87 ± 0.34	4.71 ± 0.19
S30	45.4 ± 1.36	51.0 ± 2.82	52.3 ± 0.78	5.01 ± 0.21	4.77 ± 0.04
S00R50	12.7 ± 0.66	13.0 ± 1.20	14.0 ± 1.12	2.66 ± 0.07	1.92 ± 0.06
S10R50	27.2 ± 1.14	30.9 ± 1.01	31.9 ± 1.00	4.00 ± 0.22	3.42 ± 0.15
S20R50	28.7 ± 0.92	33.4 ± 1.67	35.6 ± 0.87	4.24 ± 0.16	3.69 ± 0.11
S30R50	36.0 ± 0.74	40.9 ± 3.28	43.0 ± 0.84	4.36 ± 0.25	4.16 ± 0.13
S00R100	12.2 ± 0.75	13.0 ± 0.04	13.7 ± 1.16	2.19 ± 0.18	1.66 ± 0.02
S10R100	22.1 ± 1.12	26.5 ± 2.52	27.5 ± 1.46	3.37 ± 0.17	2.63 ± 0.13
S20R100	30.5 ± 1.00	34.5 ± 1.68	34.8 ± 1.54	3.91 ± 0.14	2.95 ± 0.12
S30R100	34.1 ± 2.63	37.9 ± 0.85	38.1 ± 1.66	4.22 ± 0.32	3.54 ± 0.06

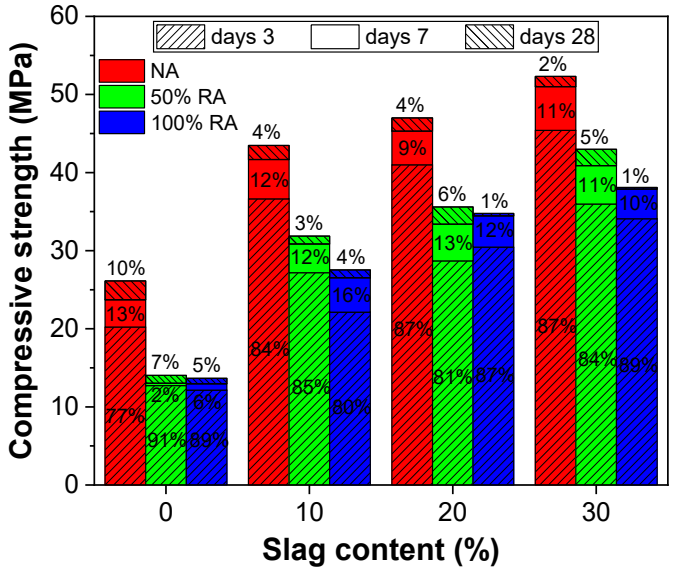

Figure 3.11. Compressive strength of geopolymeric concrete at 3, 7, and 28 days of age

Additionally, Figure 3.11 shows that the use of slag equips the geopolymeric concrete with higher compressive strength, regardless of the aggregate type and curing age. For

instance, the mixtures having 10%, 20%, and 30% slag of total binder achieved more than 67%, 79%, and 100% higher compressive strength at 28 days, respectively, than the mixtures without slag. This rise is consistent with the existing literature (Deb et al. 2014; Lee & Lee 2013; Li & Liu 2007; Nath & Sarker 2014). The improvement in compressive strength after slag addition could be attributed to the high calcium content in slag, which results in the formation of gel phase (C-A-S-H) and improves the compactness of microstructure (Kumar et al. 2010). Puligilla & Mondal (2013) also reported that the free calcium ions could prolong fly ash dissolution and therefore enhance the formation of geopolymer type gel.

As shown in Figure 3.11, the compressive strength was adversely affected by the RA replacement and declined with the increasing content of RA, because of the lower strength of RA compared with NA. Moreover, the adverse influence of RA on the compressive strength was more pronounced in the mixtures based on fly ash only. For example, the strength reduction factor due to the full replacement of NA by RA was more than 43% for the fly ash based geopolymeric concrete, while the factors were less than 36%, 26%, and 27%, respectively, for the mixtures containing 10%, 20% and 30% slag of the total binder.

3.5.2 Flexural strength

As shown in Figure 3.12, the flexural strength of the mixture with RA is lower than that of the corresponding mixture with NA, and decreases with the increase in RA content. The reasons for the flexural strength drop might include the poor quality of RA and the low bonding strength between the RA and the geopolymeric matrix. However, the flexural strength showed an ascending trend when the content of slag was increased. After the inclusion of 10%, 20%, and 30% slag, the strengths increased by 30%, 39%, and 43% respectively for the mixtures without RA; by 51%, 60%, and 64% respectively for the mixtures with 50% RA; and by 54%, 78% and 92% respectively for the mixtures with 100% RA. It also can be seen that the mixtures incorporating slag underwent less reduction in flexural strength incurred by the replacement of NA by RA, compared with the mixtures based on fly ash only. Specifically, for the mixtures based on fly ash only,

the reductions in flexural strength were 24% and 37%, respectively, at the RA content of 50% and 100%, while for the mixtures based on fly ash and slag combination, the reductions were less than 13% and 26%, respectively.

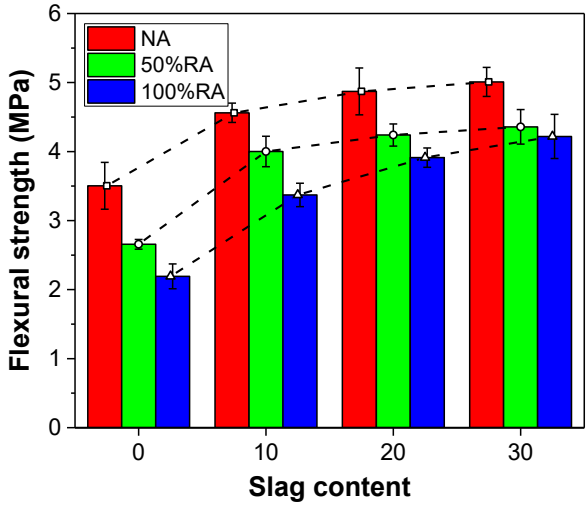

Figure 3.12. Flexural strength of geopolymeric concrete at 28 days of age

Figure 3.13 shows the relationship between the flexural strength and the compressive strength of the test mixtures at 28 days. The predicted flexural strengths by ACI Building Code 318 and the Eurocode 2 are also presented. According to ACI Building Code 318, the relationship between the modulus of rupture of concrete f_r and the specified compressive strength of concrete f_c' is expressed as follows:

$$f_r = 0.62\sqrt{f_c'} \tag{3.1}$$

The relationship between the mean flexural strength ($f_{cm,fl}$) and the characteristic compressive cylinder strength (f_{ck}) of concrete at 28 days suggested by Eurocode 2 are as follows:

$$f_{cm,fl} = \max\left[\left(1.6 - \frac{h}{1000}\right) f_{ctm}; f_{ctm}\right] \tag{3.2}$$

$$\begin{cases} f_{ctm} = 0.3\left(f_{ck}\right)^{2/3}, & f_{ck} \le 50\text{MPa} \\ f_{ctm} = 2.12\times\left(1+(\frac{f_{cm}}{10})\right)^{2/3}, & f_{ck} \ge 50\text{MPa} \end{cases} \tag{3.3}$$

$$f_{cm} = f_{ck} + 8 \tag{3.4}$$

where f_{ctm} is the mean value of axial tensile strength of concrete (MPa), f_{cm} is the mean compressive strength (MPa), and h is the total member depth (mm).

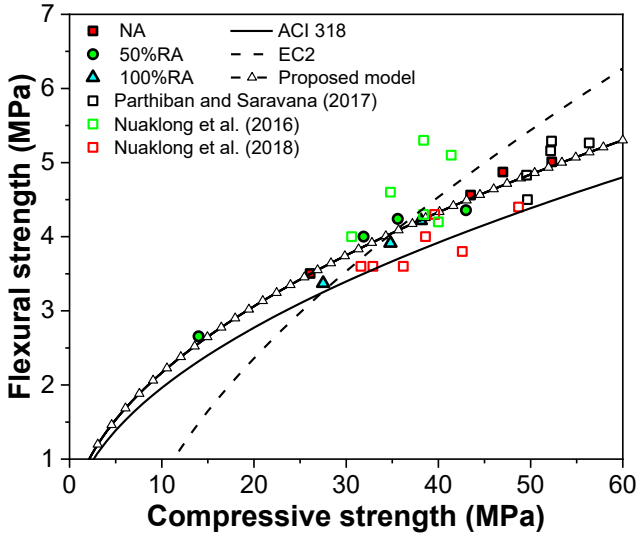

Figure 3.13. Compressive strength versus flexural strength of geopolymeric concrete at 28 days of age

The experimental results of the flexural strength were found to be larger than the predicted results as per ACI 318 code provision (with R^2=0.768) except for the mixture based on fly ash containing 100% RA. Nevertheless, the relationship suggested by Eurocode 2 (with R^2=0.693) underestimates the flexural strength when the compressive strength is under 36 MPa and overestimates when the compressive strength is above 36 MPa. Based on the obtained results, a model (Eq. (3.5) similar to that in ACI Building Code 318 is proposed here, which has been plotted in Figure 3.13. Relatively small discrepancies could be observed when comparing the proposed model with the results obtained by Parthiban & Saravana Raja Mohan (2017), Nuaklong et al. (2016), and Nuaklong et al. (2018a).

$$f_{ct,fl} = 0.68\sqrt{f_c'} \tag{3.5}$$

3.5.3 Splitting tensile strength

Figure 3.14 exhibits the variation in the tensile strength for the test mixtures. A similar trend to compressive strength or flexural strength could be observed in the case of splitting tensile strength, where the strength declines with the rise in the content of RA. The 50% and 100% replacement of NA by RA resulted in the strength loss ranging from 0.54 to 1.01 MPa, and from 1.09 to 1.76 MPa, respectively. Additionally, the addition of slag into mixtures improved the strength significantly. As shown in Figure 3.14, the strength was improved by more than 0.97, 1.28, and 1.87 MPa for the inclusion of 10, 20, and 30% slag, respectively.

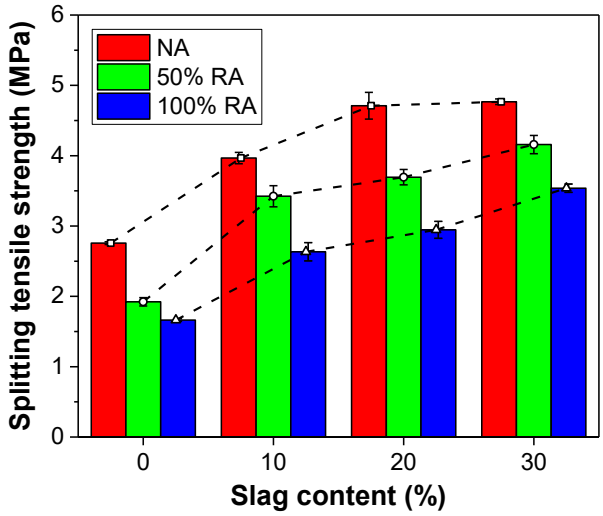

Figure 3.14. Splitting tensile strength of geopolymeric concrete at 28 days of age

As shown in Figure 3.15, the measured splitting tensile strengths were compared with the prediction by the Eurocode 2 and ACI building code 318. The relationship between the tensile strength of concrete and the compressive strength suggested by the ACI building code 318 is as follows:

$$f_{ct} = 0.56\sqrt{f_c'} \tag{3.6}$$

where f_{ct} is the splitting tensile strength (MPa).

Eurocode 2 suggests that the tensile strength of concrete $f_{ct,sp}$ can be estimated as follows:

$$f_{ctm} = 0.9 f_{ct,sp} \tag{3.7}$$

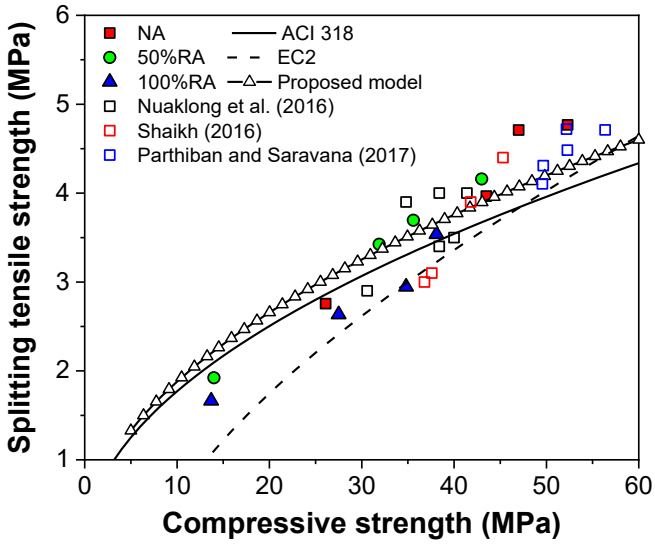

Figure 3.15. Compressive strength versus splitting tensile strength of geopolymeric concrete at 28 days of age

Most measured splitting tensile strengths are higher than the predictions by Eurocode 2, with R^2=0.791. However, the prediction by ACI Building Code 318 overestimates the splitting tensile strength at low compressive strength and underestimates at high compressive strength (R_2=0.698). Based on the test results, this paper identified an equation shown in Eq. (3.8) similar to that in the ACI building code 318 with R^2= 0.841. Additionally, a good agreement could be established between this predicted value by Eq. (3.8) with the results obtained in other studies on geopolymeric concrete with RA (Nuaklong et al. 2016; Parthiban & Saravana Raja Mohan 2017; Shaikh 2016)

$$f_{ct} = 0.59\sqrt{f_c'} \tag{3.8}$$

Figure 3.16 shows the relationship between the splitting tensile strength and flexural strength. It can be seen that the splitting tensile strength is 3% to 28% lower than the

corresponding flexural strength, but as the strength increases, the difference becomes smaller. This assertion agrees with previous work (Nuaklong et al. 2016; Nuaklong et al. 2018a; Parthiban & Saravana Raja Mohan 2017). Moreover, a linear relationship of Eq. (3.9) with R^2=0.955 could be established between the flexural strength and splitting tensile strength, as shown in Figure 3.16.

$$f_{ct,fl} = 1.12 + 0.83 f_{ct,sp} \tag{3.9}$$

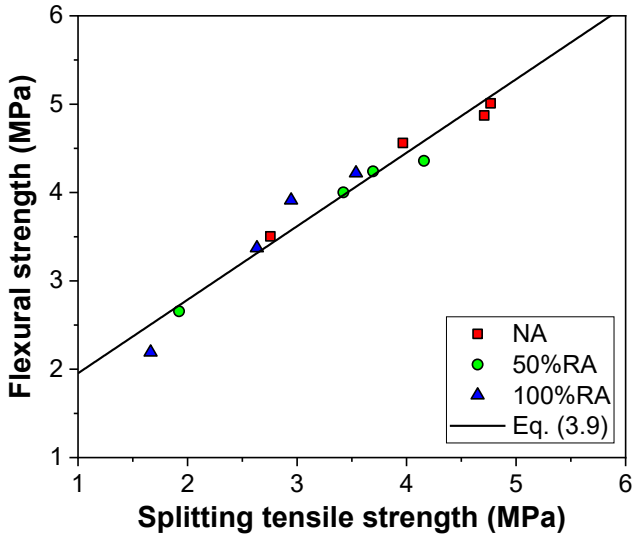

Figure 3.16. Splitting tensile strength versus flexural strength of geopolymeric concrete at 28 days of age

3.6 Microstructural observation

The microstructure images of geopolymeric concrete with NA and RA are presented in Figure 3.17 and Figure 3.18, respectively. Regardless of the type of used aggregate, the geopolymeric matrixes under different contents of slag exhibit distinct differences in the microstructure. The geopolymeric matrix without slag indicates the multiplicity of porosity and non-uniform structure, as shown in Figure 3.17(a) and Figure 3.18(a). Also, cracks are primarily formed in the geopolymeric matrix because the matrix had a lot of defects and was not dense. However, with the increase of slag content, improvement in the pore structure and density development could be observed in Figure 3.17 (b) to (d) and Figure 3.18 (b) to (d). Moreover, after the inclusion of slag, cracks almost happened

on the interface and then extended into the matrix, which could be inferred that the weaker part is in the ITZ between the aggregate and matrix. These results could explain the variation of the mechanical and physical properties of geopolymeric concrete with different slag content. By comparing the geopolymeric concrete with different aggregate types in Figure 3.17 and Figure 3.18, it can be found that, for a given slag content, there is no significant change as to the microstructure of the geopolymeric matrix and the morphology of ITZ. These findings confirm the reason for the decrease of mechanical properties caused by the RA replacement is dominated by the more defects that existed in RA compared with NA.

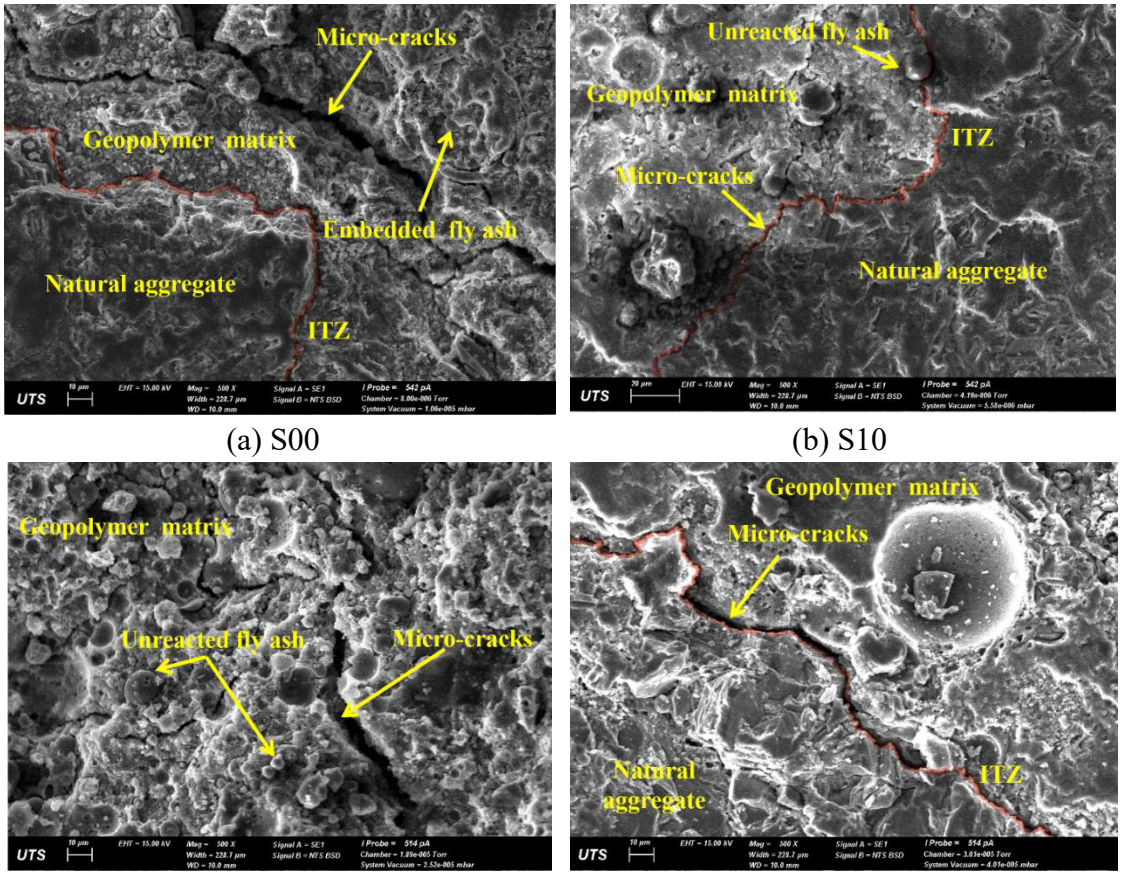

(a) S00 (b) S10

(c) S20 (d) S30

Figure 3.17. Microstructure of geopolymeric concrete containing NA

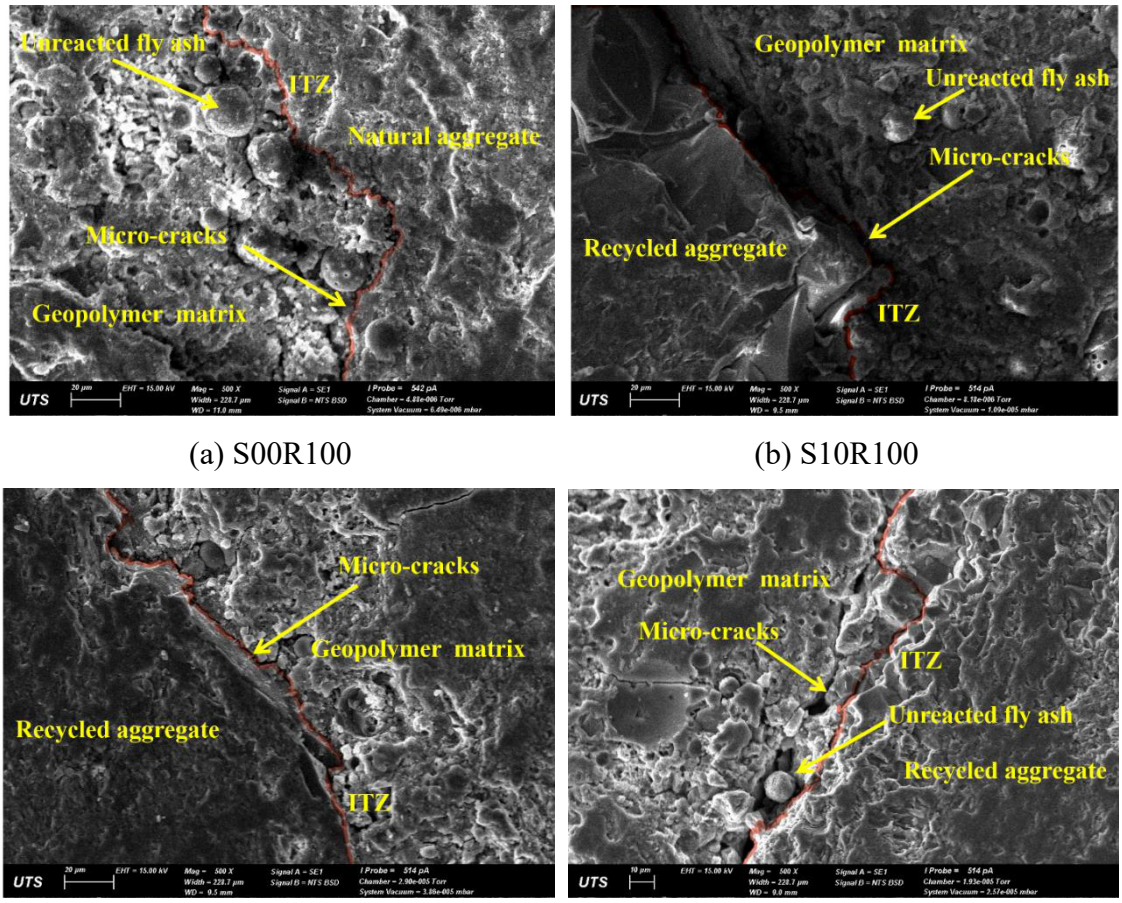

(a) S00R100 (b) S10R100

(c) S20R100 (d) S30R100

Figure 3.18. Microstructure of geopolymeric concrete containing RA

3.7 Summary

(1) The RA consisted primarily of concrete products, clay masonry units, natural stone, and glass, which could be categorized into mixed RA. The RA exhibited poor performance in terms of density, absorption, and crushing values, in comparison with NA.

(2) The substitution of slag for fly ash reduced the workability and setting time of geopolymeric concrete, while the replacement of NA by RA resulted in a slight increase in the workability and setting time.

(3) The replacement of NA by RA adversely affected the physical and mechanical properties of geopolymeric concrete. However, geopolymeric concrete with RA still

possesses sufficiently high compressive strength up to 43.1 MPa and 38.5 MPa for RA replacement ratios of 50% and 100%, respectively.

(4) The improvements in transport properties and mechanical properties of geopolymeric concrete were achieved with the substitution of slag for fly ash. Moreover, the inclusion of slag diminished the effects on mechanical properties caused by the replacement of NA by RA.

(5) Excellent correlations are identified between the water absorption, sorptivity, and volume of permeable voids, as well as among splitting tensile strength, flexural strength, and compressive strength. However, the existing empirical models suggested by the ACI Building code and Eurocode 2 exhibits large discrepancies with respect to the mechanical properties.

(6) Based on the experimental results in this study, equations with high accuracy were proposed to predict the relationship between compressive strength and other mechanical properties of geopolymeric concrete, which also fit reasonably well with the results obtained by other researchers.

(7) There was no significant change in the microstructures of the geopolymeric concrete with different aggregate types. However, the inclusion of slag resulted in denser geopolymeric matrix, and meantime led to the weak point to change from the geopolymeric matrix to the ITZ between the geopolymeric matrix and aggregate.

CHAPTER 4: STATIC COMPRESSIVE BEHAVIORS OF SUSTAINABLE GRAC

In addition to the previous chapter, some investigations concentrated on the mix proportion and corresponding basic mechanical properties for GRAC have been conducted (Liu et al. 2016; Nuaklong et al. 2016; Nuaklong et al. 2018a; Parthiban & Saravana Raja Mohan 2017; Shaikh 2016; Shi et al. 2012; Xie et al. 2019a). However, scant work is available regarding the axial stress-strain behavior of GRAC. In order to fully characterize its mechanical performance, it is crucial to investigate the stress-strain behaviors of GRAC.

Thus, this chapter explores the stress-strain behavior of GRAC under uniaxial compression. Specifically, the uniaxial compressive stress-strain behavior of fly ash/slag based GRAC with different RA contents is studied. Both the effects of RA replacement and slag incorporation on the stress-strain behavior are investigated. Furthermore, a stress-strain model is developed to describe the uniaxial stress-strain behavior of GRAC.

4.1 Experimental program

4.1.1 Raw materials

In this experiment, the coarse aggregate included NA and RA. The used NA and RA were the same as those used in Chapter 3. The ingredient proportion of RA is presented in Table 4.1, which can be classified as mixed RA according to the literature (Silva et al. 2014). Both NA and RA have a nominal maximum size of 19 mm. The particle size distributions and the main properties of NA and RA have been presented in Figure 3.2 and Table 3.4, respectively.

Table 4.1 Component proportion of RA

Concrete products	Red brick	Broken tiles	Natural stone	Glass and other
74.5%	17.6%	4.0%	2.3%	1.6%

Locally available river sand with the fineness modulus of 2.76, specific gravity of 2.61, and maximum size of 5 mm was adopted as fine aggregate. The particle size distribution of fine aggregate has been given in Figure 3.2.

Class F fly ash and GGBFS were used as the binder materials. For comparison, OPC designated Type GP (General Portland) was used to manufacture OPC concrete. All these materials were from the factory supplies in Sydney. Their chemical compositions, obtained by X-ray fluorescence, are shown in Table 3.1, together with the LOI.

Table 4.2 Chemical compositions and LOI of fly ash, GGBFS, and OPC

Oxide compositions	Fly ash	GGBFS	OPC
SiO_2	65.90	36.00	20.51
Al_2O_3	24.00	13.80	5.37
Fe_2O_3	2.87	0.30	2.10
CaO	1.59	42.60	57.05
MgO	0.42	5.80	3.86
MnO	0.06	0.40	0.02
K_2O	1.44	0.27	1.44
Na_2O	0.49	0.21	0.64
P_2O_5	0.19	0.10	0.13
TiO_2	0.92	0.80	0.16
SO_3	–	0.56	6.37
LOI	1.53	-1.00	2.35

The alkali activator was the same as that in Chapter 3, and its details can be referred from Section 3.1.1.

4.1.2 Mix proportion

A total of 15 concrete mixtures were designed in this study, 3 mixtures based on OPC concrete and 12 mixtures based on geopolymeric concrete. For geopolymeric concrete mixtures, three different RA replacement levels and four different contents of slag in the binder were considered. In detail, the RA was used as 0%, 50%, and 100% by weight replacement of the NA, and slag was used as 0%, 10%, 20%, and 30% by weight substitution of fly ash. For OPC concrete mixtures, three mixes with different percentages

of RA replacement (0%, 50%, and 100%) were included. The details of the mix proportion are given in Table 4.3.

Table 4.3 Details of mix proportion for geopolymeric and OPC concretes

Mixture	Mix proportions (unit weight: kg/m^3)								
	Fly ash	GGBFS	OPC	Na_2SiO_3	NaOH	Water	Sand	NA	RA
S00	420	0	–	165	66	–	550	1220	0
S10	378	42	–	165	66	–	550	1220	0
S20	336	84	–	165	66	–	550	1220	0
S30	294	126	–	165	66	–	550	1220	0
S00R50	420	0	–	165	66	–	550	610	610
S10R50	378	42	–	165	66	–	550	610	610
S20R50	336	84	–	165	66	–	550	610	610
S30R50	294	126	–	165	66	–	550	610	610
S00R100	420	0	–	165	66	–	550	0	1220
S10R100	378	42	–	165	66	–	550	0	1220
S20R100	336	84	–	165	66	–	550	0	1220
S30R100	294	126	–	165	66	–	550	0	1220
OPC	–	–	420	–	–	168	550	1220	–
OPCR50	–	–	420	–	–	168	550	610	610
OPCR100	–	–	420	–	–	168	550	–	1220

4.1.3 Specimen preparation

Concrete mixtures were prepared using a laboratory tilting drum mixer. Coarse and fine aggregates were prepared in saturated-surface dry condition and then were dry-mixed with the binders (fly ash and slag, or cement) thoroughly in the mixer for 2 minutes. After that, the premixed alkaline activator solution or water was slowly and evenly added into the mixer over a period of 1 minute. Then mixing was continued for further 3-5 minutes to ensure uniform mixing. The fresh concrete was cast in 100 × 200 mm cylinder moulds in two layers and was consolidated by a vibration table to ensure compaction. Subsequently, the specimens were covered with plastic films to prevent the evaporation of free water in mixtures. Three specimens were prepared for each mix. For geopolymeric concrete, the curing regime was in accordance with that introduced in Section 3.1.3. For OPC concrete, the specimens were left in the casting room for 24 hours at a temperature

of about 23°C. The specimens were then demolded and placed into the curing room. At 28 days of curing age, all specimens were measured for dimension, and then both ends were ground flat and parallel before testing started.

4.1.4 Test setup and instrument

The experiment was carried out on a MTS hydraulic compression testing machine with a capacity of 5000 kN. Specimens were subjected to uniaxial compression at a constant displacement rate of 0.2 mm/minute. A compressometer equipped with two LSCTs (linear strain conversion transducers) was mounted at the middle height on the specimens, which was used for evaluating the deformation and strain characteristics while undergoing compression testing. The LSCT model was continuously recorded together with the corresponding applied load by data acquisition systems. In order to avoid the slackness of system and eccentricity of loading, specimens were pre-loaded to around 20% of the peak load prior to the formal test. The experimental setup for the quasi-static compression test is presented in Figure 4.1. The average strain data obtained from the two LSCTs were later used to establish the quasi-static stress-strain curve.

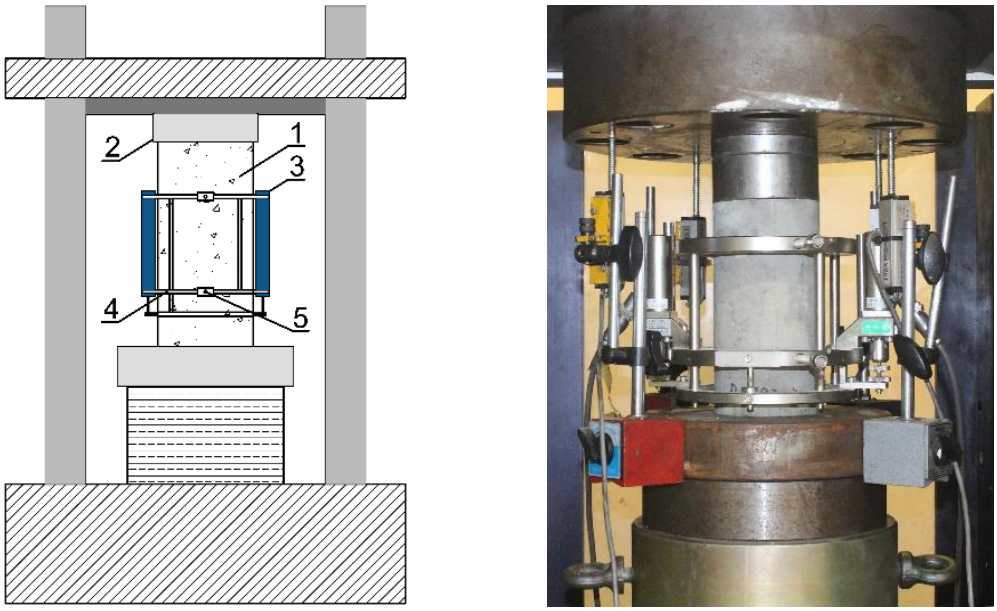

(a) Schematic illustration (b) Set up for compression

Figure 4.1. Testing setup for quasi-static compression test (1-specimen; 2-bearing block; 3-LSCT; 4-steel frame; 5-steel angle)

4.2 Results and discussions

4.2.1 Failure pattern

The failure process was similar for all the concrete specimens. The failure behavior was characterized by three stages, namely, initiation of cracks, propagation of cracks, and failure of the specimen. No obvious crack could be observed until the load was approaching the peak stress, and then, the micro-cracks gradually formed along the loading direction, as shown in Figure 4.2(a). Upon the peak stress, cracks extended to the central section with the increase of the displacement, as shown in Figure 4.2(b). Crack propagation was slower in the specimens containing RA and in the specimens with a lower content of slag. At the post-peak stage, the cracks developed from micro to macroscopic and crossed throughout the entire specimen, and simultaneously, the spallation of the lateral sides could be detected, as shown in Figure 4.2(c).

(a) 45% of peak load

(b) 100% of peak load

(c) 75% of peak load at post-peak

Figure 4.2. Failure process of concretes under different load levels (S20R50 specimen)

The failure patterns of specimens are shown in Figure 4.3. In the case of geopolymeric concrete specimens without slag, cracks were primarily formed in the matrix between the aggregate particles, which induced aggregate interlock action along the cracks. While for the other specimens (OPC concrete and geopolymeric concrete with slag), the aggregate particle and the matrix-aggregate interface underwent failure simultaneously. Furthermore, the geopolymeric concrete specimens with a higher content of slag had a more smooth failure surface because more cracks passed through the aggregate particles. It has been reported that the incorporation of slag could enhance the compaction and homogeneity of the geopolymeric mortar and the ITZ between aggregate and matrix (Shang et al. 2018; Singh et al. 2016). As the increased densification of the mortar constituent, there was greater compatibility between coarse aggregate and the

surrounding mortar with respects to the stiffness and strength, thus resulting in the increased probability of crack development through aggregates (Akçaoğlu 2017). In addition, with the enhanced matrix-aggregate bond, the fracture was forced to pass through the aggregate particles, which were observed as a planar crack face (Akçaoğlu 2017; Guinea et al. 2002).

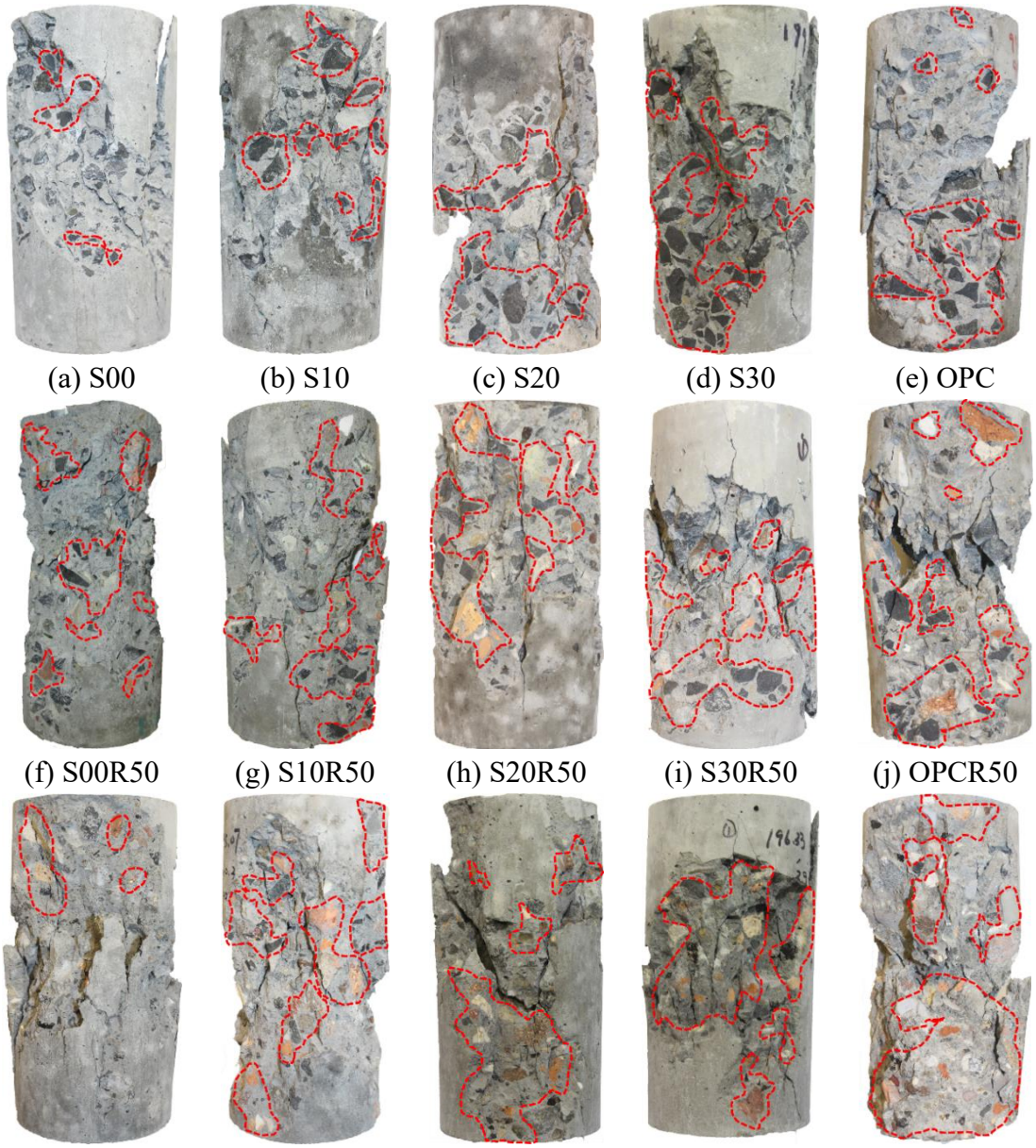

(a) S00 (b) S10 (c) S20 (d) S30 (e) OPC

(f) S00R50 (g) S10R50 (h) S20R50 (i) S30R50 (j) OPCR50

(k) S00R100 (l) S10R100 (m) S20R100 (n) S30R100 (o) OPCR100

Figure 4.3. Failure patterns of concretes (fractured aggregate particles marked with red lines)

Besides, a higher percentage of fractured aggregate particles could be observed in recycled aggregate concrete (RAC), decreasing the amount of de-bonded coarse aggregate when comparing with natural aggregate concrete (NAC). This was due, mainly, not only to the weaker strength of RA, but also to better bonding between RA and paste for the relatively high surface porosity and roughness of RA (Casuccio et al. 2008; Li et al. 2012)

4.2.2 Stress-strain behavior

For each specimen, the axial strain was calculated through the average of two LSCTs, and axial stress was calculated by dividing the load by the cross-sectional area of the specimen. Then, the axial stress was plotted against the axial strain. As shown in Figure 4.4, it can be seen that all the stress-strain curves follow a similar trend. The initial part of the curve is linear, and then the stress increases slowly up to the peak stress. The descending portion tends to reach a constant stress level at high strains.

Moreover, Figure 4.4 shows the effect of RA replacement ratios on the stress-strain behavior of concrete. The shape of the stress-strain curve for RAC is similar to that of the corresponding NAC, irrespective of geopolymeric concrete and OPC concrete. Nevertheless, the stress-strain curves become flatten with the increase in the replacement ratio of RA. Specifically, with the increase of the RA replacement ratio, the peak stress and the ascending slope decline. Also, the descending branch of the curve flattens for RAC specimens. These results agree with those obtained in the previous studies (Belén et al. 2011; Kathirvel & Kaliyaperumal 2016), which in turn indicates that the RAC behaves in a less brittle manner than NAC.

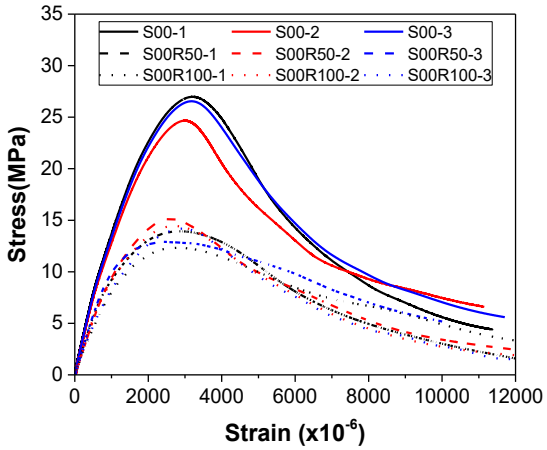

(a) Geopolymeric concretes without slag

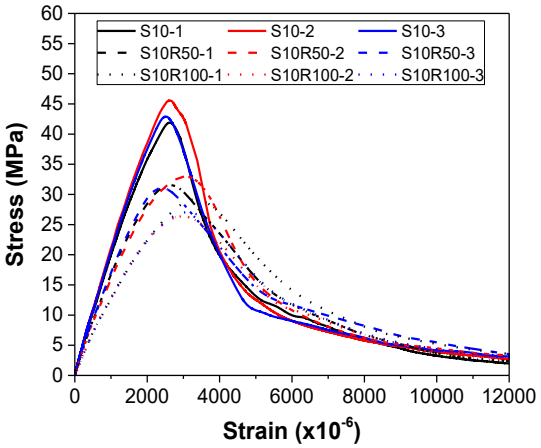

(b) Geopolymeric concretes with 10% slag

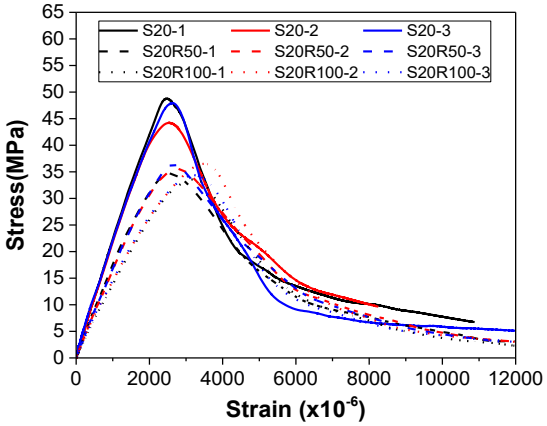

(c) Geopolymeric concretes with 20% slag

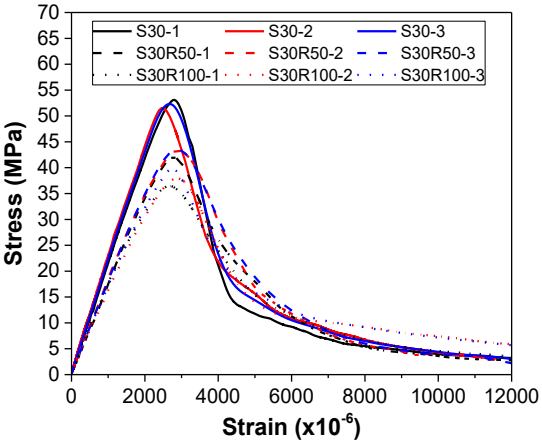

(d) Geopolymeric concretes with 30% slag

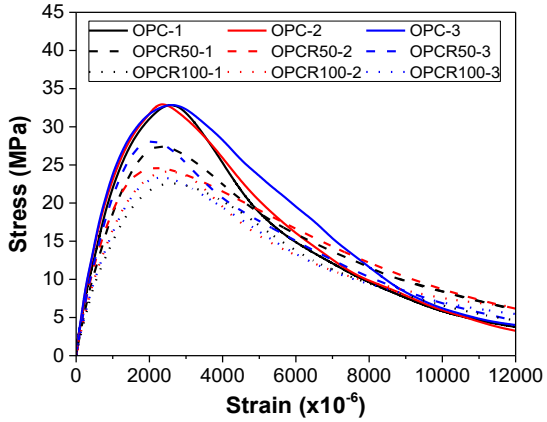

(e) OPC concretes

Figure 4.4. Stress-strain behaviors of concretes with different RA replacement ratios

Figure 4.5 presents the typical stress-strain curves of concretes based on different binders. The stress-strain behavior of geopolymeric concrete specimens is similar to that of OPC

concrete specimens in the ascending branch, while geopolymeric concrete shows a lower initial slope of the curve. Additionally, geopolymeric concrete shows a rapid decline in stress during post-peak strain softening in comparison with OPC concrete. This high brittle behavior is attributed to the ceramic-like nature of geopolymeric material (Bhutta et al. 2017; Noushini et al. 2016; Pan et al. 2011). For all the combinations of geopolymeric concrete, the higher peak point, increased ascending slope, and steeper descending part could be observed with the increase in the content of slag, reflecting the stronger and stiffer, but more brittle behavior of geopolymeric concrete containing slag.

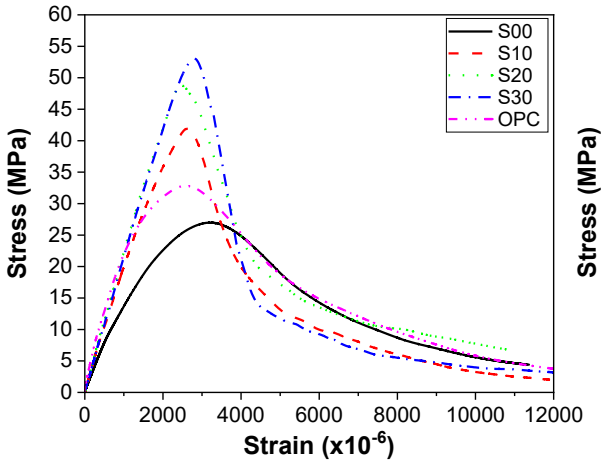

(a) Concretes without RA

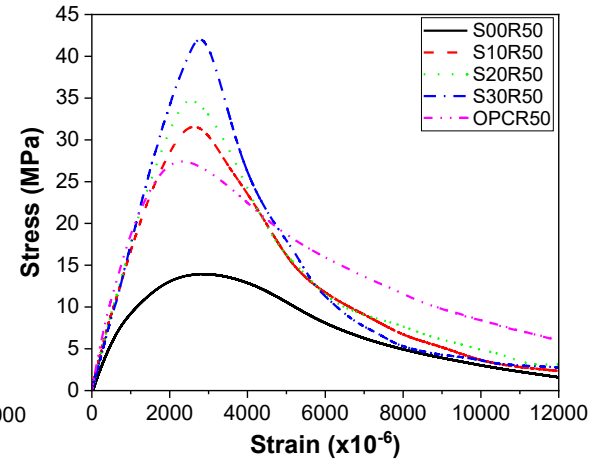

(b) Concretes with 50% replacement ratio of RA

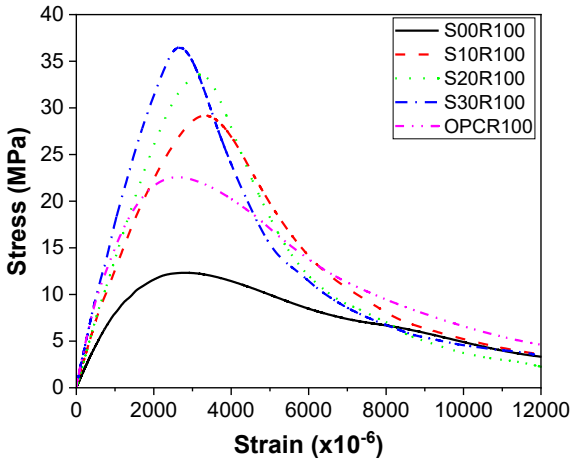

(c) Concretes with 100% replacement ratio of RA

Figure 4.5. Stress-strain behaviors of concretes based on different binders

4.2.3 Stress-strain curve

Based on the experimental results, Table 4.4 lists the average values of the elastic modulus (E_c), secant modulus (E_{sec}), peak stress (f_{cm}), peak strain (ε_0), ultimate stress (σ_{cu}), and ultimate strain (ε_{cu}) for each mixture, as well as the corresponding coefficient of variation (CoV). The axial stress and the corresponding strain at peak point are defined as peak stress (f_{cm}) and peak strain (ε_0) respectively, while the axial stress and the corresponding strain at the inflection point of the descending branch are defined as residual stress (σ_{cu}) and ultimate strain (ε_{cu}). The elastic modulus (E_c), determined according to ASTM C469-14 (Standard Test Method for Static Modulus of Elasticity and Poisson's Ratio of Concrete in Compression), was defined as the slope of the line drawn from the stress of zero to the stress of 40% peak stress, while the secant modulus (E_{sec}) is based on the slope of the straight line from the origin to the peak point.

Table 4.4 Stress-strain characteristics of test specimens

Mixture	E_c [GPa] (CoV [%])	E_{sec} [GPa] (CoV [%])	E_c / E_{sec} (CoV [%])	f_{cm} [MPa] (CoV [%])	ε_0 [×10^{-6}] (CoV [%])	ε_{cu} [×10^{-6}] (CoV [%])	$\varepsilon_{cu} / \varepsilon_0$ (CoV [%])	σ_{cu} [MPa] (CoV [%])	σ_{cu} / σ_c
S00	13.34 (4.65)	8.33 (1.74)	1.60 (10.48)	26.1 (4.71)	3126 (3.06)	4328 (10.42)	1.38 (5.28)	21.29 (5.28)	0.82
S00R50	11.65 (6.75)	5.33 (8.69)	2.20 (14.16)	14.0 (8.00)	2631 (8.34)	4485 (11.99)	1.70 (5.92)	11.36 (7.98)	0.82
S00R100	9.59 (9.69)	4.86 (10.11)	1.97 (2.45)	13.7 (8.47)	2814 (4.24)	4423 (13.98)	1.57 (14.25)	11.29 (11.75)	0.83
S10	20.75 (2.84)	16.83 (4.52)	1.23 (3.17)	43.5 (4.37)	2581 (2.28)	3244 (3.70)	1.26 (6.05)	34.89 (3.16)	0.80
S10R50	16.78 (6.09)	11.94 (9.38)	1.41 (7.08)	31.9 (3.13)	2689 (12.58)	4272 (4.23)	1.61 (13.77)	21.72 (11.74)	0.68
S10R100	12.78 (6.20)	8.76 (0.44)	1.46 (5.76)	27.5 (5.31)	3141 (5.40)	4572 (3.58)	1.46 (8.30)	21.10 (17.85)	0.76
S20	21.79 (2.42)	18.48 (6.16)	1.18 (4.02)	47.0 (5.17)	2544 (2.63)	3279 (1.81)	1.29 (4.07)	37.07 (3.01)	0.79
S20R50	16.95 (3.33)	13.43 (3.54)	1.26 (3.11)	35.6 (2.44)	2651 (4.11)	3884 (2.00)	1.47 (5.53)	26.87 (7.51)	0.76
S20R100	14.33 (3.22)	10.55 (1.22)	1.36 (3.45)	34.8 (4.43)	3301 (5.34)	4208 (1.84)	1.30 (3.41)	27.59 (10.12)	0.79
S30	22.32 (3.90)	19.79 (4.57)	1.13 (0.65)	52.3 (1.49)	2648 (5.99)	3596 (7.33)	1.36 (2.57)	34.33 (2.95)	0.66
S30R50	17.96 (2.92)	15.02 (0.73)	1.20 (3.61)	43.0 (1.95)	2862 (2.39)	3648 (3.12)	1.27 (0.85)	34.28 (2.82)	0.80
S30R100	17.03 (4.12)	13.82 (4.67)	1.23 (4.36)	38.1 (4.36)	2757 (3.79)	3536 (6.13)	1.28 (3.99)	29.93 (6.92)	0.79
OPC	27.88 (6.29)	13.13 (6.48)	2.13 (1.87)	32.9 (0.21)	2510 (6.06)	4154 (2.79)	1.66 (6.11)	25.61 (4.16)	0.78
OPCR50	23.80 (8.58)	12.20 (10.47)	1.96 (10.46)	26.7 (6.89)	2193 (5.81)	3562 (11.33)	1.62 (5.59)	23.13 (5.05)	0.87
OPCR100	19.61 (5.64)	9.39 (7.00)	2.09 (4.52)	23.3 (3.35)	2491 (5.53)	4108 (16.47)	1.64 (12.73)	19.51 (9.04)	0.84

4.2.4 Peak stress

Figure 4.6 shows the average peak stress values of geopolymeric and OPC concrete specimens with different RA replacement ratios. Regardless of geopolymeric or OPC concrete, the peak stress was adversely affected by the replacement of RA and declined with the rising replacement ratios. This was primarily due to the poor quality of RA, such as existing cracks in RA (Shi et al. 2016). On the other hand, the inclusion of slag equipped geopolymeric concrete with higher peak stress. For instance, geopolymeric natural aggregate concrete (GNAC) with 10%, 20%, and 30% slag showed peak stress higher than GRAC without slag, by 66.7%, 80.1%, and 100.4%, respectively. This rise was consistent with previous studies (Deb et al. 2014; Lee & Lee 2013; Li & Liu 2007; Nath & Sarker 2014; Xie et al. 2019a). Also, the effect of slag inclusion, in terms of the peak stress improvement, was more significant in GRAC compared with GNAC. The inclusion of slag resulted in the formation of gel phases such as calcium silicate hydrate (C-S-H) and calcium alumino-silicate hydrate (C-A-S-H), and these gels mainly contributed to the improvement of compressive strength (Kumar et al. 2010). It has also been reported that the nucleation effect of calcium ions would accelerate the dissolution of fly ash and thus enhance the formation of geopolymer gel (Puligilla & Mondal 2013).

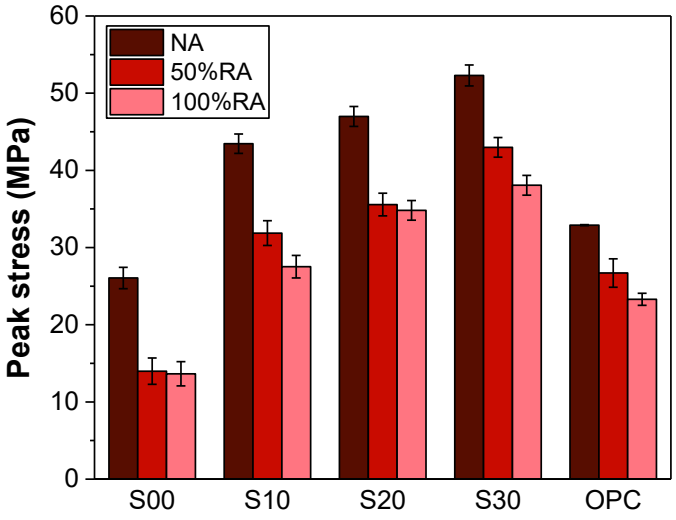

Figure 4.6. Peak stress of concretes with various binder types and RA replacement ratios

Although the effect of RA replacement in terms of peak stress reduction was more pronounced for geopolymeric concrete without slag than OPC concrete, such adverse effects could be reduced by the inclusion of slag. For the full replacement of RA, the reduction in peak stress was about 43% for the geopolymeric concrete without slag, while this value was reduced to 36%, 26%, and 27%, respectively, for geopolymeric concretes containing 10%, 20%, and 30% slag. It could be explained that slag could increase the binding between the geopolymeric matrix and RA significantly due to its compactness of microstructure (Xie et al. 2019a).

4.2.5 Elastic modulus

Figure 4.7 shows the average elastic modulus values of geopolymeric and OPC concretes under different RA replacement ratios. The elastic modulus decreases with the increase in the RA replacement ratio. For OPC concrete specimens, the reductions due to 50% and 100% RA replacement were 15% and 30%, respectively. For geopolymeric concrete, the reductions were about 20% and 40%, respectively, for 50% and 100% replacement ratio of RA, except for geopolymeric concrete with 30% slag that the reductions were 15% and 22%, respectively. The elastic modulus decreases were attributed to the weak and porous RA with a comparatively low modulus of elasticity (Xiao et al. 2012b; Xiao et al. 2013b).

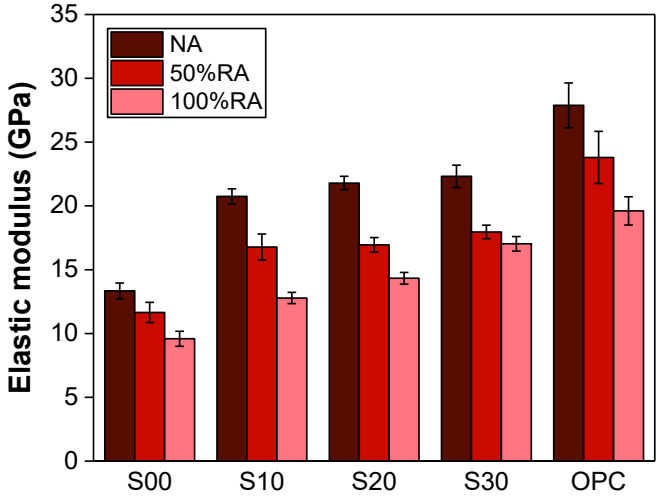

Figure 4.7. Elastic modulus of concretes with various binder types and RA replacement ratios

Figure 4.7 also shows that under the same RA replacement ratio, the moduli of elasticity of geopolymeric concrete, even with higher peak stress, are 13.1%-52.2% less than that of OPC concrete, coinciding with the previous studies for GNAC and GRAC (Fernandez-Jimenez et al. 2006; Liu et al. 2016; Nath & Sarker 2017; Olivia & Nikraz 2012; Shi et al. 2011; Xie et al. 2019a). For instance, according to the study of Liu et al. (2016), fly ash based GRAC showed an elastic modulus of 33.3-91.2% lower than that of OPC-based RAC. Additionally, the elastic moduli of geopolymeric concrete with slag are higher than that of neat fly ash based geopolymeric concrete. Specifically, the neat fly ash based geopolymeric concrete achieved elastic moduli in the range of 9.6-13.3 GPa, which are 33.3%-55.5%, 45.4%-63.3%, and 54.2%-77.6% less than the values of geopolymeric concretes with 10%, 20%, and 30% inclusion of slag, respectively. It was mainly attributed to the different reaction products, that sodium alumino-silicate hydrate (N-A-S-H) gel was the main hydration product of geopolymeric concrete without slag, while additional C-A-S-H gel was formed after the incorporation of slag. The Young's modulus of C-A-S-H gel formed in the alkali-activated slag is in the range of 12 to 43 GPa, which is higher than the N-A-S-H gel generated in alkali-activated fly ash, ranging from 10 to 20 GPa (Fernandez-Jimenez et al. 2006; Němeček et al. 2011; Puertas et al. 2011). Besides the high-stiffness gel phases, the improved ITZs are also responsible for the increase in the elastic modulus of geopolymeric concrete with the inclusion of slag (Fonseca et al. 2011).

As shown in Table 4.4, a similar trend to elastic modulus can be observed for secant modulus, which decreases with the increase in RA replacement ratios while increases after the incorporation of slag. The ratios of elastic modulus to secant modulus are also listed in Table 4.4. This ratio, to a certain extent, reflects the linearity of the stress-strain curve within the ascending branch. Under the same RA replacement ratio, OPC concrete generally exhibits higher values than geopolymeric concrete, indicating additional brittle behavior of geopolymeric concrete. Furthermore, this value increases as the slag content increases but decreases as the RA replacement ratios increases.

4.2.6 Peak strain

Figure 4.8 shows the average peak strain values of geopolymeric and OPC concrete specimens with different RA replacement ratios. The RA replacement has different impacts on the peak strain of concretes based on various binders. Specifically, for OPC concrete, the 50% RA replacement results in a reduction of 14.5% in the peak strain, while the full replacement of RA has a limited influence on the peak strain. For the neat fly ash based geopolymeric concrete, reductions in peak strain could be observed after the RA replacement, while converse trends are identified in the geopolymeric concretes with 10% and 20% addition of slag. Moreover, as for the geopolymeric concrete with 30% addition of slag, RA replacement has a slight increase in the peak strain. The variation of peak strain caused by the RA replacement in geopolymeric concrete could be considered from the properties of aggregate and geopolymeric matrix, as well as their interaction (Piasta et al. 2017). As for neat fly ash based geopolymeric concrete, the failure is mainly controlled by cracking of matrix (see Figure 4.3). Due to the lower stiffness, the RA has the low ability to mitigate the stress of the geopolymeric matrix, which results in the premature failure of the matrix in GRAC at a relatively low strain. However, after the inclusion of slag, the compaction of the geopolymeric matrix and the ITZ between aggregate and matrix were enhanced, and subsequently, the deformable advantage of RA could be fully used (Han & Xiang 2017). On the other hand, the greater compatibility between the RA and the surrounding mortar reduced the stress concentration under a certain strain, and in turn, supported the strain development (Akçaoğlu 2017; Chiaia et al. 1998; Giaccio & Zerbino 1998).

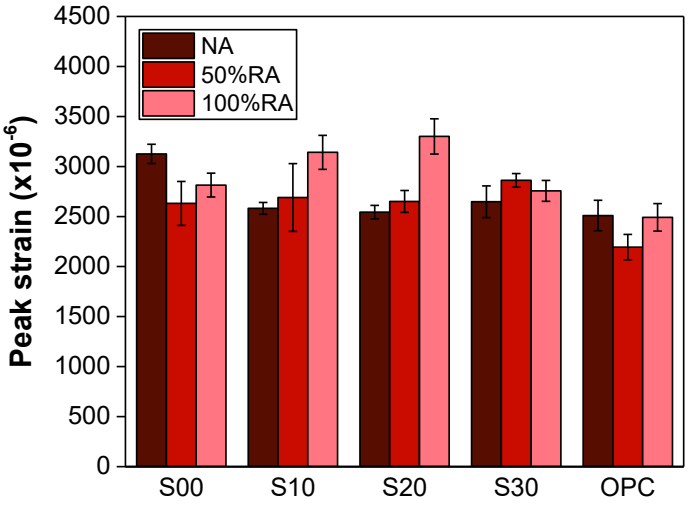

Figure 4.8. Peak strain of concretes with various binder types and RA replacement ratios

Figure 4.8 also shows that the peak strain of geopolymeric concrete is higher than that of OPC concrete with the same replacement ratio of RA, which is mainly due to the lower elastic modulus of geopolymeric concrete. In addition, the effect of slag inclusion on the peak strain of geopolymeric concrete varies under different replacement ratios of RA. For GNAC, the peak strains of geopolymeric concrete with slag inclusion are lower than that of geopolymeric concrete based on neat fly ash. In the case of GRAC with 50% replacement ratio, the slag incorporation has a limited effect on the peak strain, which is in the range from 0.0025 to 0.0028. With the full replacement of RA, the geopolymeric concrete without slag shows an average peak strain of 0.0028, which is lower than 0.0031 and 0.0033 for the geopolymeric concretes with 10% and 20% slag, respectively; but is slightly higher than the average peak strain for the geopolymeric concrete with 30% slag.

4.2.7 Ultimate strain

Figure 4.9 shows the ultimate strain of geopolymeric and OPC concretes with different RA replacement ratios. The trend for the ultimate strain as a function of the RA replacement ratios in different groups follows similar trends to peak strains in Figure 4.8, except that the neat fly ash based geopolymeric concrete has slightly increased average ultimate strain after the RA replacement. Moreover, the geopolymeric concretes with slag

inclusion have a lower average ultimate strain compared with geopolymeric concrete without slag. This is attributed to the more brittle characteristic of the geopolymeric concrete after slag incorporating (Bhutta et al. 2017; Noushini et al. 2016; Pan et al. 2011).

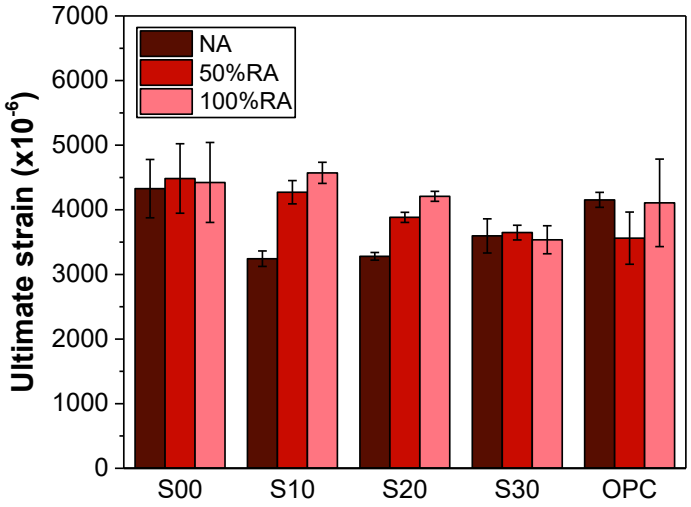

Figure 4.9. Ultimate strain of concretes with various binder types and RA replacement ratios

The ratios of ultimate strain to peak strain of test concrete mixtures are presented in Figure 4.10. The RA replacement has different influences on this value for concretes based on various binders. For OPC concrete, there is no significant influence on this value by the RA replacement. For geopolymeric concrete without slag and geopolymeric concrete with 10% and 20% slag, the RA replacement increases this ratio, and the increase caused by 50% RA replacement is higher than that caused by full RA replacement. However, the impacts of RA replacement, in terms of the ratio of ultimate strain to peak strain, could be diminished after the inclusion of slag. Moreover, for geopolymeric concrete with 30% slag, the differences between the ratios of ultimate strain to peak strain are less than 0.08 for different RA replacement ratios. Besides, geopolymeric concrete has a lower ratio of ultimate strain to peak strain than OPC concrete, demonstrating the additional brittle characteristic of axial stress-strain behavior of geopolymeric concrete at the post-peak stage. Besides, a decline in the ratio of ultimate strain to peak strain is observed with the increase in slag content, especially in the GRAC.

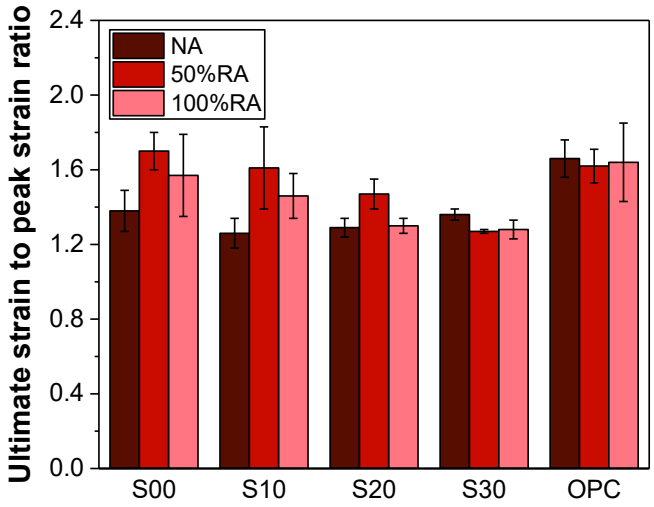

Figure 4.10. Ratios of ultimate strain to peak strain of concretes with various binder types and RA replacement ratios

4.2.8 Energy absorption

The energy absorption capacity of concrete under compression was examined through the toughness, which is determined by calculating the area under the stress-strain curves up to the peak point (Nataraja et al. 1999; Tasdemir et al. 1998). As shown in Figure 4.11(a), the toughness was adversely affected by the RA replacement ratio, regardless of geopolymeric concrete and OPC concrete. Previously, Kazmi et al. (2019) also observed the reduction in the toughness of OPC concrete for the replacement of RA. The reduction in the toughness of NAC as compared to RAC might be related to the significantly decreased peak stress of concrete after RA replacement (Kazmi et al. 2019; Nematzadeh & Baradaran-Nasiri 2018). However, less reduction in toughness due to the RA replacement is observed in the geopolymeric concrete specimens with a higher content of slag. For instance, the drop in average toughness from the GNAC to the GRAC with 100% RA reduces from 50% to 14% after the 30% slag addition. Therefore, the addition of slag could reduce the effect of RA replacement on the toughness of geopolymeric concrete. Furthermore, an increase in toughness is observed with the increase in the slag content regardless of the type of coarse aggregate, which is consistent with the findings reported by Xie et al. (2019a).

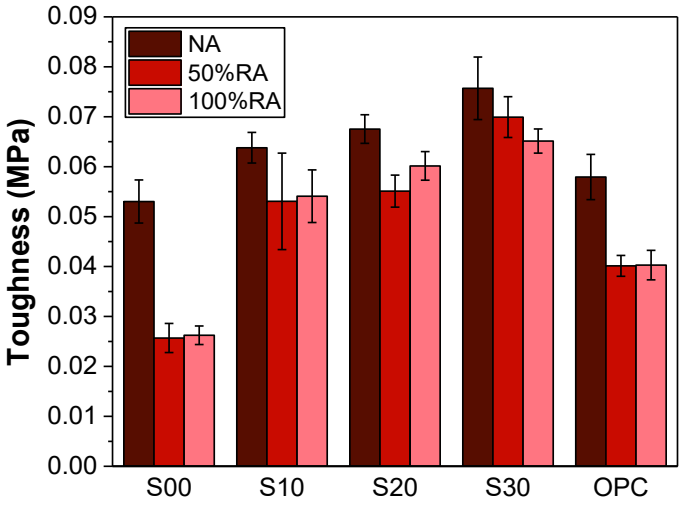

(a) Toughness

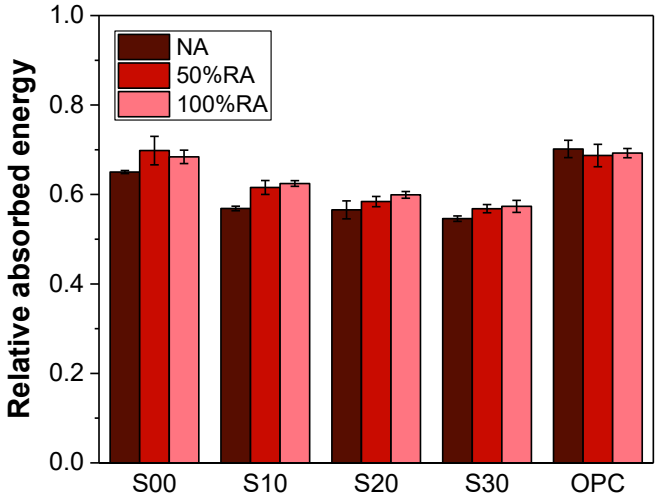

(b) Relative energy absorbed

Figure 4.11. Toughness and relative energy absorbed of various concretes

The relative absorbed energy was also measured in this study, which can be calculated by dividing the toughness by the peak stress and peak strain (Nematzadeh et al. 2016). Generally, as the stress-strain curve of concrete is concave downward in the ascending branch, the relative absorbed energy of concrete varies between 0.5 and 1. With this value increasing and tending to 1, the curve's concavity increases, resulting in an increased energy absorption level as well as more ductile behavior (Tasdemir et al. 1998). Figure 4.11(b) shows the values of relative absorbed energy of concrete mixtures with various binder types and RA replacement ratios. For geopolymeric concrete, the average relative

absorbed energy was within the range of 0.55 to 0.68 and was lower than that of OPC concrete, which was about 0.70. In addition, the values of relative absorbed energy in the geopolymeric concrete are decreased with the increase in the slag content. It can also be observed in Figure 4.11(b) that the amounts of relative absorbed energy by RAC are higher compared with the corresponding NAC, demonstrating the higher ductile behavior after the replacement of RA.

The toughness versus peak stress for geopolymeric concretes with different RA replacement ratios is presented in Fig. 4.12. It can be seen that the toughness increases as the peak strength increases, but the magnitude of the toughness increase is affected by the RA replacement ratio. The peak stress-toughness relationships are proposed for geopolymeric concrete under different RA replacement ratios and are shown in Eq. (4.1) to Eq. (4.3).

$$U = 0.031 + 8.06 \times 10^{-4} \times f_{cm} \text{ (NA)} \tag{4.1}$$

$$U = 0.004 + 14.92 \times 10^{-4} \times f_{cm} \text{ (50\% RA)} \tag{4.2}$$

$$U = 0.006 + 15.80 \times 10^{-4} \times f_{cm} \text{ (100\% RA)} \tag{4.3}$$

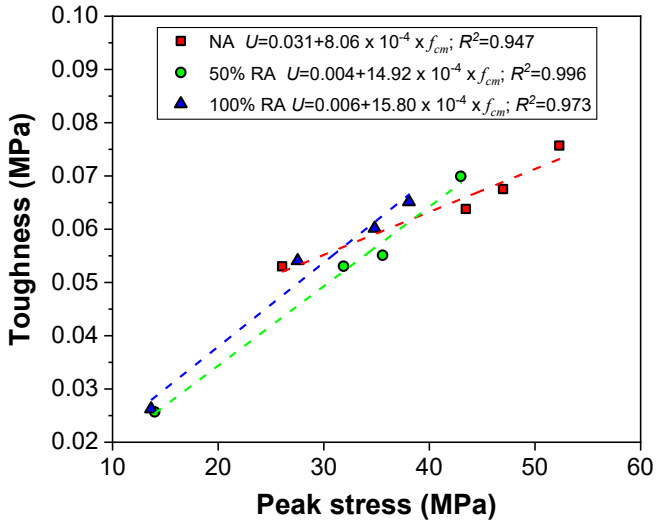

Fig. 4.12. Toughness versus compressive strength curves for geopolymeric concretes

Figure 4.13 presents the relative absorbed energy versus peak stress for tested geopolymeric concretes with different RA replacement ratios. An inverse trend could be observed between the relative absorbed energy and peak stress, which is consistent with the research performed by Tasdemir et al. (1998) and Nematzadeh et al. (2016), that as the compressive strength increases, the stress-strain curve exhibits smaller concavity, resulting in more brittle behavior of concrete. A relationship between the relative energy absorbed and the peak stress is given in Eq. (4.4), which is similar to the relationship proposed for OPC concrete in the literature (Nematzadeh et al. 2016).

$$U_r = 1.1 \times f_{cm}^{-0.17} \tag{4.4}$$

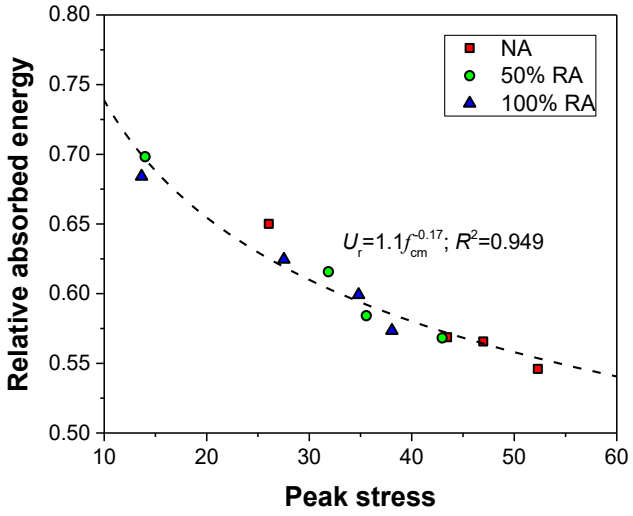

Figure 4.13. Relative energy absorbed versus compressive strength curves for geopolymeric concretes

4.3 Empirical model

4.3.1 Stress-strain curve

A comparative analysis of the experimental results obtained in this study with the existing stress-strain models. Table 4.5 shows the details of these existing models. The comparison between these above-mentioned stress-strain models with the experimental

results is presented in Figure 4.14, while the values of peak stress (f_{cm}) and peak strain (ε_0) are based on the experimental results measured in this study.

Comparison specifies that there are some discrepancies between all these models and the experimental stress-strain curves of geopolymeric concrete. Specifically, the model of CEB-FIP underestimates the ascending part of the curves for the specimens with low peak stress and the descending part of the curves for all the specimens, in fact, a slower drop is observed for the experimental results than the prediction. This trend has been observed in the previous study by Yang et al. (2012a). A similar result could be seen when comparing the model proposed by Dong et al. (2017) with the experimental results, while this model shows minor differences for the specimens with high peak stress. Furthermore, the model proposed by Noushini et al. (2016) overestimates the ascending branch of the curves while underestimates the descending branch. However, smaller discrepancies are observed in the specimens with high peak stress. The model by Prachasaree et al. (2014) overestimates the ascending branch and predicts a flatter descending branch as compared with the experimental results, particularly for the specimens with low peak stress. As for the model of Xiao et al. (2005), which is developed by modifying the parameters of the stress-strain model proposed by Guo et al. (1982), the prediction fits relatively well with the experimental results, especially for the GRAC. The stress-strain curves predicted by the model of Collins & Mitchell (1991) are observed very close to the experimental results except for the specimens of the neat fly ash based GRAC (S00R50 and S00R100).

Table 4.5 Empirical models for stress-strain behavior of OPC concrete, geopolymeric concrete, and RAC

Model	Elastic modulus	Peak strain	Stress-strain model
CEB-FIP	$E_c = 0.85 \times 2.15 \times 10^4 (f_{cm}^{'} / 10)^{(1/3)}$	$\varepsilon_0 = 0.0022$	$0 \le \varepsilon_c \le \varepsilon_{\max} : \sigma_c = f_{cm} \left[\frac{\left(\frac{E_c}{E_{sec}}\right)\left(\frac{\varepsilon_c}{\varepsilon_0}\right) - \left(\frac{\varepsilon_c}{\varepsilon_0}\right)^2}{1 + \left(\frac{E_c}{E_{sec}} - 2\right)\left(\frac{\varepsilon_c}{\varepsilon_0}\right)} \right]$ $\varepsilon_c > \varepsilon_{\max} : \sigma_c = \frac{f_{cm}}{\left[\frac{1}{(\varepsilon_{\max}/\varepsilon_0)}\zeta - \frac{2}{(\varepsilon_{\max}/\varepsilon_0)^2}\right]\left(\frac{\varepsilon_c}{\varepsilon_0}\right)^2 + \left[\frac{4}{(\varepsilon_{\max}/\varepsilon_0)} - \zeta\right]\left(\frac{\varepsilon_c}{\varepsilon_0}\right)}$ $\varepsilon_{\max} = \varepsilon_o \left[\frac{1}{2}\left(\frac{1}{2}\frac{E_c}{E_{sec}} + 1\right) + \sqrt{\frac{1}{4}\left(\frac{1}{2}\frac{E_c}{E_{sec}} + 1\right)^2 - \frac{1}{2}} \right]$ $\zeta = \frac{4\left[\left(\frac{\varepsilon_{\max}}{\varepsilon_o}\right)^2 (\frac{E_c}{E_{sec}} - 2) + 2\left(\frac{\varepsilon_{\max}}{\varepsilon_o}\right) - \frac{E_c}{E_{sec}}\right]}{\left[\left(\frac{\varepsilon_{\max}}{\varepsilon_o}\right)(\frac{E_c}{E_{sec}} - 2) + 1\right]^2}$ $E_{sec} = f_c^{'} / \varepsilon_0$

Collins & Mitchell (1991)	$E_c = 3320\sqrt{f_{cm}} + 6900$	$\varepsilon_0 = \frac{f_{cm}}{E_c}\frac{n}{n-1}$	$\sigma_c = f_{cm}\frac{\varepsilon_c}{\varepsilon_0}\frac{n}{n-1+(\varepsilon_c/\varepsilon_0)^{nk}}$ $n = 0.8 + \left(\frac{f_{cm}}{17}\right)$ $k = 0.67 + \left(\frac{f_{cm}}{62}\right)$ when $\frac{\sigma_c}{f_{cm}} > 1$; k=1.0 when $\frac{\sigma_c}{f_{cm}} \le 1$
Prachasaree et al. (2014)	$E_c = 0.840 - 0.886\sqrt{f_{cm}} + 0.647 f_{cm}$	$\varepsilon_0 = 0.0051 - 4(f_{cm})/10^5$	$\sigma_c = f_{cm}\frac{\varepsilon_c}{\varepsilon_0}\frac{n}{n-1+(\varepsilon_c/\varepsilon_0)^{n}}$ $n = 0.5 + (f_{cm}/14.3) - (3f_{cm}^2/10^4)$
Noushini et al. (2016)	$E_c = -11400 + 4712\sqrt{f_{cm}}$	$\varepsilon_0 = \frac{2.23\times10^{-7}\left(E_c\right)^{1.74}}{\left(f_{cm}\right)^{1.98}}$	$\sigma_c = f_{cm}\frac{\varepsilon_c}{\varepsilon_0}\frac{n}{n-1+(\varepsilon_c/\varepsilon_0)^{n}}$
Noushini et al. (2018)	$E_c = 4000 + 3500\sqrt{f_{cm}}$	$\varepsilon_0 = \frac{0.92\times10^{-7}\left(E_c\right)^{1.75}}{\left(f_{cm}\right)^{2.0}}$	$n = n_1 = \left[1.02 - 1.17(E_{sec}/E_c)\right]^{-0.45}$ if $\varepsilon_c \le \varepsilon_0$ $n = n_2 = n_1 + (\varpi + 28\times\xi)$ if $\varepsilon_c \le \varepsilon_0$ $\varpi = C(12.4 - 0.015 f_c^{'})^{-0.5}$ $\xi = 0.83e^{(-911/f_{cm})}$

			$C=\begin{Bmatrix}15 & \text{water and internal curings}\\ 7 & \text{heat curing - OPCC}\\ 17 & \text{heat curing - GPC}\end{Bmatrix}$
Dong et al. (2017)	–	–	$\sigma_c=\dfrac{0.65E_c\varepsilon_c}{\left(1+\left(\dfrac{0.091\varepsilon_c}{\varepsilon_0}\right)^4\right)^3}$
Xiao et al. (2005)	–	–	$y=\begin{cases}c_1x+(3-2c_1)x^2+(c_1-2)x^3 & 0\le x<1\\ \dfrac{x}{c_2(x-1)^2+x} & x>1\end{cases}$ $y=\dfrac{\sigma_c}{f_{cm}};x=\varepsilon/\varepsilon_0;\ \begin{matrix}c_1=2.2(0.748r^2-1.231r+0.975)\\ c_2=0.8(7.6483r+1.142)\end{matrix}$
Proposed	$E_c=\begin{cases}-11400+4712\sqrt{f_{cm}} & \text{for GNAC}\\ E_c=2977(f_c)^{0.474} & \text{for GRAC}\end{cases}$	$\varepsilon_0=2.35\dfrac{(f_{cm})^{0.45}}{E_c^{0.86}}$	$\dfrac{\sigma_c}{f_{cm}}=\begin{cases}\dfrac{\varepsilon_c}{\varepsilon_0}\dfrac{n}{n-1+(\varepsilon_c/\varepsilon_0)^n} & 0\le\dfrac{\varepsilon_c}{\varepsilon_0}<1\\ \dfrac{\varepsilon_c}{\varepsilon_0}\dfrac{n}{n-1+(\varepsilon_c/\varepsilon_0)^{nk}} & \dfrac{\varepsilon_c}{\varepsilon_0}\ge1\end{cases}$ $n=1.515+0.051f_{cm};\ k=(1.592+\dfrac{f_{cm}}{15})/n$

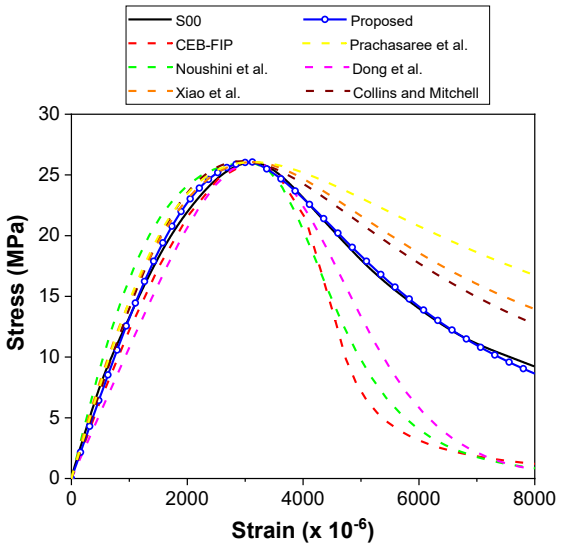

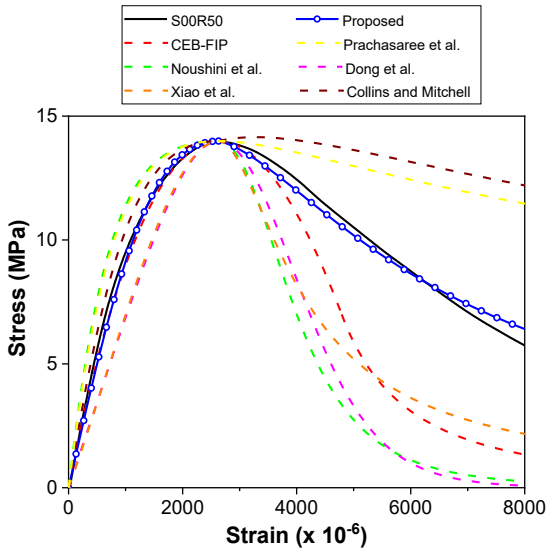

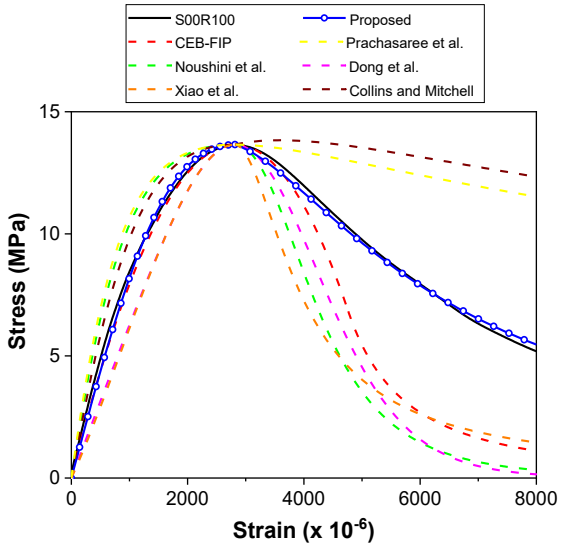

Parameters for proposed models			Parameters for proposed models			Parameters for proposed models		
n	k	R^2	n	k	R^2	n	k	R^2
2.569	1.203	0.9962	2.073	1.102	0.9894	2.199	1.162	0.9946

(a) S00 (b) S00R50 (c) S00R100

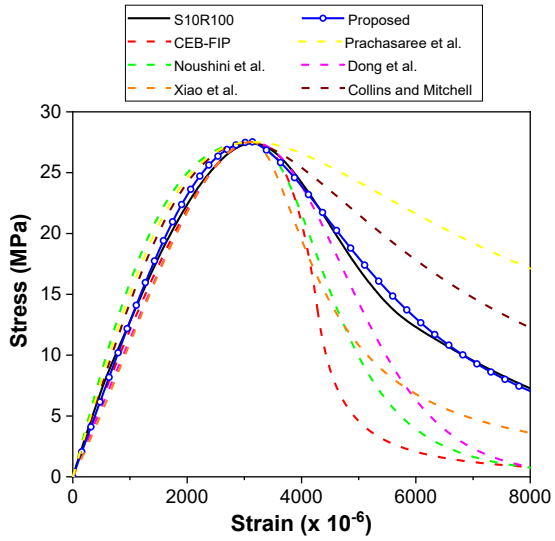

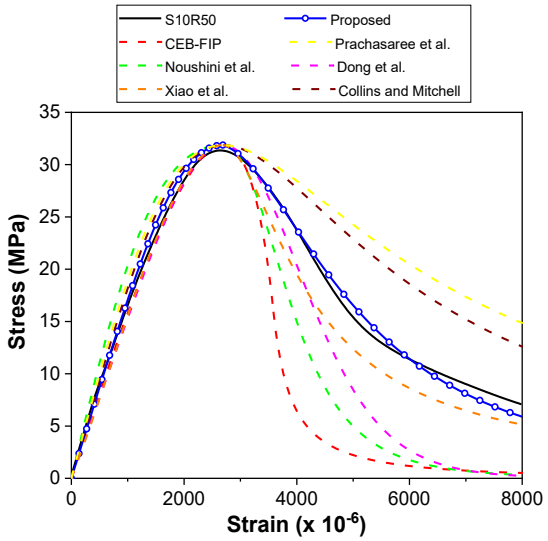

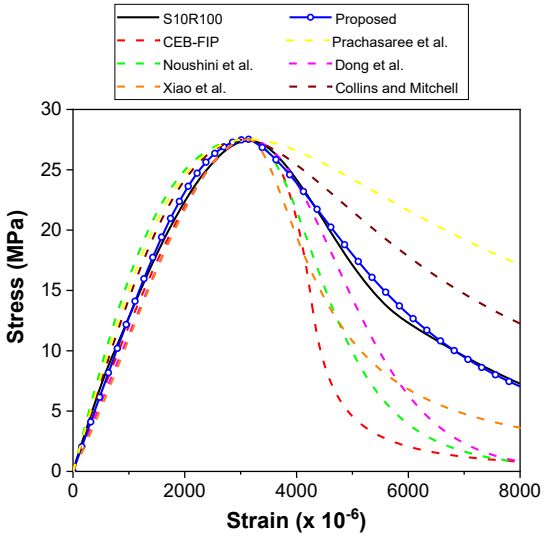

Parameters for proposed models			Parameters for proposed models			Parameters for proposed models		
n	k	R^2	n	k	R^2	n	k	R^2
3.483	1.312	0.9569	3.121	1.139	0.9931	3.099	1.187	0.9951

(d) S10 (e) S10R50 (f) S10R100

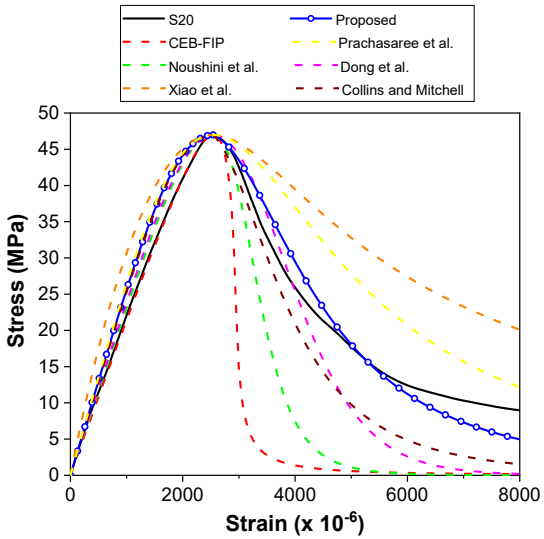

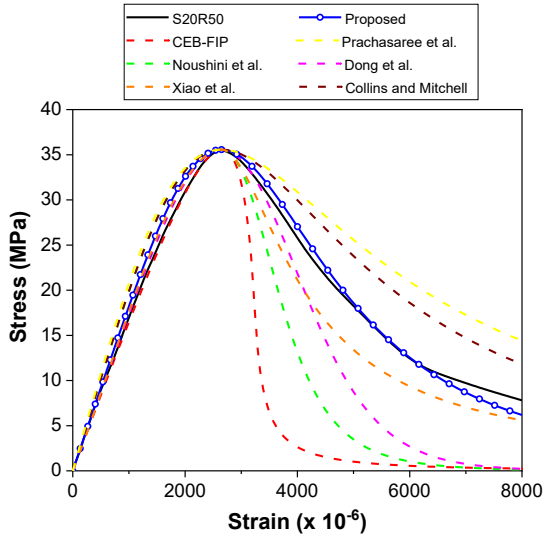

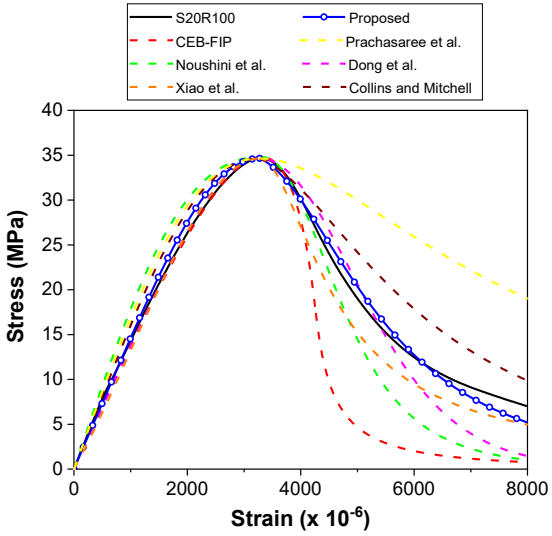

Parameters for proposed models			Parameters for proposed models			Parameters for proposed models		
n	k	R^2	n	k	R^2	n	k	R^2
3.429	1.172	0.9560	3.697	1.009	0.9890	3.561	1.263	0.9910

(g) S20 (h) S20R50 (i) S20R100

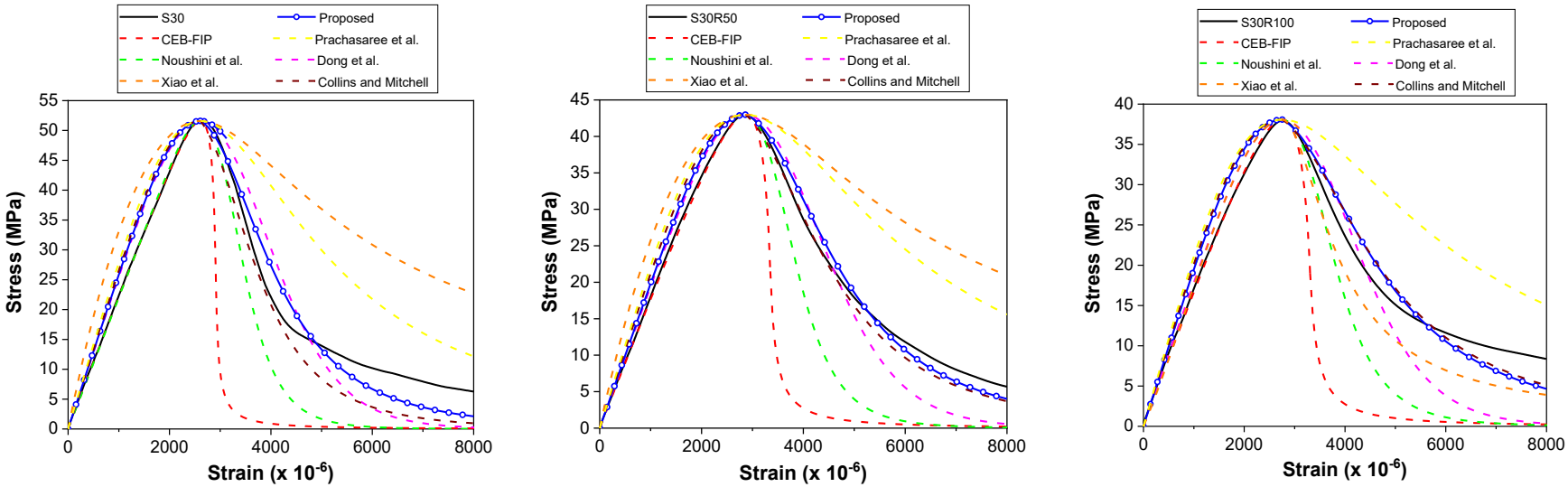

Parameters for proposed models			Parameters for proposed models			Parameters for proposed models		
n	k	R^2	n	k	R^2	n	k	R^2
4.188	1.222	0.9495	4.076	1.141	0.9840	3.314	1.228	0.9496

(j) S30 (k) S30R50 (l) S30R100

Figure 4.14. Comparison between existing and proposed stress-strain models and experimental results

Overall, comparative analysis shows that the model proposed by Collins & Mitchell (1991) (for stress-strain behavior of OPC concrete) can be used to describe the stress-strain behavior of the tested geopolymeric concretes. Furthermore, this model has been extensively applied to predict the stress-strain behavior of various concrete mixtures. Therefore, a stress-strain model is developed in this work by modifying the parameters of this model to describe the stress-strain curves of geopolymeric concretes tested, which can be express as:

$$\frac{\sigma_c}{f_{cm}} = \begin{cases} \dfrac{\varepsilon_c}{\varepsilon_0}\dfrac{n}{n-1+(\varepsilon_c/\varepsilon_0)^n} & 0 \le \dfrac{\varepsilon_c}{\varepsilon_0} < 1 \\ \dfrac{\varepsilon_c}{\varepsilon_0}\dfrac{n}{n-1+(\varepsilon_c/\varepsilon_0)^{nk}} & \dfrac{\varepsilon_c}{\varepsilon_0} \ge 1 \end{cases} \tag{4.5}$$

Figure 4.14 shows the fitting outcomes of the proposed models as well as the corresponding values of the parameters. It is concluded that the proposed relationship is well coincident with the experimental curves, both for the ascending and descending parts. Also, the coefficient of determination (R^2) is higher than 0.9495, demonstrating high accuracy. Based on the regression analysis, Eq. (4.6) and Eq. (4.7) are proposed to predict the parameters in the proposed model for different types of geopolymeric concrete. From the values of R^2, the proposed relationships fit reasonably well with the results.

$$n = 1.515 + 0.051 f_{cm} \quad (R^2=0.840) \tag{4.6}$$

$$k = (1.592 + \frac{f_{cm}}{15}) / n \quad (R^2=0.860) \tag{4.7}$$

4.3.2 Peak strain

In the proposed stress-strain relationship so far, peak stress (f_{cm}) and peak strain (ε_0) are the only parameters that remain to be determined. Different existing models in Table 4.5 have been used to predict the peak strain for concrete. The performance of the existing models is presented in Figure 4.15. It is shown that the existing models show large discrepancies with the experimental results. For instance, models by Prachasaree et al.

(2014), Noushini et al. (Noushini et al. 2016), and Collins & Mitchell (1991) overestimate the peak strain of tested geopolymeric concrete. However, the model of Noushini et al. (Noushini et al. 2018) underestimates the peak strain of tested geopolymeric concrete. Therefore, based on the regression analysis of test results, Eq. (4.8) is proposed to predict the peak strain of geopolymeric concrete. As shown in Figure 4.15, predicted values of peak strain by the proposed model are observed close to the corresponding experimental values.

$$\varepsilon_0 = 2.35\frac{(f_{cm})^{0.45}}{E_c^{0.86}} \quad (R^2=0.855) \tag{4.8}$$

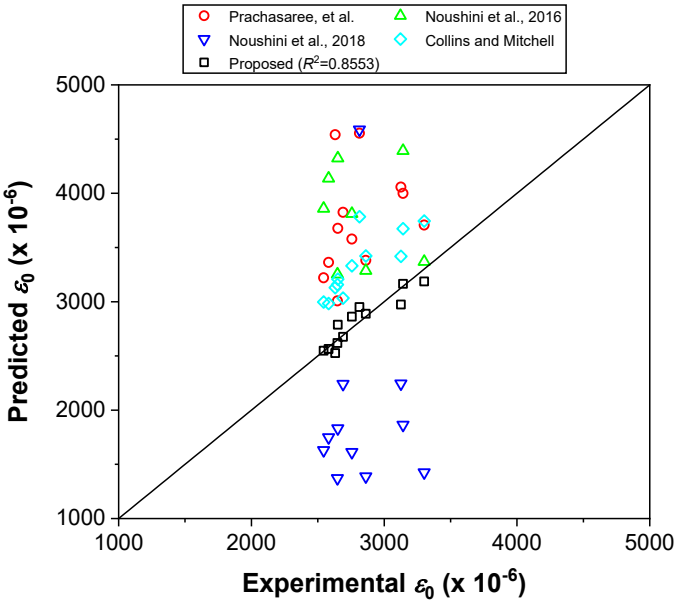

Figure 4.15. Performance of existing and proposed peak strain models for geopolymeric concrete

4.3.3 Elastic modulus

Although the proposed peak strain model in Eq. (4.8) can fit well with the test results, the elastic modulus is unknown in some cases. Based on the existing studies, different existing models were used to predict the elastic modulus of concrete. The details of the existing models are presented in Table 4.5. Besides, Ding et al. (2016) and Thomas & Peethamparan (2015) proposed Eq. (4.9) and Eq. (4.10) respectively for geopolymeric

concrete. The performance of these existing models is presented in Figure 4.16. As for CEB-FIP model, the experimental elastic modulus was 31% to 55% lower than the prediction. A similar trend was reported by Fernandez-Jimenez et al. (2006), Lee & Lee (2013), and Noushini et al. (2016), that the experimental results were lower than the prediction by this model. Additionally, the empirical models proposed by Noushini et al. (Noushini et al. 2018), Thomas & Peethamparan (2015), and Collins & Mitchell (1991) also overestimated the elastic modulus of tested geopolymeric concretes. While the model of Ding et al. (2016) fits relatively well with the results of this study, with R^2 value of about 0.63. Moreover, Noushini et al. (2016)'s model fits very well with the results of tested GNAC, with a difference less than 5.2%. Eq. (4.11) is proposed in this work to predict elastic modulus for GRAC, based on the regression analysis of the experimental results. As shown in Figure 4.16, the proposed relationship can accurately predict the elastic modulus of GRAC. Moreover, most results in the previous studies on GRAC reported by Xie et al. (2019a), Shaikh (2016) and Liu et al. (2016) fit reasonably well with this prediction.

$$E_c = 5300(f_c')^{1/3} \tag{4.9}$$

$$E_c = 2900(f_c')^{3/5} \tag{4.10}$$

$$E_c = 2977(f_c)^{0.474} \ (R^2=0.845) \tag{4.11}$$

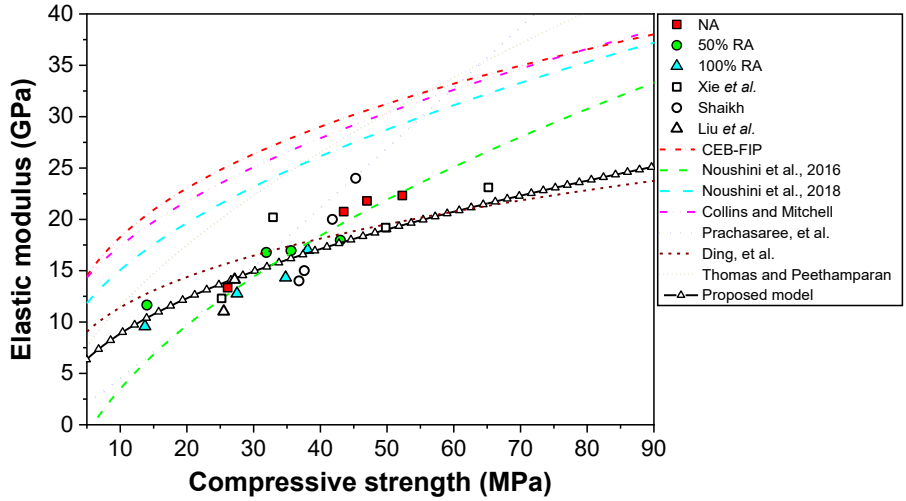

Figure 4.16. Performance of existing and proposed elastic modulus models for geopolymeric concrete

4.3.4 Model verification

The proposed compressive stress-strain relationship for geopolymeric concrete has been developed as presented in Eq. (4.5), in which the peak strain and modulus of elasticity can be predicted through Eq. (4.8), and Eq. (4.9) and Eq. (4.11) respectively. Also, the details of the proposed model are provided in Table 4.5. To verify the proposed stress-strain model, the stress-strain curves obtained by the proposed model were compared with the experimental data, as shown in Figure 4.17. Overall, the proposed model can predict the stress-strain curves for the geopolymeric concrete with a relatively small error, that the total mean R^2 being 0.9622.

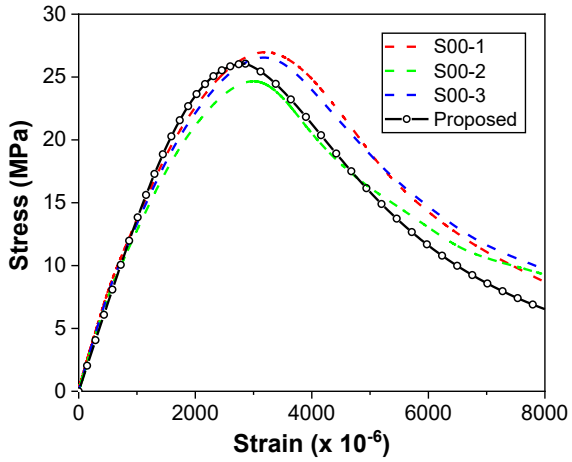

(a) S00

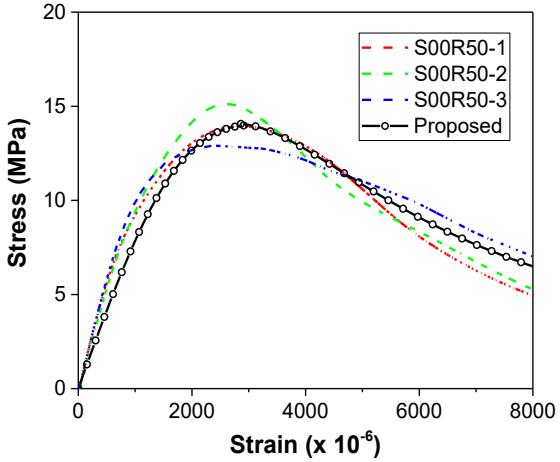

(b) S00R50

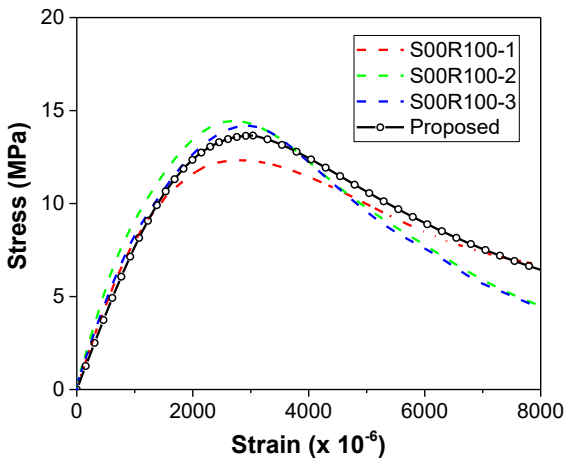

(c) S00R100

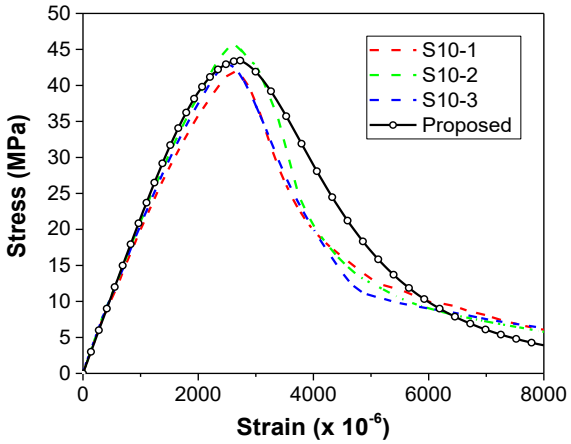

(d) S10

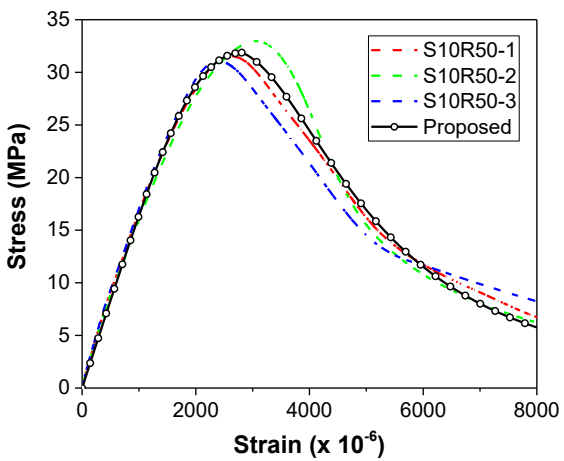

(e) S10R50

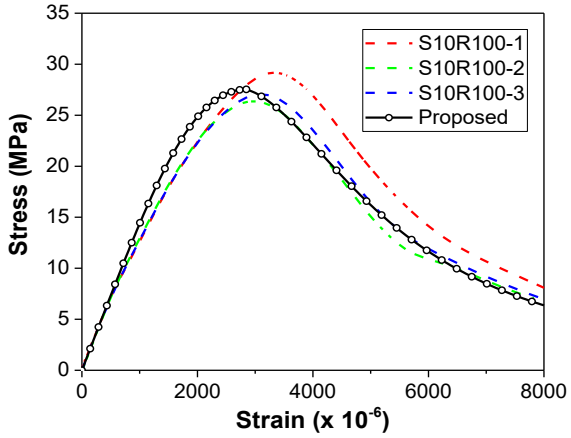

(f) S10R100

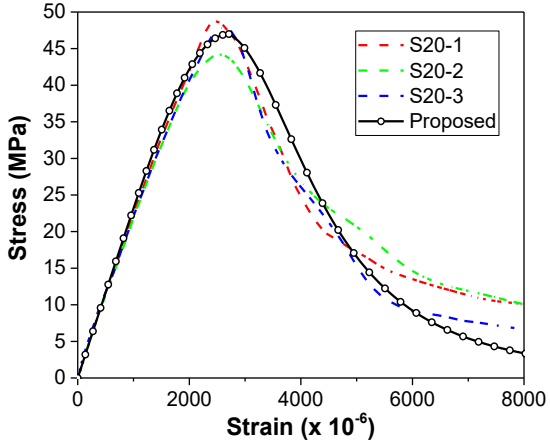

(g) S20

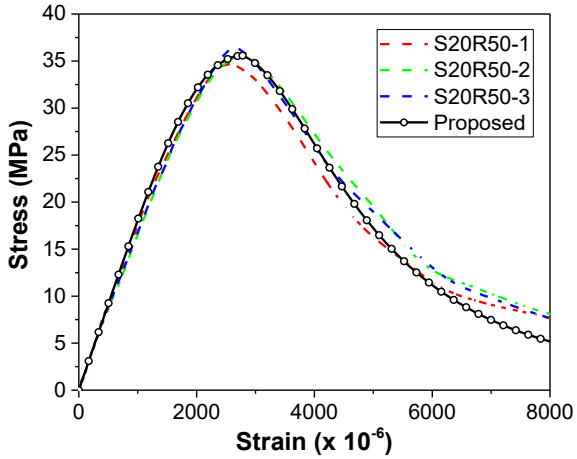

(h) S20R50

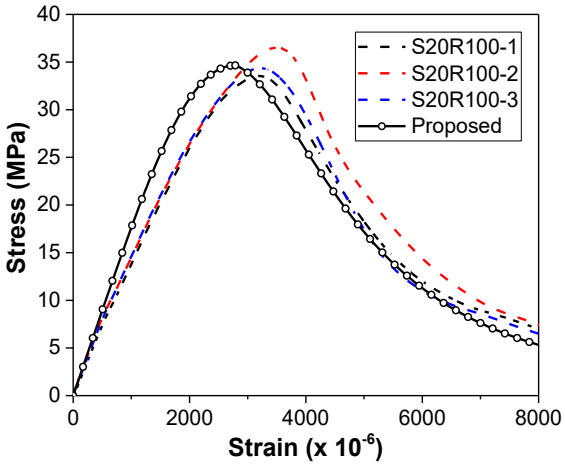

(i) S20R100

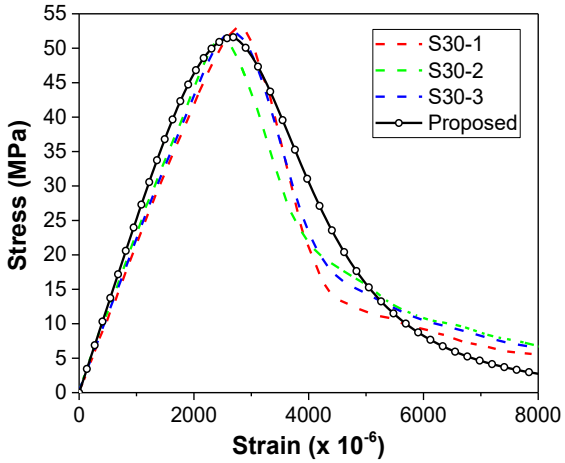

(j) S30

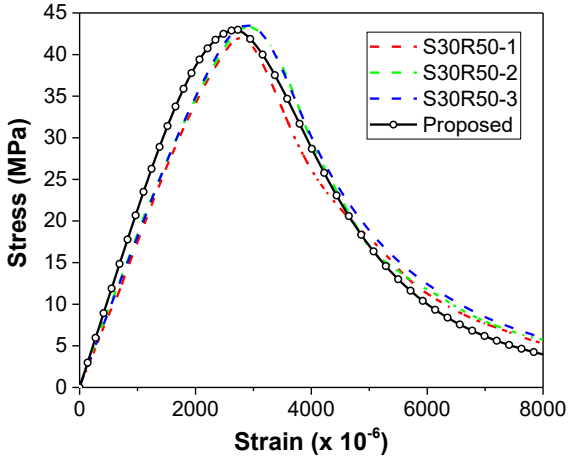

(k) S30R50

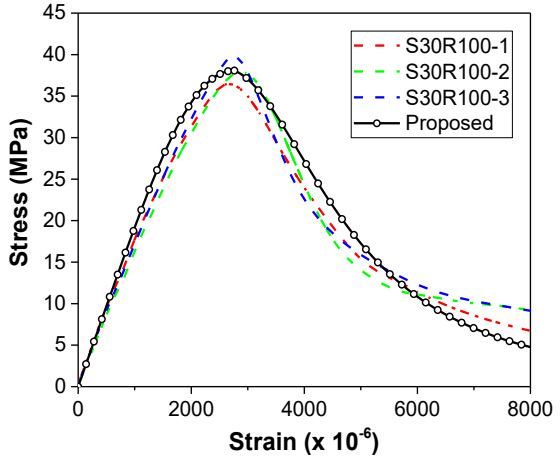

(l) S30R100

Figure 4.17. Comparison between proposed stress-strain model and experimental results

4.4 Summary

(1) All the tested geopolymeric concretes had a similar failure process under compression. However, the probability of crack development through aggregates increased as the RA replacement ratio increased, and a higher percentage of fractured aggregate particles were observed in geopolymeric concrete with a higher content of slag.

(2) All the stress-strain curves of geopolymeric concretes showed a decrease in peak stress, elastic modulus, and energy absorption (toughness), but an improvement in ductility, with the increase in the RA replacement ratio. However, opposite trends were observed as the slag content increases. Moreover, the inclusion of slag can alleviate the effects of RA replacement on these properties.

(3) The peak strain and ultimate strain of geopolymeric concrete were influenced by the RA replacement ratio and the content of slag. RA replacing resulted in the increases in peak strain and ultimate strain for geopolymeric concrete with 10% and 20% inclusion of slag, but comparatively in fewer impacts on the neat fly ash-based geopolymeric concrete and geopolymeric concrete with 30% inclusion of slag.

(4) The existing stress-strain models previously developed for OPC concrete, geopolymeric concrete, and OPC-based RAC cannot accurately predict the stress-strain behaviors of geopolymeric concrete in the current study. Similar results were observed in the comparison between the experimental results and predictions by the existing models for the peak strain and elastic modulus. However, the model proposed by Collins and Mitchell (1991) fits relatively well with the experimental stress-strain curves of geopolymeric concrete.

(5) By comparing the proposed stress-strain models with the experimental results of the current study, it is concluded that the proposed model has very good accuracy in determining the actual complete compressive stress-strain curve for both GNAC and GRAC.

CHAPTER 5: DYNAMIC COMPRESSIVE BEHAVIORS OF SUSTAINABLE GRAC

It is worth mentioning that all structures and facilities are likely to be subjected to dynamic loadings, such as earthquakes, high-velocity impact, and accidental explosion. Also, the dynamic behaviors of engineering materials or structures are extremely different from the static ones (Khosravani & Weinberg 2018; Su et al. 2016; Yoo & Banthia 2017). Thus, the response of GRAC to dynamic loading is of considerable significance for the reliable design and accurate assessment of structural performance in future applications.

Therefore, to fill such a research gap, this chapter aims to provide a comprehensive study of the dynamic properties of GRAC. The effects of the strain rate on compressive behaviors of GRAC were investigated, including the stress-strain behavior, energy dissipation, and failure pattern.

5.1 Experimental program

5.1.1 Raw materials

The raw materials used in this study, including fine aggregate, fly ash, slag, and alkali activator, were in accordance with that in Chapter 3. Thus, the details for these materials could be referred to in Section 3.1.1.

For coarse aggregate, both NA and RA have a nominal maximum size of 9.5 mm, and the sieve analysis results are presented in Figure 5.1. The NA used was crushed basalt. The RA was locally obtained from a C&D waste recycling plant. Table 5.1 shows the composition analysis for a 5 kg sample of the RA used. The result indicates that the RA can be categorized as mixed RA according to the reference (Silva et al. 2014). Table 5.1 also provides the physical properties of the NA and RA.

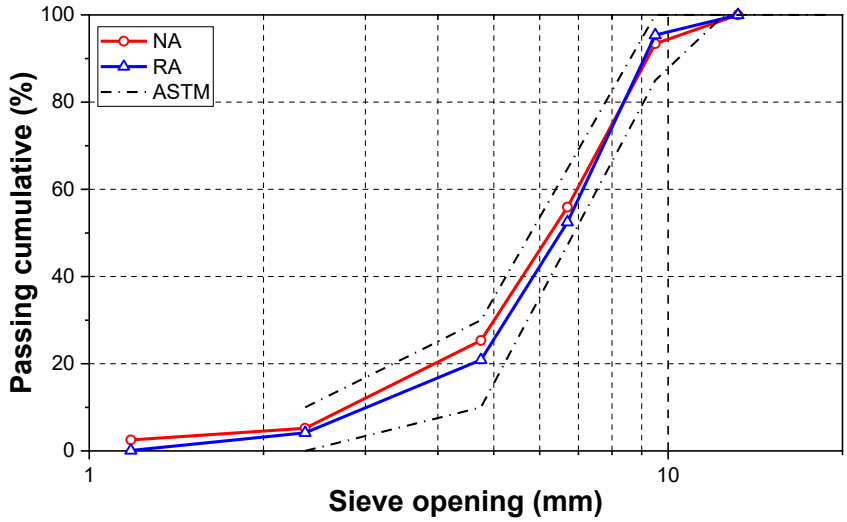

Figure 5.1. Sieve analysis results of coarse aggregates

Table 5.1 Physical properties of coarse aggregates

	Relative density (SSD)	Relative density (oven-dry)	Water absorption (wt. %)	Crushing value (wt. %)
NA	2.76	2.70	1.81	14.32
RA	2.30	2.13	8.02	22.68
Constituents of RA (wt. %)				
Concrete products	Brick	Tile	Natural stone	Glass and others
79.5%	9.7%	5.4%	2.9%	2.5%

5.1.2 Mix proportions

In this test, eight geopolymeric concrete mixtures were designed. The mix proportions of the reference mixtures made of 100% NA and the mixtures made of 100% RA are given in Table 4.3. The precursor content kept constant at 420 kg/m^3 for all the mixtures, and four different fly ash/slag proportions were adopted as 100/0, 90/10, 80/20, and 70/30. The activator solution to binder ratio and the sodium silicate solution to sodium hydroxide solution ratio were taken as 0.55 and 2.5, respectively, by mass.

Table 5.2 Mix proportions of geopolymeric concrete

Mix	Mix proportions (unit weight: kg/m^3)						
	Fly ash	Slag	Na_2SiO_3	NaOH	Sand	NA	RA
S00	420	0	165	66	550	1220	–
S10	378	42	165	66	550	1220	–
S20	336	84	165	66	550	1220	–
S30	294	126	165	66	550	1220	–
S00R	420	0	165	66	550	–	1220
S10R	378	42	165	66	550	–	1220
S20R	336	84	165	66	550	–	1220
S30R	294	126	165	66	550	–	1220

5.1.3 Specimen preparation

The concrete mixing process and curing regime in this study were in accordance with the method reported in Section 3.1.3.

In the quasi-static compression test, a set of three cylinders with the dimension of Ø100×200 mm was fabricated for each concrete mixture. Before testing, both ends of the specimens were ground flat and parallel. While for the dynamic compression test, the cylinders with the dimension of Ø75×37.5 mm were prepared by cutting from the cylinder specimens with the dimension of Ø75×150 mm. The dimension of dynamic compression specimens followed the recommendation of L/D =0.50 to avoid the axial inertial effect and end-friction effect during impact loading (Gray 2000). The cut surface of the specimens was polished with a polisher to achieve a smooth and perpendicular surface to the axis rotation.

5.1.4 Experimental methods

Quasi-static compression test

The experimental method and set-up for the quasi-static compression test were in accordance with that in Section 4.1.4. The average strain data obtained from the two LSCTs were later used to establish the quasi-static stress-strain curve.

Dynamic compression test

The dynamic compression test was performed by using an 80-mm splitting Hopkinson pressure bar (SHPB) apparatus. The schematic of the SHPB apparatus is presented in

Figure 5.2. The SHPB apparatus primarily consists of three uniform cross-section bars having the same diameter of 80 mm: a striker bar (400 mm in length), an incident bar (3060 mm in length), and a transmission bar (1800 mm in length). The three bars are made of stainless steel with a Young's modulus (E) of 208 GPa and a density of (ρ) of 7800 kg/m^3. Thus the velocity of the elastic wave propagating in the bars, C_0, can be calculated by $\sqrt{E/\rho} = 5164$ m/s.

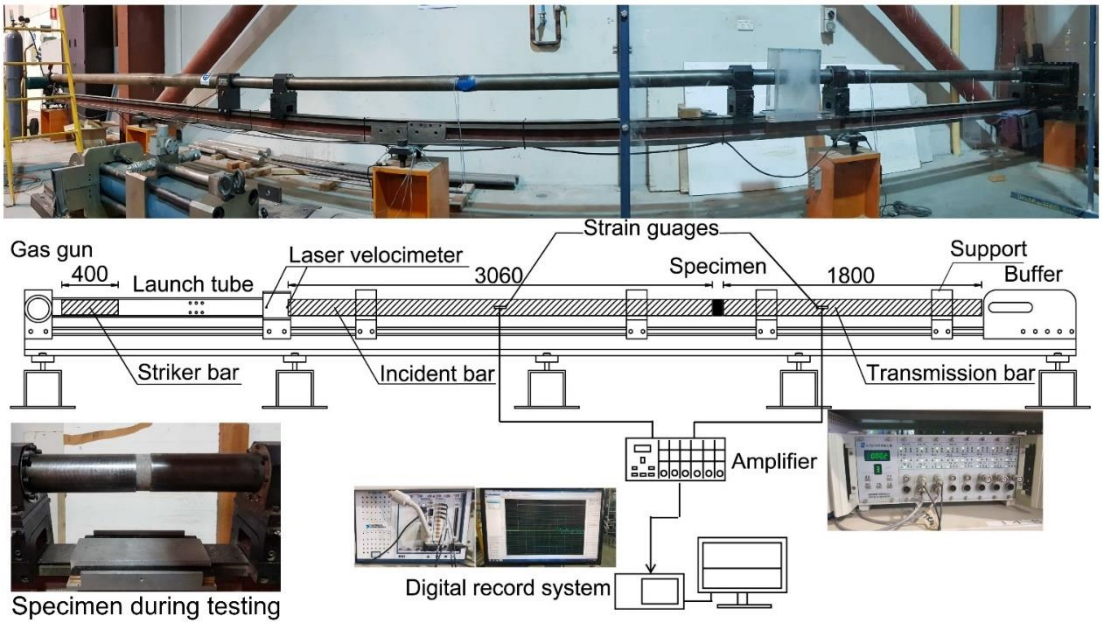

Figure 5.2. SHPB test system for impact testing

For each test, the specimen was placed between the ends of the incident bar and the transmission bar, as shown in Figure 5.2. Vaseline was applied uniformly to the contact surfaces between the specimen and the incident/transmission bar to reduce the friction. The striker bar was accelerated by the gas launcher charged with pressurized gas and then impacted against the incident bar. The velocity of the strike bar was measured by the laser velocimeter. Upon the impact of the striker bar on the incident bar, an incident compressive pulse was generated and then propagated through the incident bar. Because of the impedance mismatch, once the incident pulse reached the specimen, part of the incident pulse was reflected as the reflected pulse back towards the incident bar, and part of the incident pulse was transmitted through the specimen as the transmitted pulse into the transmission bar. At the end of the transmission bar,

a cushion buffer made of four commercial elevator buffers was installed to absorb the impact energy.

The strain waves carried by the incident and reflected pulses were measured by a pair of strain gauges mounted on the incident bar through Wheatstone bridge, and likewise, the strain wave carried by the transmitted pulse was recorded by the other pair of strain gauges mounted on the transmission bar, as shown in Figure 5.2. By using a strain amplifier, the signals of strain gauges were amplified by 200 times and filtered using a low-pass filter with a frequency of 100 kHz. Eventually, a data acquisition system with a sampling frequency of 5 MHz was used to record the processed signals.

SEM test

SEM test was performed on the fracture pieces after the SHPB test. Concrete pieces containing geopolymeric matrix and coarse aggregate were selected, and then were coated with a gold film. Zeiss FEG-SEM was employed for SEM microstructural observation with an accelerating voltage of 15 kV.

5.2 Quasi-static compression

5.2.1 Failure characteristics

The typical failure patterns of geopolymeric concrete under the quasi-static state are presented in Figure 5.3. All the failure patterns are similar to each other. It was observed that most cracks propagated in the direction parallel to the compressive loading. Moreover, there are always several main cracks running through the specimens. However, some differences could be identified between these failure patterns. Owing to the RA possessed the lower crushing strength and high intensity of bonding interface, more fracture planes tend to penetrate through the aggregate particles in GRAC compared with GNAC (Casuccio et al. 2008). Besides, regardless of the type of coarse aggregate, more fractured aggregate particles could be observed in geopolymeric concrete with the increasing slag content. This was mainly due to the condensation of microstructure after the incorporation of slag (Puligilla & Mondal 2013; Shang et al. 2018; Xie et al. 2019b). With the densification of the mortar constituent increasing, higher compatibility between coarse aggregate and the surrounding mortar could result in the increase of fractured aggregate (Akçaoğlu 2017;

Chiaia et al. 1998; Giaccio & Zerbino 1998). Also, the enhanced matrix-aggregate bond, resulting from the compacted mortar, forced the facture to pass through the aggregate particles (Akçaoğlu 2017; Chiaia et al. 1998).

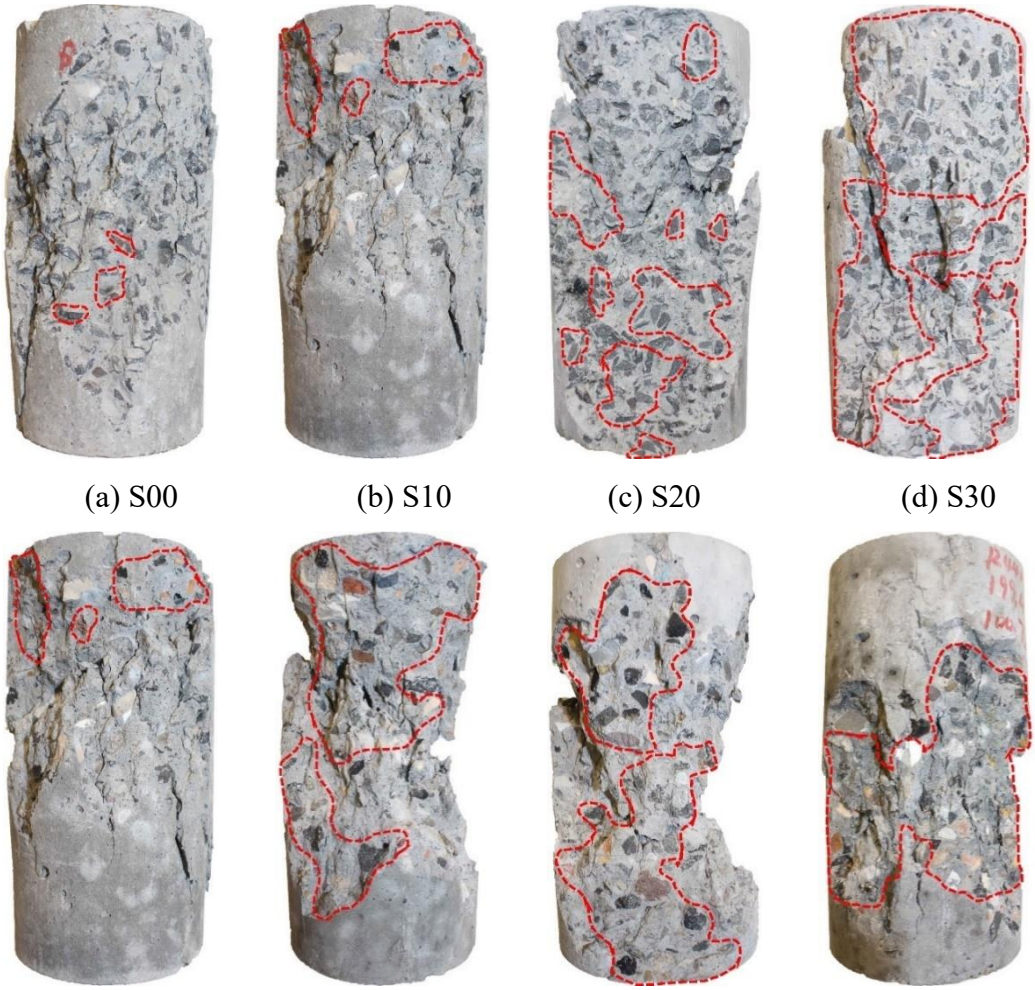

(a) S00 (b) S10 (c) S20 (d) S30

(e) S00R (f) S10R (g) S20R (h) S30R

Figure 5.3. Failure patterns of geopolymeric concrete under quasi-static loading(fractured aggregate particles marked within red lines)

5.2.2 Stress-strain curves

The stress-strain responses obtained from the quasi-static compression tests of geopolymeric concrete are plotted in Figure 5.4.

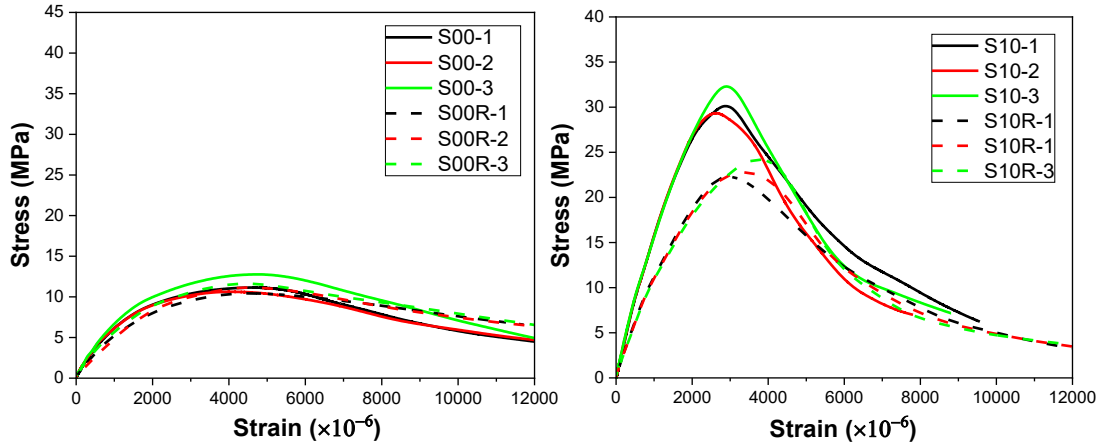

(a) Geopolymeric concrete without slag (b) Geopolymeric concrete with 10% slag

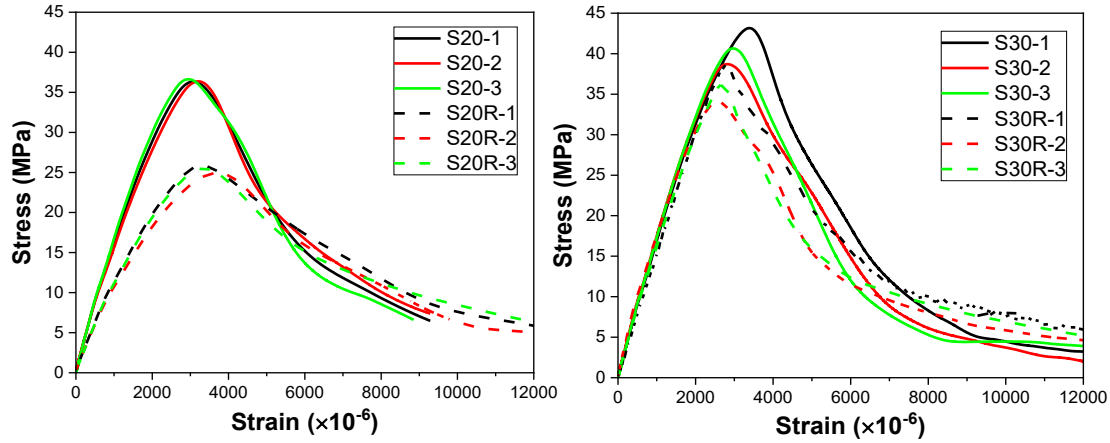

(c) Geopolymeric concrete with 20% slag (d) Geopolymeric concrete with 30% slag

Figure 5.4. Comparison of quasi-static stress-strain curves of GNAC and GRAC

All the stress-strain curves exhibit a similar profile, consisting of three regions, specifically, the initial linear elastic region, the followed non-linear region, and the final softening region. Figure 5.4 also shows the effect of the RA replacement on the stress-strain response of geopolymeric concrete under quasi-static compression. Generally, in the ascending part of the curve, with the same unit stress increase, the strain developed in GRAC is higher than that achieved in GNAC. In other words, the RA replacement decreased the elastic modulus of geopolymeric concrete. This was mainly attributed to the lower elastic modulus of the RA in comparison with NA. Also, the RA replacement decreases the extent of the linear elastic region and increases the extent of the subsequent non-linear phase, thus resulting in the increased curvature of the curves in the ascending part. This result is consistent with that obtained by Xiao et al. (2005) and Belén et al. (2011). Another notable fact is that the descending stage

of the stress-strain curve is much flatter for GRAC in comparison with GNAC. This is compatible with the trend observed by the previous researchers (Belén et al. 2011; Rqhl & Atkinson 1999; Xie et al. 2019a). Accordingly, Beshr et al. (2003) explained that the weaker aggregate tended to produce more ductile concrete than the stronger aggregate.

Figure 5.5 presents the stress-strain curves of geopolymeric concretes with different contents of slag. Obviously, the inclusion of slag has a significant effect on the stress-strain response of geopolymeric concrete irrespective of the aggregate type. With the increase of the slag content, the initial slope of the ascending region increases, as well as the linearity of the curve and the height of the peak. In addition, the descending stage is much more abrupt and steeper for the geopolymeric concrete with a higher content of slag. Overall, the stress-strain relationship of geopolymeric concrete with a higher content of slag behaves in a much stiffer but more brittle manner. The reason for these observations is that the high content of slag could accelerate the reaction and generate a much stiffer matrix in geopolymeric concretes (Xie et al. 2019a). Additionally, the brittle manner could be explained by the different crack propagation behavior. Specifically, due to the strength enhancement of matrix and ITZ by the incorporation of slag (Kürklü 2016; Puligilla & Mondal 2013; Shang et al. 2018), more cracks propagated through aggregate, as observed in Figure 5.3. This crack propagation led to the contraction of the fracture process zone at the tip of the crack and caused fractal dimensions to reach their minimum value due to higher rupture in the aggregate phase, and consequently, concrete exhibited an additional brittle behavior (Beygi et al. 2013).

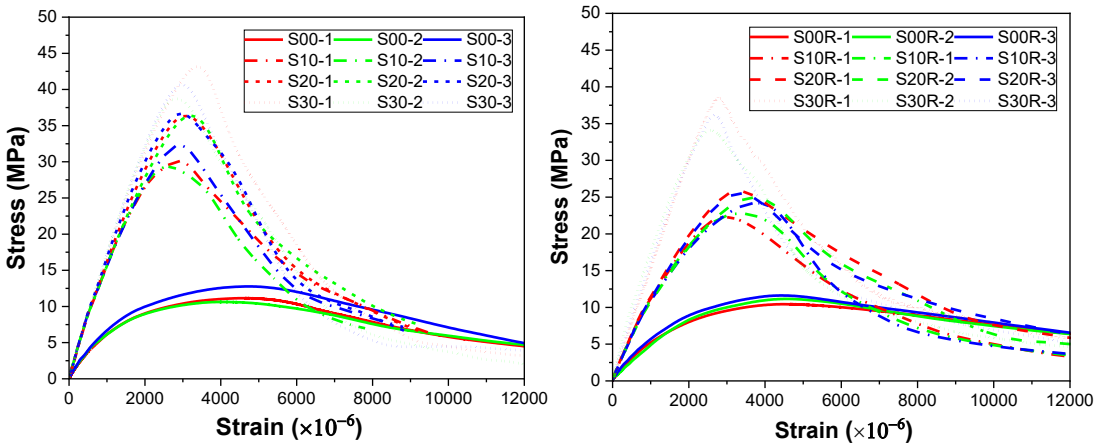

(a) GNAC (b) GRAC

Figure 5.5. Comparison of quasi-static stress-strain relation of geopolymeric concrete under different slag content

5.2.3 Compressive strength

The measured compressive strengths are compared in Figure 5.6. The quasi-static compressive strength of geopolymeric concrete decreases after the replacement of RA. The lower strength in GRAC was due to the poor quality of RA, such as the cracks that existed in RA (Shi et al. 2016). In addition, the relative strengths (ratio of the strength of GRAC to that of GNAC) are presented in Figure 5.6. It was found that the relative strengths were within the range from 70% to 96%. This result is in agreement with the values reported in the previous studies on OPC-based RAC (Tu et al. 2006; Xiao et al. 2005) or geopolymeric concrete (Nuaklong et al. 2016; Nuaklong et al. 2018a).

As shown in Figure 5.6, the inclusion of slag provided both GNAC and GRAC with higher compressive strength. The improvement is more significant with the increase of slag content. For instance, the GRAC containing 10%, 20%, and 30% slag inclusion had the compressive strengths higher than the GRAC without slag, by 109%, 129%, and 207%, respectively. This improvement is mainly attributed to the formation of calcium-based hydrate gel (calcium alumino-silicate hydrate) after the addition of slag (El-Hassan & Ismail 2017; Ling et al. 2019; Xie et al. 2019a). It suggests that the microstructure of the calcium-based hydrate gel is denser than that of aluminosilicate-type gel forming in neat fly ash based geopolymer (Burciaga-Díaz et al. 2013; Provis et al. 2012). Also, the additional calcium sourced from the inclusion of slag could

accelerate the dissolution of fly ash due to the nucleation effect, and therefore enhance the hydration product formation (Puligilla & Mondal 2013).

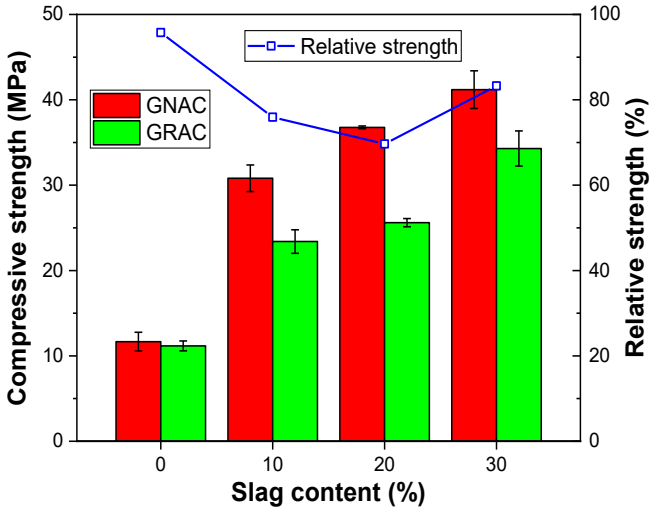

Figure 5.6. Quasi-static compressive strength of geopolymeric concrete

5.3 Dynamic compression

5.3.1 Data processing and determination of strain rates

Figure 5.7 shows the typical signals monitored from the strain gauges during the SHPB test, which includes the incident wave and reflected wave recorded by the strain gauges on the incident bar, and the transmitted wave recorded by the strain gauges on the transmission bar. According to the one-dimensional stress wave theory, time histories of stress $\sigma(t)$, strain $\varepsilon(t)$, and strain rate $\dot{\varepsilon}(t)$ within the specimen can be obtained by following Eqs. (5.1) to (5.3).

$$\sigma(t)=\frac{AE}{A_s}\varepsilon_T(t) \tag{5.1}$$

$$\varepsilon(t)=\int_0^t \dot{\varepsilon}(\tau)d\tau \tag{5.2}$$

$$\dot{\varepsilon}(t)=\frac{2C_0}{l_0}\varepsilon_R(t) \tag{5.3}$$

where A, E, and C_0 refer to the cross-sectional area, the elastic modulus, and the elastic wave velocity of the SHPB bars, respectively; A_s and l_0 are the cross-sectional

area and the thickness of the specimens, respectively; $\varepsilon_R(t)$ and $\varepsilon_T(t)$ are the reflected strain and the transmitted strain, respectively.

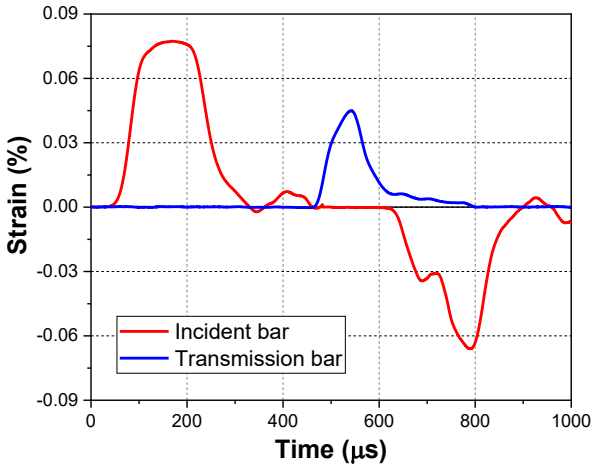

Figure 5.7. Typical impact signals of SHPB test

However, it should be noted that these above equations are valid only when the longitudinal stress in the specimens reaches the equilibrium state. The stress equilibrium can be checked by Eq. (5.4), in which the stress waves at the end surfaces of the specimen are compared.

$$\Delta\sigma(t)=\frac{A}{A_s}E\left[\varepsilon_I(t)+\varepsilon_R(t)-\varepsilon_T(t)\right] \tag{5.4}$$

where the $\Delta\sigma(t)$ denotes the difference between the stress waves at the end surfaces of the specimen.

The typical signal after the removal of time lags is presented in Figure 5.8(a). It was observed that $\varepsilon_I(t)+\varepsilon_R(t)$ is consistent with $\varepsilon_T(t)$, indicating the achievement of stress equilibrium by Eq. (5.4). To further quantity stress equilibrium in the specimen, a stress equilibrium factor R is adopted and defined by Eq. (5.5). It has been suggested that the stress in the specimen could be treated as uniform when $R \leq 0.05$ (Guo et al. 2017).

$$R(t)=2\left|\frac{\varepsilon_I(t)+\varepsilon_R(t)-\varepsilon_T(t)}{\varepsilon_I(t)+\varepsilon_R(t)+\varepsilon_T(t)}\right| \tag{5.5}$$

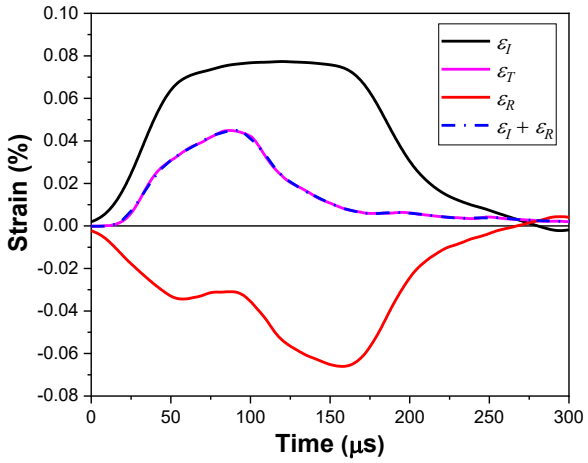

(a) Typical signal after the removal of time lags

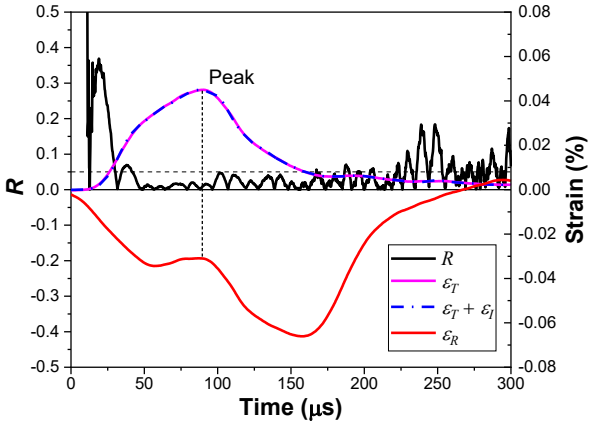

(b) Stress uniformity in the specimen

Figure 5.8. Typical dynamic stress equilibrium relationship between stress and time

Figure 5.8(b) presents the variation of factor R with time: the value is initially large but then decreases quickly, and becomes less than 0.05 before the peak point of transmitted strain signal. According to Eq. (5.3), the strain rate is linearly related to the reflected strain. Although the strain rate is not constant throughout the test duration, it reached a plateau with a relatively constant value before the peak of the transmitted strain, as shown in Figure 5.8(b). Therefore, the strain rate at the peak stress is taken as the representative strain rate in this study.

5.3.2 Failure pattern

The failure patterns of geopolymeric concrete at different strain rates after the test are presented in Figure 5.9. The failure mode of the GRAC was similar to that of the corresponding GNAC. Generally, the size and number of generated fragments were strongly related to the strain rate. With the increase of the strain rate, the failure pattern of geopolymeric concrete was transformed from broking into several large pieces to fracturing into fine fragments or even powder. Such a rate-dependent failure mode was attributed to the effect of strain rate on the fracture of concrete. As the dynamic loading time is short, the path of least resistance in the mortar and the ITZ cannot be tracked. Instead, the failure occurred through the initiation of both the new cracks and the expansion of existing ones (Vegt et al. 2007). Also, the high strain rate resulted in another phenomenon that more cracks propagated through the coarse aggregate, as shown in Figure 5.9. In other words, the concrete specimens failed mainly by the inter-granular crack propagation under low strain rates, while failed more through the trans-granular crack propagation at high strain rates. Comparatively, this phenomenon was more evident in the geopolymeric concrete after the inclusion of slag or the replacement of RA.

strain rate 85 s^{-1} strain rate 109 s^{-1} strain rate 160 s^{-1} strain rate 195 s^{-1}

(a) S00

strain rate 77 s^{-1} strain rate 104 s^{-1} strain rate 153 s^{-1} strain rate 174 s^{-1}

(b) S10

strain rate 43 s^{-1} strain rate 68 s^{-1} strain rate 116 s^{-1} strain rate 165 s^{-1}

(c) S20

strain rate 33 s^{-1} strain rate 77 s^{-1} strain rate 110 s^{-1} strain rate 176 s^{-1}

(d) S30

strain rate 82 s^{-1} strain rate 128 s^{-1} strain rate 167 s^{-1} strain rate 193 s^{-1}

(e) S00R

strain rate 46 s^{-1} strain rate 86 s^{-1} strain rate 116 s^{-1} strain rate 169 s^{-1}

(f) S10R

strain rate 52 s^{-1} strain rate 68 s^{-1} strain rate 84 s^{-1} strain rate 134 s^{-1}

(g) S20R

strain rate 26 s^{-1} strain rate 51 s^{-1} strain rate 102 s^{-1} strain rate 149 s^{-1}

(h) S30R

Figure 5.9. Failure patterns of geopolymeric concrete under different strain rates

5.3.3 Dynamic stress-strain curve

The typical dynamic stress-strain curves of geopolymeric concrete under different strain rates are displayed in Figure 5.10, and also are compared with the corresponding stress-strain curves under quasi-static actions. The dynamic stress-strain curves exhibit a high level of geometric similarity to the quasi-static stress-strain curve: specifically, with the increase of strain, the stress increases up to a peak value and then decreases. Nevertheless, the dynamic compressive stress-strain curves possess higher peak stress compared with the corresponding quasi-static compressive stress-strain curve, and the peak stress is sensitive to the strain rate. It is believed that such strain rate dependence can be explained from the multiple physical mechanisms, including 1) the viscous effect of free water in the micropores, known as Stefan effect (Rossi et al. 1994); 2) the cracking propagation effect, specifically cracks are forced to propagate through the areas of higher resistance (Yan & Lin 2006); and 3) the inertia-induced lateral confinement effect (Bischoff & Perry 1991). Moreover, the initial slope of dynamic compressive stress-strain curves is higher than that in the quasi-static compression test, which is more evident with the increase of strain rate. This could be attributed to the sharp increase in strength at higher strain rates but the decrease of internal micro-cracking (Bischoff & Perry 1991).

The effects of RA replacement and the inclusion of slag on the dynamic stress-strain curve agree with those on the quasi-static stress-strain curve. Generally, at a certain level of strain rate, the stress-strain curves of geopolymeric concrete have decreased linearity in the ascending part and flatter behavior in the descending part due to the replacement of RA, while the reverse tendency could be detected after the inclusion of slag.

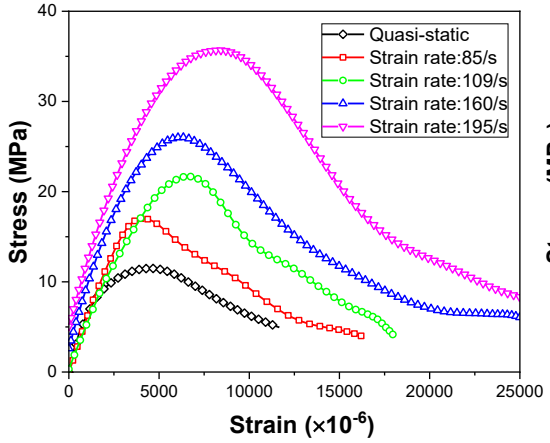

(a) S00

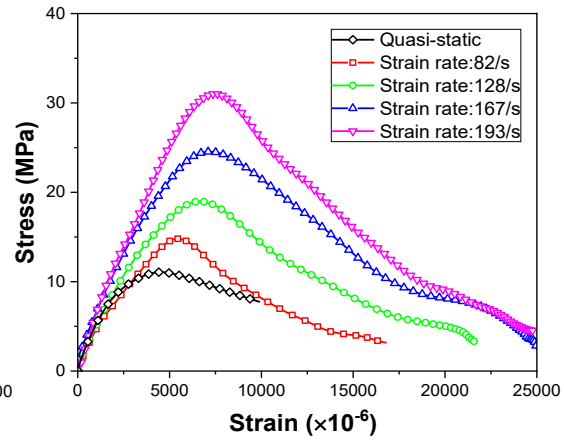

(b) S00R

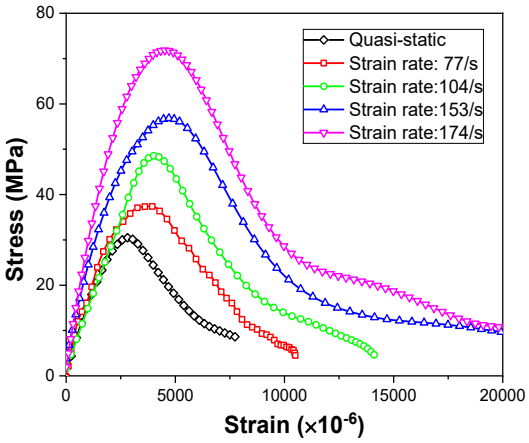

(c) S10

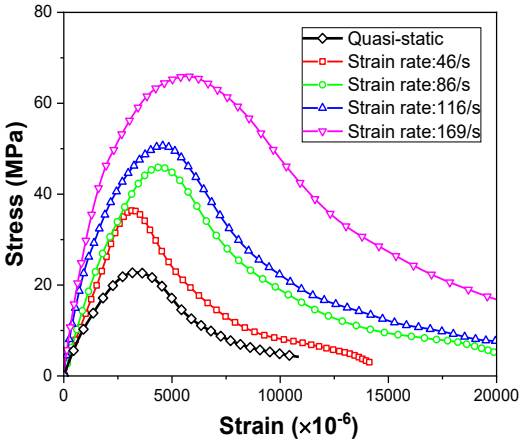

(d) S10R

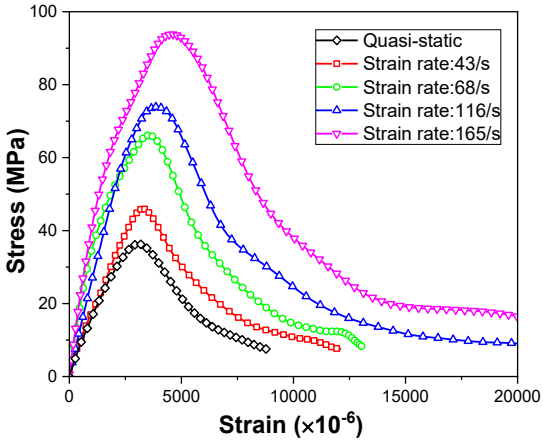

(e) S20

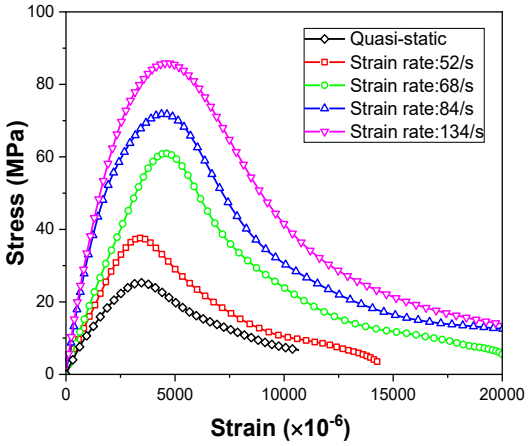

(f) S20R

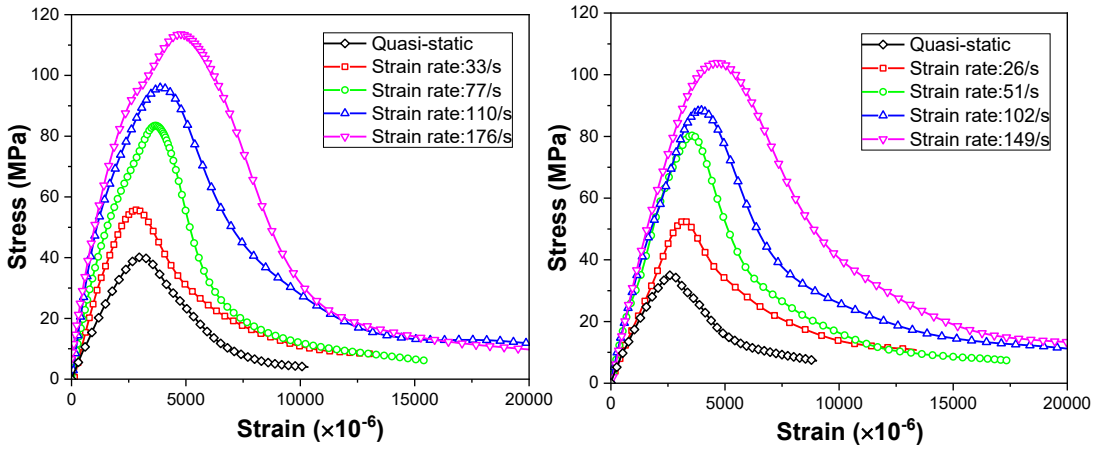

(g) S30 (h) S30R

Figure 5.10. Stress-strain curves of geopolymeric concrete under dynamic compression

5.3.4 Compressive strength and dynamic increase factor

The dynamic compressive strength versus the strain rate for geopolymeric concrete is depicted in Figure 5.11. It is obvious that the compressive strength is strain-rate dependent and increases with the increase of strain rates. Figure 5.11 also shows that within the same regime of strain rate, the dynamic compressive of geopolymeric concrete increases with the content of slag, which is consistent with the tendency observed in other studies, that at a specific strain rate, the stronger concrete (under quasi-static state) usually exhibits higher dynamic compressive strength (Bischoff & Perry 1991; Cusatis 2011). Also, this observation coincides with the previously mentioned failure patterns that, at a certain strain rate, a high percentage of fractured aggregate particles were observed in geopolymeric concrete with a higher content of slag. Specifically, more energy would be consumed by generating more cracks in the aggregate, thus resulting in higher strengths. On the other hand, the replacement of RA has a limited effect on the dynamic compressive strength of geopolymeric concrete, which is different from that observed in the quasi-static compression test. A similar result has been previously reported in the study on RAC based on OPC by Xiao et al. (2015).

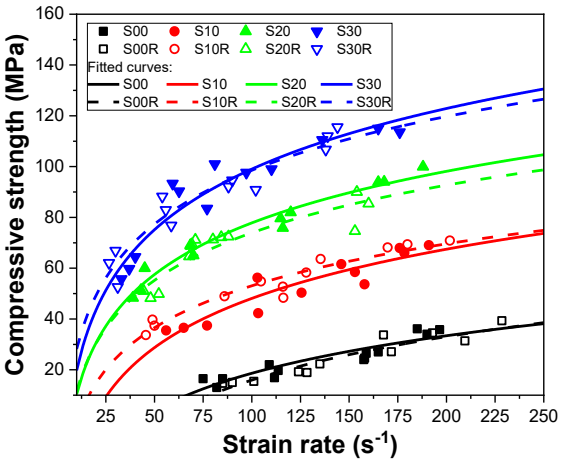

Figure 5.11. Relationship between dynamic compressive strength and strain rate for geopolymeric concrete

The dynamic increase factor (DIF) (i.e., the ratio of dynamic compressive strength to quasi-static compressive strength) is usually employed for the characterization of the strain-rate sensitivity of concrete. Figure 5.12 compares the DIF for GNAC and GRAC. At a given strain rate, the GRAC displays a higher DIF compared with the GNAC with the same slag content. This is reasonable as the replacement of RA causes a decrease in quasi-static compressive strength but a negligible influence on dynamic compressive strength, which is also consistent with the study on the RAC based on OPC (Xiao et al. 2015). Several reasons might account for this observation. Firstly, in this study, the coarse aggregate used was under SSD condition, and therefore, the GRAC would contain a relatively large volume of free water due to the higher porosity of RA, as shown in Table 5.1. It has been well documented that the free water in the micropores exhibits the so-called Stefan effect (Rossi et al. 1992), which results in the strengthening effect in concrete under high loading rates, and this effect is more prominent in GRAC because of higher free water content. Therefore, the increasing volume of free water caused by the replacement of RA may be one of the reasons causing the increased strain rate sensitivity in GRAC.

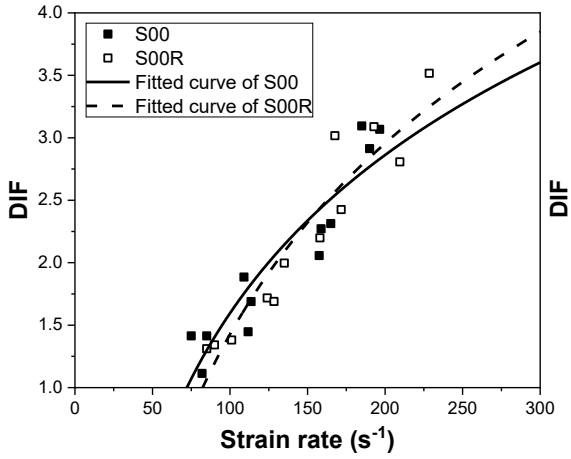

(a) Geopolymeric concrete without slag

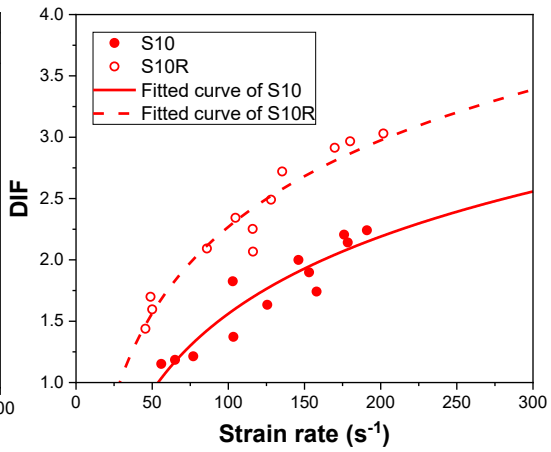

(b) Geopolymeric concrete with 10% slag content

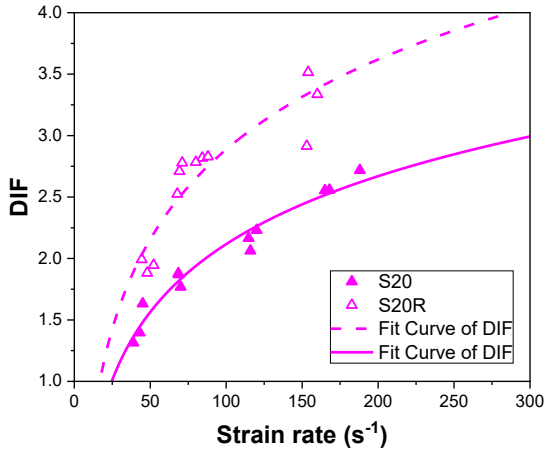

(c) Geopolymeric concrete with 20% slag content

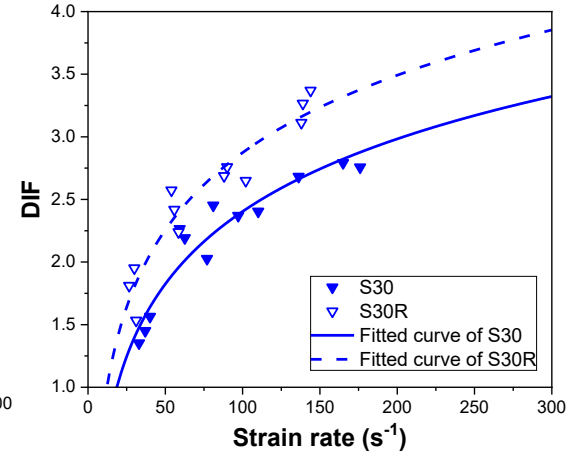

(d) Geopolymeric concrete with 30% slag content

Figure 5.12. Relationships between DIF and strain rate for GNAC and GRAC

Additionally, Figure 5.13 demonstrates the ITZ between the geopolymeric matrix and aggregates. No significant gap or separation could be detected in these interphase regions, indicating that the geopolymeric matrix was well-bonded to the NA, as well as the RA and the attached cement paste. Also, some studies have reported that the ITZ in GRAC even exhibited better bonding intensity and frictional strength in comparison with that in GNAC, attributing to that RA has the relatively high surface porosity and roughness, and also the geopolymeric matrix has the ability to fill the pre-existing incomplete interphase within the RA (Casuccio et al. 2008; Khedmati et al. 2019; Ren & Zhang 2018). This feature could equip GRAC with higher strain rate sensitivity, as the aggregate that exhibits a good bond strength with the surrounding

mortar matrix will yield the concrete with a good impact resistance (Bischoff & Perry 1991). Furthermore, the test by Sparks & Menzies (1973) demonstrated that the concrete with stiffer aggregates was less strain-rate sensitive. Thus, the difference in stiffness between the RA and NA may serve as one factor for the high strain rate sensitivity of GRAC. Other factors, such as less binder content in GRAC due to the low density of RA, might also have influences on the strain rate sensitivity but still need further studies (Li et al. 2016b).

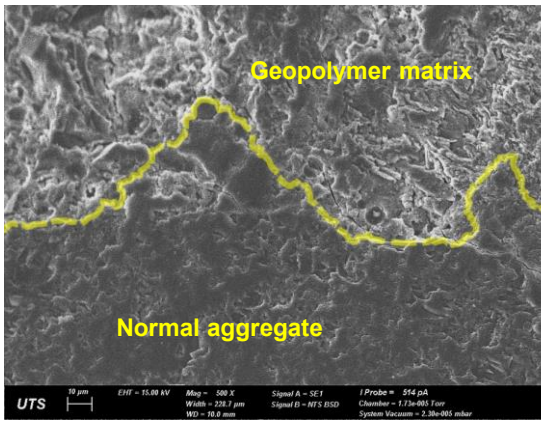

(a) ITZ of GNAC

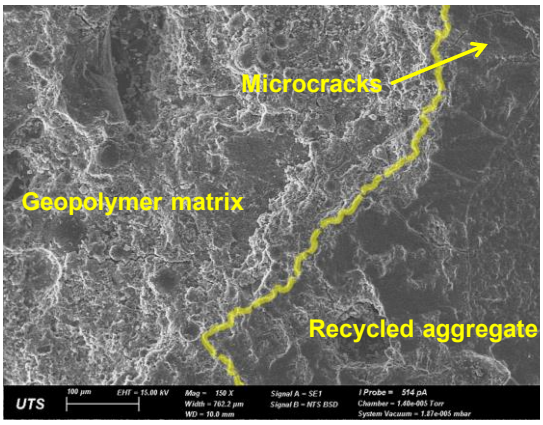

(b) ITZ of GRAC

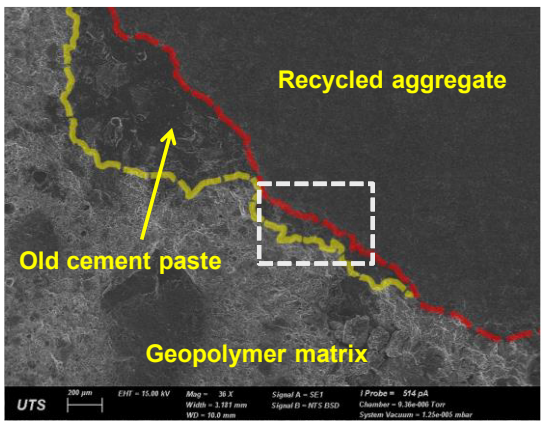

(c) ITZ of GRAC with old cement mortar

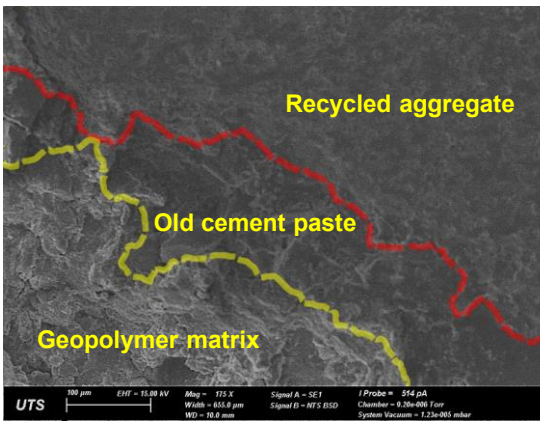

(d) Zoom-in of (c)

Figure 5.13. SEM micrograph of GNAC and GRAC

The DIFs of GNAC and GRAC under different contents of slag are shown in Figure 5.14. It could be observed that at relatively low strain rates, the geopolymeric concretes with higher contents of slag have higher DIF values. However, with the increase of strain rate, geopolymeric concrete with lower content of slag shows a more noticeable increase in DIFs. Whereas, the mechanism for the different strain rate

sensitivity of geopolymeric concrete with different slag content needs further study. It has been reported that the geopolymeric concrete based on different compositions exhibited different strain rate sensitivity. For instance, Feng et al. (2015) and Luo et al. (2014) reported that the alkali activator type had a significant impact on the dynamic compressive behavior of geopolymeric concrete. Moreover, Yao et al. (2019) recently investigated the dependences of the dynamic compressive and tensile strength of alkali-activated mortars synthesized from different precursors and alkali activators on the loading rate and curing time. Test results showed that the dynamic compressive and tensile strength of alkali-activated mortar were much influenced by the composition of raw materials and curing time. Therefore, accounts may need to be taken into the different reaction products and pore structures for geopolymers based on different compositions, as well as the interaction between geopolymeric matrix and aggregates (Yang et al. 2012b; Zhang et al. 2014).

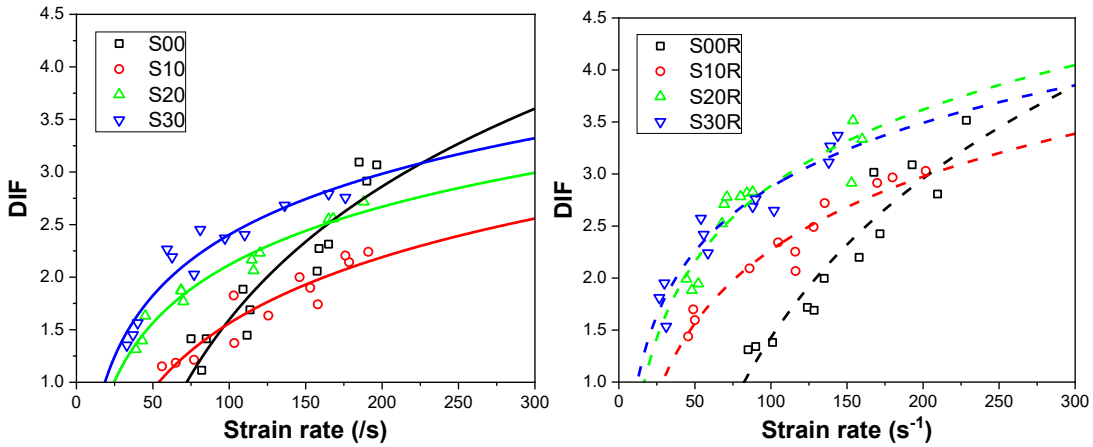

(a) GNAC (b) GRAC

Figure 5.14. Relationship between DIF and strain rate for geopolymeric concrete with different slag contents

For the quantification of material behavior at high strain rates and the easy prediction of structural response against impact loadings, different empirical formulae have been proposed to account for the DIF on the compressive strength of concrete. As a reference, several of them are here recalled as:

(a) The DIF formula suggested by the Comite Euro-International du Beton (CEB), which is recommended for OPC concrete:

$$\mathrm{DIF}_{\mathrm{CEB}}=\begin{cases}(\dot{\varepsilon}_c/\dot{\varepsilon}_{c0})^{0.014} & \dot{\varepsilon}_c \le 30\ \mathrm{s}^{-1}\\ 0.012(\dot{\varepsilon}_c/\dot{\varepsilon}_{c0})^{1/3} & \dot{\varepsilon}_c > 30\ \mathrm{s}^{-1}\end{cases} \tag{5.6}$$

(b) The DIF formula proposed by Luo et al. (2013), which is recommended for geopolymeric concrete:

$$\mathrm{DIF}_{\mathrm{Luo}}=\begin{cases}0.037\ln\dot{\varepsilon}_c+1.387 & \dot{\varepsilon}_c \le 28.89\ \mathrm{s}^{-1}\\ 0.481\ln\dot{\varepsilon}_c-0.119 & \dot{\varepsilon}_c > 28.89\ \mathrm{s}^{-1}\end{cases} \tag{5.7}$$

(c) The DIF formula proposed by Li & Xu (2009), which is recommended for geopolymeric concrete:

$$\mathrm{DIF}_{\mathrm{Li}}=\begin{cases}0.0158\log\dot{\varepsilon}_c+1.079 & 30 \le \dot{\varepsilon}_c \le 40.9\ \mathrm{s}^{-1}\\ 1.322\log\dot{\varepsilon}_c-1.025 & \dot{\varepsilon}_c > 40.9\ \mathrm{s}^{-1}\end{cases} \tag{5.8}$$

(d) The DIF formula proposed by Lu et al. (2014), which is recommended for OPC-based RAC:

$$\mathrm{DIF}_{\mathrm{Lu}}=\begin{cases}0.0071\log\dot{\varepsilon}_c+1.03 & \dot{\varepsilon}_c \le 19.95\ \mathrm{s}^{-1}\\ 1.00\log\dot{\varepsilon}_c-0.25 & \dot{\varepsilon}_c > 19.95\ \mathrm{s}^{-1}\end{cases} \tag{5.9}$$

Figure 5.15 presents these relationships against the experimental results. Comparison specifies that the above equations do not fit the evolution of the DIFs of geopolymeric concrete in this study very well. These relationships often underestimate the DIF of geopolymeric concrete, especially at high strain rates. Comparatively, the relatively small discrepancy could be observed for the DIF formula suggested by CEB. Among a large number of existing formulae on the relationship between the strain rate and DIF of concrete, most adopt a linear relationship between the DIF and the log10 of strain rate, which can be expressed below (Ross et al. 1995):

$$\mathrm{DIF}=A\log(\dot{\varepsilon}_c/\dot{\varepsilon}_{c0})+1 \tag{5.10}$$

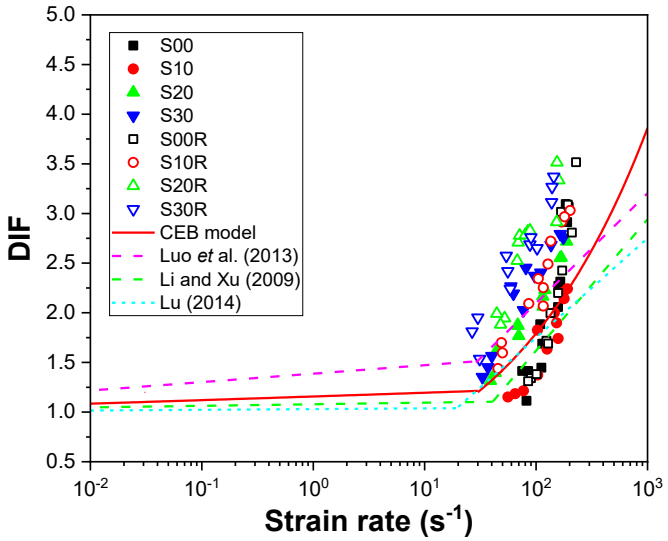

Figure 5.15. Comparison of DIF between the tests results and existing models

The fitted results of the DIF formulae based on Eq. (5.10) for the experimental results are given in Table 5.3, and also the corresponding curves have been plotted in Figure 5.12 and Figure 5.14. Meanwhile, the goodness of fitting R^2 for the fitting curve of the test data is evaluated, and the value close to 1 signifies that the fit curve can predict the test data with high accuracy. Therefore, these empirical formulae fit reasonably can be used to simulate the behavior of the studied geopolymeric concrete at high strain rates.

Table 5.3 Parameters for the fitted DIF relationship described by Eq. (5.10)

Parameters	S00	S10	S20	S30	S00R	S10R	S20R	S30R
A	4.21	2.19	1.84	1.92	5.07	2.34	2.43	2.05
$\dot{\varepsilon}_{c0}$	72.15	53.86	24.64	18.65	82.35	28.72	16.72	12.20
R^2	0.860	0.865	0.963	0.907	0.892	0.931	0.837	0.911

5.3.5 Energy absorption capacity

Based on the one-dimensional stress wave theory, the stress wave energy can be express as Eq. (5.11), which is calculated based on the strain signals of the incident, reflected, and transmitted stress waves during the test. According to the conservation of energy incorporated with ignoring the energy loss between the specimen and incident or transmitted bar, the energy absorption of the specimen can be defined as Eq. (5.12).

$$\begin{cases} W_I = AC_0E \cdot \int_0^t \varepsilon_I^2(\tau)d\tau \\ W_R = AC_0E \cdot \int_0^t \varepsilon_R^2(\tau)d\tau \\ W_T = AC_0E \cdot \int_0^t \varepsilon_T^2(\tau)d\tau \end{cases} \tag{5.11}$$

$$W_S = W_I - W_R - W_T \tag{5.12}$$

where W_S stands for the energy absorption by the specimen; W_I , W_R , and W_T represent the incident wave energy, reflected wave energy, and transmitted wave energy, respectively.

Figure 5.16 presents the relationship between the incident wave energy and energy absorption by the test specimens. It is obvious that the energy absorption by the specimen increases with incident wave energy. The increase in energy absorption with the increase of incident wave energy is caused by the generation of more cracks and fracture planes under high strain rate loading (Vegt et al. 2007). Also, the ratios of absorbed energy to incident energy are within the range from 0.2 to 0.45. This is consistent with the theoretical derivations by Lundberg (1976), that the ratio of absorbed energy to incident energy owns a maximum value of 0.5, and this value could be achieved only when the amplitude of the incident pulse is twice the specimen's yield stress. To get further insight into the energy dissipation ability of the test geopolymeric concrete, the specific energy absorption (E_v) is investigated, which is used for representing the energy absorption characteristic and can be expressed as Eq. (5.13).

$$E_v = \frac{W_S}{V} \tag{5.13}$$

where V is the volume of the specimen.

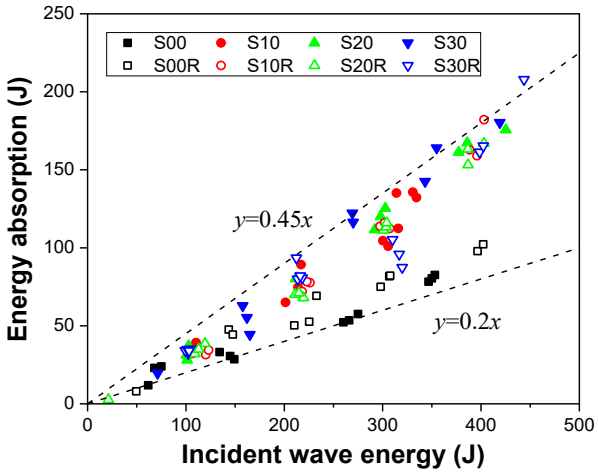

Figure 5.16. Relationship between incident wave energy and energy absorption for geopolymeric concrete

The relationship between the strain rate and the specific energy absorption of GNAC and GRAC are compared in Figure 5.17. The specific energy absorption exhibits a significant strain rate dependency. As the strain rate increases, the specific energy absorption of geopolymeric concrete enhances, while the enhancing rate decreases. Moreover, the specific energy absorption of GRAC is higher than that of GNAC, except for geopolymeric concrete based on neat fly ash. It has been reported that the specific energy absorption is associated with strength capacity and deformation behaviors (Lu et al. 2017). The replacement of RA has an insignificant influence on the dynamic compressive strength of geopolymeric concrete, while it could enhance the strain capacity, resulting in the more ductile behavior of GRAC, as shown in Figure 5.10. Besides, it has been reported that the aggregate with a relatively porous and loose structure could contribute to the enhanced energy absorption capacity for concrete (Ma et al. 2019).

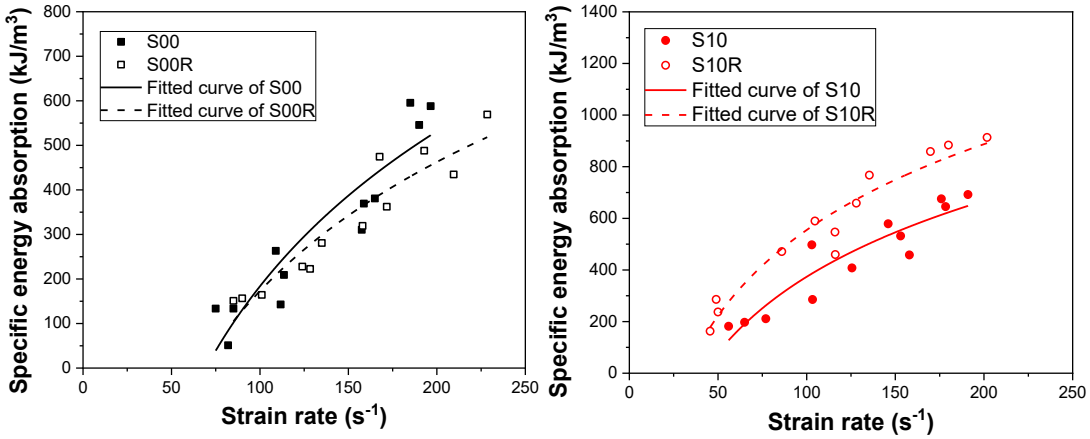

(a) Geopolymeric concrete without slag (b) Geopolymeric concrete with 10% slag

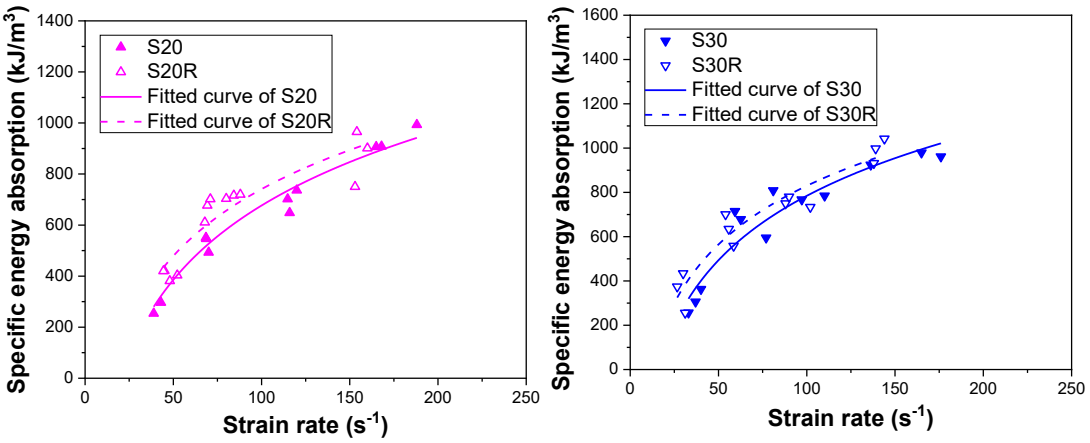

(c) Geopolymeric concrete with 20% slag (d) Geopolymeric concrete with 30% slag

Figure 5.17. Relationships between specific energy absorption and strain rate for GNAC and GRAC

The specific energy absorption of GNAC and GRAC under different slag contents are compared in Figure 5.18. The result indicates that the inclusion of slag effectively improves the specific energy absorption for both GNAC and GRAC under the impact, and the improvement is more significant at the higher content of slag. This is mainly attributed to the larger loading-carrying capacity of geopolymeric concrete after the slag incorporation. The relationship between the specific energy absorption and strain rate can be expressed as Eq. (5.14) (Lu et al. 2017). Based on the experimental results, the fitted results are given in Table 5.4, and also plotted in Figure 5.17 and Figure

5.18. It could be observed that the fitted relationships correlate well with the test results.

$$E_v = B \log \dot{\varepsilon}_c + C \tag{5.14}$$

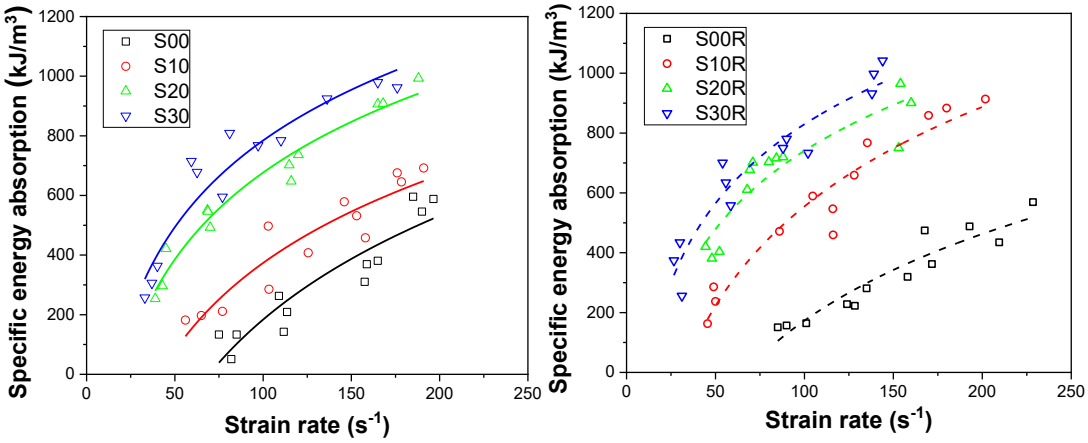

(a) GNAC (b) GRAC

Figure 5.18. Relationships between specific energy absorption and strain rate for geopolymeric concrete with different slag contents

Table 5.4 Parameters for the fitted relationship described by Eq. (5.14)

Parameter	S00	S10	S20	S30	S00R	S10R	S20R	S30R
B	1156	978	967	965	962	1105	870	879
C	-2128	-1582	-1258	-1147	-1751	-1655	-999	-928
R^2	0.860	0.865	0.963	0.907	0.892	0.931	0.837	0.911

5.4 Summary

(1) Under quasi-static compression, the replacement of RA decreased the compressive strength and elastic modulus of geopolymeric concrete; however, the incorporation of slag caused the reverse trend along with more brittle characteristics. All the geopolymeric concrete exhibited a similar failure process; however, the probability of crack development through aggregate was higher when using RA or incorporating higher slag content.

(2) The dynamic compressive strength of geopolymeric concrete and DIF increased with the increase of strain rates. At a certain strain rate, the dynamic compressive strengths exhibited no much difference between GNAC and GRAC; whereas, the

DIF increased after the RA replacement. Irrespective of the coarse aggregate types (i.e., NA or RA), the dynamic compressive strength of geopolymeric concrete and DIF both increased with the content of slag under a particular strain rate.

(3) The DIF of the geopolymeric concrete was found to increase approximately linearly with the log10 of the strain rate. The existing formulae for DIF show some discrepancies when comparing with the test results. The proposed empirical formulae accounting for the relationship between strength enhancement and strain rates have a good performance in predicting the test results.

(4) The ratios of energy absorption to the incident wave energy were in the range of 0.2 to 0.45. At a certain level of strain rate, the specific energy absorption of GRAC was higher than that of GNAC. Additionally, the energy absorption capacity was increased with the increase in the slag content. The specific energy absorption is proportional to the logarithm of the strain rate.

(5) Under dynamic compression, the failure modes of all GNAC and GRAC showed a similar pattern. At low strain rates, the specimens were broken into several large pieces, whereas at high strain rates, the specimens were ground into numerous small fragments. The high strain rate also results in more cracks propagating through the coarse aggregates.

CHAPTER 6: FAILURE PROCESS AND MECHANISM OF SUSTAINABLE GRAC

Existing studies have shown that cracking is the main cause of structural damage in concrete materials (Tasdemir et al. 1990). Crack generation and propagation is the dominant mechanism responsible for the nonlinear stress-strain response of concrete materials. Also, the crack behavior has a significant impact on concrete structure performance, including the loading carrying capacity, energy absorption capacity, ductility factor, and toughness (Faron & Rombach 2020; Zeng et al. 2020). Furthermore, the crack morphology significantly affects the transport properties of concrete materials, such as absorptivity, diffusivity, and permeability, which are strongly related to the concrete long-term durability (Dehghanpoor Abyaneh et al. 2014; Mengel et al. 2020; Picandet et al. 2001). All these suggest that effective estimation and prediction of the crack propagation in concrete can better evaluate or even enhance the stability and safety of concrete structures. Accordingly, comprehension of the crack behavior of GRAC is essential for its practical application and rational design.

In light of this demand, this chapter experimentally investigates the failure process of GRAC under static compression. GRAC specimens with different RA replacement ratios (i.e., 0, 25%, 50%, and 100%) were prepared and tested. Special attention is devoted to the crack evolution and failure mode of the specimens. Also, the displacement field and strain distribution over the specimen surfaces were monitored and analyzed by using the DIC technique.

6.1 Experimental program

6.1.1 Raw materials

The raw materials used in this study, including fine aggregate, coarse aggregate, fly ash, slag, and alkali activator, were in accordance with those in Chapter 4. Thus, the details for the raw materials could be found in Section 4.1.1.

6.1.2 Mix proportion

The mix proportions of geopolymeric concrete are given in Table 6.1, in which different RA replacement ratios (i.e., 0, 25%, 50%, and 100%) are considered. The ratio of fly ash/slag was adopted as 80/20. The activator solution to binder ratio and the sodium silicate solution to sodium hydroxide solution ratio were taken as 0.55 and 2.5, respectively, by mass.

Table 6.1 Mix proportion and compressive strength for geopolymeric concrete

Mixture	Replacement ratio	Mix proportion (unite weight: kg/m^3)						
		Fly ash	Slag	Na_2SiO_3	NaOH	Sand	NA	RA
NAC	0%	336	84	165	66	550	1220	0
RAC25	25%	336	84	165	66	550	915	305
RAC50	50%	336	84	165	66	550	610	610
RAC100	100%	336	84	165	66	550	0	1220

6.1.3 Specimen preparation

The concrete mixing process and curing regime were followed that reported in Chapter 3 (as shown in Section 3.1.3). Prismatic specimens with a dimension of 100×100×100 mm were cast and then were cut into sliced specimens with a dimension of 100×100×10 mm at the age of 28 days. The surfaces of sliced specimens were roughened by sandpaper, and then cleaned by using acetone to remove contaminants. Besides, reference cylinders with a dimension of Ø100×100 mm were manufactured for compressive strength, elastic modulus, and splitting tensile strength tests at 28 days to determine the mechanical properties of the concrete mixtures.

6.1.4 Test setup

The test arrangement is presented in Figure 6.1. The sliced specimen was subjected to uniaxial compression. A rigid electro-hydraulic servo testing machine was used to perform the compression test. The loading was controlled by the displacement pattern with a rate of 0.10 mm/min. During the entire loading procedure, a DIC system was used to track the deformation behavior over the specimen surface. The imaging system of the DIC system was mainly based on a camera with a resolution of 2560 × 2160 pixels (256

gray levels). The image capture frequency applied in this study was 1 Hz. After the test, the full-field displacement and strain over the surface of the specimens can be achieved from these captured images using a 2D DIC software package, Ncorr (Blaber et al. 2015). Moreover, a vertical strain gauge with a gauge length of 50 mm was placed on the opposite of the DIC detected surface to measure the axial strain, and meantime, to validate the accuracy of the DIC results.

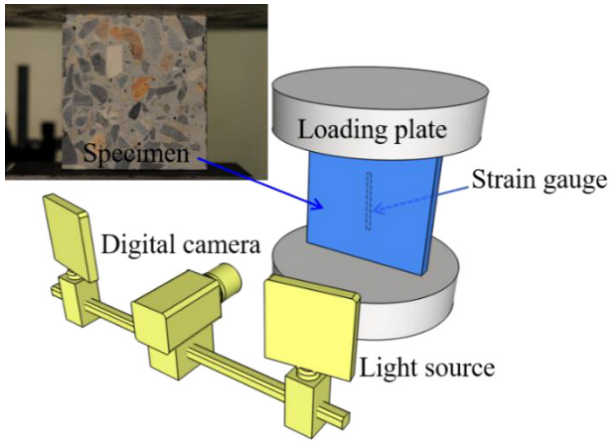

Figure 6.1. The loading and measure system

Besides, the tests for the compressive strength, elastic modulus, and splitting tensile strength were conducted on the reference specimens with a dimension of Ø100×100 mm, in accordance with ASTM C39-18 (Standard Test Method for Compressive Strength of Cylindrical Concrete Specimens), C469-14 (Static Modulus of Elasticity and Poisson's Ratio of Concrete in Compression), and C496-17 (Standard Test Method for Splitting Tensile Strength of Cylindrical Concrete Specimens), respectively. The reported test results were based on the three nominally identical specimens.

6.1.5 DIC technique

DIC is a non-interferometric optical technique for surface measurement (Peters & Ranson 1982). This method could track the full-field displacement and strain by comparing the digital images of an object's surface under the un-deformed (namely, the reference) state and the deformed (namely, the current) state. In addition to the relative ease of implementation and use, DIC allows for the deformation measurement at various length

scales from the nanoscale to even meters. Moreover, the achieved results can exhibit high accuracy and reliability. Owing to the above merits, DIC has been widely accepted and extensively employed in the investigation of material deformation and crack propagation in both academic research and real-world applications (Pan et al. 2009).

The schematic of the DIC is illustrated in Figure 6.2. The full-field deformation is obtained based on the displacements at the points of evenly spaced virtual grids. For tracking the movements of the grid points on the successive images, a series of square subsets with the grid points as the center are imposed, as shown in Figure 6.2(a). Subsequently, the tracking of subsets is performed by employing the normalized cross-correlation function, which is given by Eq. (6.1). The concept behind this is that the distribution of grey values in a subset from the deformed image corresponds to that of the same subset from the reference image.

$$C_{cc} = \frac{\sum_{(i,j)\in S}\left(f\left(\tilde{x}_{ref_i}, \tilde{y}_{ref_i}\right) - f_m\right)\left(g\left(\tilde{x}_{cur_i}, \tilde{y}_{cur_i}\right) - g_m\right)}{\sqrt{\sum_{(i,j)\in S}\left[f\left(\tilde{x}_{ref_i}, \tilde{y}_{ref_i}\right) - f_m\right]^2 \sum_{(i,j)\in S}\left[g\left(\tilde{x}_{cur_i}, \tilde{y}_{cur_i}\right) - g_m\right]^2}} \tag{6.1}$$

where C_{cc} is the correlation coefficient; S is a set which contains all the points within a certain subset; f and g are the reference and current image grayscale intensity functions, respectively; $\left(\tilde{x}_{ref_i}, \tilde{y}_{ref_i}\right)$ is the coordinate of a reference subset point; $\left(\tilde{x}_{cur_i}, \tilde{y}_{cur_i}\right)$ is the coordinate of a current subset point; f_m and g_m are the average image grayscale values for the reference and current subsets respectively.

Once the new location of the subset in the deformed images is identified, the displacement vector can be derived from calculating the difference in the position of the reference subset center $P(\mathrm{x}, \mathrm{y})$ and the corresponding subset center $P'(\mathrm{x}', \mathrm{y}')$ (as shown in Figure 6.2(b)). Afterward, the strain fields can be derived by smoothing and differentiating the displacement fields, as expressed by Eqs (6.2) to (6.4).

$$\varepsilon_{xx} = \frac{1}{2}\left(2\frac{\partial u}{\partial x} + \left(\frac{\partial u}{\partial x}\right)^2 + \left(\frac{\partial v}{\partial x}\right)^2\right) \tag{6.2}$$

$$\varepsilon_{xy} = \frac{1}{2}\left(\frac{\partial u}{\partial y} + \frac{\partial v}{\partial x} + \frac{\partial u \partial u}{\partial x \partial y} + \frac{\partial v \partial v}{\partial x \partial y}\right) \tag{6.3}$$

$$\varepsilon_{yy} = \frac{1}{2}\left(2\frac{\partial v}{\partial y} + \left(\frac{\partial u}{\partial y}\right)^2 + \left(\frac{\partial v}{\partial y}\right)^2\right) \tag{6.4}$$

where ε_{xx}, ε_{yy}, and ε_{xy} are, respectively, the longitudinal strain, transverse strain, and shear strain; u and v represents the displacement fields in x-axis and y-axis, respectively.

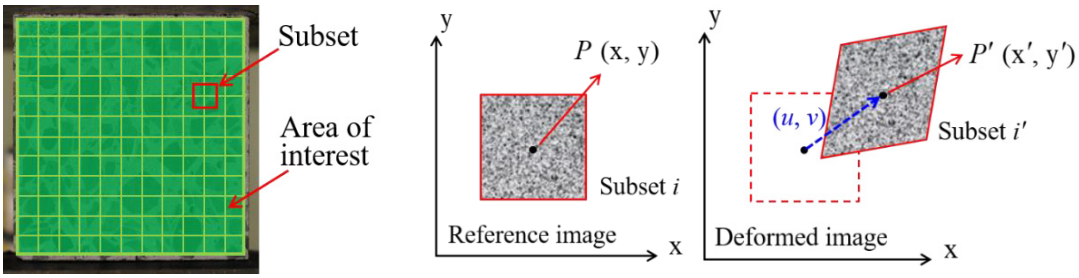

(a) Subsets in a reference image (b) A subset before deformation and after deformation

Figure 6.2. Schematic illustration of DIC method

6.2 Results and discussions

6.2.1 Mechanical properties

The test results of compressive strength, elastic modulus, and splitting tensile strength are given in Table 4.3. It could be observed that the mechanical properties were adversely affected by the replacement of NA by RA, and the effects were more significant as the content of RA rising. It was mainly due to the lower properties of RA compared with NA.

Table 6.2 Mechanical properties of geopolymeric concrete

Label	Compressive strength (MPa)	Elastic modulus (GPa)	Splitting tensile strength (MPa)
NAC	43.2 ± 2.28	21.63 ± 1.72	4.02 ± 0.24
RAC25	41.7 ± 1.91	17.90 ± 1.43	3.86 ± 0.27
RAC50	38.0 ± 0.96	15.78 ± 0.61	3.75 ± 0.06
RAC100	35.0 ± 1.27	13.91 ± 0.68	3.54 ± 0.14

6.2.2 Crack evolution and failure modes

The crack evolution, including the crack initiation, crack propagation, and final crack morphology, is presented in Figure 6.3. In the initial stage, the micro-cracks were hardly captured by naked eyes. While with the increase of the compressive stress, the micro-cracks propagated, connected, and developed into the macro cracks. In general, the macro cracks initiated in the ITZs between aggregate and geopolymeric matrix. This was attributed to that the local stress level was intensified around the aggregates because of the stiffness mismatch between the aggregate and geopolymeric matrix, and also, the ITZs possessed poorer properties in comparison with the geopolymeric matrix, existing as the weakest region in the concrete. In addition, the cracks usually nucleated around NA rather than around RA, as shown in Figure 6.6(a–c). It can be explained that as the RA had lower stiffness compared with the NA, there was higher compatibility between the RA and the surrounding geopolymeric matrix in terms of stiffness, and therefore the stress concentration around the aggregate could be relieved in the case of RA.

Subsequently, the cracking process entered into a stable development stage. Specifically, the cracks mainly propagated along the aggregate surfaces or the narrow paths in the geopolymeric matrix. Also, the cracks angled less than 10º from the loading direction. As a result, a crack propagated throughout the entire cross-section and resulted in that the specimen lost the integrity. Afterward, additional cracks abruptly developed in other regions of the specimen, and a crack network was formed over the whole specimen.

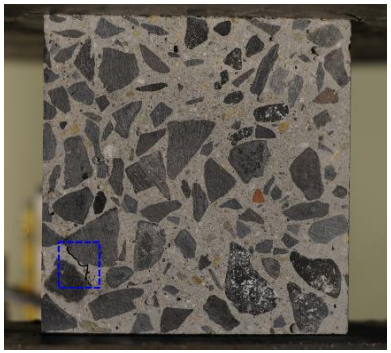

Crack initiation

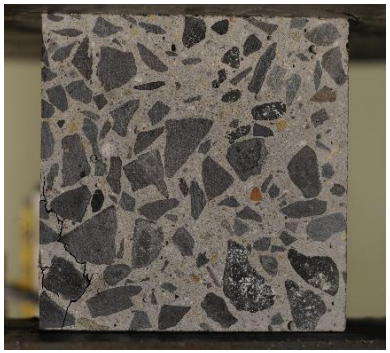

Crack propagation

Failure pattern

(a) NAC

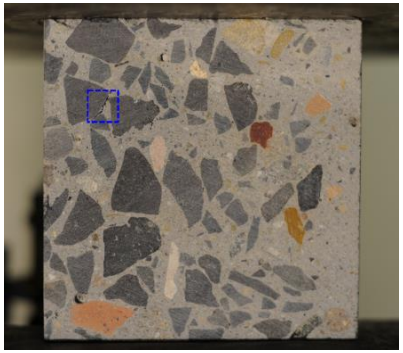

Crack initiation

Crack propagation

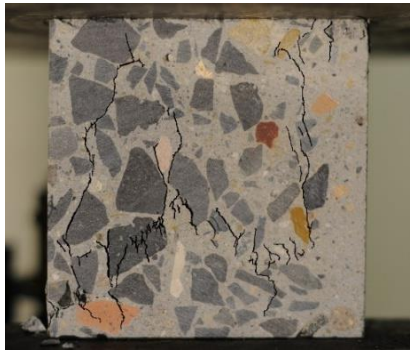

Failure pattern

(b) RAC25

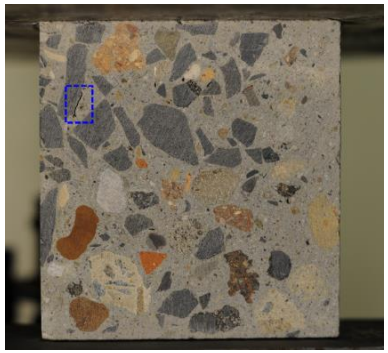

Crack initiation

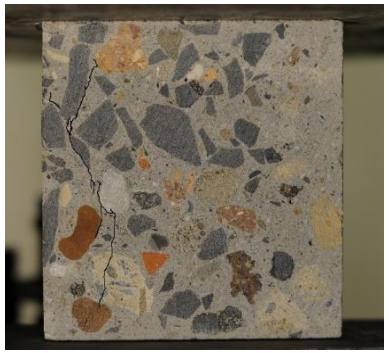

Crack propagation

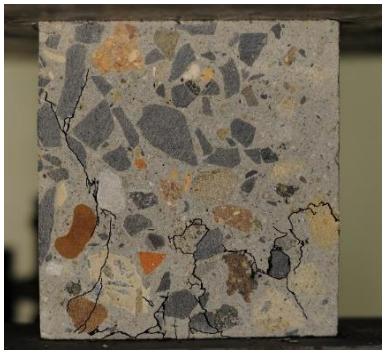

Failure pattern

(c) RAC50

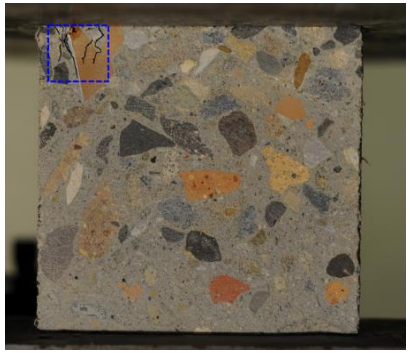

Crack initiation

Crack propagation

Failure pattern

(d) RAC100

Figure 6.3. Crack patterns of test specimens

From the final crack patterns of different specimens, it could be found that most of the cracks propagated around the aggregate, and only a few cracks propagated through the aggregates and resulted in the fractured aggregates. A careful inspection also shows that the fractured NA usually had a flaky or elongated shape, while the fractured RA had not only a flaky or elongated shape but also a rounded and less angular shape. In other words, it was more frequent for RA that cracks passed through the aggregate, in comparison with NA. This was due, mainly, not only to the weaker strength of RA, but also to the relatively good bonding strength between RA and geopolymeric matrix for the relatively high surface porosity and roughness of RA (Khedmati et al. 2019; Liu et al. 2019d).

6.2.3 Stress-strain curves

Table 6.3 gives the mechanical characteristics of the test sliced specimens, including the average and deviation values of the peak stress and peak strain. Although the coefficients of variation are relatively high, up to 15%, such variability of data is acceptable because of the high intrinsic randomness of sliced specimens and the complexity of concrete materials (Huang et al. 2019c). As shown in Table 6.3, the RA replacement decreases the peak stress but increases the peak strain, and the effects are more significant as the increment of the RA replacement ratio.

Table 6.3 Mechanical characteristics of test specimens

Specimen	Peak stress			Peak strain		
	Average value (MPa)	Standard deviation (MPa)	Coefficient of variation (%)	Average value (%)	Standard deviation (%)	Coefficient of variation (%)
NAC	45.3	4.94	10.9	0.0225	0.0032	14.2
RAC25	41.8	5.35	12.8	0.0247	0.0031	12.6
RAC50	35.6	4.68	13.2	0.0276	0.0030	10.9
RAC100	33.6	5.01	14.9	0.0318	0.0041	12.9

Typical stress-strain curves for test specimens are presented in Figure 6.4. It could be observed that the shape of the stress-strain curve is influenced by the RA replacement. Specifically, with the increase of the RA replacement ratio, the ascending branch of the curve exhibits a declined slope at the initial stage but a more prolonged inelastic region

in the later stage. On the other hand, the descending branch of the curve is more flatten for the specimens with higher RA replacement ratios. These observations agree well with the results reported in the previous studies (Belén et al. 2011; Kathirvel & Kaliyaperumal 2016; Tang et al. 2019b), indicating that the incorporation of RA could decrease the brittleness of concrete.

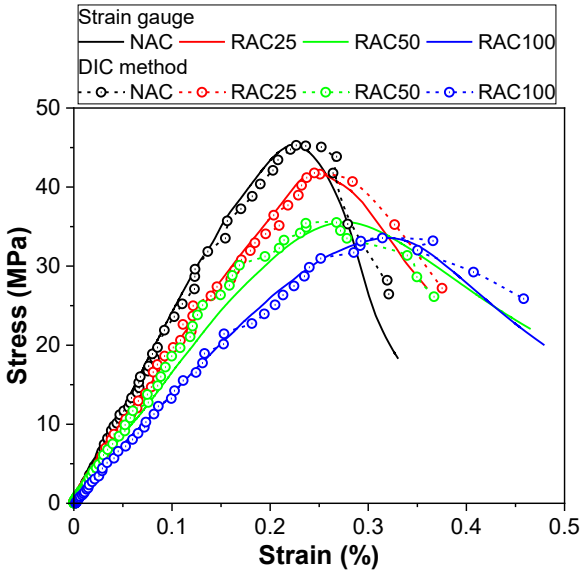

Figure 6.4. Typical stress-strain curves of test specimens

As shown in Figure 6.4, the strain result obtained from the DIC system is also compared with that based on the strain gauge. The strain result obtained from the DIC system was calculated from the average of the strain values in the mid-height region of the specimen. Apparently, the evolution of strains measured from the DIC system and the strain gauge shows a reasonable consistency with only a slight difference. The minor difference could be attributed to that the specimen had nonuniform deformation, and the measured strains by different methods (i.e., DIC and strain gauges) were from the different regions of specimens. Besides, the error in the DIC system was also related to the difference. For instance, the illumination condition during the test, the setting of calculation parameters, and the implementation of correlation algorithms all had influences on the accuracy of the DIC results (Pan et al. 2009).

The lateral-axial strain curves of test specimens are presented in Figure 6.5, which are obtained from the DIC method. Initially, the axial-lateral strain curves follow a linear relationship. The axial strain is caused by the vertical compression of the specimen, while the lateral strain is introduced due to the lateral dilation of the specimen. When the axial strain reaches about 60–80% of the peak strain, the axial-lateral strain curve exhibits a sharp increase in the slope or a significant increase in the lateral strain, which is due to the unrestrained microcrack propagation.

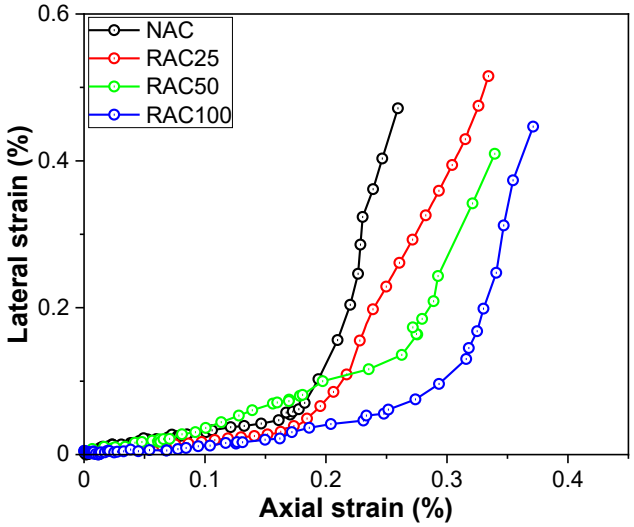

Figure 6.5. Axial-lateral strain curves of test specimens

6.2.4 Displacement distribution

Figure 6.6 presents the images of the displacement vector field for the test specimens at four loading stages (i.e., 40%, 80%, and 100% of peak load in pre-peak range, as well as, 80% of peak load in post-peak range). At the initial loading stage, the displacement vectors were mainly along the loading direction. While, the displacement vectors at the region near the vertical edges showed some horizontal components, indicating the lateral expansion of the specimen. This was due to the Poisson effect, in which the material tends to expand in directions perpendicular to the direction of compression. Also, it should be noted that the variation of the displacement vectors, in the aspects of both direction and magnitude, was relatively moderate between the adjacent regions.

With the increase of loading, the magnitude of the displacement vectors increased, resulting in the increased compression in the direction of loading and increased expansion in the direction perpendicular to loading. It could also be observed that the displacement vectors within some regions appeared significant inconsistencies. That is to say, there was a dramatic alteration in terms of the direction or magnitude between the displacement vectors within these regions. Moreover, these regions are consistent with the crack network, as presented in Figure 6.3. Afterward, the part, from the above-mentioned region to the near edge, showed a great horizontal displacement, indicating that this part was experiencing a split from the specimen due to the cracks propagating throughout the entire cross-section.

By comparing the results between the specimens with different RA replacement ratios, there are some differences that could be detected. At a given load stage, the specimens with higher RA replacement ratios generally had a higher magnitude for the displacement vectors. It means that the specimens with higher RA replacement ratios showed higher degrees of axial compression and lateral expansion. This was mainly attributed to the decreased elastic modulus of specimens after the RA replacement, which also has been presented in Table 6.2. On the other hand, the differences or variations between the displacement vectors within the crack regions were generally smaller for the specimens with higher RA replacement ratios. This, to some degree, indicates the relatively moderate failure process for the specimens after the RA replacement.

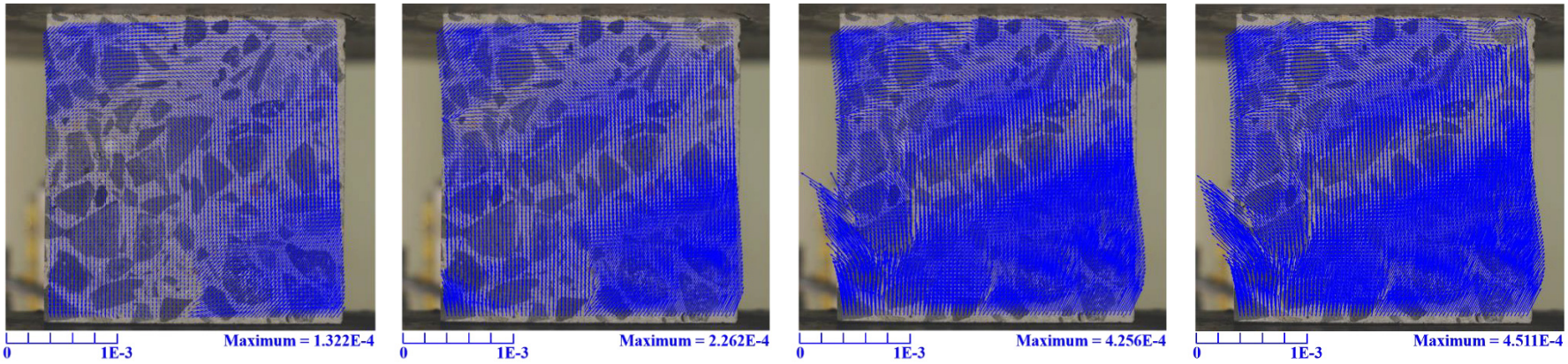

40% pre-peak 80% pre-peak peak 80% post-peak

(a) NAC

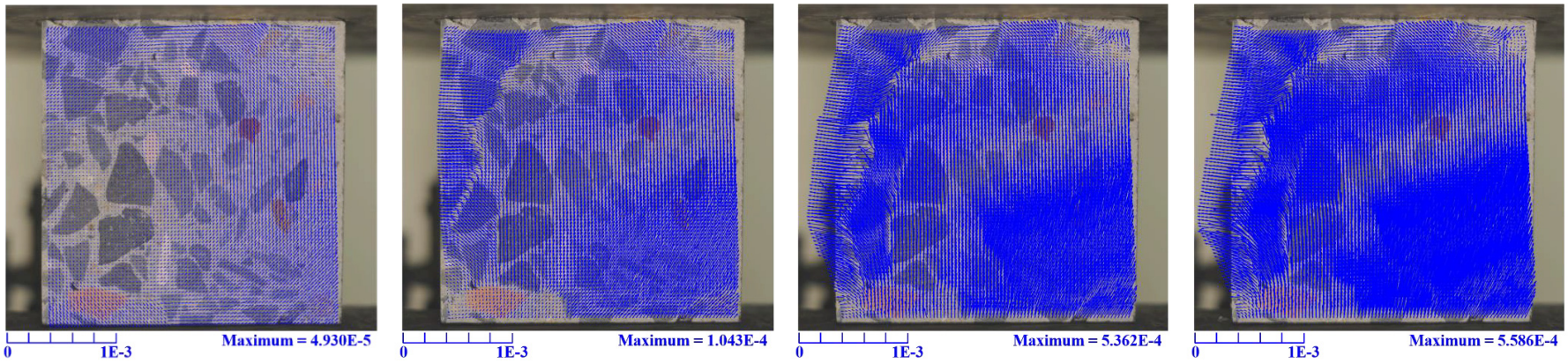

40% pre-peak 80% pre-peak peak 80% post-peak

(b) RAC25

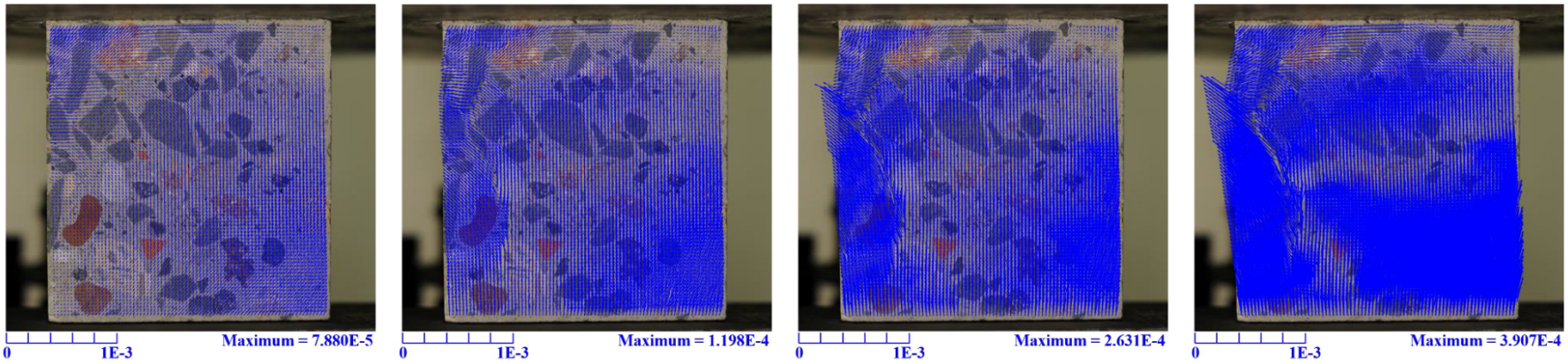

40% pre-peak 80% pre-peak peak 80% post-peak

(c) RAC50

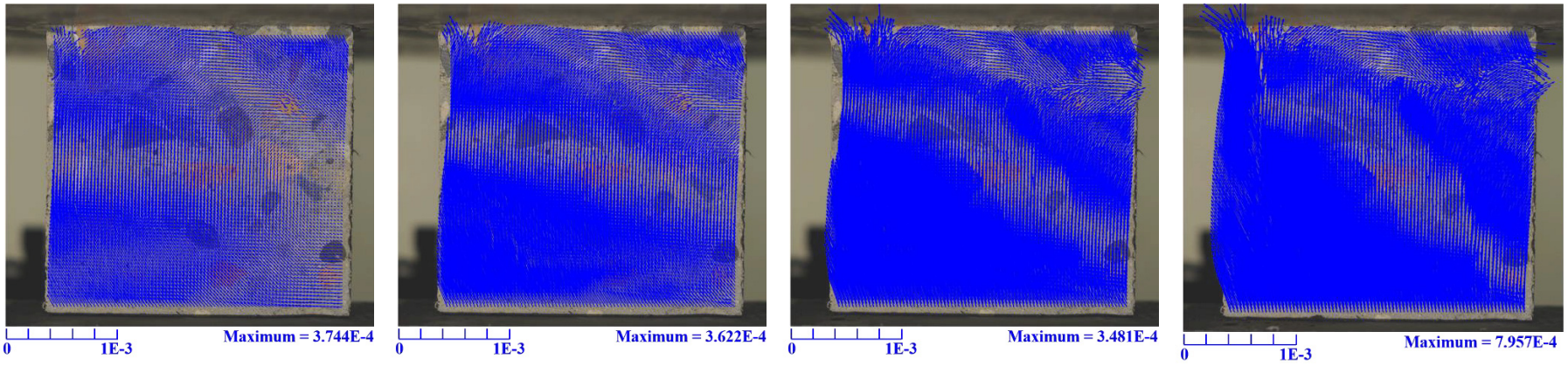

40% pre-peak 80% pre-peak peak 80% post-peak

(d) RAC100

Figure 6.6. Displacement vector fields image of test specimens (unit = m)

6.2.5 Strain distribution

Based on the strains (i.e., ε_{xx}, ε_{yy}, and ε_{xy}) obtained by the DIC system, the maximum principal strain ($\varepsilon_{\max}$), minimum principal strain ($\varepsilon_{\min}$), and maximum shear strain ($\gamma_{\max}$) can be calculated with the following equations:

$$\varepsilon_{\max} = \frac{\varepsilon_{xx} + \varepsilon_{yy}}{2} + \sqrt{\left(\frac{\varepsilon_{xx} - \varepsilon_{yy}}{2}\right)^2 + \left(\varepsilon_{xy}\right)^2} \tag{6.5}$$

$$\varepsilon_{\min} = \frac{\varepsilon_{xx} + \varepsilon_{yy}}{2} - \sqrt{\left(\frac{\varepsilon_{xx} - \varepsilon_{yy}}{2}\right)^2 + \left(\varepsilon_{xy}\right)^2} \tag{6.6}$$

$$\gamma_{\max} = \sqrt{\left(\frac{\varepsilon_{xx} - \varepsilon_{yy}}{2}\right)^2 + \left(\varepsilon_{xy}\right)^2} \tag{6.7}$$

The fields of maximum principal strain, minimum principal strain, and maximum shear strain at four loading stags (i.e., 40%, 80%, and 100% of peak load in pre-peak range, as well as, 80% of peak load in post-peak range) are presented in Figure 6.7 to Figure 6.10. For the maximum principal strain maps, the color scale bar, having a wide range between 0.04 in tension (indicated by red in the scale) and 0.005 in compression (indicated by blue in the scale), was used. For the minimum principal strain maps, the color scale bar, having a wide range between 0.005 in tension (indicated by blue in the scale) and 0.03 in compression (indicated by red in the scale), was adopted. For the maximum shear strain maps, the color scale bar, having a wide range between -0.005 (indicated by blue in the scale) and 0.03 (indicated by red in the scale), was adopted. Also, the blank area in the strain maps represents that the strain value in that area is over the range of the corresponding scale bar.

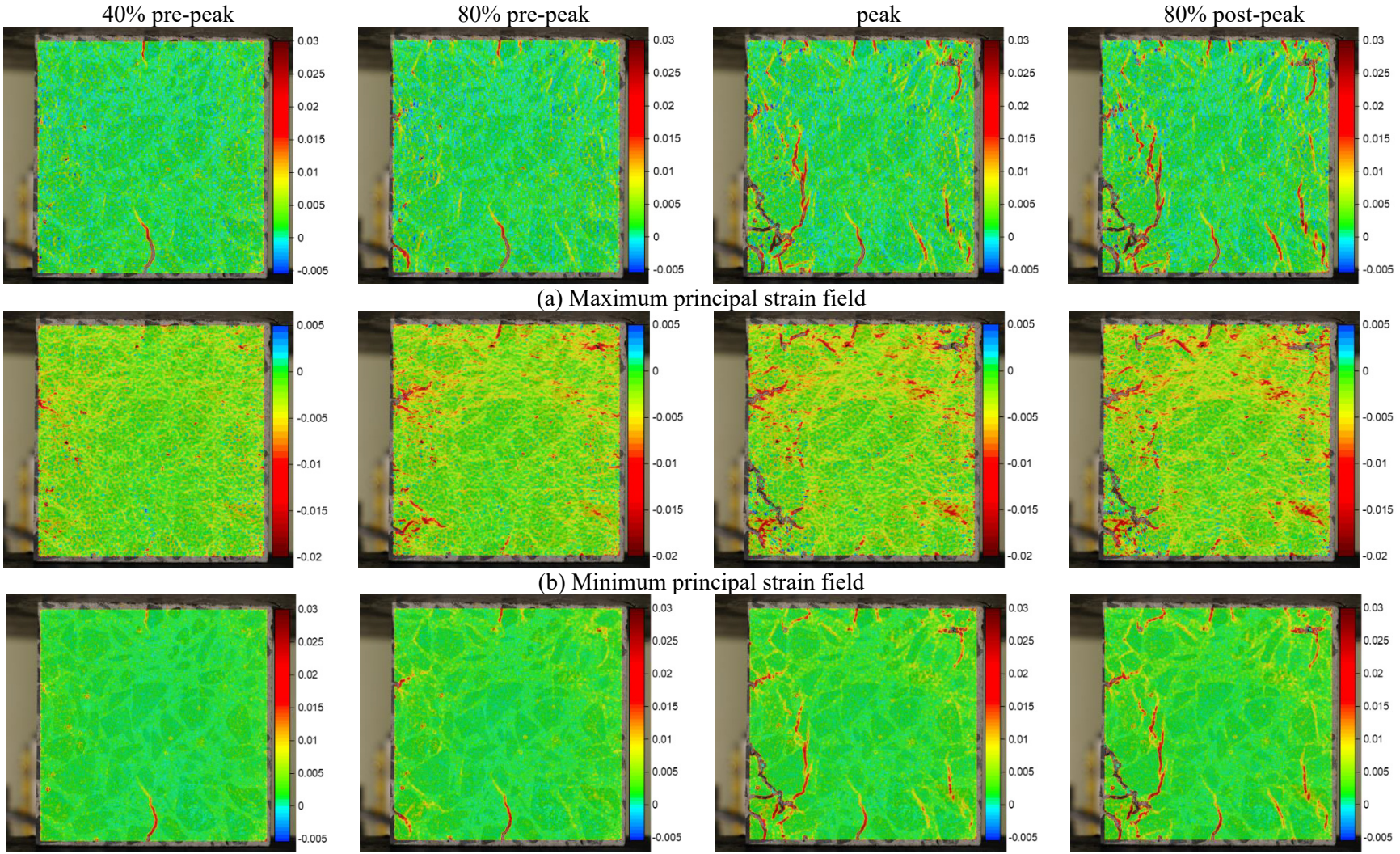

(a) Maximum principal strain field

(b) Minimum principal strain field

(c) Maximum shear strain field

Figure 6.7. Strain distribution of specimen NAC

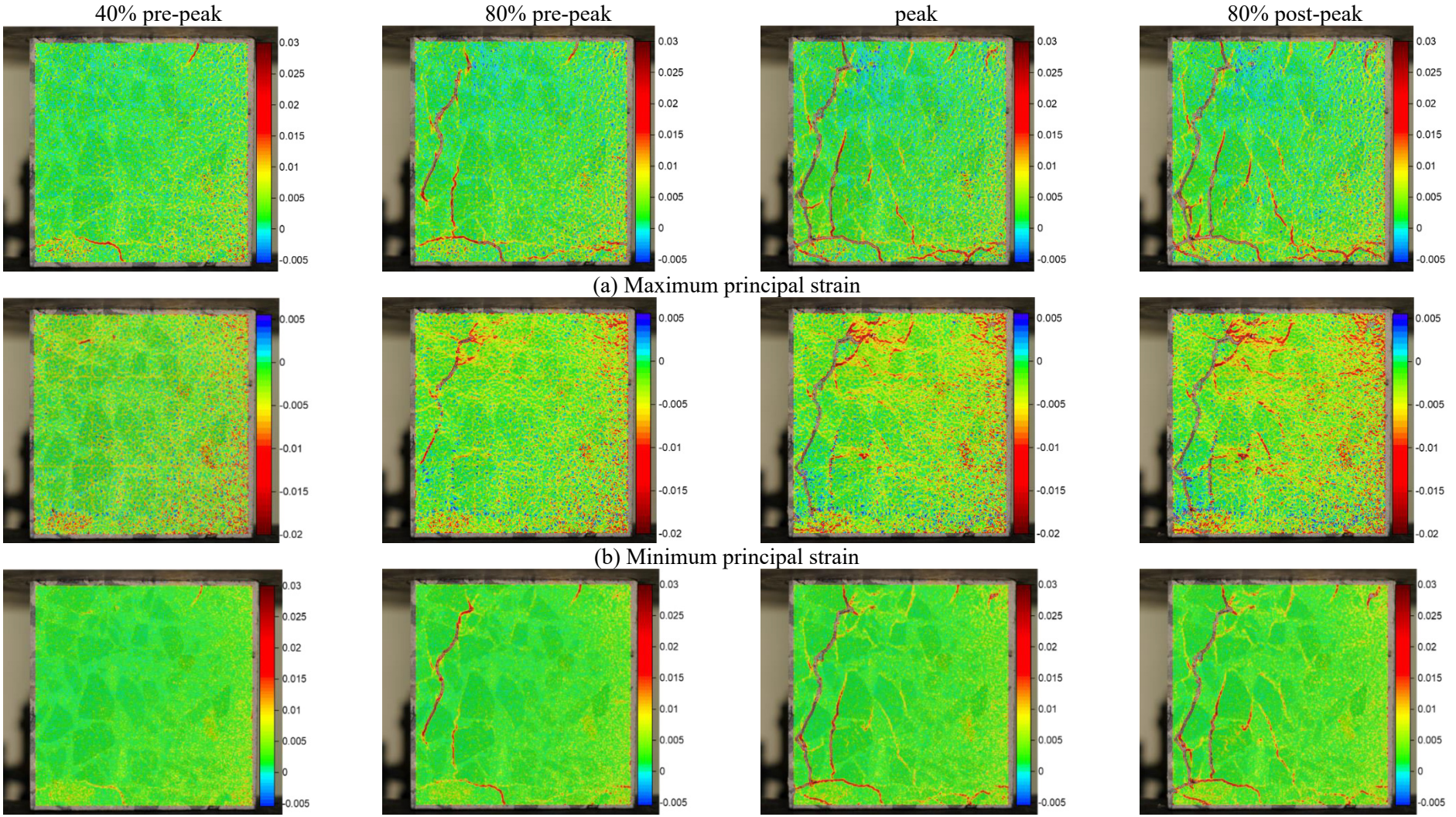

(a) Maximum principal strain

(b) Minimum principal strain

(c) Maximum shear strain field

Figure 6.8. Strain distribution of specimen RAC25

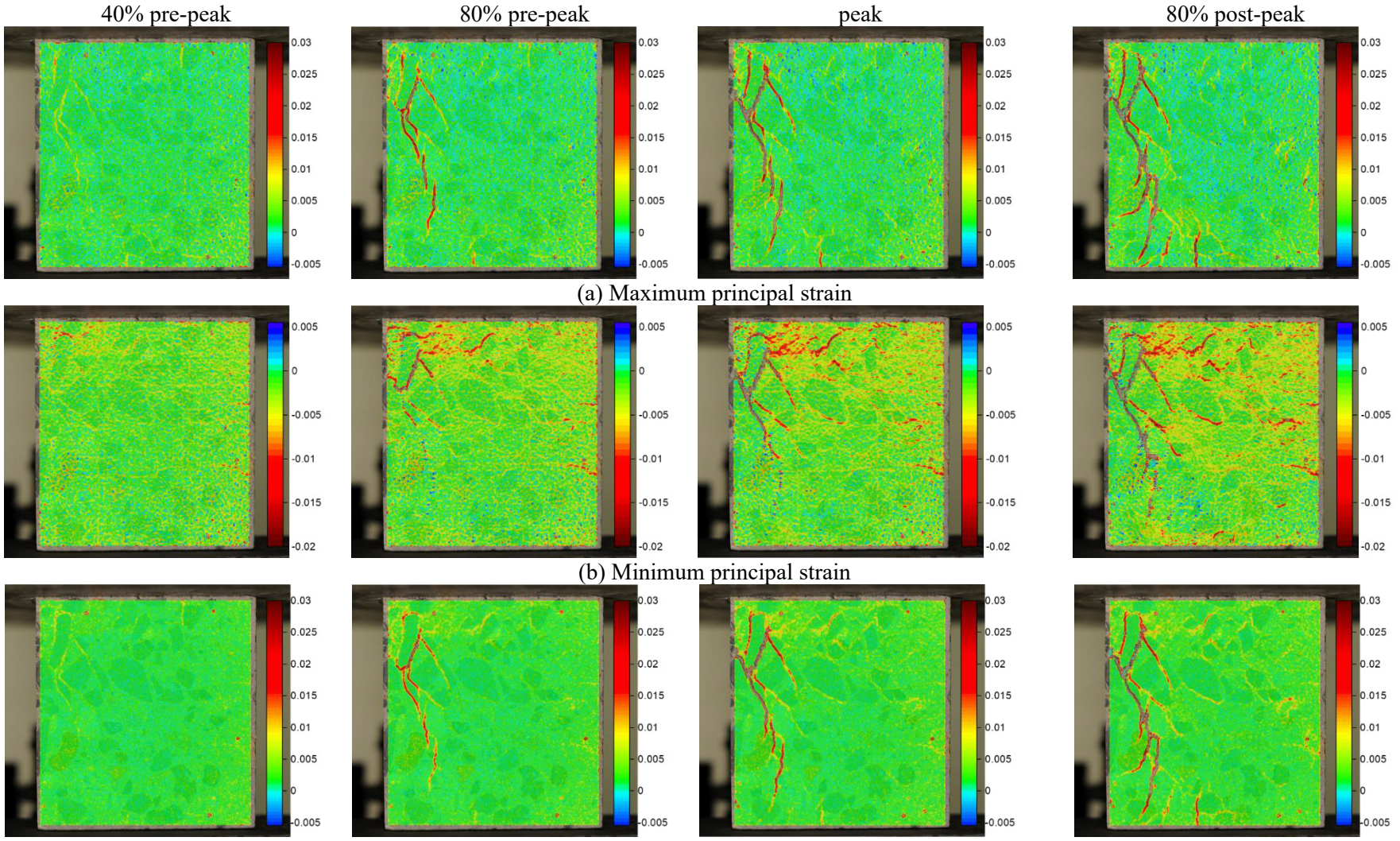

(a) Maximum principal strain

(b) Minimum principal strain

(c) Maximum shear strain field

Figure 6.9. Strain distribution of specimen RAC50

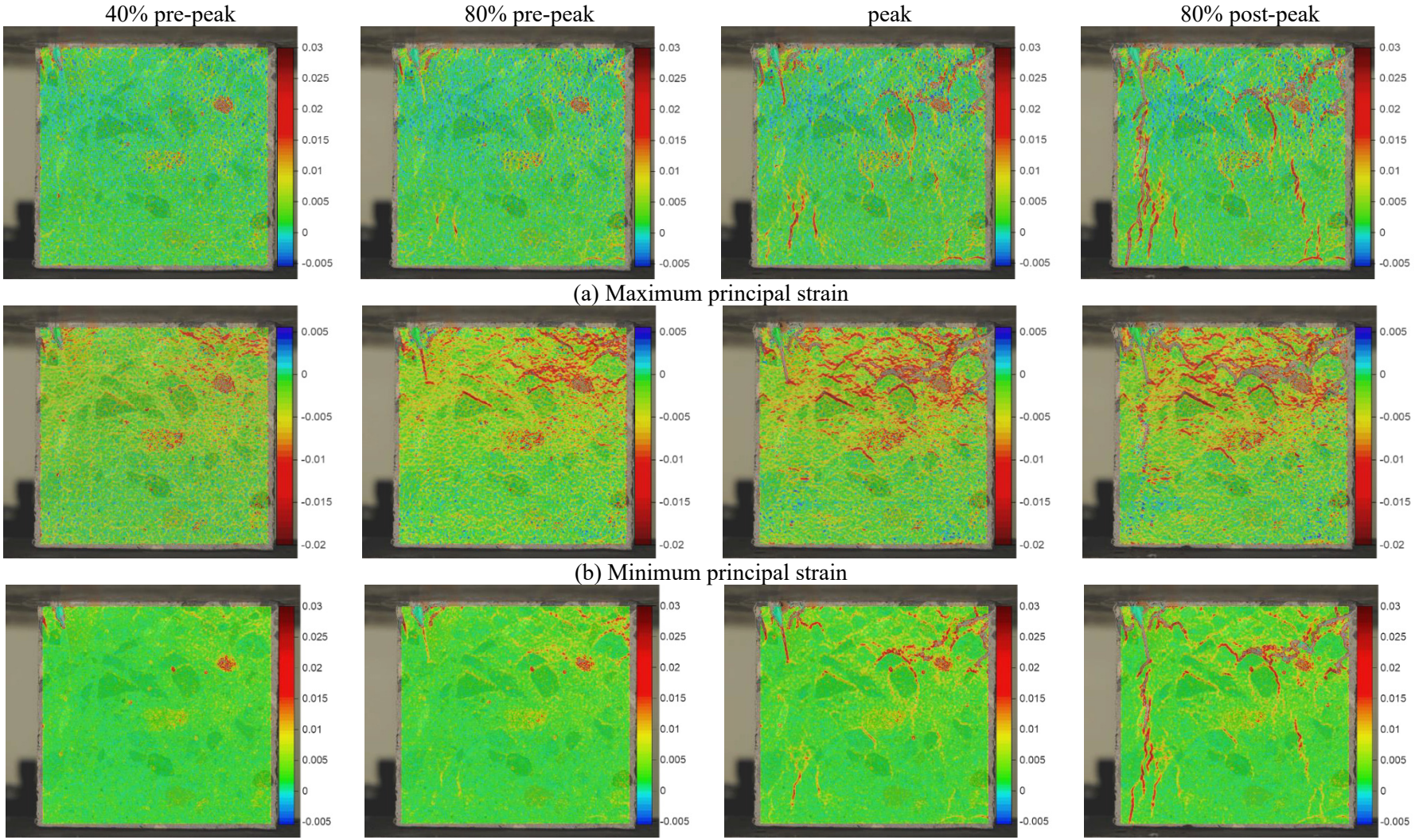

(a) Maximum principal strain

(b) Minimum principal strain

(c) Maximum shear strain field

Figure 6.10. Strain distribution of specimen RAC100

Obviously, the strain of the specimens distributed non-uniformly, even at the initial stage of loading. It was mainly attributed to the inhomogeneous feature of concrete material, including the different mechanical properties, especially the stiffness and hardness, between the aggregates, geopolymeric matrix, and ITZs, as well as, the asymmetrical geometry of these components. An attentive observation also shows that the magnitude of the strain in the ITZs was higher, existing as a strain concentration region. Specifically, for the fields of maximum principal strain and maximum shear strain, the strain concentration mainly occurred at the lateral side of the aggregate. Several previous studies have explained that large tensile and shear stresses develop at the lateral interface, as a result of the large difference in the stiffness between the aggregate and the matrix (Li & Joan 1990; Xiao et al. 2012c). Considering the weak bonding between aggregate and geopolymeric matrix, the stress concentration, therefore, can easily cause the interfacial crack. While for the field of minimum principal strain, the strain concentration mainly occurred at the interface on the top and below the aggregates, which agrees well with the results of an existing study on the crack phenomenology by using the elastic solution (Stroeven). Additionally, these places with minimum principal strain concentration correspond to the regions where local compressive crushing occurs in the porous ITZ regions (Bongers & Rutten 1998).

With the increase of the global strain due to the increasing load, the strain magnitude in the previously observed strain concentration region experienced a considerable increase. Also, the regions with strain concentration expanded or extended into the vicinity of the geopolymeric matrix and were lined up in the direction of loading. But the extension of the strain concentration region stopped when it met the aggregate particle, and then propagated around the aggregate at the tensile or shear side in the fields of maximum principal strain and maximum shear strain, or around the aggregate at the compression side in the field of maximum shear strain. But there were some exceptions that could be observed in the specimens with RA. Specifically, the strain concentration occurred in the RA region after the extension of the strain concentration met the aggregate particle, which is evident in Figure 6.10. That is to say, the strain concentration could be observed in the

region of RA, which was hard to be found in NA. It shows an agreement with the trends previously observed in the result of crack evolution.

In the post-peak regime, more strain concentration regions occurred throughout the entire specimen. Also, the strain concentration regions in the fields of maximum principal strain, minimum principal strain, and maximum shear strain had a large number of overlapping areas. In other words, the failure for shear and tension and the compressive crushing were joint together and then formed the overall failure surface (Bongers & Rutten 1998).

By comparing the strain distributions in Figure 6.7 to Figure 6.10 and the corresponding crack patterns presented in Figure 6.3, it could be found that the location of the strain concentration region, especially in the maximum principal strain field and maximum shear strain field, is closely consistent with that of the observed macro cracks. It, however, should be noted that the macro cracks that can be detected by naked eyes occurred only under a relatively high level of stress. This indicates that the initiation of micro-cracks that are invisible to naked eyes could be effectively identified by the DIC system. Therefore, the DIC system could provide real-time early warning of micro-damage for the engineering structure and enable the carrying out of special preventive measures.

6.2.6 Failure curve

To better illustrate the variation in the strain distribution of the test specimens throughout the whole process, the strain distribution in statistics is analyzed. Figure 6.11 presents typical statistic distributions of the strain value in the various strain fields under different stress stages. Apparently, the strains vary within a certain range, indicating the uneven strain distribution. Under the low stress level, there is a peak could be found for each strain statistic distribution curve. In other words, most of the strain values cluster around the strain value of the peak, and the probabilities for the strain values further away from the strain value of the peak off in both directions. However, the increase of the global stress shifts the peak location toward the direction in which the absolute strain value increases. For instance, the peak location of the maximum principal strain distribution moves right on the strain-axis as the global stress increases. Besides, with the increase of

global stress, the strain distribution is more spread out, which results in the lower count magnitude of the peak point, and higher count magnitude of the nearby strain values. It means the strain distribution is more non-uniformed under the higher stress level.

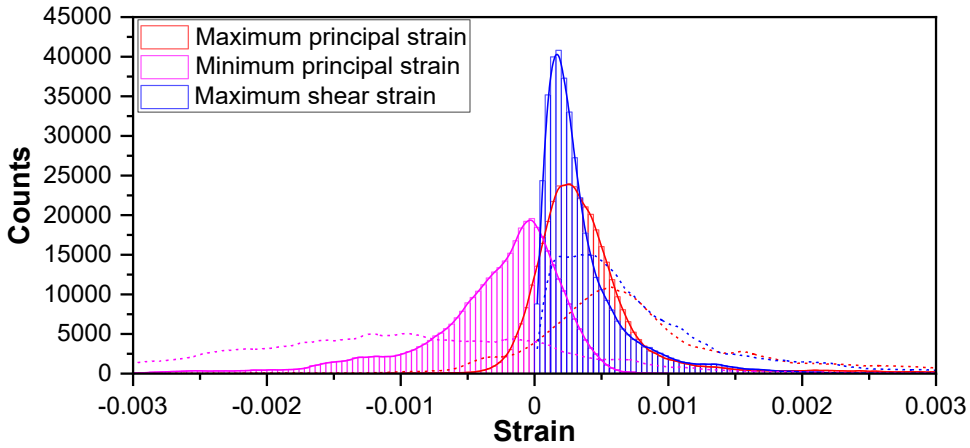

Figure 6.11. Statistic distribution of the strain fields (based on the results of RAC25. Solid line is under 40% pre-peak stress, while the dashed line is under peak stress)

Based on the existing studies on the fracture properties of geopolymeric matrix, the compressive strain, tensile strain, and shear strain at failure can be taken as 0.45%, 0.02%, and 0.02% (Ding et al. 2018a; Ding et al. 2018b; Wan et al. 2020). It is assumed that the region or subset experiences compression failure, tensile failure, and shear failure respectively when its minimum principal strain meets the ultimate compressive strain, its maximum principal strain meets the ultimate tensile strain, and its maximum shear strain meets the ultimate shear strain. Figure 6.12 shows the compression, tension, and shear failure curves, which are represented by the percentage of the area of regions experience the corresponding failure to the whole measured area. It should be noted that there are some regions that experience multiple failures at the same time.

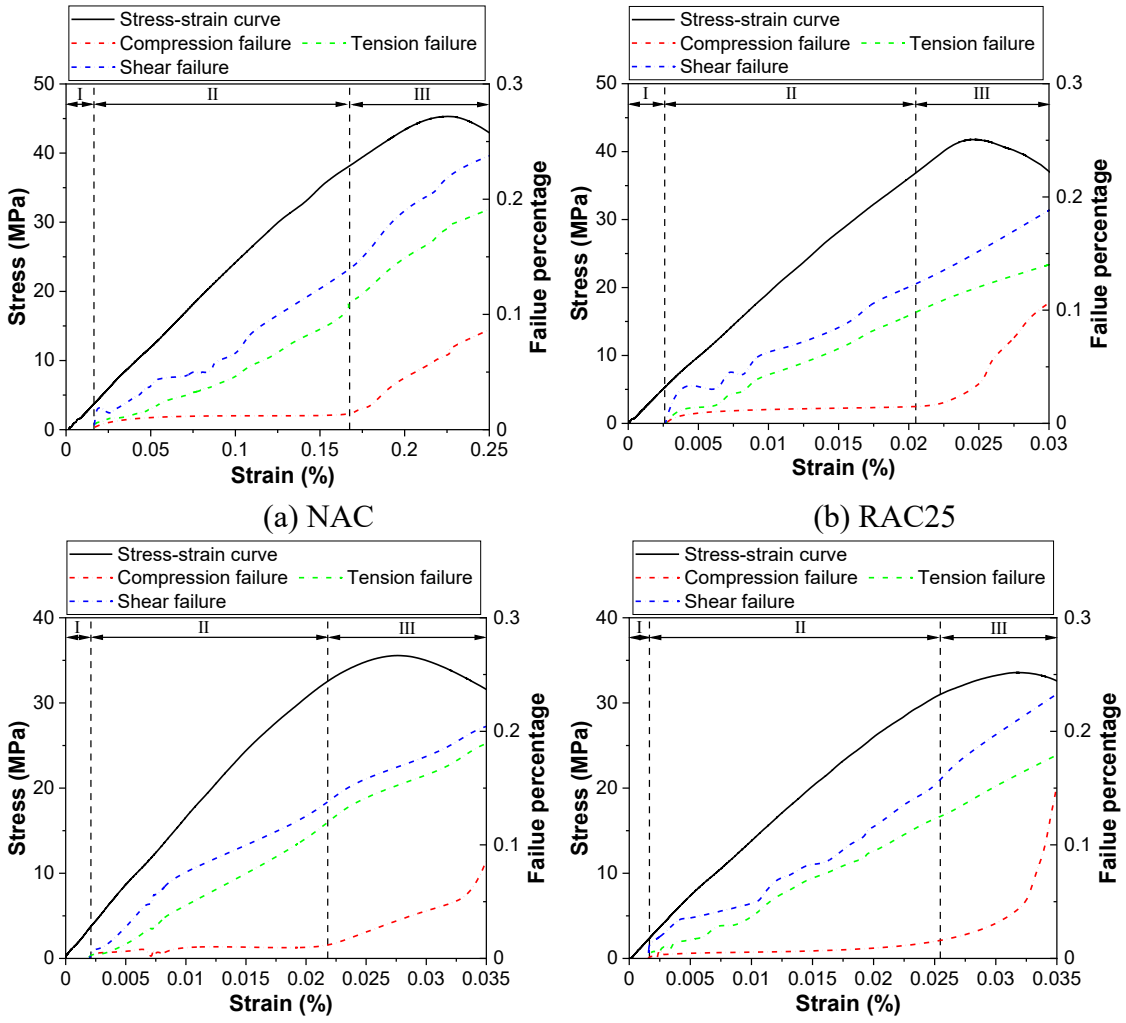

Figure 6.12. Failure curves of the test specimens

It can be seen that the failure curves of all the test specimens demonstrate high similarity and can be classified into three stages. In stage I, no failure is produced because the global strain is very limited. In Stage II, the failure percentages due to compression, tension, and shear increase continuously. The previous studies have explained that this failure stage is mainly attributed to the contact surface failure between the geopolymeric matrix and the aggregate (Bongers & Rutten 1998; Sun et al. 2019). During this period, the tension or shear microcracks or compression crushing appears in the ITZ due to the weak property of the contact and the stress intensification in this region. After this period, the failure percentages for shear failure and tension failure increase with the increment of global strain because the microcracks begin to extend and also appears inside the geopolymeric

matrix. However, there is only a slight increase in compression failure as the further compressive crushing of ITZs is insignificant. In Stage III, the specimens undergo rapid destruction, exhibiting an increase in all the failure percentages. Specifically, the failure percentages for shear failure and tension failure keep rising with a similar growth rate to the previous stage. As for the compression failure, there is a noticeable increase in this stage, which is mainly due to that some regions lose the loading capacity completely and then experience large deformation and high strain.

6.3 Summary

(1) The RA replacement adversely affected geopolymeric concrete's mechanical properties, including the compressive strength, elastic modulus, and splitting tensile strength. In addition, these properties declined with the increment of the RA substitution ratios.

(2) For all the specimens, cracks mainly initiated near the ITZs, and usually nucleated around NA rather than RA. As observed from the final crack patterns, it was more frequent for the RA that cracks passed through the aggregate particles, in comparison with the NA.

(3) DIC method can accurately determine the full-field displacement and strain distribution of the test specimens under various stages of stress. Therefore, the DIC technic has the potential to replace the conventional measurement setup and provide rich information to help understand the deformation behavior.

(4) At a given global stress level, the specimens with higher RA replacement ratios generally had a higher magnitude for the displacement vectors. Additionally, the differences between the displacement vectors within the crack regions are smaller for the specimens with higher RA replacement ratios.

(5) The location of the strain concentration region, especially in the maximum principal strain field and maximum shear strain field, is closely consistent with that of the observed micro-cracks. Hence, the DIC technic could effectively provide a warning for the initiation of micro-damage and accurately determine the location and degree of micro-damage.

CHAPTER 7: MECHANICAL PERFORMANCE OF CFRP-CONFINED SUSTAINABLE GRAC UNDER MONOTONIC COMPRESSION

This chapter experimentally investigates the axial compressive behaviors of CFRP-confined GRAC in terms of the stress-strain relationship, the dilation behavior, and the ultimate condition. Moreover, the feasibility of existing stress-strain models to CFRP-confined GRAC was examined by using the database collected in this work

7.1 Experimental program

7.1.1 Specimen design

Forty-eight CFRP-confined specimens were manufactured and tested, which covered two RA replacement ratios (i.e., 0% and 100%), four slag contents (i.e., 0, 10%, 20%, and 30%), and three thickness of CFRP jackets (i.e., 1, 2 and 3 layers). In addition, twenty-four unconfined control specimens with the same material and geometric properties as the CFRP-confined specimens were tested to establish the test-day unconfined concrete strengths of the specimens. The specimen details are given in Table 7.1. All specimens had a nominal diameter of 100 mm (diameter of the concrete core) and a height of 200 mm. The name of each specimen starts with the letter S, followed by an Arabic numeral to represent the slag content in the binder (0%, 10%, 20%, and 30%). If there is letter R followed, it is suggested that the concrete is based on RAC. Otherwise, the concrete is based on NAC. A subsequent letter-number combination is used for the CFRP-confined specimens to indicate the number of the layer of CFRP jackets (1, 2, or 3 layers). Finally, an Arabic numeral is used to differentiate nominally identical specimens. For instance, the specimen of S10R-C2-1 denotes the first specimen of the two specimens of GRAC with 10% slag confined by a two-ply CFRP jacket.

Table 7.1 Details of test specimens

Series	Specimen	Slag content	Aggregate type	CFRP layer
1	S00-1,2,3	0%	NA	–
	S00-C1-1,2			1
	S00-C2-1,2			2
	S00-C3-1,2			3
2	S00R-1,2,3	0%	RA	–
	S00R-C1-1,2			1
	S00R-C2-1,2			2
	S00R-C3-1,2			3
3	S10-1,2,3	10%	NA	–
	S10-C1-1,2			1
	S10-C2-1,2			2
	S10-C3-1,2			3
4	S10R-1,2,3	10%	RA	–
	S10R-C1-1,2			1
	S10R-C2-1,2			2
	S10R-C3-1,2			3
5	S20-1,2,3	20%	NA	–
	S20-C1-1,2			1
	S20-C2-1,2			2
	S20-C3-1,2			3
6	S20R-1,2,3	20%	RA	–
	S20R-C1-1,2			1
	S20R-C2-1,2			2
	S20R-C3-1,2			3
7	S30-1,2,3	30%	NA	–
	S30-C1-1,2			1
	S30-C2-1,2			2
	S30-C3-1,2			3
8	S30R-1,2,3	30%	RA	–
	S30R-C1-1,2			1
	S30R-C2-1,2			2
	S30R-C3-1,2			3

7.1.2 Raw materials

The raw materials, including fine aggregate, coarse aggregate, fly ash, slag, and alkali activator, were in accordance with that in Chapter 5. Thus, the details for these materials could be found in Section 5.1.1.

Additionally, continuous unidirectional carbon fiber sheets were used to form the CFRP jacket. To determine the tensile properties of CFRP composite materials, several 6-ply

flat coupons of CFRP composite were prepared as per ASTM D7565–10 (Standard Test Method for Determining Tensile Properties of Fiber Reinforced Polymer Matrix Composites Used for Strengthening of Civil Structures), which have a width of 20 mm and a length of 250 mm. Then steel tabs (width of 25 mm, length of 60 mm, and thickness of 1.5 mm) were tabbed on both ends of the coupons, as shown in Figure 7.1(a). The tensile coupon test was carried out according to ASTM D3039-17 (Standard Test Method for Tensile Properties of Polymer Matrix Composite Materials), that the prepared flat coupon was mounted in the grips of a mechanical testing machine and monotonically loaded in tension while recording the force. Additionally, the coupon strain was monitored by two extensometers with a gauge length of 50 mm, which were fixed at mid-height.

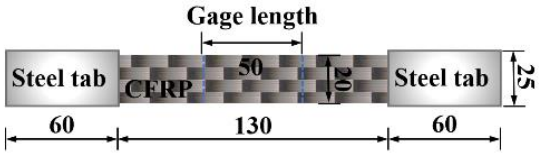

(a) Coupon details and test setup (Unit: mm)

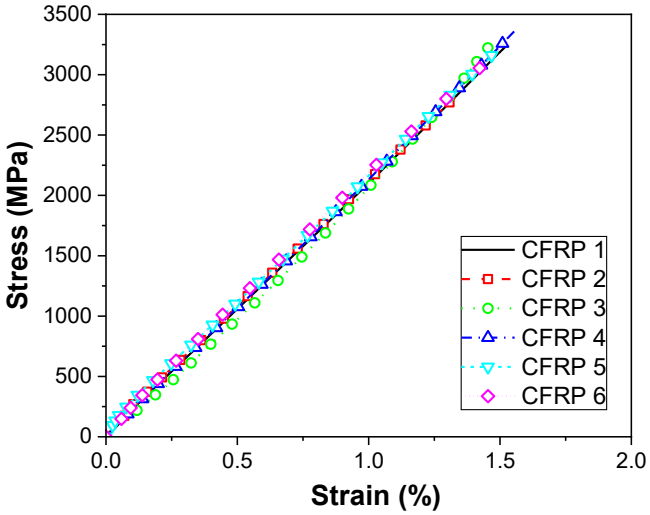

(b) Tensile stress-strain curves

Figure 7.1. Tensile coupon test of CFRP composites

Figure 7.1(b) presents the stress-strain responses of these tested CFRP coupons, in which the nominal thickness of one-ply CFRP was taken as 0.17 mm. The results show that the

CFRP composite has the average values of the tensile strength (f_{frp}), ultimate tensile strain (ε_{frp}), and secant elastic modulus (E_{frp}) (between the origin and the ultimate strain point) being 3203 MPa, 1.52%, and 211 GPa, respectively.

7.1.3 Mix proportions

The details of concrete mixes are given in Table 7.2, including four batches of GNAC and four batches of GRAC. The total binder content was kept constant at 420 kg/m^3 for all mixes, and four levels of slag content were adopted (i.e., 0, 10, 20, and 30% by weight of the total binder mass). The ratio of activator solution to binder was kept constant at 0.55, and the mass of Na_2SiO_3 solution used was 2.0 times that of NaOH solution.

Table 7.2 Details of mix proportion for geopolymeric concrete

Mixture	Mix proportion (kg/m^3)						
	Fly ash	Slag	Na_2SiO_3	NaOH	Sand	NA	RA
S00	420	0	165	66	550	1220	0
S10	378	42	165	66	550	1220	0
S20	336	84	165	66	550	1220	0
S30	294	126	165	66	550	1220	0
S00R	420	0	165	66	550	0	1220
S10R	378	42	165	66	550	0	1220
S20R	336	84	165	66	550	0	1220
S30R	294	126	165	66	550	0	1220

7.1.4 Specimen preparation

The concrete mixing process and curing regime were followed that reported in Chapter 3 (as shown in Section 3.1.3). After 28 days of curing age, both ends of the specimens were ground flat and parallel, and then the specimens were measured for the dimensions. The surfaces of the specimens to be confined by CFRP jackets were then roughened by sandpaper, and cleaned and wiped with acetone to remove contaminants. In this study, the CFRP jackets were formed via a wet layup procedure. Firstly, a thin layer of matching epoxy resin was applied to the concrete surface. The voids in the concrete substrate were filled with the resin by carefully applying pressure to the surface. Meanwhile, an even

layer of the resin was applied to the CFRP sheet over its full length. Then, the CFRP sheet was wrapped in the hoop direction onto the concrete surface with an overlap of 100 mm. Subsequently, a uniform pressure by a hard rubber roller was applied to expel the excess resin from the sides of the CFRP jacket. Finally, the CFRP-confined specimens were left to cure at room temperature for five days before the compression test.

7.1.5 Experimental program

The compression tests were conducted by a 5000 kN MTS servo-hydraulic load frame with the displacement control at a rate of 0.2 mm/min. For unconfined specimens, a pair of strain gauges with a gauge length of 50 mm were installed to measure the hoop strains, at the specimen mid-height and at 180º spacing. For CFRP-confined specimens, five strain gauges with a gauge length of 20 mm were installed at mid-height to measure the hoop strains. It is well-known that as the larger thickness of FRP jackets in the overlapping zone, the hoop strains are lower within the overlapping zone compared to the non-overlap region, and the strain gauge readings coming from the overlap region were usually excluded in the calculations of the average values of hoop strain (Jiang et al. 2019; Ozbakkaloglu & Lim 2013). Therefore, the hoop strain gauges were located outside the overlapping zone and were equally spaced at 45º, as shown in Figure 7.2. For confined and unconfined specimens, the axial strain was measured by a compressometer equipped with two LVDTs at 180º spacing and covering the mid-height region of 100 mm, as shown in Figure 7.2. Furthermore, a pair of strain gauges with a gauge length of 50 mm were placed at the specimen mid-height and at 180º spacing to measure the axial strain and also validate LVDT measurements at the early stage of the test. Each specimen was preloaded to 5% of the estimated peak load before the actual loading to check the alignment and avoid the slackness of the system. All the test data, including the axial strain, hoop strain, and applied load were recorded by a synchronous data acquisition system.

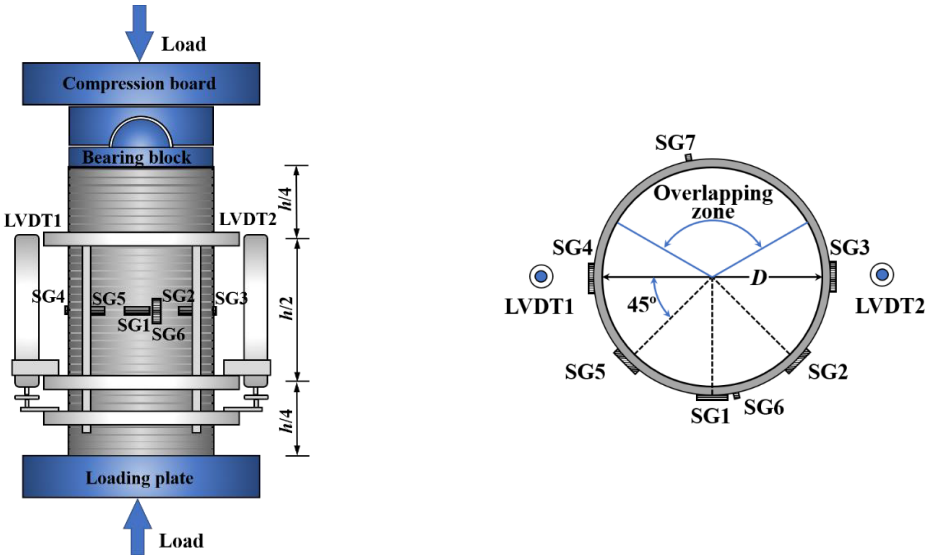

(a) Test setup (b) Distribution of strain gauges

Figure 7.2. Test setup and instrumentation for confined specimens

7.2 Unconfined specimens

For unconfined specimens, the micro-cracks emerged on the surface of the cylinder when the applied load approached the peak stress and then cracked extended to the central section with the displacement increasing. At the post-peak stage, the cracks developed from micro to macroscopic and crossed throughout the entire specimen. Finally, the cylinder failed with several major vertical cracks and the spallation of the lateral surfaces, as shown in Figure 7.3. Besides, a more brittle failure process was observed in the specimens containing NA or the specimens having higher contents of slag.

(a) Unconfined GNAC

(b) Confined GNAC

(c) Unconfined GRAC

(d) Confined GRAC

Figure 7.3. Typical failure modes of specimens under compression

The typical compressive stress-strain curves of unconfined specimens are shown in Figure 7.4. The axial strain was averaged from the readings of the two LVDTs. Furthermore, Table 7.3 lists the averaged values for the mechanical properties of unconfined specimens in each series (the peak stress $f_{co}^{'}$, the axial strain at peak stress ε_{co}, and the elastic modulus E_c), and the corresponding standard deviations. The elastic modulus was determined according to ASTM C469 (Static Modulus of Elasticity and Poisson's Ratio of Concrete in Compression). The test results indicate that the peak stress and elastic modulus decrease after the RA replacement. This finding agrees with those previous studies on GRAC (Nuaklong et al. 2018b; Tang et al. 2019a; Wongsa et al. 2018b; Xie et al. 2019a). The inferior properties of GRAC were mainly attributed to that

there were many defects such as voids and cracks that existed in the RA, resulting in the lower strength of RA in comparison with NA (Tang et al. 2019b). However, the peak stress and elastic modulus showed an ascending tendency after the incorporation of slag, regardless of GNAC and GRAC. The improvements in the peak stress and elastic modulus were mainly due to that the slag has high alkali activation reactivity and the generated reaction products possess higher compactness and stiffness (Ding et al. 2018b; Puligilla & Mondal 2013; Song et al. 2019).

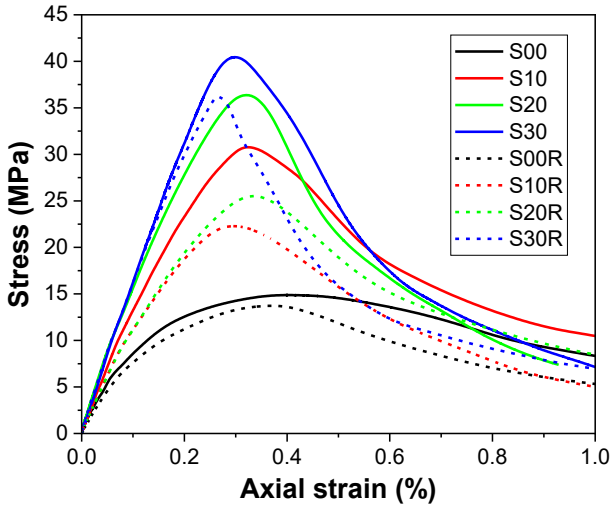

Figure 7.4. Typical compressive stress-strain curves of unconfined concrete

Table 7.3 Summary of mechanical properties results

Series	Specimen	$f_{co}^{'}$ (MPa)	E_c (GPa)	ε_{co} (%)	$f_{cc}^{'}$ (MPa)	$f_{cc}^{'} / f_{co}^{'}$	ε_{cu} (%)	$\varepsilon_{cu} / \varepsilon_{co}$	$\varepsilon_{h,rup}$ (%)	$f_{lu,a}^{'}$ (MPa)	$f_{lu,a}^{'} / f_{co}^{'}$
1	S00-C1-2	14.29	11.21	0.448	48.49	3.33	2.15	4.63	-1.17	8.45	0.58
	S00-C1-2	(1.77)	(1.06)	(0.064)	50.94	3.49	1.96	4.22	-1.11	8.00	0.55
	S00-C2-1				80.10	5.49	2.95	6.35	-1.16	16.66	1.14
	S00-C2-2				75.32	5.17	2.60	5.59	-1.00	14.40	0.99
	S00-C3-1				95.38	6.54	3.20	6.88	-1.09	23.61	1.62
	S00-C3-2				94.56	6.49	3.36	7.22	-0.99	21.31	1.46
2	S00R-C1-1	14.21	8.77	0.372	46.94	3.30	2.16	5.81	-1.05	7.57	0.53
	S00R-C1-2	(0.48)	(0.12)	(0.002)	43.42	3.06	1.85	4.98	-1.19	8.58	0.60
	S00R-C2-1				63.74	4.49	2.47	6.64	-0.91	13.15	0.93
	S00R-C2-2				69.30	4.88	2.90	7.79	-1.08	15.59	1.10
	S00R-C3-1				90.08	6.34	3.58	9.62	-1.04	22.42	1.58
	S00R-C3-2				88.19	6.21	4.00	10.76	-1.15	24.81	1.75
3	S10-C1-1	30.76	15.59	0.267	59.75	1.94	1.38	5.16	-1.01	7.26	0.24
	S10-C1-2	(1.11)	(0.26)	(0.021)	56.98	1.85	1.32	4.94	-1.01	7.30	0.24
	S10-C2-1				89.72	2.92	1.79	6.70	-0.97	13.99	0.45
	S10-C2-2				95.93	3.12	1.89	7.06	-1.00	14.43	0.47
	S10-C3-1				116.52	3.79	2.36	8.85	-0.99	21.37	0.69
	S10-C3-2				119.30	3.88	2.49	9.31	-0.99	21.42	0.70
4	S10R-C1-1	22.66	11.45	0.264	50.39	2.22	1.81	6.86	-1.02	7.34	0.32
	S10R-C1-2	(1.61)	(0.70)	(0.013)	53.74	2.37	1.82	6.90	-1.09	7.89	0.35
	S10R-C2-1				84.20	3.72	2.44	9.22	-1.13	16.30	0.72
	S10R-C2-2				78.71	3.47	2.12	8.02	-1.06	15.22	0.67
	S10R-C3-1				102.15	4.51	2.66	10.07	-1.08	23.34	1.03

	S10R-C3-2				96.75	4.27	2.86	10.80	-1.12	24.20	1.07
5	S20-C1-1	36.96	16.53	0.305	70.52	1.91	1.03	3.39	-0.84	6.06	0.16
	S20-C1-2	(0.35)	(1.26)	(0.014)	69.02	1.87	1.02	3.36	-1.02	7.35	0.20
	S20-C2-1				105.08	2.84	2.12	6.94	-1.09	15.74	0.43
	S20-C2-2				104.89	2.84	2.18	7.15	-1.09	15.66	0.42
	S20-C3-1				128.79	3.48	2.10	6.88	-0.82	17.79	0.48
	S20-C3-2				126.65	3.43	2.01	6.58	-0.80	17.24	0.47
6	S20R-C1-1	25.61	11.78	0.345	62.60	2.44	1.30	3.76	-1.08	7.79	0.30
	S20R-C1-2	(0.48)	(0.43)	(0.026)	60.42	2.36	1.37	3.97	-1.05	7.59	0.30
	S20R-C2-1				82.35	3.22	2.17	6.28	-1.07	15.40	0.60
	S20R-C2-2				80.91	3.16	1.93	5.58	-0.94	13.52	0.53
	S20R-C3-1				108.70	4.24	2.59	7.51	-0.97	20.93	0.82
	S20R-C3-2				105.60	4.12	2.30	6.67	-0.85	18.34	0.72
7	S30-C1-1	41.09	16.72	0.303	76.55	1.86	1.05	3.49	-1.11	7.98	0.19
	S30-C1-2	(1.81)	(0.43)	(0.028)	74.44	1.81	1.03	3.41	-1.11	8.00	0.19
	S30-C2-1				97.55	2.37	1.50	4.97	-0.84	12.08	0.29
	S30-C2-2				97.82	2.38	1.49	4.91	-0.84	12.14	0.30
	S30-C3-1				142.32	3.46	2.47	8.18	-1.08	23.32	0.57
	S30-C3-2				135.42	3.30	2.15	7.11	-0.88	18.95	0.46
8	S30R-C1-1	35.38	15.58	0.256	66.91	1.95	0.81	3.18	-1.04	7.46	0.22
	S30R-C1-2	(2.06)	(0.49)	(0.022)	67.92	1.98	0.81	3.16	-1.05	7.58	0.22
	S30R-C2-1				83.39	2.43	1.12	4.39	-0.83	11.96	0.35
	S30R-C2-2				79.25	2.31	1.52	5.92	-0.89	12.88	0.38
	S30R-C3-1				132.83	3.87	2.30	8.99	-0.97	20.91	0.61
	S30R-C3-2				123.63	3.61	1.89	7.39	-0.84	18.18	0.53

7.3 Confined specimens

7.3.1 Failure mode

All the CFRP-confined specimens failed with the rupture of CFRP jackets due to the lateral expansion of the core concrete. The rupture of CFRP jackets occurred suddenly, accompanied by big sound, and was located in the mid-height region of the specimens and outside the overlapping zones. Besides, a slight difference could be observed among the different series of specimens. That is, the specimens with higher slag contents or based on GNAC behaved in a more brittle manner, manifesting as an explosion of the core concrete after the CFRP rupture. The typical failure modes of CFRP-confined specimens are depicted in Figure 7.3.

7.3.2 Stress-strain relationships

The stress-strain curves of tested CFRP-confined specimens are presented in Figure 7.5. In addition, the typical stress-strain curves of the corresponding unconfined specimens are provided for reference. The axial strains were based on the average values of the LVDTs and are defined to be positive when the specimens are subjected to axial compressive strain. The hoop strains were averaged from the readings of two hoop strain gauges mounted at the surface of concrete for unconfined specimens, while from the readings of five strain gauges mounted at the surface of CFRP jackets for the confined specimens. In addition, the hoop tensile strain is defined to be negative.

Figure 7.5 shows that all the stress-strain curves of confined specimens behave in a bilinear pattern, and with a transition zone between two linear portions. The first portion of the stress-strain curve of confined specimens is almost identical to that of the corresponding unconfined specimen. It can be explained that the confinement effect is negligible because of the small dilation of the core concrete during the preliminary loading stage. However, as the stress approaching the peak stress of the core concrete, the confinement mechanism of CFRP jackets is activated. This, subsequently, results in that the first portion of the stress-strain curve of confined specimens ends at higher stress, in comparison with that of the corresponding unconfined concrete. As for the second

portion of the stress-strain curves, the confined specimens are featured with an ascending shape because the confining pressure increases rapidly as the result of the significant dilation of the core concrete. Besides, the slope of the second portion of the curves is larger for the specimens with a larger thickness of CFRP jackets. Upon specimen failure, remarkable improvements in both the compressive strength and the ultimate axial strain can be observed for the CFRP-confined specimen compared with the unconfined specimens. In addition, under comparable hoop rupture strains, a more pronounced enhancement is obtained with the increase in the thickness of CFRP jackets.

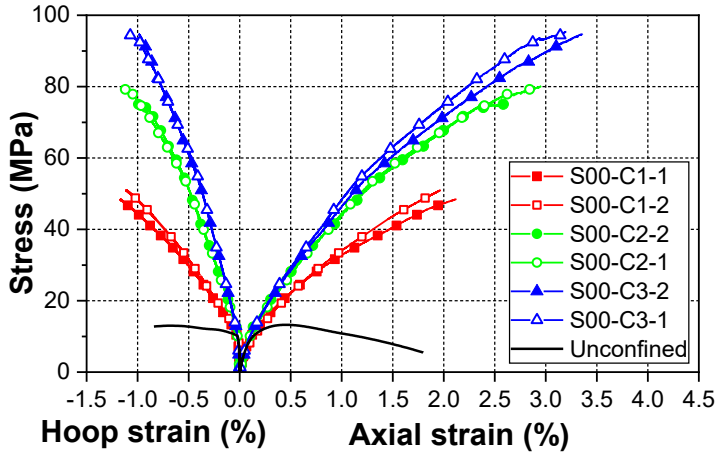

(a) S00

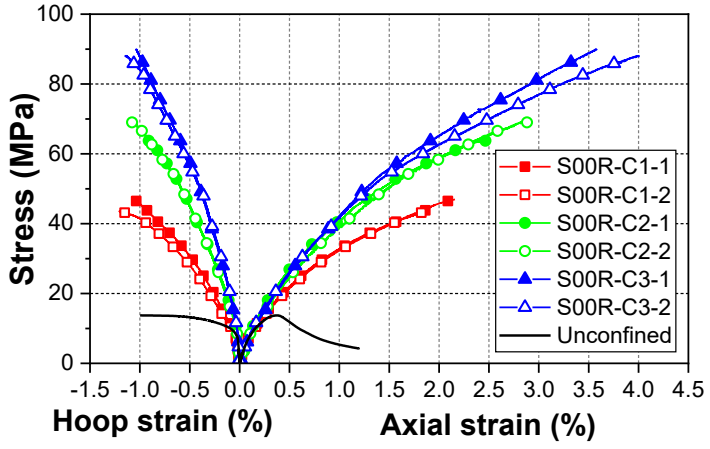

(b) S00R

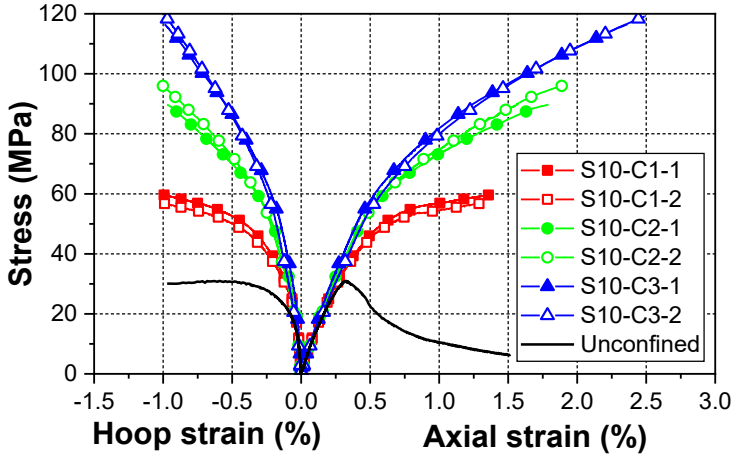

(c) S10

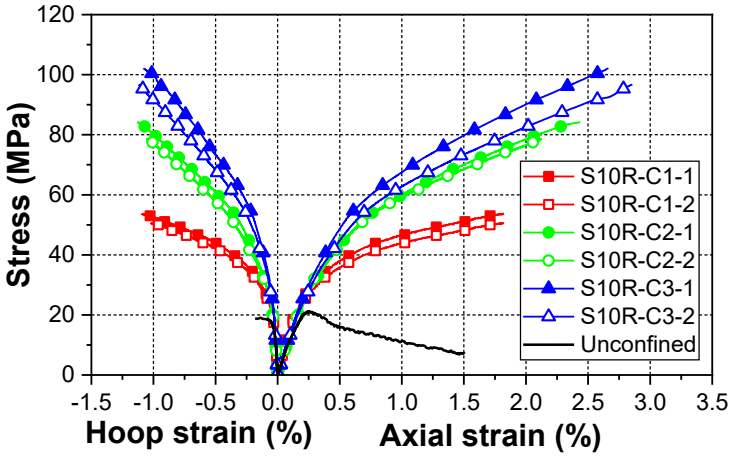

(d) S10R

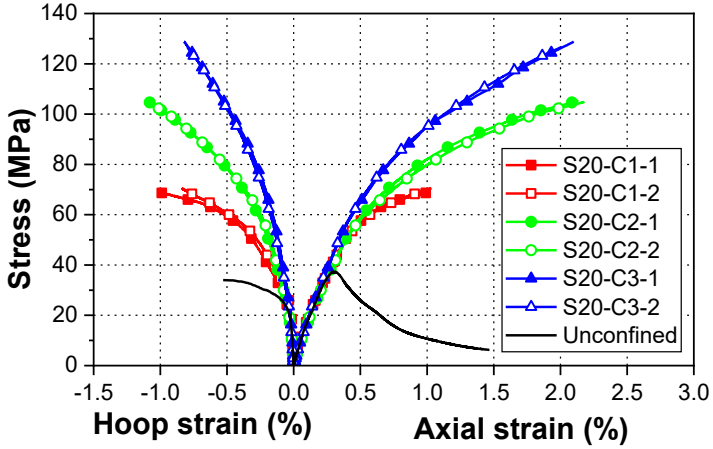

(e) S20

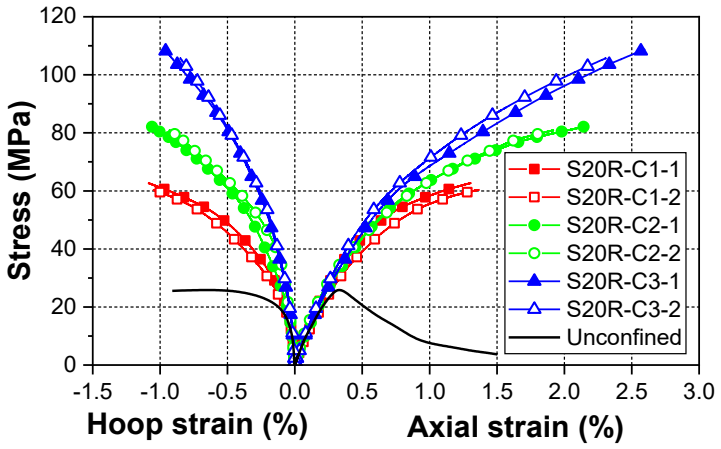

(f) S20R

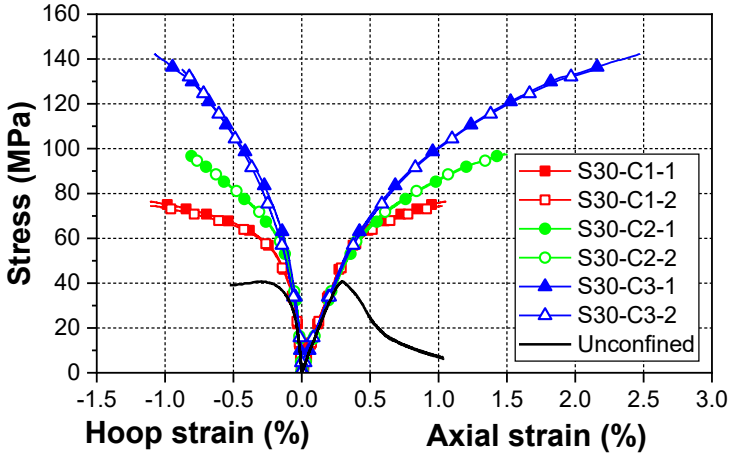

(g) S30

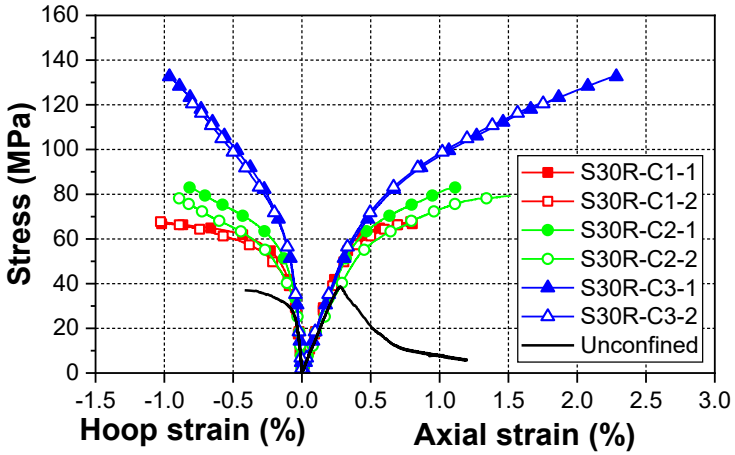

(h) S30R

Figure 7.5. Stress-strain behaviors of confined geopolymeric concrete with different thickness of CFRP confinement

The stress-strain curves of confined specimens are reassembled in Figure 7.6, where the specimens with the same thickness of CFRP jackets are shown together to examine the effects of RA replacement and slag incorporation. To avoid redundancy, only the stress-strain curve of a typical specimen from two nominally identical specimens is presented in Figure 7.6. The first portion of the stress-strain curves of GRAC possesses a lower slope and ends at lower stress, in comparison with that of GNAC. This is easy to understand because the first portion of the stress-strain curves mainly depends on the properties of unconfined concrete, and the RA replacement results in a smaller elastic modulus and lower compressive strength for unconfined concrete. Figure 7.6 also shows that with the same thickness of CFRP jackets, a more circular transition zone (i.e., a smoother change in the slope of the curves) could be found in GRAC compared with GNAC (Zhao et al. 2014). Similar observations have been reported in the previous studies that the transition between the two portions of the stress-strain curve appeared to be smoother after the RA replacement (Gao et al. 2016; Zhao et al. 2014; Zhou et al. 2016). This can be explained by the decreased brittleness caused by the RA replacement (Lim & Ozbakkaloglu 2015). The reverse trends to these above characteristics are observed with the increase of slag content. Specifically, with the increase of slag content, the first linear portion has a larger slope and a higher ending point, and the transition part of the curves possesses a reduced radius.

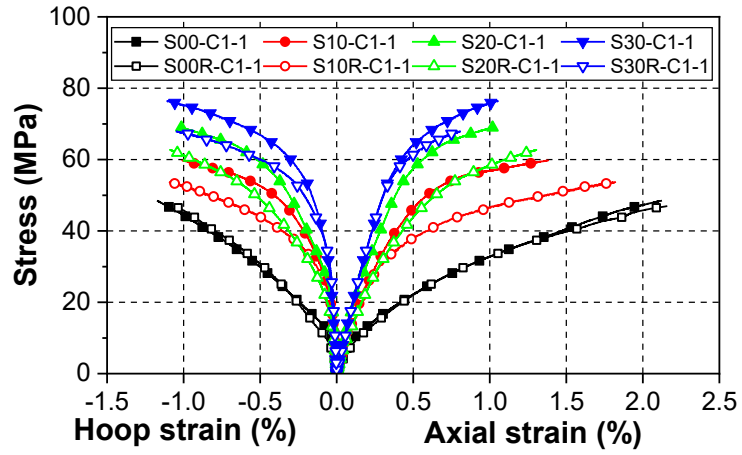

(a) 1-ply CFRP jacket

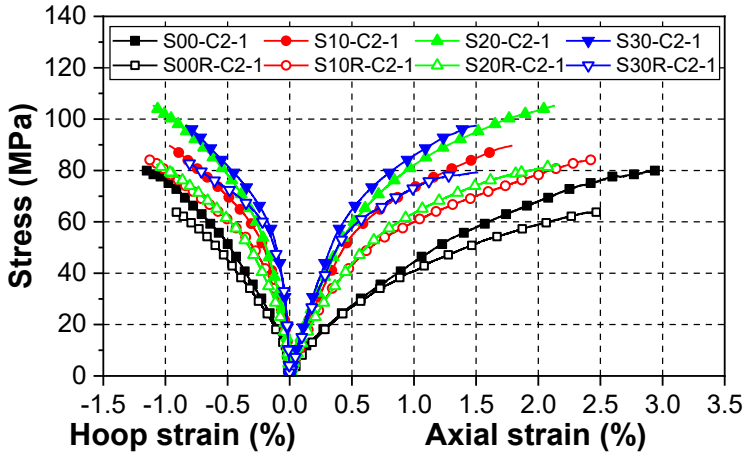

(b) 2-ply CFRP jacket

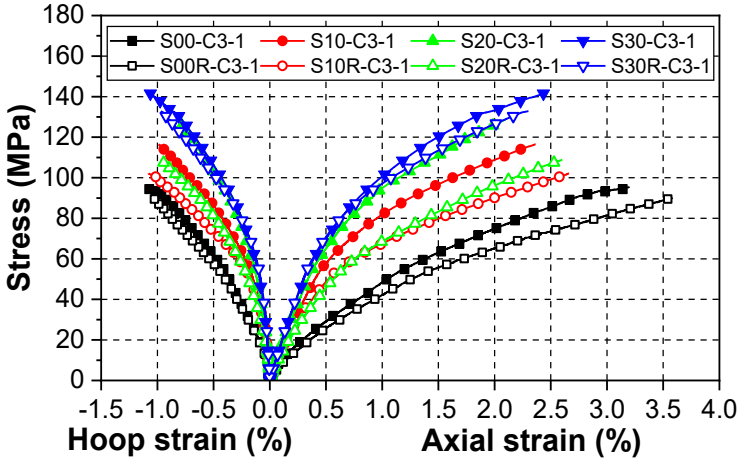

(c) 3-ply CFRP

Figure 7.6. Effects of binder type and RA replacement on stress-strain behavior of confined geopolymeric concrete

7.3.3 Axial-hoop strain responses

The axial-hoop strain curves of test specimens are illustrated in Figure 7.7. The initial axial-hoop strain responses of the confined specimens developed linearly and followed the response of the corresponding unconfined specimen. It was because, at this stage, the confining pressure by the CFRP jacket was quite insignificant as the microcrack of concrete hardly developed and lateral expansion was insignificant. When the axial strain reached about 60–80% of the peak strain of unconfined concrete, the axial-hoop strain curve of the unconfined specimen exhibited a sharp increase in the slope due to the unrestrained microcrack propagation, whereas the curve of the CFRP-confined specimen entered the second approximately linear region with the slope rising slowly. Moreover, the slope of the second part of the curves for the CFRP-confined specimen is strongly influenced by the CFRP jacket thickness. As shown in Figure 7.7, the secant slope of the second part of the curves reduces with an increase in the CFRP jacket thickness. Therefore, the specimen with a larger thickness of CFRP jackets has a larger axial strain at a given hoop strain.

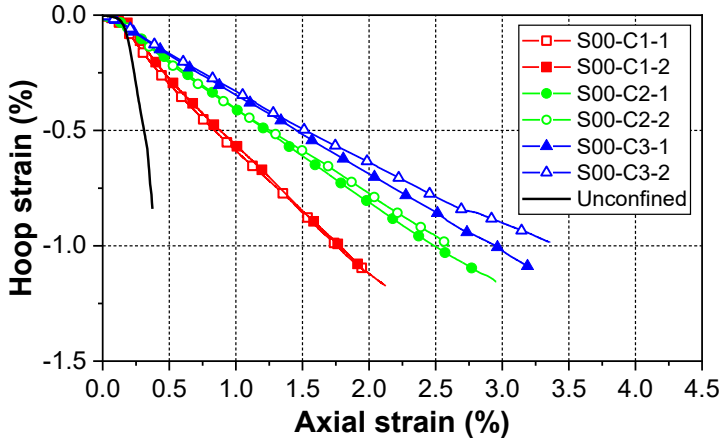

(a) S00

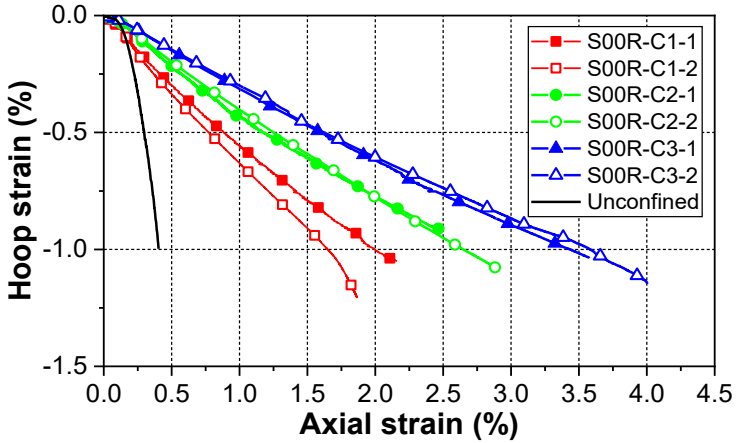

(b) S00R

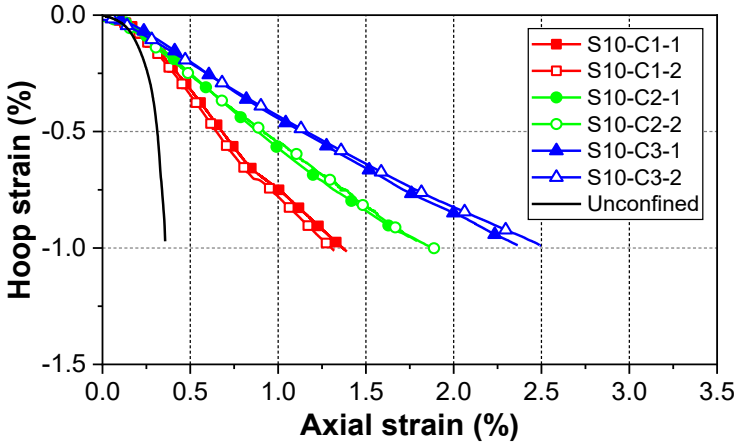

(c) S10

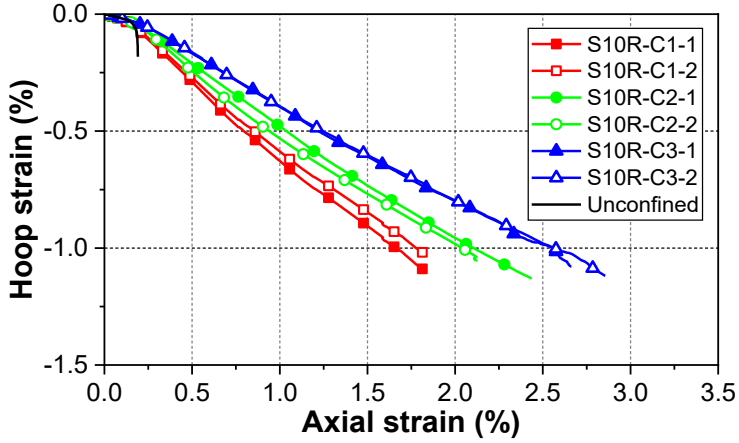

(d) S10R

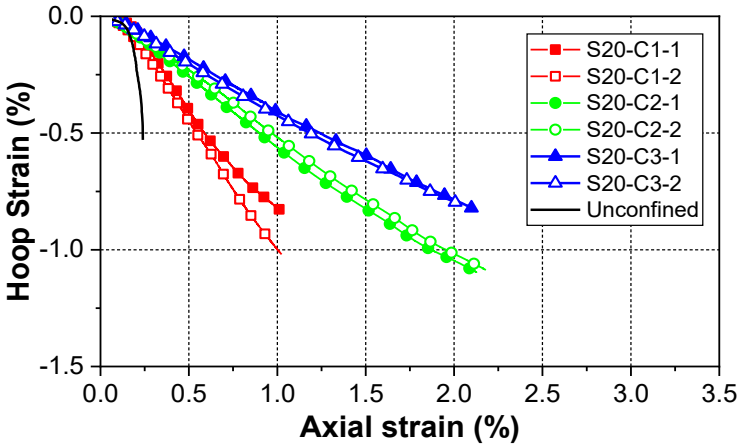

(e) S20

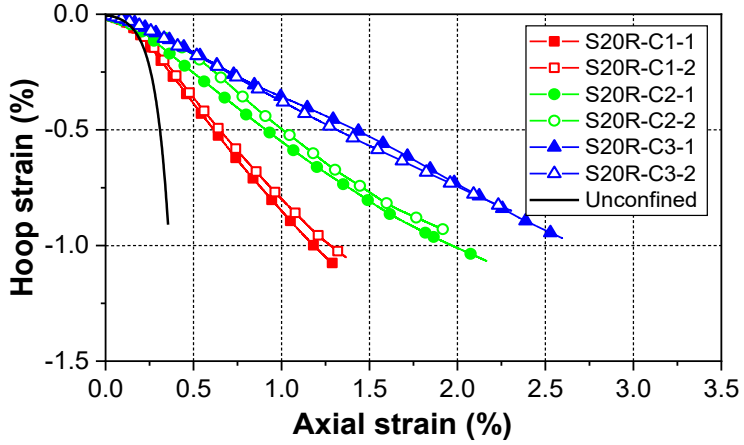

(f) S20R

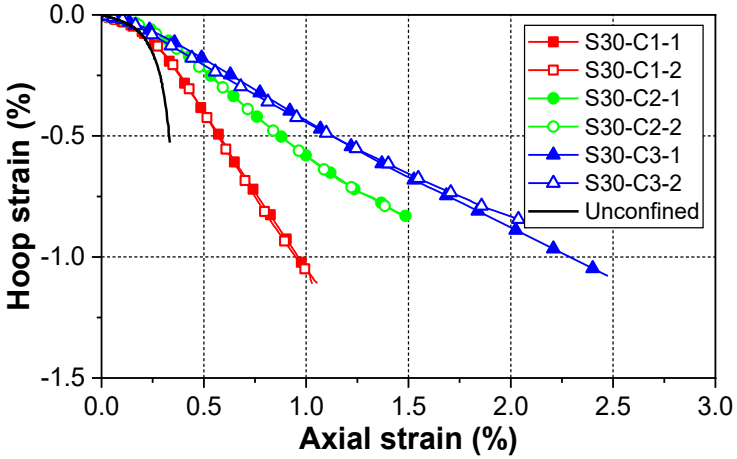

(g) S30

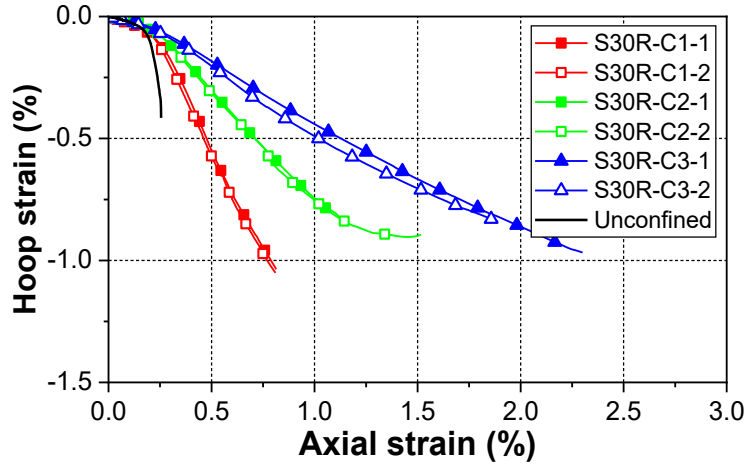

(h) S30R

Figure 7.7. Axial-hoop strain responses of confined geopolymeric concrete with different thickness of CFRP jackets

Figure 7.8 groups the axial-hoop strain curves in terms of the CFRP jacket thickness to examine the effects of the RA replacement and slag inclusion on the axial-hoop strain response. In which, only the stress-strain curve of a typical specimen from two nominally identical specimens is presented. It can be observed that under the same CFRP jacket thickness, the axial-hoop strain curves are generally higher for GRAC compared with GNAC, that in fact, at a given hoop strain, the corresponding axial strain is generally larger. Similar trends have also been noted in the previous tests on FRP-confined OPC-based RAC by Zhao et al. (2014) and Chen et al. (2016a). The explanation for this observation may be: the confinement degree (i.e., the ratio of the confinement stiffness to the unconfined strength of core concrete) is marked for RAC as the RA replacement decreases the compressive strength of unconfined concrete (Figure 7.4). Teng et al. (2007) reported that at a given lateral strain, the axial strain was larger under a higher confinement degree. However, the reverse trend has been found in the study of Gao et al. (2016), that the axial strain was higher in the confined RAC based on recycled brick aggregate than that in the confined NAC at a given hoop strain. Similarly, this trend is also observed in this study, specifically the groups based on the geopolymeric concrete with 30% slag content. It is believed to be due to that, in addition to the confinement degree, other properties such as the peak strain and elastic modulus of the core concrete also influence the axial-hoop strain relationship of confined concrete (Lim & Ozbakkaloglu 2015). As shown in Table 5, the geopolymeric concrete with different slag concrete exhibits different trends in terms of the peak strain and elastic modulus after the RA replacement. But, systematic work is needed in the future to investigate the specific effects of these factors on the axial-hoop strain response. On the other hand, Figure 7.8 also illustrates that the slag incorporation results in the reduction in the axial strain under a given hoop strain, mainly attributed to the enhancement in the unconfined concrete strength but the decrease in the unconfined concrete strain after the slag inclusion.

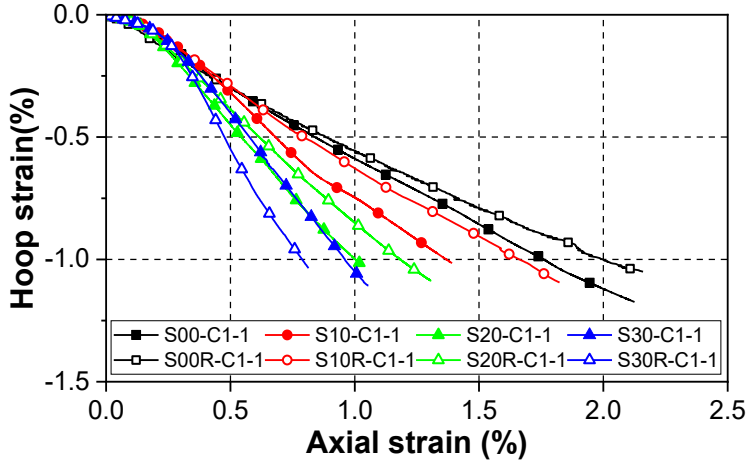

(a) 1-ply CFRP

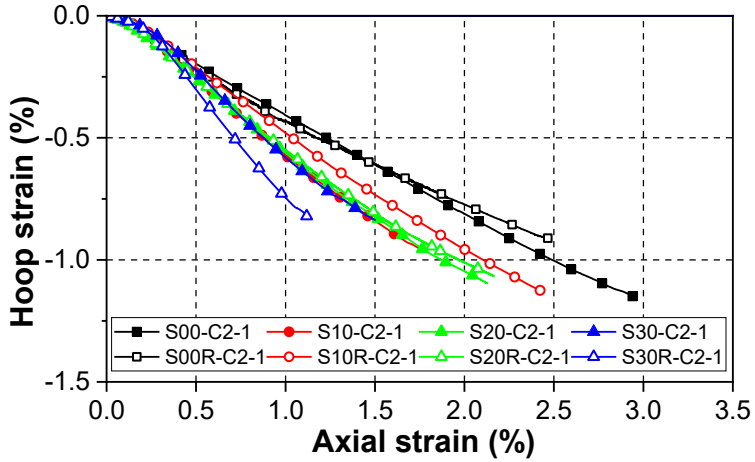

(b) 2-ply CFRP

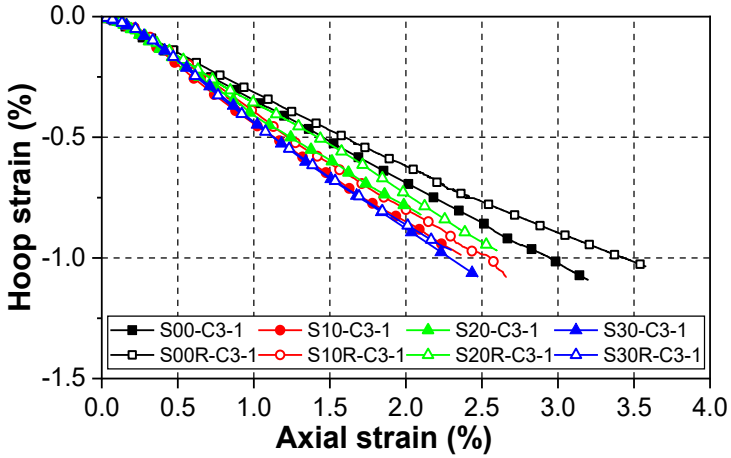

(c) 3-ply CFRP

Figure 7.8. Effects of binder type and RA replacement on axial-hoop strain responses of confined geopolymeric concrete

7.3.4 Volumetric strain

The volumetric strain change of core concrete under compression can be represented by the volumetric strain (ε_{vol}) using the following equation (Lam & Teng 2003).

$$\varepsilon_{vol} = \varepsilon_c + \varepsilon_l + \varepsilon_\theta = \varepsilon_c + 2\varepsilon_r \tag{7.1}$$

where ε_θ = circumferential strain and = ε_r = lateral (radial) strain.

If the FRP composites could provide effective and strong confinement effects to the core concrete, the specimen will undergo the volumetric compaction when subjected to compression; otherwise, the specimen will experience a high degree of volumetric dilation before the failure. In this work, a positive volumetric strain ε_{vol} indicates volume reduction (or compaction) of the core concrete, while a negative volumetric strain indicates volume increase (or dilation) of the core concrete.

The volumetric strain of test specimens is presented in Figure 7.9 against the normalized axial stress $\sigma_c / f_{co}^{'}$, which is defined as the ratio of the axial stress to the peak stress of the corresponding unconfined concrete. As shown in Figure 7.9, for unconfined specimens, the volumetric strain showed volumetric compaction until the stress reached about 70% of the peak stress. But thereafter, the volumetric strain dramatically decreased, and then concrete exhibited volumetric dilation. This kind of behavior has been extensively reported in previous studies (Choi et al. 2013; Lam & Teng 2003). For confined specimens, the volumetric behavior is distinctly different. In general, the decrease in the volumetric strain of confined specimens started at higher axial stress, in comparison with the corresponding unconfined specimen. In addition, the volumetric strain declined more slowly for the confined specimen due to the lateral restrain by the CFRP jacket. For some of the specimens, such as S10R-C2 and S20R-C2, the trend of increasing dilation was even reversed prior to the end of loading. This observation was attributed to that the linearity of CFRP provided a continuously increasing confining pressure as the increasing hoop strain, and therefore had the potential to limit the lateral strain of core concrete to the hoop rupture strain of CFRP. Furthermore, it could be

observed that if the CFRP jacket has enough thickness, the volumetric expansion of the specimen could be curtailed effectively, and consequently, no dilation was found during the entire loading history.

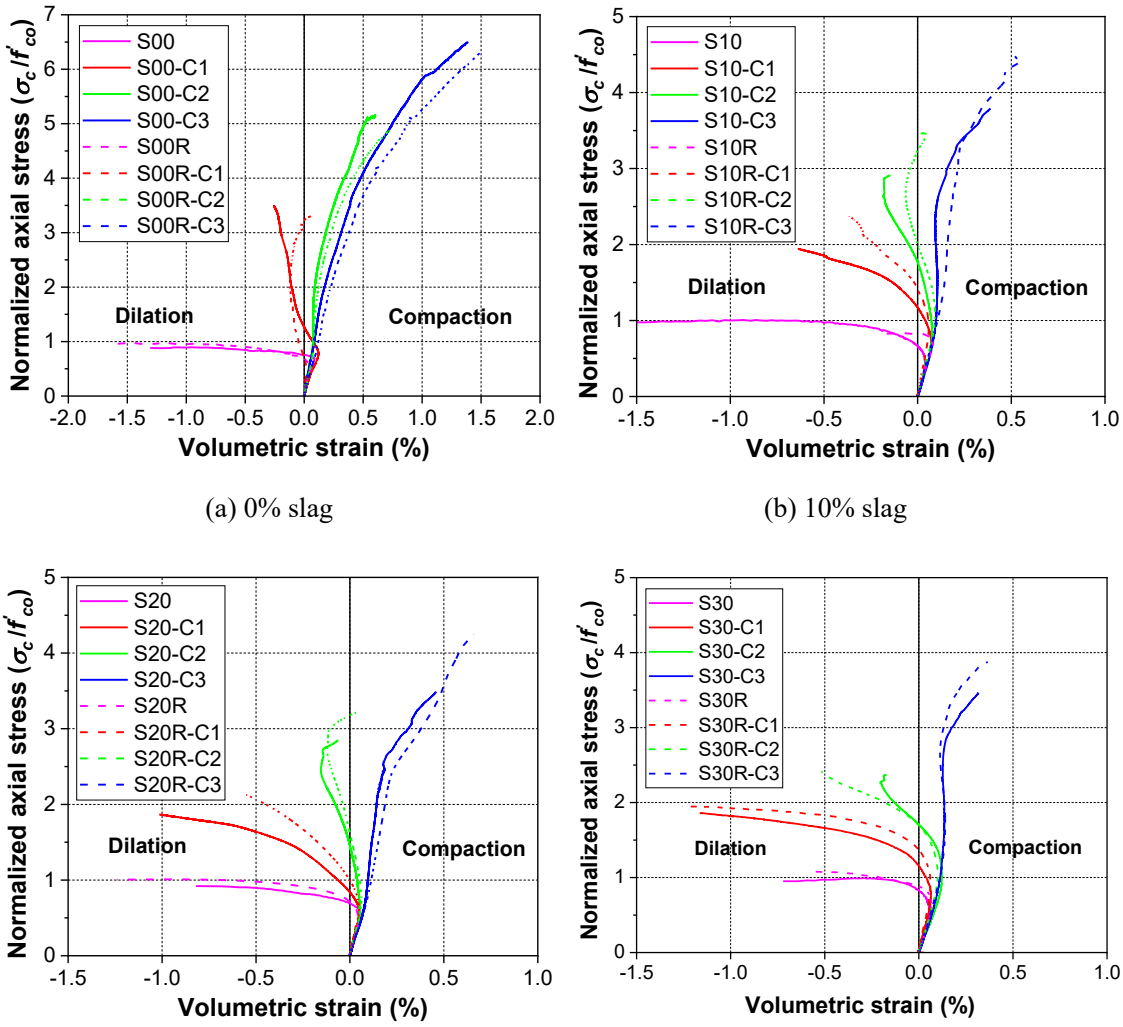

(a) 0% slag

(b) 10% slag

(c) 20% slag

(d) 30% slag

Figure 7.9. Dilation behavior of confined geopolymeric concrete

In addition, it could be found that under the same level of normalized axial stress, the GRAC showed higher volumetric compaction in comparison with the GNAC with the same CFRP jacket thickness. This can be explained by that the confinement degree is more pronounced for the GRAC as its lower unconfined compressive strength (Lam & Teng 2003). However, such differences in the volumetric strain due to the RA

replacement become negligible with the increased thickness of CFRP jackets. Besides, it could be seen from Figure 7.9 that under the same thickness of CFRP jackets, the dilation behavior is more obvious for the geopolymeric concrete with higher slag content. That was mainly attributed to that the geopolymeric concrete with higher slag content had a higher unconfined concrete strength, and therefore resulted in the reduced confinement degree under a given thickness of the CFRP jacket

7.3.5 Ultimate condition

The test results for the ultimate conditions of all 48 confined specimens are listed in Table 7.3, including the peak stress ($f_{cc}^{'}$) and the ultimate axial strain (ε_{cu}), the hoop rupture strain ($\varepsilon_{h,rup}$), and the actual lateral confining pressure ($f_{lu,a}^{'}$). The actual lateral confining pressure could be expressed as Eq. (7.2) (Lam & Teng 2003).

$$f_{lu,a} = \frac{2E_{frp}\varepsilon_{h,rup}t_{frp}}{D} \tag{7.2}$$

where D represents the diameter of core concrete, t_{frp} denotes the total thickness of CFRP jackets

The hoop rupture strain ratio ($\varepsilon_{h,rup} / \varepsilon_{frp}$), defined as the ratio of the hoop rupture strain to the ultimate tensile strain of CFRP material ($\varepsilon_{frp} = 1.52\%$), has been presented in Figure 7.10. The hoop rupture strain ratio ranges from 0.522 to 0.801 and has an average value of 0.665. This average value is closed to the average hoop rupture strain ratio of 0.682 reported by Ozbakkaloglu & Lim (2013), which was determined from the test results of 116 CFRP-confined conventional concrete.

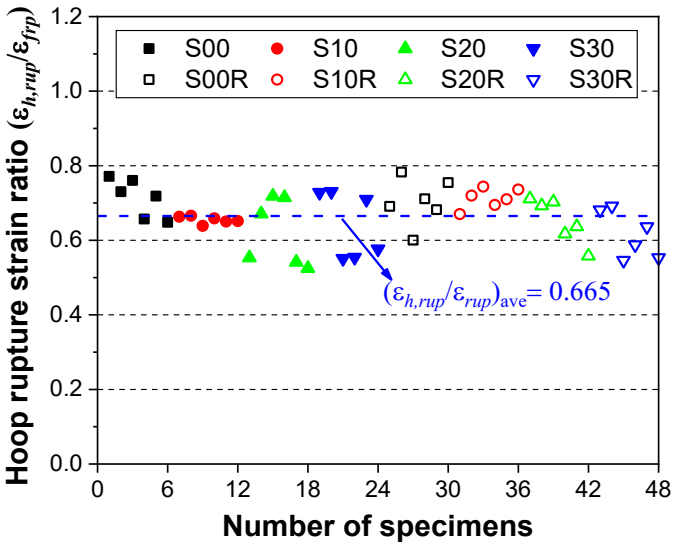

Figure 7.10. CFRP hoop rupture strain ratios

As for the compressive strength, it can be seen from Table 7.3 that the compressive strength increases with the CFRP jacket layers, demonstrating the improvement effect provided by the CFRP confinement. Besides, the effects of the RA replacement and the slag inclusion on the compressive strength of confined specimens are similar to those on the compressive strength of unconfined specimens. Specifically, the RA replacement decreases the compressive strength, while the slag inclusion increases the compressive strength. Analogous results have been previously reported in the studies of the confined conventional concrete, that the concrete with higher unconfined compressive strength usually results in higher confined compressive strength under the same confinement layer (Chen et al. 2016a; Gao et al. 2016; Xiao et al. 2012a; Zhao et al. 2014). Figure 7.11 illustrates the relationship between the strength enhancement ratio ($f_{cc}^{'} / f_{co}^{'}$) and the confinement ratio ($f_{lu,a}^{'} / f_{co}^{'}$). It can be seen that the strength enhancement ratio ranges from 1.81 to 6.54, which confirms the enhancement effect by the CFRP confinement again. In addition, the specimens with a similar confinement ratio developed comparable strength enhancement ratios regardless of the aggregate type or the content of slag inclusion. That is to say, the geopolymeric concrete mix (i.e., the aggregate type and the slag content) does not have a significant effect on the CFRP confinement performance for geopolymeric concrete in terms of the strength enhancement ratio.

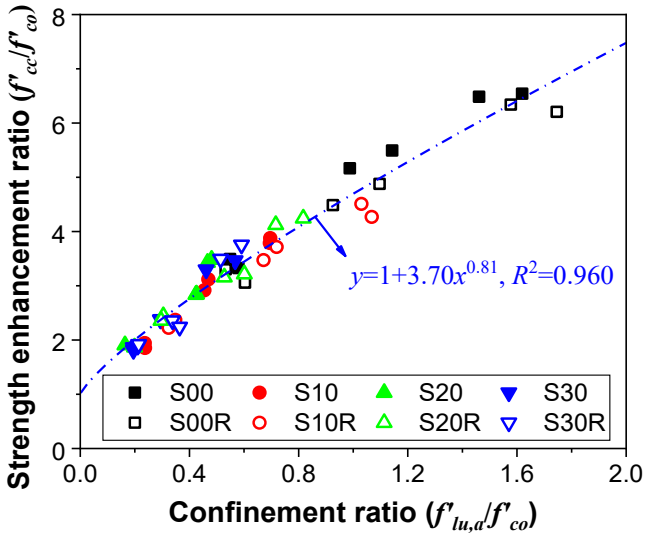

Figure 7.11. Relationship between strength enhancement ratio and confinement ratio

As shown in Table 7.3, the ultimate axial strains of CFRP-confined specimen are higher than the axial strain at the peak stress of the corresponding unconfined concrete, indicating that the CFRP confinement could also enhance the ultimate axial strain of geopolymeric concrete. In addition, the enhancement by CFRP confinement is significantly remarkable with the increase of the CFRP jacket layers. Figure 7.12 further examines the relationship between the strain enhancement ratio ($\varepsilon_{cu}/\varepsilon_{co}$) and the confinement ratio ($f'_{lu,a}/f'_{co}$). It can be observed that the relationship between the strain enhancement ratio and the confinement ratio varies with the aggregate type and the slag content. For instance, under a similar confinement ratio, a more significant improvement in ultimate strain could be observed in the GNAC than GRAC with 20% slag content. A similar trend was also noted in the test on FRP-confined RAC based on conventional concrete by Chen et al. (2016a). However, a reversed trend was observed when the geopolymer is based on fly ash only. On the other hand, the ultimate strain improvement due to the increase of confinement ratios is more noticeable for the geopolymeric concrete with slag than the geopolymeric concrete based on fly ash only. It can be concluded that the CFRP confinement performance for the ultimate axial strain is influenced by the variation in the intrinsic response of the core concrete, in this work, attributing to the different aggregate type and slag content.

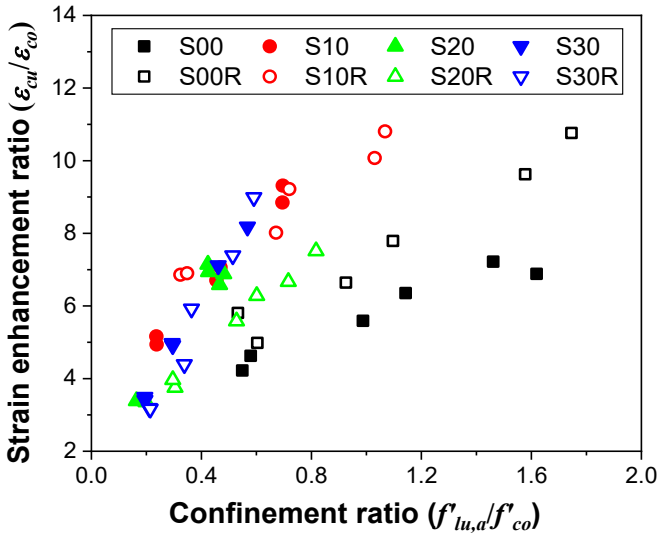

Figure 7.12. Relationship between the strain enhancement ratios and confinement ratios

7.4 Comparison of stress-strain models

7.4.1 Existing models

To realize a reliable and cost-effective design of CFRP-confined geopolymeric concrete, an accurate model for predicting its behavior is a prerequisite. In the literature, numerous models have been proposed to predict the compressive strength and ultimate axial strain of FRP-confined concrete. For instance, 88 stress-strain models developed for FRP-confined concrete in circular sections have been reviewed and assessed by Ozbakkaloglu et al. (2013). The experimental results of the current study had been compared with the predicted values using the existing models. While in this study, only five models that exhibit relatively high accuracy in predicting the results of the current study were presented, i.e., the models proposed by Ozbakkaloglu & Lim (2013), Yu & Teng (2011), Teng et al. (2009), Lam & Teng (2003), and Xiao & Wu (2000). It is noteworthy that all these selected models employ the actual confinement pressure ($f'_{lu,a}$) instead of the tensile strength of FRP material (f_{frp}). Additionally, the model proposed by Lim & Ozbakkaloglu (2014) for actively confined concrete was examined, which has recently

been confirmed to be feasible for the actively confined geopolymeric concrete (Gholampour et al. 2019). The details for these selected models are given in Table 7.4.

Table 7.4 Models used to predict the ultimate strength and ultimate axial strain of confined specimens

	Strength enhancement ratio	Strain enhancement ratio
Ozbakkaloglu & Lim (2013)	$f_{cc}^{'} = c_1 f_{co}^{'} + k_1 \left(f_{lu,a} - f_{lo} \right)$ $c_1 = \frac{f_{c1}^{'}}{f_{co}^{'}} = 1 - 0.0058 \frac{K_l}{f_{co}^{'}}$ $K_l = \frac{2E_f t_f}{D}$ and $K_l \geq f_{co}^{'\,1.65}$ $f_{lo} = E_l \varepsilon_{l1}$ $\varepsilon_{l1} = \left(0.43 + 0.009 \frac{E_l}{f_{co}^{'}} \right) \varepsilon_{co}$ $E_l = \frac{2E_f t_f}{D}$ and $E_l \geq f_{co}^{'\,1.65}$ $k_1 = 3.67$ (for CFRP wrapped concrete)	$\varepsilon_{cu} = c_2 \varepsilon_{co} + k_2 \left(\frac{E_l}{f_{co}^{'}} \right)^{0.9} \varepsilon_{h,rup}^{1.35}$ $c_2 = 2 - \frac{\left(f_{co}^{'} - 20 \right)}{100}$ and $c_2 \geq 1$ $k_2 = 0.682$ (for CFRP wrapped concrete)
Yu & Teng (2011)	$f_{cc}^{'} = f_{co}^{'} + 3.5 E_l \left(1 - 6.5 \frac{f_{co}^{'}}{E_l} \right) \varepsilon_{h,rup}$	$\varepsilon_{cu} = 0.0033 + 0.6 \left(\frac{E_l}{f_{co}^{'}} \right)^{0.8} \varepsilon_{h,rup}^{1.45}$
Teng et al. (2009)	$\frac{f_{cc}^{'}}{f_{co}^{'}} = 1 + 3.5 \left(\frac{E_l}{\left(f_{co}^{'} / \varepsilon_{co} \right)} - 0.01 \right) \left(\frac{\varepsilon_{h,rup}}{\varepsilon_{co}} \right)$	$\frac{\varepsilon_{cu}}{\varepsilon_{co}} = 1.75 + 6.5 \left(\frac{E_l}{\left(f_{co}^{'} / \varepsilon_{co} \right)} \right)^{0.8} \left(\frac{\varepsilon_{h,rup}}{\varepsilon_{co}} \right)^{1.45}$
Lam & Teng (2003)	$\frac{f_{cc}^{'}}{f_{co}^{'}} = 1 + 3.3 \frac{f_{lu,a}}{f_{co}^{'}}$	$\frac{\varepsilon_{cu}}{\varepsilon_{co}} = 1.75 + 5.53 \left(\frac{f_{lu,a}}{f_{co}^{'}} \right) \left(\frac{\varepsilon_{h,rup}}{\varepsilon_{co}} \right)^{0.45}$
Xiao & Wu (2000)	$\frac{f_{cc}^{'}}{f_{co}^{'}} = 1 + k_1 \frac{f_{lu,a}}{f_{co}^{'}}$ $k_1 = 4.1 - 0.75 \left(\frac{E_l}{f_{co}^{'\,2}} \right)^{-1.0}$	$\varepsilon_{cu} = \frac{\varepsilon_{h,rup} + \varepsilon_o}{\mu_{tu}}$ $\mu_{tu} = 7 \left(\frac{E_l}{f_{co}^{'}} \right)^{-0.8}$
Lim & Ozbakkaloglu (2014)	$f_{cc}^{*} = f_{co}^{'} + 5.2 f_{co}^{'\,0.91} \left(\frac{f_l^{*}}{f_{co}^{'}} \right)^{a}$ $a = f_{co}^{'\,-0.06}$	$\varepsilon_{cc}^{*} = \varepsilon_{co} + 0.045 \left(\frac{f_l^{*}}{f_{co}^{'}} \right)^{1.15}$

7.4.2 Performance of existing strength and strain models

Figure 7.13 illustrates the comparisons between the prediction values and the experimental results in this study. In addition, four statistical indicators are presented in Figure 7.13 and also summarized in Table 7.5, to quantify the accuracy and consistency of these models. Among them, the average absolute error (*AAE*) and the mean square error (*MSE*) are used to assess the overall accuracy of models, which can be expressed as Eqs. (7.3) and (7.4), respectively. The standard deviation (*SD*), defined by Eq. (7.5), is used to evaluate the degree of associated scatter. The linear trend slope (*LTS*), the slop of the fitting straight line through the origin, was used to determine whether the prediction is an overestimation or underestimation. For instance, an underestimation by a model is presented with a *LTS* lower than 1.

$$AAE = \frac{\sum_{i=1}^{N} \left| \frac{\mathrm{mod}_i - \mathrm{exp}_i}{\mathrm{exp}_i} \right|}{N} \tag{7.3}$$

$$MSE = \frac{\sum_{i=1}^{N} (\mathrm{mod}_i - \mathrm{exp}_i)^2}{N} \tag{7.4}$$

$$SD = \sqrt{\frac{\sum_{i=1}^{N} \left[\frac{\mathrm{mod}_i}{\mathrm{exp}_i} - \left(\frac{\mathrm{mod}}{\mathrm{exp}} \right)_{avg} \right]^2}{N-1}} \tag{7.5}$$

where N is the number of data points; exp_i and mod_i are the ith experimental value and theoretical value, respectively; $\left(\frac{\mathrm{mod}}{\mathrm{exp}} \right)_{avg}$ is the average of the ratios between the theoretical value and corresponding experimental value.

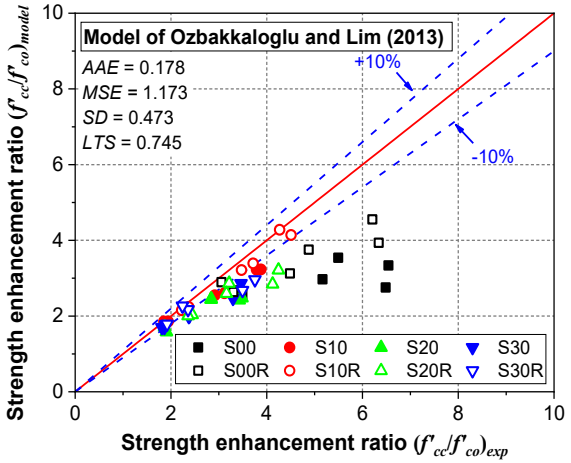

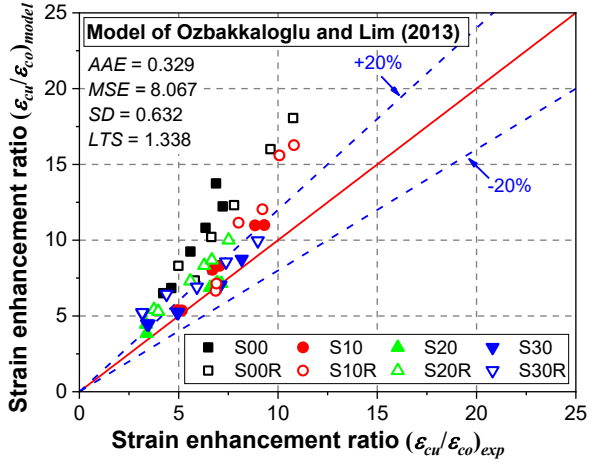

(a) Model of Ozbakkaloglu & Lim (2013)

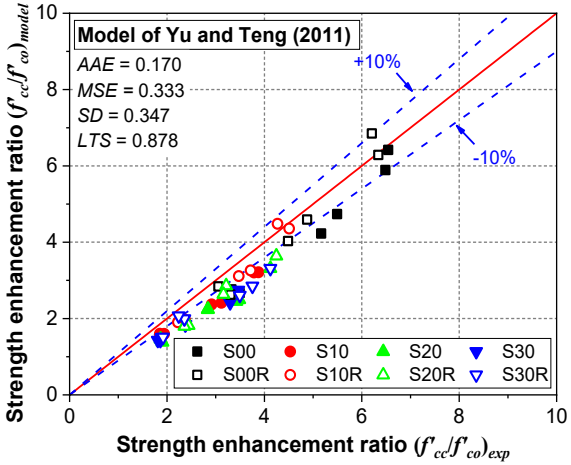

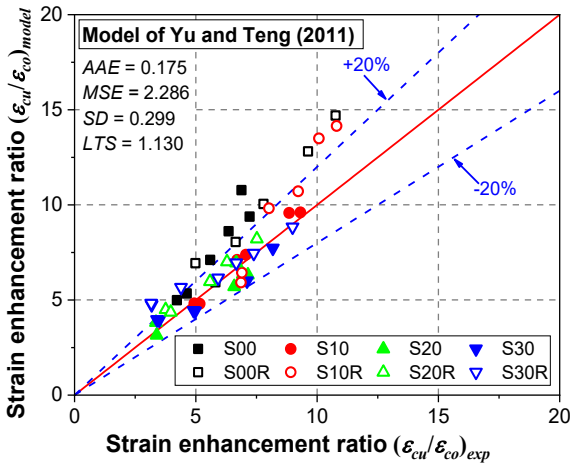

(b) Model of Yu & Teng (2011)

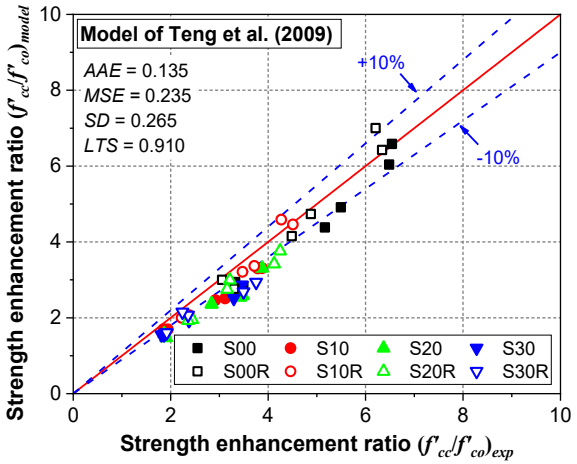

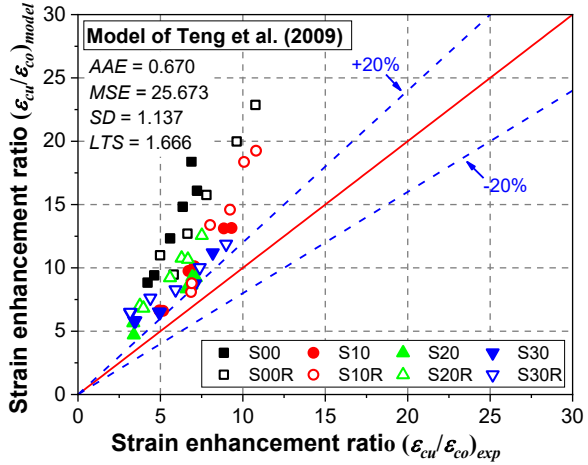

(c) Model of Teng et al. (2009)

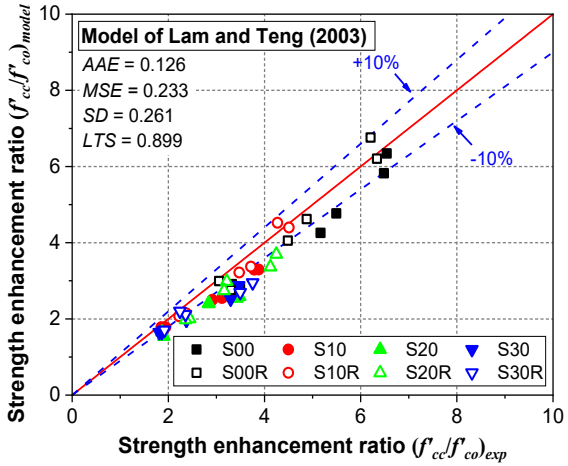

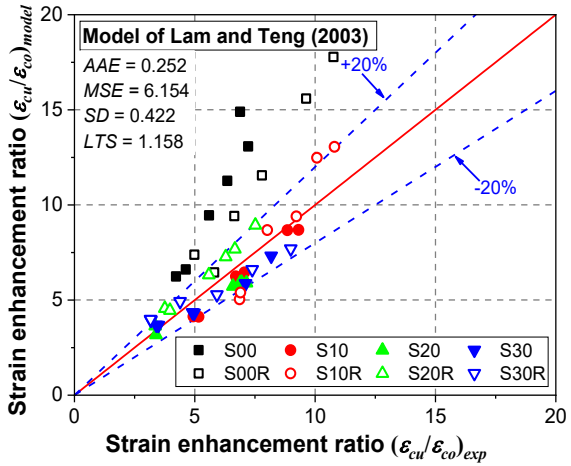

(d) Model of Lam & Teng (2003)

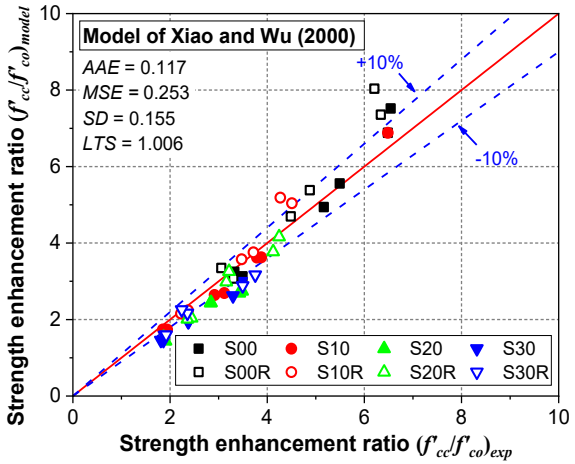

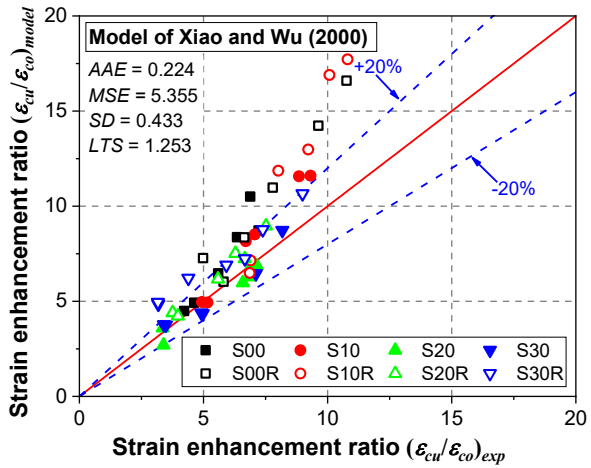

(e) Model of Xiao & Wu (2000)

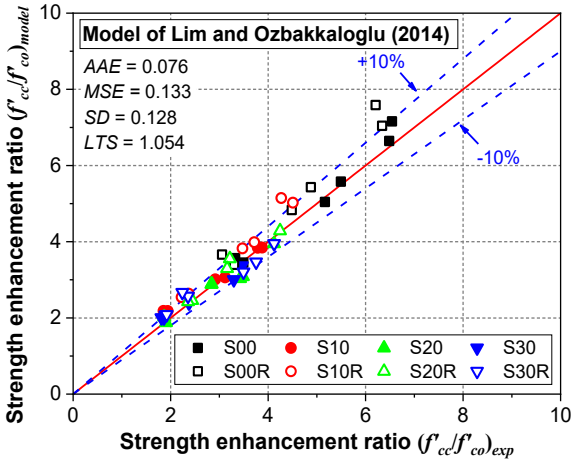

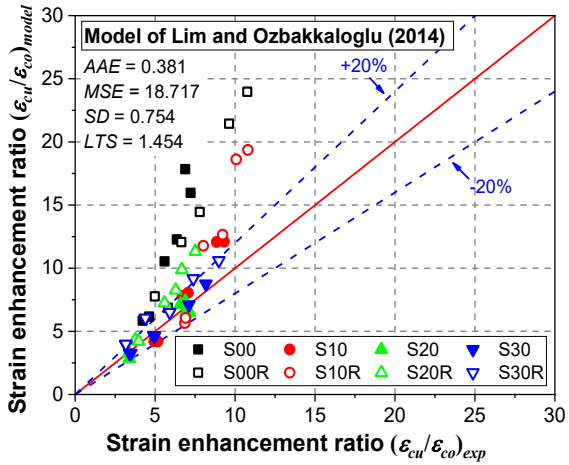

(f) Model of Lim & Ozbakkaloglu (2014)

Figure 7.13. Performance of existing models for strength and strain enhancement ratios

Table 7.5 Statistical assessment of models for the ultimate conditions of confined specimens

Model	Prediction of $f_{cc}^{'} / f_{co}^{'}$				Prediction of $\varepsilon_{cu} / \varepsilon_{co}$			
	AAE	*MSE*	*SD*	*LTS*	*AAE*	*MSE*	*SD*	*LTS*
Ozbakkaloglu & Lim (2013)	0.178	1.173	0.473	0.745	0.329	8.067	0.632	1.338
Yu & Teng (2011)	0.170	0.333	0.347	0.878	0.175	2.286	0.299	1.130
Teng et al. (2009)	0.135	0.235	0.265	0.910	0.670	25.673	1.137	1.666
Lam & Teng (2003)	0.126	0.233	0.261	0.899	0.252	6.154	0.422	1.158
Xiao & Wu (2000)	0.117	0.253	0.155	1.006	0.224	5.355	0.433	1.253
Lim & Ozbakkaloglu (2014)	0.076	0.133	0.128	1.054	0.381	18.717	0.754	1.454
Proposed model	0.061	0.066	0.078	0.996	0.111	0.501	0.157	0.993

As shown in Figure 7.13, it is clear that all the examined models could provide a relatively accurate prediction for CFRP-confined geopolymeric concrete regarding compressive strength. Comparatively, the models developed by Xiao & Wu (2000) and Lim & Ozbakkaloglu (2014) perform better in predicting the test results of compressive strength, while other models predict the compressive strength a little conservative. As for the ultimate axial strain, these selected models all overestimate the test results of this study. However, it can be observed that some models can reasonably fit well for the test results of certain concrete mixes. For instance, the models developed by Yu & Teng (2011) and Lam & Teng (2003) can reasonably fit well the test results except for the results of CFRP-confined geopolymeric concrete based on the mixes of S00, S00R, and S10R. The models developed by Lim & Ozbakkaloglu (2014) and Xiao & Wu (2000) exhibit a satisfactory agreement with the results of CFRP-confined geopolymeric concrete based on the mixes of S20 and S30. This indicates that these extensively used strain models could not apply for all the test CFRP-confined geopolymeric concrete. It is mainly due to that most of the existing models for FRP-confined concrete were based on the test results of FRP-confined conventional concrete, while the prepared geopolymeric concrete has different intrinsic responses from the conventional one. Some researchers have also observed a similar

phenomenon that the existing models could not provide an accurate prediction for the behavior of non-conventional concrete under confinement (Abdesselam et al. 2019; Chan et al. 2019; Gao et al. 2016; Li et al. 2010; Wang et al. 2018)

7.4.3 Proposed models for CFRP-confined geopolymeric concrete

Following the lead of the above comparison, the necessity of alternative models for the prediction of the ultimate conditions for CFRP-confined geopolymeric concrete is evident. Based on the review work by Ozbakkaloglu et al. (2013), most of the better performing expressions have the form of a power function of the strength enhancement ratio ($f_{cc}^{'} / f_{co}^{'}$) and the confinement ratio ($f_{lu,a}^{'} / f_{co}^{'}$), which can be expressed as Eq. (7.6) and with the exponent no more than 1.0. Also, this kind of format is consistent with the trend observed in Figure 7.11, in which with the increase of the confinement ratio, the strength enhancement ratio increases but at a decreased pace.

$$\frac{f_{cc}^{'}}{f_{co}^{'}} = 1 + k_1 \left(\frac{f_{lu,a}}{f_{co}^{'}} \right)^n \tag{7.6}$$

where k_1 is the coefficient of strength enhancement, and n is the exponent to be determined.

Therefore, Eq. (7.6) was utilized to predict the compressive strength of CFRP-confined geopolymeric concrete. Based on the regression analysis using the test results, the fitting coefficients k_1= 3.70 and n = 0.81 was determined, as illustrated in Figure 7.11. Thus, the compressive strength model for CFRP-confined geopolymeric concrete can be expressed by Eq. (7.7). Figure 7.14(a) shows the theoretical values by the proposed model against the experimental results. In addition, Table 7.5 provides the statistical indicators of the proposed model. Apparently, the proposed model could provide highly accurate and consistent prediction results for the test CFRP-confined geopolymeric concrete.

$$\frac{f_{cc}^{'}}{f_{co}^{'}} = 1 + 3.70\left(\frac{f_{lu,a}}{f_{co}^{'}}\right)^{0.81} \tag{7.7}$$

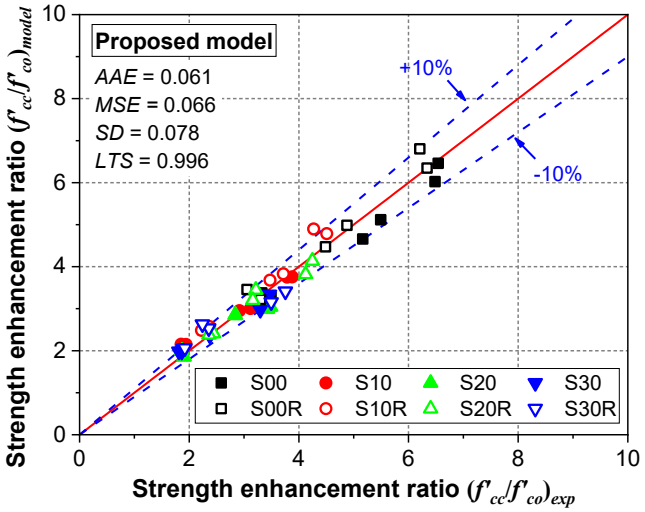

(a) Strength enhancement ratio

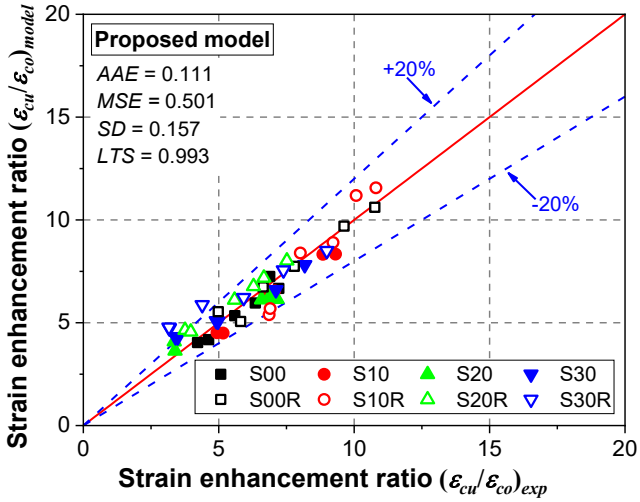

(b) Strain enhancement ratio

Figure 7.14. Performance of proposed model for strength and strain enhancement ratios

As for the strain enhancement ratio, numerous studies have suggested that it can be correlated with the confinement ratio. However, it can be seen from Figure 7.12 that the strain enhancement ratio of CFRP-confined geopolymeric concrete can be related linearly

to the confinement ratio for a given type of concrete mix, but separate expressions are needed for different concrete mixes. Therefore, the confinement ratio is not the only parameter that accounts for the variation of strain enhancement ratio. Based on the unified expression for the ultimate strain proposed in the study by Lam & Teng (2003), the strain enhancement ratio can be taken as Eq. (7.8), which is a function of the confinement stiffness (E_l), hoop rupture strain ($\varepsilon_{h,rup}$), and unconfined concrete elastic modulus (E_c).

$$\varepsilon_{cu} = c\varepsilon_{co} + k_2 \left(\frac{E_l}{E_c} \right)^{\alpha} \varepsilon_{h,rup}^{\beta} \tag{7.8}$$

where c is the normalized ultimate strain of unconfined concrete; k_2 is the strain enhancement coefficient; α and β are the exponents to be determined.

The values of the parameters in Eq. (7.8) were determined using the experimental results of this study, and thus the following expression is suggested for CFRP-confined geopolymeric concrete:

$$\varepsilon_{cu} = 1.69\varepsilon_{co} + 12.1 \left(\frac{E_l}{E_c} \right)^{0.8} \varepsilon_{h,rup}^{1.07} \tag{7.9}$$

Figure 7.14(b) shows the comparison between the strain enhancement ratio predictions by the proposed model against the test results. A perfect agreement between the test results and the predicted results by Eq. (7.9) is observed. Furthermore, the statistical assessment (as shown in Table 7.5) confirms the superior performance of the proposed model over those existing models in predicting the test results of this study. However, more test data should be obtained in the future for further verification of the proposed stress and strain models.

7.5 Summary

(1) For unconfined concrete, the RA replacement adversely affects the performance of geopolymeric concrete in terms of compressive strength and elastic modulus, while the inclusion of slag results in the improvement in these properties.

(2) The confinement by CFRP jackets has an enhancement on both compressive strength and ultimate strain for geopolymeric concrete, e.g., for the GRAC with 30% slag content, the compressive strength and ultimate axial strain were increased by up to 98% and 218%, respectively, due to the confinement by 1-ply CFRP jacket. Moreover, the enhancement is more pronounced with the increase in the thickness of CFRP jackets.

(3) In addition to the decreased compressive strength, the RA replacement results in the reduced volumetric dilation of CFRP-confined geopolymeric concrete. Besides, the stress-strain relationships of CFRP-confined GRAC show a longer transition zone than the counterpart based on GNAC. On the other hand, the reverse trend was achieved due to the incorporation of slag, including the increased compressive strength and obvious volumetric dilation, as well as, the reduced radius for the transition part of the stress-strain curves.

(4) The aggregate types and slag content do not have a significant effect on the CFRP confinement performance for geopolymeric concrete in terms of compressive strength. In addition, the existing FRP-confined concrete models could provide a reasonable prediction for the strength enhancement ratio of the test CFRP-confined geopolymeric concrete.

(5) The confinement performance of CFRP jackets for the ultimate axial strain of CFRP-confined geopolymeric concrete is influenced by the aggregate type and the slag content. The examined models all overestimate the ultimate strain values of the test CFRP-confined geopolymeric concrete, but some models can reasonably fit well for the test results based on certain geopolymeric concrete mixes.

(6) By comparing the proposed stress and strain models with the experimental results of the current study, it is concluded that the proposed models have very good accuracy and consistency in determining the ultimate conditions for the CFRP-confined geopolymeric concrete in this study.

CHAPTER 8: MECHANICAL PERFORMANCE OF CFRP-CONFINED SUSTAINABLE GRAC UNDER CYCLIC COMPRESSION

The RA replacement usually causes a reduction in the compressive strength and stiffness (Tam et al. 2018; Xiao et al. 2012b). Moreover, this adverse effect has been reported to be pronounced when the concrete is subjected to repeated unloading and reloading (Hu et al. 2018; Liu et al. 2019a; Ma et al. 2013; Xiao et al. 2013a). Therefore, for the further safe and reliable design of FRP-confined GRAC, it is necessary to comprehend its mechanical behavior under cyclic loading. Moreover, the mechanical behavior of concrete under cyclic axial compression is of particular importance for the accurate modeling of the corresponding structure members under seismic loading because the current practice for evaluating the seismic performance is mainly based on the response under cyclic loading.

In light of these research demands, this chapter presents an experimental study on the static and cyclic compression behaviors of CFRP-confined GRAC. Special attention is devoted to the failure model, compressive stress-strain behavior, and axial-lateral strain relationship. Meanwhile, the results are compared with the predictions by existing models for evaluating the applicability of these models to CFRP-confined GRAC.

8.1 Experimental program

8.1.1 Specimen design

In the present study, eight series, a total of 24 CFRP-confined geopolymeric concrete cylinders, were prepared and tested, which covered four RA replacement ratios (i.e., 0%, 25%, 50%, and 100%) and two thicknesses of CFRP jackets (i.e., 1 and 2 layers). The details of the test specimens are listed in Table 7.1. It has been observed the low scatter for the test results of the identical FRP-confined specimens in previous studies (Chen et al. 2016a; Gao et al. 2016; Ozbakkaloglu & Xie 2016). Therefore, for each series of specimen designs, one specimen was made for the test of monotonic compression, and

two specimens were made for the test of cyclic compression. All the specimens had a nominal diameter of 100 mm (the diameter of the concrete core) and a height of 200 mm. The identification of the specimens in Table 7.1 starts with the letter R, followed by an Arabic numeral to represent the RA replacement ratio (i.e., 0%, 25%, 50%, and 100%). The subsequent letter-number combination indicates the number of CFRP layers (i.e., 1 and 2 layers). As for the next letter of the identification, M and C denote the monotonic load pattern and cyclic load pattern, respectively. Finally, an Arabic numeral is used to differentiate the nominally identical specimens under cyclic loading. For instance, the specimen of R25F1C1 denotes the first specimen of the two specimens of GRAC with the replacement ratio of 25% confined by a one-ply CFPR jacket under cyclic loading.

Table 8.1 Details of CFRP-confined geopolymeric concrete

Series	Specimen	Replacement ratio	Number of CFRP layers	Load pattern
1	R00F1M	0%	1	M
	R00F1C1,2		1	C
2	R00F2M	0%	2	M
	R00F2C1,2		2	C
3	R25F1M	25%	1	M
	R25F1C1,2		1	C
4	R25F2M	25%	2	M
	R25F2C1,2		2	C
5	R50F1M	50%	1	M
	R50F1C1,2		1	C
6	R50F2M	50%	2	M
	R50F2C1,2		2	C
7	R100F1M	100%	1	M
	R100F1C1,2		1	C
8	R100F2M	100%	2	M
	R100F2C1,2		2	C

Note: M and C denote the monotonic load pattern and cyclic load pattern, respectively

8.1.2 Raw materials

The raw materials for geopolymeric concrete preparation, including fine aggregate, coarse aggregate, fly ash, slag, and alkali activator, were in accordance with that in

Chapter 4. Thus, the details for these materials could be found in Section 4.1.1. Additionally, the properties of CFRP composite materials could be found in Chapter 7 (as shown in Section 7.1.2).

8.1.3 Specimen preparation

The details of the concrete mixture proportion are presented in Table 8.2. Cylindrical specimens with a diameter of 100 mm and a height of 200 mm were prepared in accordance with the concrete mixing and curing processes reported in Chapter 3 (as shown in Section 3.1.3). Three plain concrete specimens were tested as the control specimen of each mix design group to obtain the mechanical properties. The average values of peak axial compressive strength ($f_{co}^{'}$), the axial strain at peak axial compressive strength (ε_{co}), and the elastic modulus (E_c) are shown in Table 8.3. The increase in the RA replacement ratios leads to the reduction in compressive strength; specifically, the reductions of 1.0%, 18.6%, and 18.8% are identified for the replacement ratios of 25%, 75%, and 100%, respectively. Similar results can also be observed in the trend of elastic modulus. As for the axial strain at peak axial compressive strength, there is no noticeable difference between the concrete with different RA replacement ratios, except that a significant increase is found in the specimen with full replacement of RA.

Table 8.2 Mix proportion for geopolymeric concrete

Replacement ratio	Mix proportion (unite weight: kg/m^3)						
	Fly ash	Slag	Na_2SiO_3	NaOH	Sand	NA	RA
0%	336	84	165	66	550	1220	0
25%	336	84	165	66	550	915	305
50%	336	84	165	66	550	610	610
100%	336	84	165	66	550	0	1220

As for the specimens to be confined by CFRP jackets, the preparation procedure was followed that in the previous chapter (as shown in Section 7.1.4).

Table 8.3 Test results for CFRP-confined geopolymeric concrete

Specimen	$f_{co}^{'}$ (MPa)	E_c (GPa)	ε_{co} (%)	$f_{cc}^{'}$ (MPa)	$f_{cc}^{'} / f_{co}^{'}$	ε_{cu} (%)	$\varepsilon_{cu} / \varepsilon_{co}$	$\varepsilon_{h,rup}$ (%)	$f_{lu,a}^{'}$ (MPa)	$f_{lu,a}^{'} / f_{co}^{'}$
R00F1M	43.17	21.63	0.254	64.80	1.50	0.740	2.91	-0.793	5.72	0.13
R00F1C1				64.31	1.49	0.868	3.41	-0.879	6.34	0.15
R00F1C2				60.32	1.40	0.773	3.04	-0.820	5.91	0.14
R00F2M				89.81	2.08	1.173	4.61	-0.831	11.98	0.28
R00F2C1				91.98	2.13	1.332	5.24	-0.970	13.99	0.32
R00F2C2				90.96	2.11	1.202	4.73	-0.841	12.13	0.28
R25F1M	42.73	21.70	0.280	63.77	1.49	0.799	2.86	-0.882	6.35	0.15
R25F1C1				69.61	1.63	1.087	3.89	-1.161	8.37	0.20
R25F1C2				66.66	1.56	0.926	3.31	-1.044	7.52	0.18
R25F2M				84.61	1.98	1.123	4.01	-0.700	10.09	0.24
R25F2C1				84.80	1.98	1.264	4.52	-0.721	10.40	0.24
R25F2C2				80.61	1.89	1.182	4.22	-0.712	10.27	0.24
R50F1M	35.14	18.05	0.271	57.51	1.64	0.710	2.62	-0.892	6.43	0.18
R50F1C1				57.83	1.65	0.766	2.82	-0.911	6.57	0.19
R50F1C2				59.75	1.70	0.950	3.50	-1.182	8.52	0.24
R50F2M				90.69	2.58	1.332	4.91	-0.766	11.04	0.31
R50F2C1				95.95	2.73	1.772	6.53	-0.923	13.30	0.38
R50F2C2				96.92	2.76	1.858	6.85	-0.964	13.89	0.40
R100F1M	35.03	13.91	0.339	61.92	1.77	1.147	3.38	-1.058	7.62	0.22
R100F1C1				62.88	1.79	1.221	3.60	-1.136	8.19	0.23
R100F1C2				64.88	1.85	1.290	3.80	-1.107	7.98	0.23
R100F2M				91.11	2.60	1.990	5.87	-1.001	14.43	0.41
R100F2C1				93.05	2.66	2.050	6.04	-1.007	14.52	0.41
R100F2C1				93.87	2.68	2.113	6.23	-1.092	15.75	0.45

8.1.4 Experimental program

The test setup and instrumentation were the same as that in Chapter 7 (as shown in Section 7.1.5). While in this study, two loading patterns were employed, specifically the monotonic loading pattern and cyclic loading pattern. For the monotonic loading scheme, the increasing load was applied to the specimen until failure. For the cyclic loading scheme, cyclic loading involving unloading and reloading cycles was applied with approximately 0.15% axial strain increments before failure. That is, the specimen was loaded by increasing the axial strain to a prescribed value, and then was unloaded to a target load level. The specimen was next reloaded to the next prescribed axial strain for cyclic loading. The target load, at which unloading was terminated and reloading started, was adopted at about 10 kN to prevent any undesired movement of the specimen and the slackness of the test system.

8.2 Experimental results

8.2.1 Failure patterns

All the specimens failed by the rupture of CFRP jackets due to the lateral expansion of the core concrete. The CFRP rupture was generally found to occur outside the overlap zone and at the mid-region of the specimen. Upon failure, plentiful macrocracks could be observed in the core concrete. Additionally, only a slight difference was found between the specimens with different RA replacement ratios and CFRP jacket thicknesses. Specifically, the specimens with lower RA replacement ratios or thicker CFRP jackets behaved in a more brittle manner at failure, exhibiting an explosion of the core concrete upon the CFRP rupture. On the other side, the presence of cyclic loading did not significantly alter the failure pattern. This agrees with the test results of the CFRP-confined OPC-based RAC under static and cyclic compression reported by Li et al. (2019a). Typical failure models are shown in Figure 8.1.

(a) Replacement ratio of 0%, number of CFRP layers of 2

(b) Replacement ratio of 100%, number of CFRP layers of 2

Figure 8.1. Typical failure modes of CFRP-confined geopolymeric concrete

8.2.2 Stress-strain curves

Figure 8.2 shows the axial stress against the axial and lateral strains of test specimens under various RA replacement ratios and thicknesses of CFRP jackets. For each figure, three specimens, including one subjected to monotonic loading and two subjected to cyclic loading, are put together for comparison. In this study, the axial strain was calculated from the average value of the two LVDTs, and the lateral strain was calculated from the average value of the five lateral strain gauges within the non-overlap zone. Additionally, the axial compressive strain is defined to be positive, while the lateral tensile strain is defined to be negative.

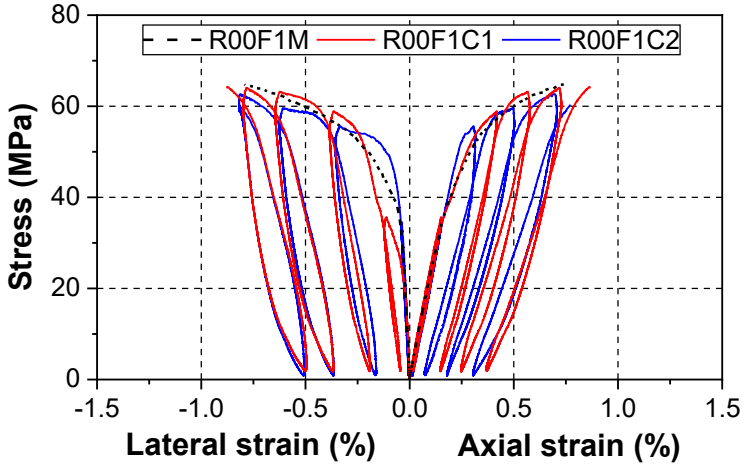

(a) Replacement ratio of 0%, number of CFRP layers of 1

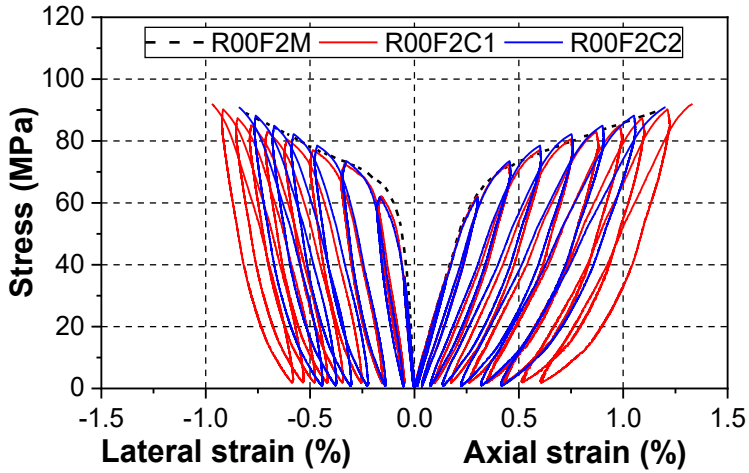

(b) Replacement ratio of 0%, number of CFRP layers of 2

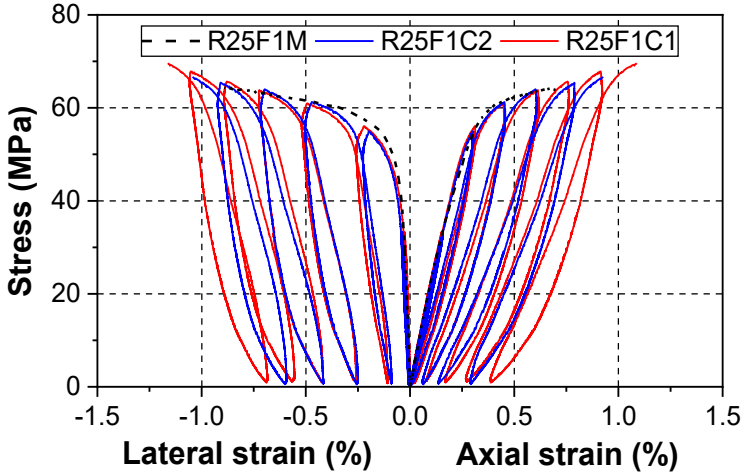

(c) Replacement ratio of 25%, number of CFRP layer of 1

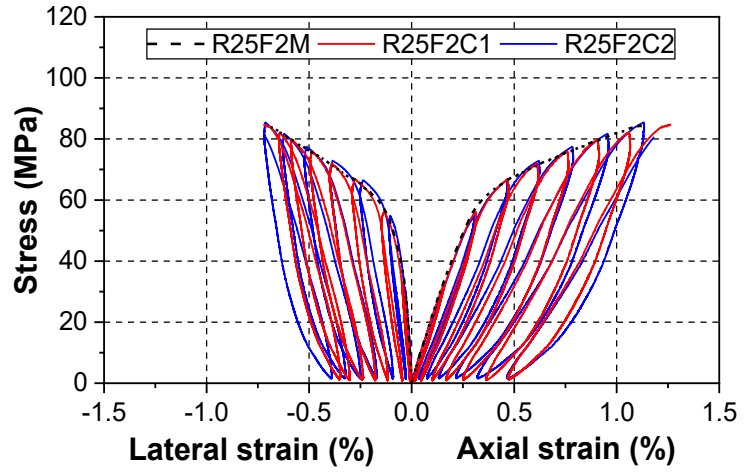

(d) Replacement ratio of 25%, number of CFRP layer of 2

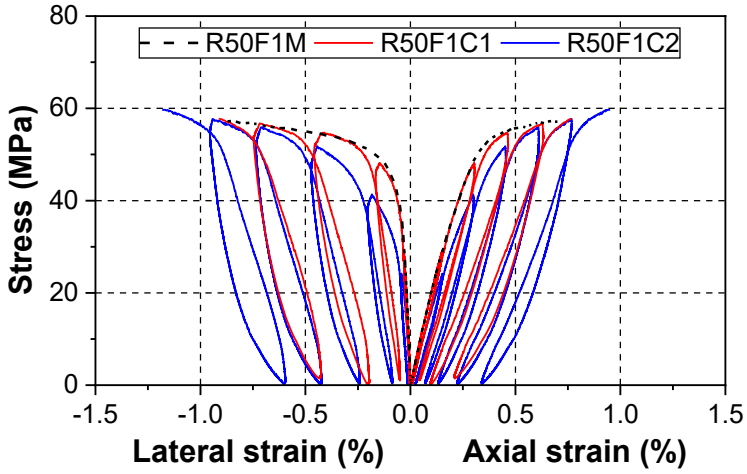

(e) Replacement ratio of 50%, number of CFRP layer of 1

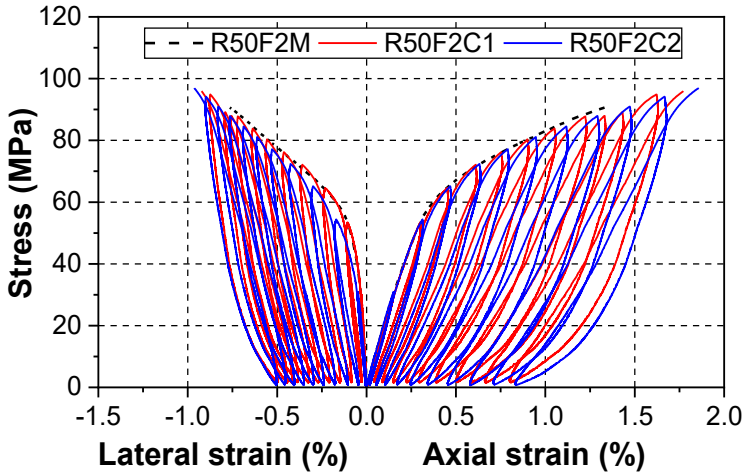

(f) Replacement ratio of 50%, number of CFRP layer of 2

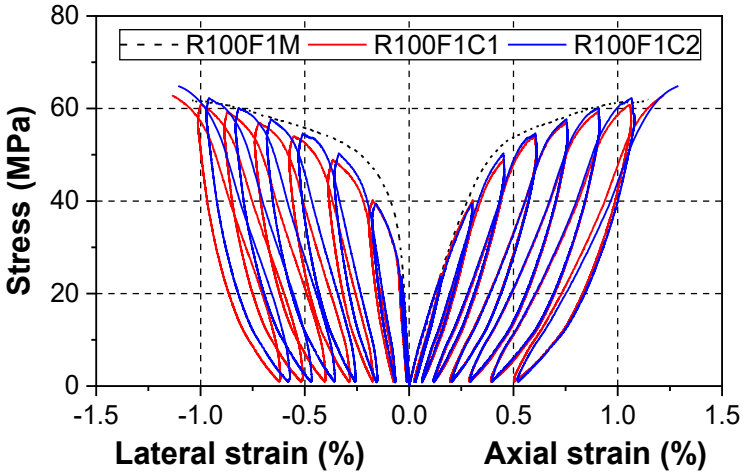

(g) Replacement ratio of 100%, number of CFRP layer of 1

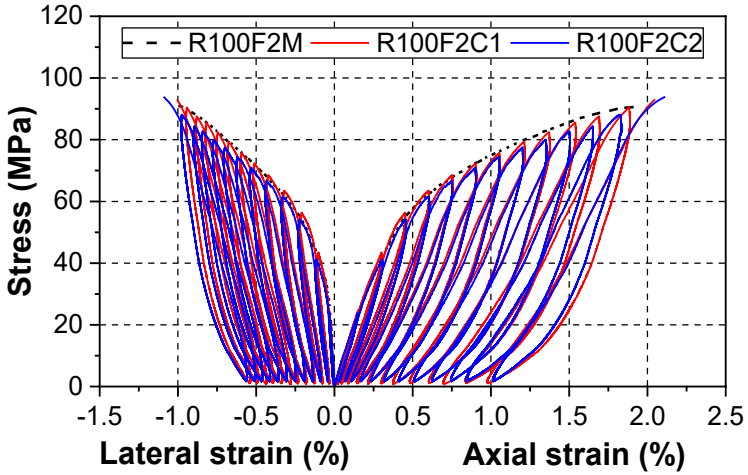

(h) Replacement ratio of 100%, number of CFRP layer of 2

Figure 8.2. Stress-strain curves of CFRP-confined geopolymeric concrete

As shown in Figure 8.2, under monotonic loading, the stress-strain curve behaves in a bilinear pattern with a transition zone between the two linear portions. As for the cyclic stress-strain curve, regardless of the axial strain and lateral strain, the line that connects the upper boundary, or namely the envelope curve, is consistent with the corresponding monotonic loading curve (Lam et al. 2006). While, exceptions could be seen in the specimens R00F1C1, R00F1C2, and R50F1C2, where the envelope curve of the stress-strain curve under cyclic loading deviates from the corresponding stress-strain curve under monotonic loading. However, it should be noted that these discrepancies are relatively insignificant. This type of phenomenon has also been reported by previous studies (Abbasnia & Ziaadiny 2010; Li et al. 2019a; Li & Wu 2016; Li et al. 2016a), and it is probably due to some inevitable test measurement errors (Li et al. 2019a). Thus, the envelope hypothesis, which has been previously validated for confined OPC-based NAC or even confined OPC-based RAC, is firstly validated as applicable to CFRP-confined GNAC or GRAC (Abbasnia et al. 2012; Li et al. 2019a; Ozbakkaloglu & Akin 2012). The envelope hypothesis could be described as that the envelope curve of the stress-strain curve under cyclic loading can be assumed to be the same as the stress-strain curve obtained from monotonic loading (Lam & Teng 2009).

8.2.3 Axial-lateral strain relationship

Figure 8.3 presents the curves of axial strain versus lateral strain for the test specimens under various RA replacement ratios and thicknesses of CFRP jackets, where three specimens, including one subjected to monotonic loading and two subjected to cyclic loading, are collected and illustrated in one figure for comparison. It could be observed that the initial axial-lateral strain response of the specimens under monotonic loading develops linearly, and then the axial-lateral strain curve enters the second approximately linear region with a slowly increasing slope. As for the cyclic axial-lateral strain relationship under the first several unloading/reloading cycles, the upper boundary is consistent with the corresponding monotonic axial-lateral strain curve. However, with an increase in the unloading/reloading cycles, the reloading part of the cyclic axial-lateral strain curve is above the corresponding monotonic axial-lateral strain curve. In other words, under a certain lateral strain, a larger axial strain is observed for the reloading

branch of cyclic axial-lateral strain curve, in comparison with the corresponding monotonic axial-lateral strain. Moreover, this phenomenon is more obvious for the specimens with two-layer CFRP jackets as it has relatively high ultimate axial strains. This observation is reasonable and can be explained as that with an increase in the unloading/reloading cycles, the core concrete experienced severe degradation in the strength, and consequently, the confinement degree (i.e., the ratio of the confinement stiffness to the unconfined strength of core concrete) significantly increased. It has been reported that under a given lateral strain, the axial strain is larger for a higher confinement degree (Jiang & Teng 2007). Even though, it should be noted that the endpoint of the reloading path still lays on the corresponding monotonic axial-lateral strain curve. Accordingly, to some extent, the envelope hypothesis could be applied to the axial-lateral strain relationship of CFRP-confined geopolymeric concrete. That is, the envelope curve of the axial-lateral strain curve under cyclic loading, obtained by consecutively connecting the terminating points of reloading paths, is consistent with the axial-lateral strain curve obtained from monotonic loading.

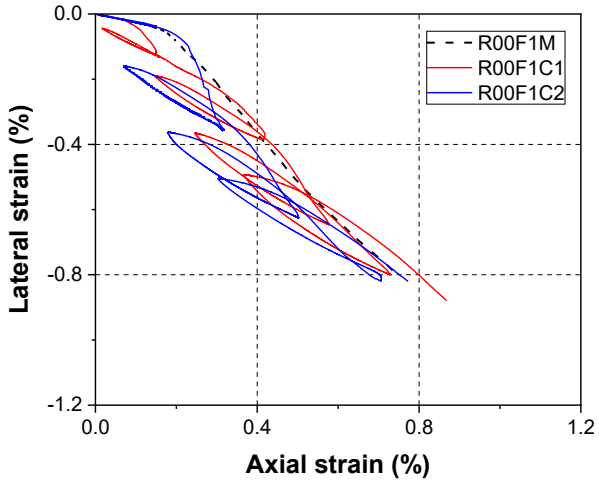

(a) Replacement ratio of 0%, number of CFRP layer of 1

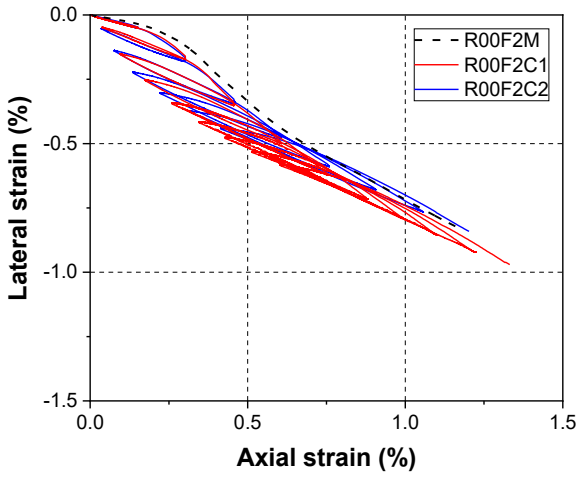

(b) Replacement ratio of 0%, number of CFRP layer of 2

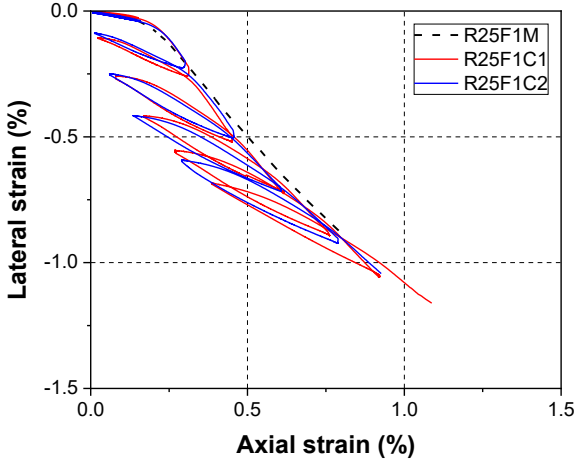

(c) Replacement ratio of 25%, number of CFRP layer of 1

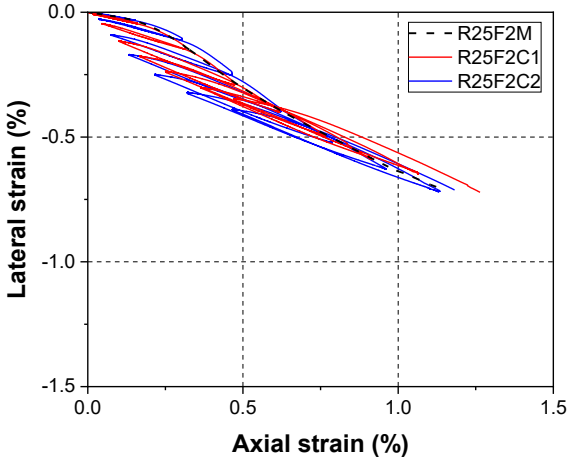

(d) Replacement ratio of 25%, number of CFRP layer of 2

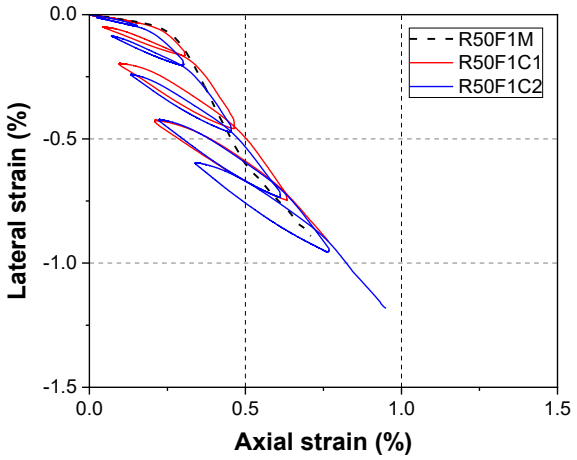

(e) Replacement ratio of 50%, number of CFRP layer of 1

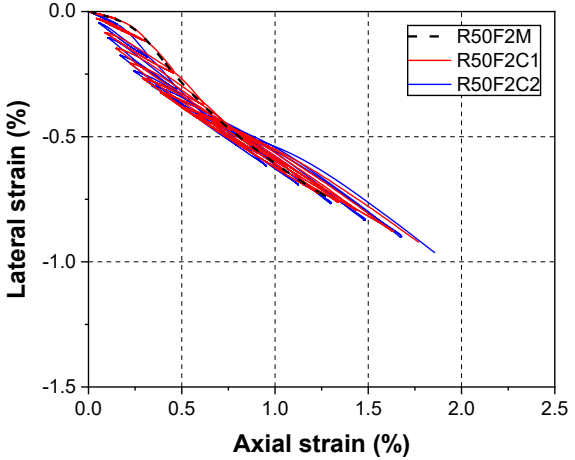

(f) Replacement ratio of 50%, number of CFRP layer of 2

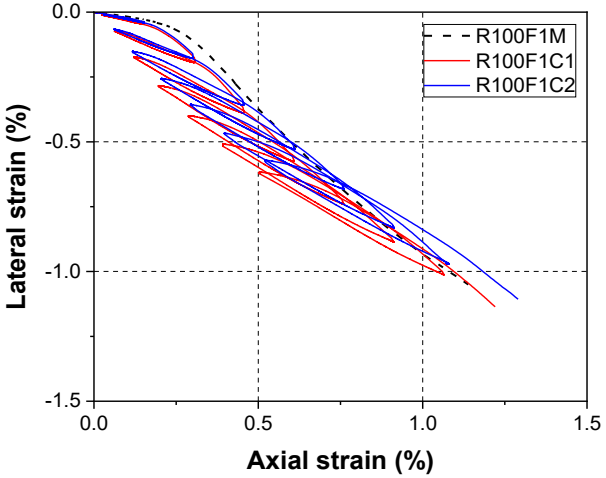

(g) Replacement ratio of 100%, number of CFRP layer of 1

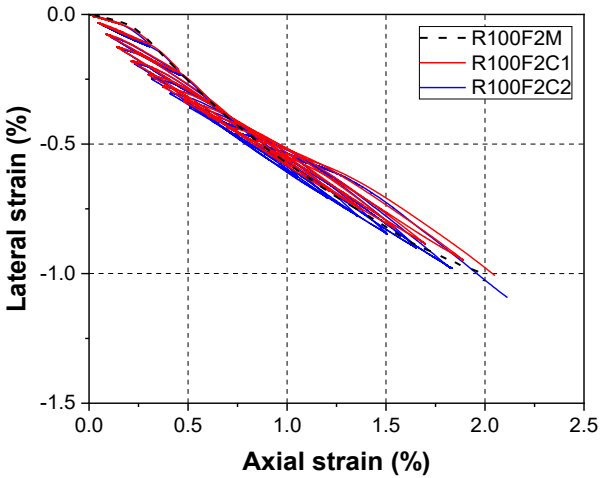

(h) Replacement ratio of 100%, number of CFRP layer of 2

Figure 8.3. Axial-lateral strain curves of CFRP-confined geopolymeric concrete

8.3 Results and discussions

Based on the above observations, the typical framework of stress-strain relationships of FRP confined specimens subjected to cyclic loading is presented in Figure 8.4.

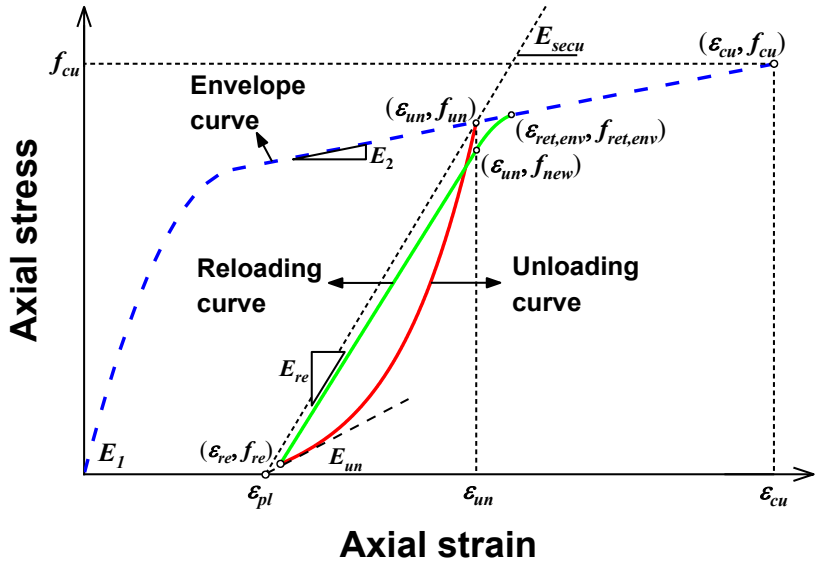

Figure 8.4. Typical stress-strain curve of CFRP-confined geopolymeric concrete

The typical cyclic behavior of FRP-confined concrete includes the unloading and reloading paths. The unloading path is from the unloading point (ε_{un}, f_{un}) on the envelope curve to the terminating point (ε_{re}, f_{re}). In some previous studies, the unloading path intersects the strain axis at a strain value, which is referred to as the plastic strain or permanent strain (ε_{pl}) (Abbasnia et al. 2013; Abbasnia & Ziaadiny 2010). While, since the unloading path was terminated at a stress value slightly above zero in the present study, the plastic strain was estimated from the stress-strain curves by extending the unloading path smoothly to the zero stress point (Lam & Teng 2009). In addition, the tangent slope of the unloading curve at this point is defined as the residual modulus ($E_{un,0}$). The reloading path is from the reloading point (ε_{re}, f_{re}) to the envelope curve at the envelope returning point ($\varepsilon_{ret,env}$, $f_{ret,env}$). The slope of the initial linear part of the reloading path is defined as the reloading modulus (E_{re}). In order to evaluate the degree of stress

deterioration under cyclic loading, the stress on the reloading path at the last unloading strain is obtained as the new stress (f_{new}).

Additionally, E_1 and E_2 represent the slopes of the initial branch and the second branch of the envelope curve respectively, and $E_{\sec u}$ denotes the unloading secant modulus, which equals the slope of the line connecting the beginning point (ε_{un}, f_{un}) and the endpoint (ε_{pl}, 0) of the unloading curve. In the following section, the key shape factors that govern the cyclic stress-strain curves are discussed.

8.3.1 Ultimate condition

Table 8.3 summarizes the key experimental results, including the peak stress ($f_{cc}^{'}$), the ultimate axial strain (ε_{cu}), the maximum CFRP hoop strain ($\varepsilon_{h,rup}$), and the actual lateral confining pressure ($f_{lu,a}^{'}$). The actual lateral confining pressure ($f_{lu,a}^{'}$) can be calculated according to Eq. (8.1).

$$f_{lu,a}^{'} = \frac{2E_{frp}\varepsilon_{h,rup}t_{frp}}{D} \tag{8.1}$$

where t_{frp} represents the thickness of CFRP jackets and D denotes the diameter of core concrete.

Figure 8.5 shows the effects of confinement ratio ($f_{lu,a}^{'} / f_{co}^{'}$) on the strength enhancement ratio ($f_{cc}^{'} / f_{co}^{'}$) and strain enhancement ratio ($\varepsilon_{cu} / \varepsilon_{co}$). The strength enhancement ratio and strain enhancement ratio vary from 1.40 to 2.76, and from 2.61 to 6.84, respectively, with the increase of confinement ratios. This confirms the enhancement effect achieved by the CFRP confinement.

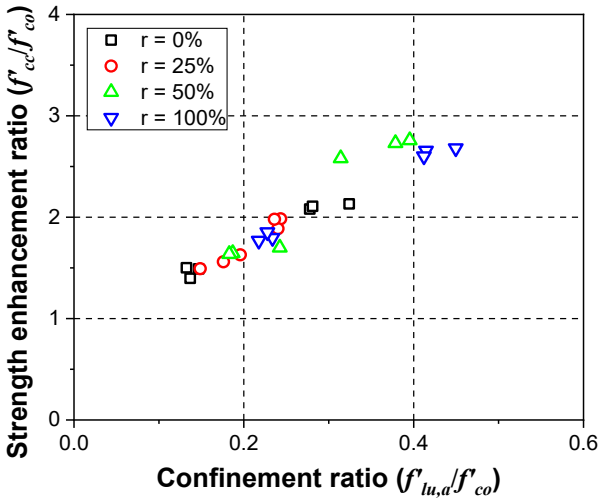

(a) Strength enhancement ratio

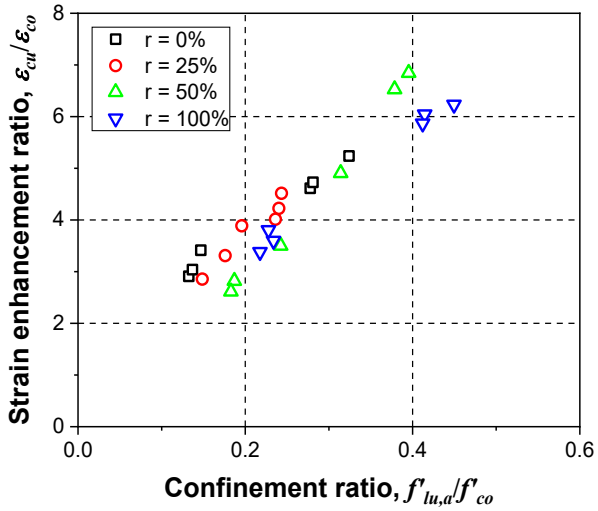

(b) Strain enhancement ratio

Figure 8.5. Effects of confinement ratio on strength enhancement ratio and stain enhancement ratio

Additionally, as shown in Figure 8.5(a), the specimens with a similar confinement ratio developed comparable strength enhancement ratios. That is to say, the RA replacement does not have an obvious effect on the CFRP confinement efficiency for geopolymeric concrete in terms of strength enhancement ratio. It also indicates that the presence of cyclic loading does not have an influence on the strength enhancement ratio in comparison with that under monotonic loading, and consequently, the confinement

efficiency regarding the strength enhancement ratio is consistent for the specimens subjected to different load patterns.

Similar results could be observed in Figure 8.5(b), that the effect of loading pattern on the strain enhancement ratio is negligible. This states that, regarding the strain enhancement, the confinement efficiency for the specimens under monotonic and cyclic loading is almost identical. However, slight differences can be detected between the relationships of strain enhancement ratios and confinement ratios for the specimens with different RA replacement ratios. This can be attributed to that the strain enhancement efficiency is influenced by the variation in the intrinsic response of core concrete, in the current study, due to the RA replacement (Lam & Teng 2003; Lim & Ozbakkaloglu 2015).

Previously, numerous models have been proposed to predict the ultimate condition of FRP-confined OPC-based concrete. The test results are further compared with existing models to examine the applicability of such models to CFRP-confined geopolymeric concrete in this study. Five models, which were widely used and also considered a large amount of experimental database of FRP-confined OPC-based concrete in the derivation of the models, were selected, i.e., the models proposed by Ozbakkaloglu & Lim (2013), Yu & Teng (2011), Teng et al. (2009), Lam & Teng (2003), and Xiao & Wu (2003). Furthermore, a model has been proposed by Lim & Ozbakkaloglu (2014) to predict the behavior of actively confined concrete and has recently been validated feasible for actively confined geopolymeric concrete (Gholampour et al. 2019). Therefore, the model by Lim & Ozbakkaloglu (2014) is also included to evaluate its feasibility to CFRP-confined geopolymeric concrete of this study. Table 7.4 provides the details of these selected models. A comparison between the experimental results from this study and the predictions of the above models is presented in Figure 8.6. Besides, three statistical indicators are present in Table 7.4, including the average absolute error (*AAE*), the mean square error (*MSE*), and the standard deviation (*SD*). The expressions of these indicators have been given by Eqs. (7.3) to (7.5).

As shown in Figure 8.6(a), these selected models can fit the test results of ultimate strength well, except that some prediction results by the models of Yu & Teng (2011) and

Lim & Ozbakkaloglu (2014) show large discrepancies of up to 20% compared with the test results. Moreover, the statistical indicators in Table 7.4 demonstrate that the model of Xiao & Wu (2003) could provide the best predictions for the test results of this study, which is followed by the models of Ozbakkaloglu & Lim (2013) and Lam & Teng (2003). As for the ultimate strain, the models of Lam & Teng (2003), Xiao & Wu (2003), and Lim & Ozbakkaloglu (2014) show excellent performance in predicting the test results of the present study. Comparatively, the model of Lim & Ozbakkaloglu (2014) performs better, having relatively high consistency and accuracy, according to the statistical indicators in Table 7.4. Overall, the models of Lam & Teng (2003) and Xiao & Wu (2003) can provide accurate predictions for both peak strength and ultimate strain of the test specimens.

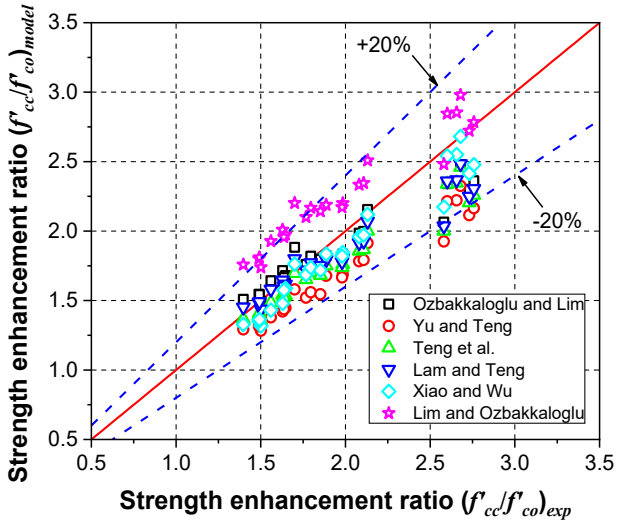

(a) Strength enhancement ratio

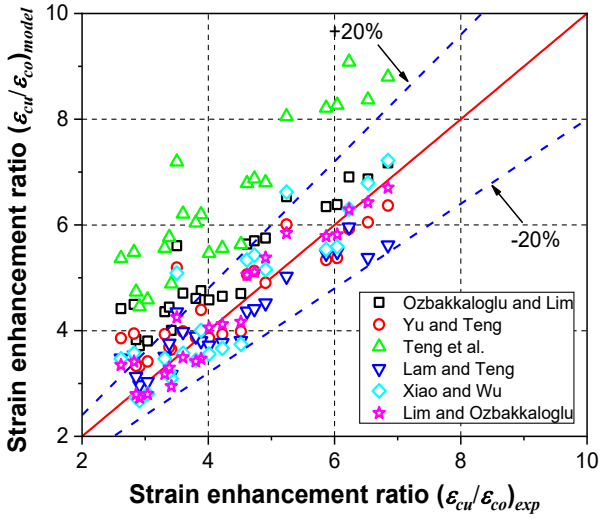

(b) Strain enhancement ratio

Figure 8.6. Performance of exiting models for the ultimate strength and ultimate strain

8.3.2 Residual modulus

Figure 8.7 shows the relationship between residual modulus ($E_{un,0}$) and unloading strain (ε_{un}). As shown in this figure, the residual modulus reduces when the unloading strain increases. In addition, the reduction rate is fast at small unloading strains, but slows down as the unloading strain increases. Moreover, it could be observed that the RA replacement affects the relationship between residual modulus and unloading strain. Specifically, the

specimens with higher RA replacement ratios exhibit lower initial residual modulus, attributing to the decreased stiffness after the RA replacement (Li et al. 2019a; Li et al. 2016a). However, the difference in the residual modulus between the specimens with different RA replacement ratios gradually vanishes at sufficiently large unloading strains. It is also found from Figure 8.7 that the thickness of CFRP jackets has a negligible effect on the trend line of residual modulus. Accordingly, these above observations support the statement by Lam & Teng (2009), that the residual modulus is mainly controlled by unloading strain and unconfined concrete strength.

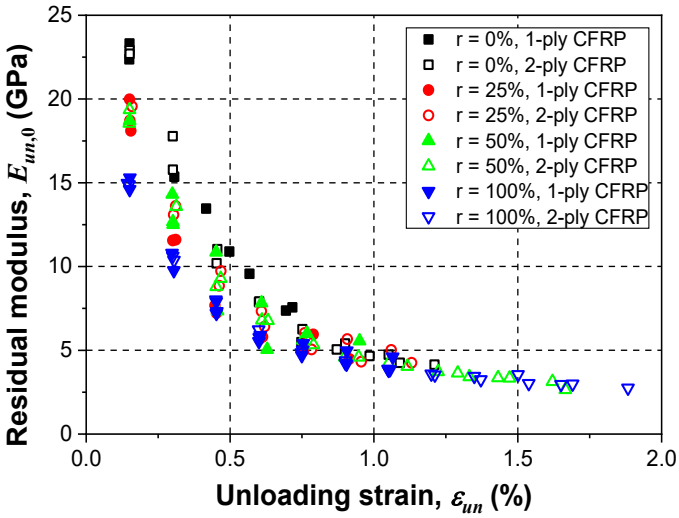

Figure 8.7. Relationship between residual modulus and unloading strain

The previous studies by Lam & Teng (2009) and Li et al. (2018) had proposed two ways of modeling residual modulus of FRP-confined OPC-based concrete. The details of these two models are given by Eqs. (8.2) and (8.3). Figure 8.8 shows a comparison of the test results in this study and the prediction results by the two models. It was seen that both two models underestimate the residual modulus measured in this study, and comparatively, the discrepancies between the prediction and the test result are more considerable for the model by Li et al. (2018). This disparity appears to indicate that geopolymeric concrete has lower stiffness degradation at a certain unloading strain in comparison with OPC concrete.

$$E_{un,0} = \min \begin{cases} \dfrac{0.5 f_{co}^{'}}{\varepsilon_{un}} \\ \dfrac{f_{un}^{'}}{\varepsilon_{un} - \varepsilon_{pl}} \end{cases} \tag{8.2}$$

$$\frac{E_{un,0}}{E_c} = 0.21 \left(\frac{f_{co}^{'}}{f_{30}} \right)^{0.195} \rho^{-0.031} \left(\frac{\varepsilon_{un}}{\varepsilon_{co}} \right)^{-1.115} \tag{8.3}$$

where f_{30} is the concrete strength of 30 MPa, and ρ is the confinement stiffness ratio, which can be defined as

$$\rho = \frac{2 E_{frp} t_{frp}}{D f_{co}^{'}} \tag{8.4}$$

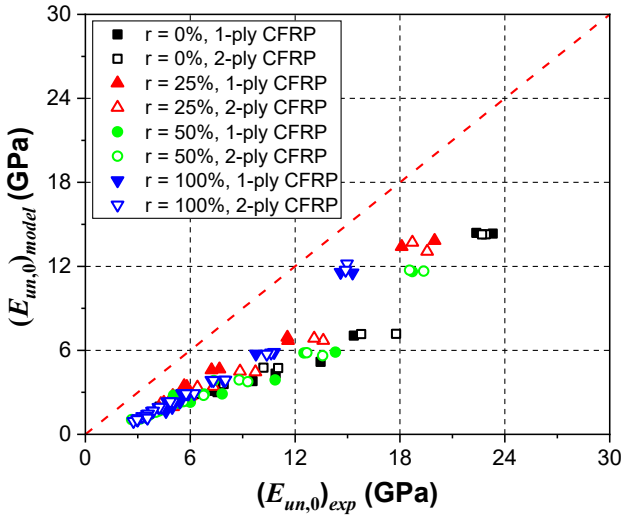

(a) Eq. (8.2) (Lam & Teng (2009))

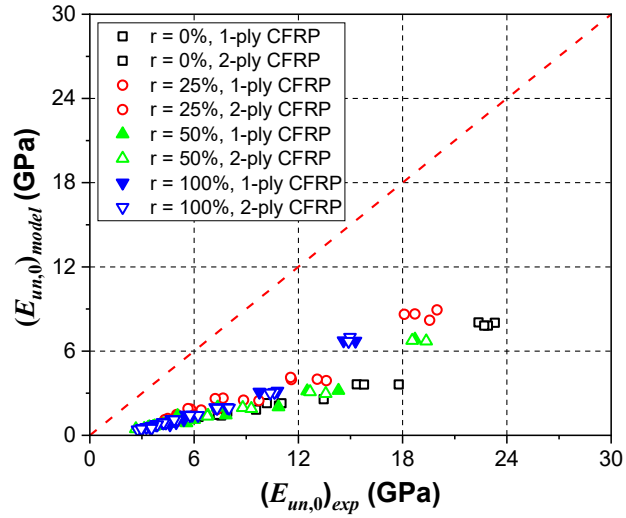

(b) Eq. (8.3) (Li et al. (2018))

Figure 8.8. Performance of existing models for residual modulus

8.3.3 Plastic strain

Figure 8.9 shows the relationship between plastic strain (ε_{pl}) and unloading strain (ε_{un}). It can be seen that, for all the specimens, the plastic strain increases when the unloading strain increases, indicating the damage accumulation of specimens when subjected to cyclic compression. Furthermore, careful inspection shows that the trend of plastic strain changes with the variations in the RA replacement ratio and the thickness of CFRP jackets. Specifically, when the thickness of CFRP jackets is identical, the plastic strain decreases

with the increase of the RA replacement ratio at a given unloading strain. On the other hand, at a certain RA replacement ratio, the specimen with a thicker CFRP jacket presents a lower plastic strain at a given unloading strain. These observations can be explained from the point of different confinement degrees. The confinement degree is more remarkable for the specimens with higher RA replacement ratios due to the decreased unconfined strength of core concrete, and also more remarkable for the specimens with thicker CFRP jackets due to the increased confinement stiffness. Moreover, a high confinement degree could restrain the crack development more effectively, thus resulting in the low plastic strain.

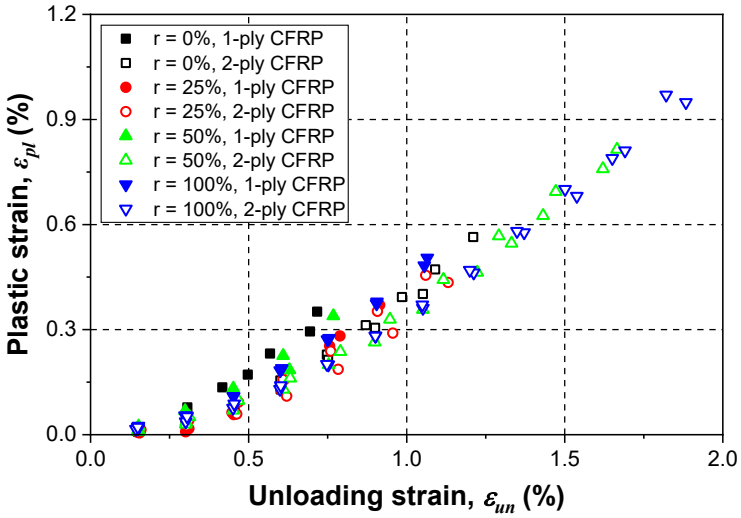

Figure 8.9. Relationship between plastic strain and unloading strain

Previous studies have investigated the relationship between plastic strain and unloading strain. However, parameter studies on plastic strain provide a contrary conclusion. Specifically, Ozbakkaloglu & Akin (2012) suggested that the plastic strain was influenced by the stiffness of FRP jackets, but not by unconfined concrete strength. In the meantime, Lam & Teng (2009) believed that the plastic strain was strongly dependent on the unconfined concrete strength, while the confinement stiffness does not change the relationship between plastic strain and unloading strain. Also, a plastic strain model has been proposed in the study by Lam & Teng (2009), which can be expressed as Eq. (8.5). More recently, Li et al. (2018) proposed a new plastic model as Eq. (8.6), in which both

the unconfined concrete strength and confinement stiffness are selected as the governing factors. In addition, this model shows very good accuracy in predicting the cyclic behavior of FRP-confined concrete. Figure 8.10 shows a comparison of the test results in this study with the predictions by the models mentioned above. It was seen that the two models both overestimate the plastic strain of the test specimens. This, to some extend, demonstrates the geopolymeric concrete may have lower damage accumulation when subjected to cyclic compression in comparison with OPC concrete. Moreover, the model proposed by Li et al. (2018) provides relatively better predictions for the test results in this study, but the necessity of adjusting the coefficients of the original model is evident.

$$\varepsilon_{pl}=\begin{cases}0, & 0<\varepsilon_{un}\le 0.001\\ \left[1.4\left(0.87-0.004f_{co}^{'}\right)-0.64\right]\left(\varepsilon_{un}-0.001\right), & 0.001<\varepsilon_{un}<0.0035\\ \left(0.87-0.004f_{co}^{'}\right)\varepsilon_{un}-0.0016, & 0.0035\le\varepsilon_{un}\le\varepsilon_{cu}\end{cases} \tag{8.5}$$

$$\varepsilon_{pl}=\begin{cases}0 & 0<\varepsilon_{un}<0.001\\ 0.353\left(\dfrac{f_{co}^{'}}{f_{30}}\right)^{-0.4}\left(\varepsilon_{un}-0.001\right)+3.36\rho^{-0.178}\left(\varepsilon_{un}-0.001\right)^{1.414} & 0.001\le\varepsilon_{un}<\varepsilon_{cu}\end{cases} \tag{8.6}$$

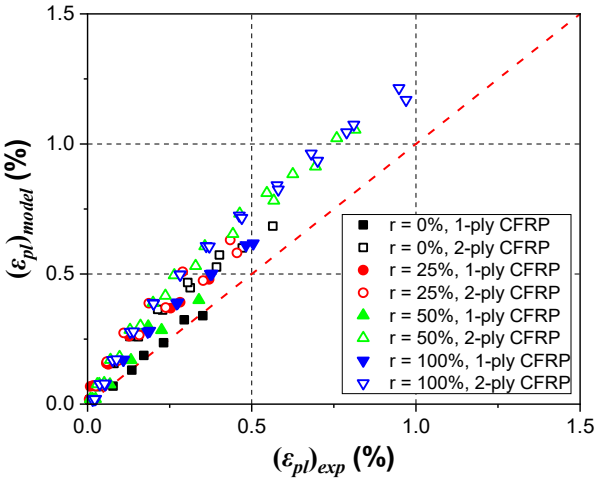

(a) Eq. (8.5) (Lam & Teng (2009))

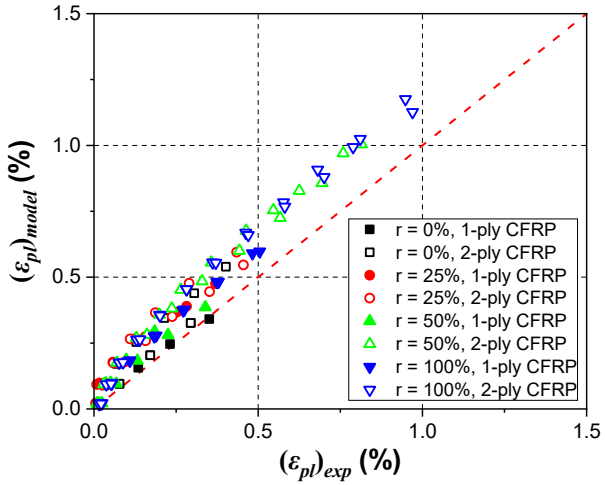

(b) Eq. (8.6) (Li et al. (2018))

Figure 8.10. Performance of existing models for plastic strain

8.3.4 Reloading modulus

Figure 8.11(a) shows the relationship of reloading modulus (E_{re}) versus unloading strain (ε_{un}). Clearly, the reloading modulus reduces gradually with an increase of unloading strain, reflecting the stiffness degradation caused by the increase in the degree of concrete damage. Besides, it follows an exponential trend in the beginning and then approaches a constant as the unloading strain increasing. Moreover, it can be seen that the RA replacement leads to a reduction in the reloading modulus, which is mainly due to the lower stiffness of RA in comparison with NA. Additionally, Figure 8.11(a) reveals that

the thickness of CFRP jackets also affects the reloading modulus: specifically, the specimen with a thicker CFRP jacket exhibits higher reloading modulus at a certain unloading strain, but such effect is relatively insignificant.

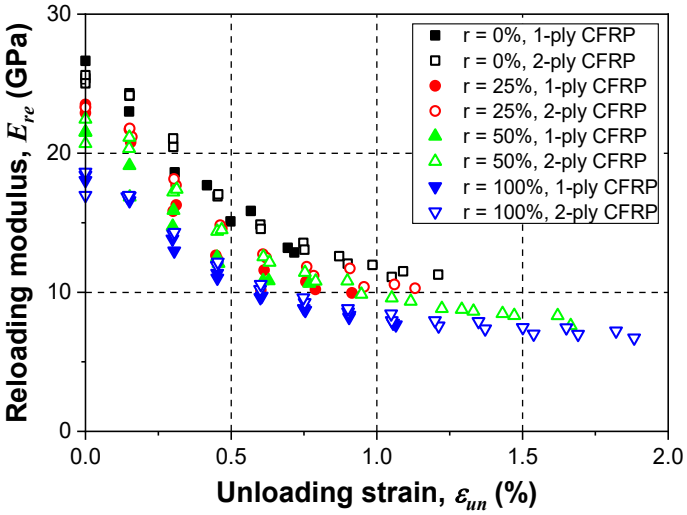

(a) Reloading modulus

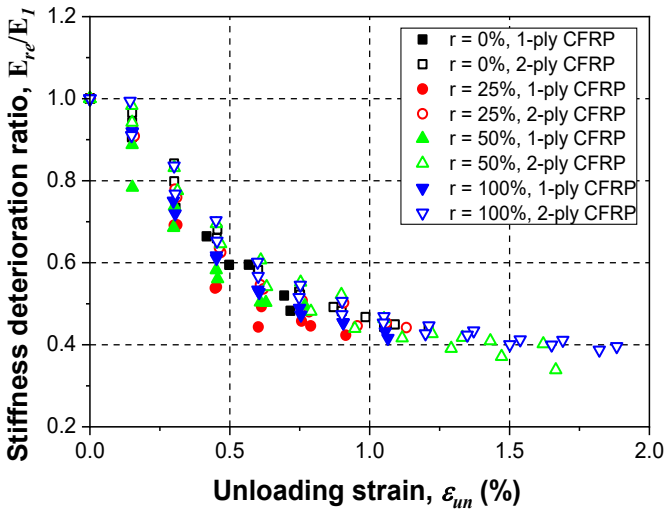

(b) Stiffness deterioration ratio

Figure 8.11. Relationship of reloading modulus and stiffness deterioration ratio versus unloading strain

Figure 8.11(b) displays the curves of the stiffness deterioration ratio against unloading strain, in which the stiffness deterioration ratio is defined as the ratio of the reloading

modulus (E_{re}) to the slopes of the initial branch of the axial stress-strain curve (E_1). A similar trend can be noted when studying the relationships of the stiffness deterioration ratio versus unloading strain for all the test specimens. To a certain extent, it indicates that the stiffness deterioration ratio is governed largely by the unloading strain, and the RA replacement ratio and thickness of CFRP jackets have a little influence on this trend line.

Previously, two models as given by Eqs. (8.7) and (8.8) has been proposed for predicting the reloading modulus of FRP-confined OPC-based concrete, which were obtained from the regression analysis of different databases (Li & Wu 2015; Li et al. 2018). Figure 8.12 gives the comparison between the predictions by the models and the test results. Some discrepancies exist between the test results and the model predictions; specifically, in most cases, the two models underestimate the test results in this study. Also, the model in the study of Li et al. (2018) exhibits better performance in predicting the reloading modulus of the test specimens.

$$\frac{E_{re}}{E_c} = 0.585\left(\frac{f_{co}^{'}}{f_{30}}\right)^{0.388} \rho^{0.021}\left(\bar{\varepsilon}\right)^{-0.266} \tag{8.7}$$

$$\frac{E_{re}}{E_c} = \left(\frac{f_{co}^{'}}{f_{30}}\right)^{0.032} \left(\bar{\varepsilon}\right)^{-0.409} - 0.317\rho^{-0.064\bar{\varepsilon}} \tag{8.8}$$

where $\bar{\varepsilon}$ is defined as follows:

$$\bar{\varepsilon} = \begin{cases} \dfrac{\varepsilon_{un}}{\varepsilon_{co}}, & \varepsilon_{un}/\varepsilon_{co} \le 10 \\ 10, & \varepsilon_{un}/\varepsilon_{co} > 10 \end{cases} \tag{8.9}$$

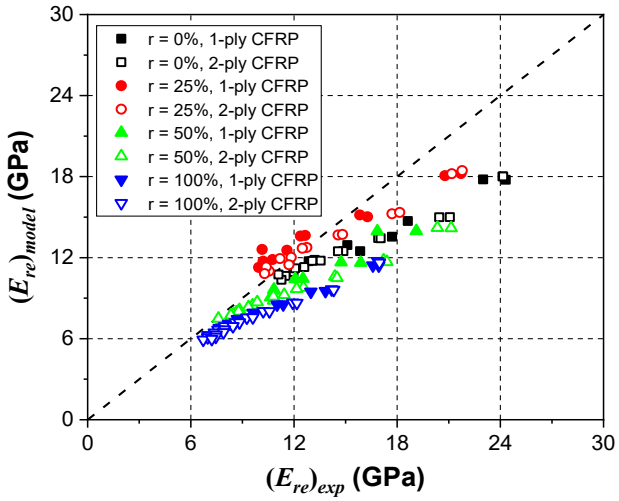

(a) Eq. (8.7) (Li & Wu (2015))

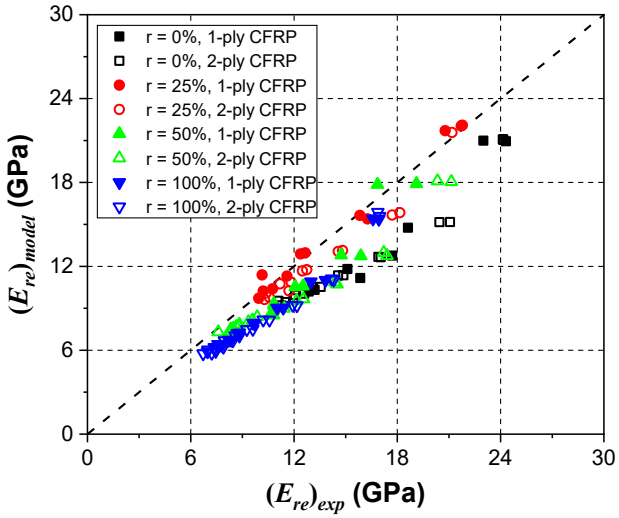

(b) Eq. (8.8) (Li et al. (2018))

Figure 8.12. Performance of existing models for reloading modulus

8.3.5 Stress deterioration

It has been commonly reported that the new stress at the unloading strain (f_{new}) is lower than the corresponding unloading stress (Abbasnia et al. 2012; Lam et al. 2006). This phenomenon is referred to as stress deterioration. In the work by Lam & Teng (2009), the stress deterioration ratio was proposed and is defined as the ratio of the new stress at the unloading strain to the unloading stress (f_{un}). Figure 8.13 shows the relationship between the stress deterioration ratio (ϕ_1) and unloading strain (ε_{un}). The stress deterioration ratio

follows a declining trend in the first three unloading/reloading cycles (i.e., $\varepsilon_{un} \leq 0.0045$), and with the increase of unloading strain, the stress deterioration ratio shows a slight recovery and eventually reaches a constant value when $\varepsilon_{un} > 0.009$. Moreover, for all the specimens, the stress deterioration ratio has an identical trend, and therefore it can be deduced that the stress deterioration is independent of the RA replacement ratio and thickness of CFRP jackets.

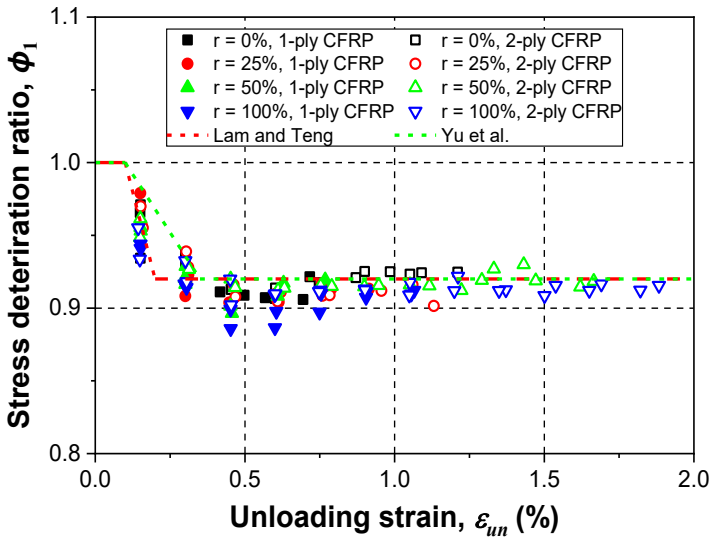

Figure 8.13. Relationship between stress deterioration and unloading strain

In literature, there exist two models for the stress deterioration ratio of FRP-confined OPC-based concrete. The two models are proposed by Lam & Teng (2009) and Yu et al. (2015), which are given by Eqs. (8.10) and (8.11), respectively. It can be seen that the only difference between the two models lays between the unloading strains ranging from 0.001 to 0.035. Specifically, the model proposed by Lam & Teng (2009) suggests that the stress deterioration has a sharper decline and thus has a lower threshold value. Figure 8.13 compares the performance of Eqs. (8.10) and (8.11) against the experimental results. Notably, both models fit reasonably well with the test results, suggesting that the CFRP-confined GRAC might have a similar stress deterioration trend to FRP-confined OPC-based concrete. Moreover, the model of Lam & Teng (2009) provides better predictions for the test specimens in this study, in comparison with the model of Yu et al. (2015).

$$\phi_1 = \begin{cases} 1, & 0 < \varepsilon_{un} \le 0.001 \\ 1 - 80(\varepsilon_{un} - 0.001), & 0.001 < \varepsilon_{un} < 0.002 \\ 0.92, & 0.002 \le \varepsilon_{un} < \varepsilon_{cu} \end{cases} \tag{8.10}$$

$$\phi_1 = \begin{cases} 1, & 0 < \varepsilon_{un} \le 0.001 \\ 1 - 32(\varepsilon_{un} - 0.001), & 0.001 < \varepsilon_{un} < 0.0035 \\ 0.92, & 0.0035 \le \varepsilon_{un} < \varepsilon_{cu} \end{cases} \tag{8.11}$$

8.4 Summary

(1) The envelope hypothesis is valid for CFRP-confined geopolymeric concrete, in which the envelope stress-strain curve of the cyclically loaded specimen closely follows the stress-strain curve of the specimen under monotonic loading. Additionally, the presence of cyclic loading has an insignificant influence on the peak strength and ultimate strain compared with that under monotonic loading.

(2) The plastic strain increases with the increment of unloading strain, and this relationship is affected slightly by the RA replacement ratios and confinement stiffness. The trend of plastic strain changes with the variations in the RA replacement ratios and confinement stiffness.

(3) Both the residual modulus and reloading modulus reduce gradually with the increases of unloading strain, which follows a negative exponential trend in the beginning and then approaches a constant. Furthermore, the relationships of residual modulus and reloading modulus against unloading strain are affected significantly by the RA replacement ratios but do not appear to be influenced significantly by the thickness of CFRP jackets.

(4) For the specimens with different RA replacement ratios and thicknesses of CFRP jackets, the stress deterioration ratio has the same trend, which decreases in the first three unloading/reloading cycles, followed by a slight recovery, and eventually reaches a constant value.

(5) The models of Lam & Teng (2003) and Xiao & Wu (2003) can provide accurate predictions for both peak strength and ultimate strain of CFRP-confined geopolymeric concrete. However, the existing models cannot accurately capture the key shape factors that govern the cyclic stress-strain curves, especially the residual modulus, plastic strain, and reloading modulus.

CHAPTER 9: CONCLUSIONS AND RECOMMENDATIONS

9.1 Summary and conclusions

9.1.1 Engineering properties of sustainable GRAC

Sustainable GRAC was developed, in which the fly ash/slag combination was used as the precursor, and RA based on C&DW was employed as coarse aggregate. The physical (i.e., workability, setting time, density, water absorption, sorptivity, and volume of voids) and mechanical (i.e., compressive strength, flexural strength, and splitting tensile strength) properties of the developed GRAC were evaluated. Moreover, the SEM was conducted to characterize the microstructure of GRAC. Based on the test results and analyses, the following conclusions could be drawn:

- The RAs consisted primarily of concrete products, clay masonry units, natural stone, and glass, which were categorized into mixed RA. The RA exhibited poorer performance in terms of density, absorption, and crushing values, in comparison with NA.

- The substitution of slag for fly ash reduced the workability and setting time of geopolymeric concrete, while the replacement of NA by RA resulted in a slight increase in the workability and setting time.

- The replacement of NA by RA adversely affected the physical and mechanical properties of geopolymeric concrete. However, geopolymeric concrete with RA still possesses sufficiently high compressive strength up to 43.1 MPa and 38.5 MPa for RA replacement ratios of 50% and 100%, respectively.

- The improvements in transport properties and mechanical properties of geopolymeric concrete were achieved with the substitution of slag for fly ash. Moreover, the inclusion of slag diminished the effects on mechanical properties caused by the replacement of NA by RA.

- Excellent correlations are identified between the water absorption, sorptivity, and volume of permeable voids, as well as among splitting tensile strength, flexural strength, and compressive strength. However, the existing empirical models suggested by the ACI Building code and Eurocode 2 exhibits large discrepancies with respect to the mechanical properties.

- Based on the experimental results in this study, equations with high accuracy were proposed to predict the relationship between compressive strength and other mechanical properties of geopolymeric concrete, which also fit reasonably well with the results obtained by other researchers.

- There was no significant change in the microstructures of the geopolymeric concrete with different aggregate types. However, the inclusion of slag resulted in a denser geopolymeric matrix, and meantime led to the weak point to change from the geopolymeric matrix to the ITZ between the geopolymeric matrix and aggregate.

9.1.2 Static and dynamic compressive behaviors of sustainable GRAC

Static compressive behaviors of sustainable GRAC

The static compressive stress-strain behavior of GRAC was studied by using a high-force servo-hydraulic test system. Special attention was devoted to the failure behaviors and patterns, stress-strain characteristics (i.e., the peak stress, elastic modulus, peak strain, and ultimate strain), and energy absorption capacity. Furthermore, a stress-strain model was developed by modifying the parameters of existing models to describe the uniaxial stress-strain behavior of GRAC. Based on the tests, the following conclusions can be drawn:

- All the tested geopolymeric concretes had a similar failure process under compression. However, the probability of crack development through aggregates increased as the RA replacement ratio increased, and a higher percentage of fractured aggregate particles were observed in geopolymeric concrete with a higher content of slag.

- All the stress-strain curves of geopolymeric concretes showed a decrease in peak stress, elastic modulus, and energy absorption (toughness), but an improvement in ductility, with the increase in the RA replacement ratio. However, opposite trends were observed as the slag content increases. Moreover, the inclusion of slag can alleviate the effects of RA replacement on these properties.

- The peak strain and ultimate strain of geopolymeric concrete were influenced by the RA replacement ratio and the content of slag. RA replacing resulted in the increases in peak strain and ultimate strain for geopolymeric concrete with 10% and 20% inclusion of slag, but comparatively in fewer impacts on the neat fly ash-based geopolymeric concrete and geopolymeric concrete with 30% inclusion of slag.

- The existing stress-strain models previously developed for OPC concrete, geopolymeric concrete, and OPC-based RAC cannot accurately predict the stress-strain behaviors of geopolymeric concrete in the current study. Similar results were observed in the comparison between the experimental results and predictions by the existing models for the peak strain and elastic modulus. However, the model proposed by Collins and Mitchell (1991) fits relatively well with the experimental stress-strain curves of geopolymeric concrete.

- By comparing the proposed stress-strain models with the experimental results of the current study, it is concluded that the proposed model has very good accuracy in determining the actual complete compressive stress-strain curve for both GNAC and GRAC.

Dynamic compressive behaviors of sustainable GRAC

A Ø80-mm split Hopkinson pressure bar apparatus was employed in this study. The dynamic compressive stress-strain behavior of GRAC was investigated and then compared with that under quasi-static loading. The effects of the strain rate on compressive behaviors of GRAC were studied, including the failure patterns, stress-strain behavior, and energy dissipation. Based on the results, some conclusions were made as below:

- The dynamic compressive strength of geopolymeric concrete and DIF increased with the increase of strain rates. At a certain strain rate, the dynamic compressive strengths exhibited no much difference between GNAC and GRAC; whereas, the DIF increased after the RA replacement. Irrespective of the coarse aggregate types (i.e., NA or RA), the dynamic compressive strength of geopolymeric concrete and DIF both increased with the content of slag under a particular strain rate.

- The DIF of the geopolymeric concrete was found to increase approximately linearly with the log10 of the strain rate. The existing formulae for DIF show some discrepancies when comparing with the test results. The proposed empirical formulae accounting for the relationship between strength enhancement and strain rates were found to be satisfied with the test results.

- The ratios of energy absorption to the incident wave energy were in the range of 0.2 to 0.45. At a certain level of strain rate, the specific energy absorption of GRAC was higher than that of GNAC. Additionally, the energy absorption capacity was increased with the increase in the slag content. The specific energy absorption is proportional to the logarithm of the strain rate.

- Under dynamic compression, the failure modes of all GNAC and GRAC showed a similar pattern. At low strain rates, the specimens were broken into several large pieces, whereas at high strain rates, the specimens were ground into numerous small fragments. The high strain rate also results in more cracks propagating through the coarse aggregates.

9.1.3 Failure process and mechanism of sustainable GRAC

In this work, sliced GRAC specimens with a dimension of 100×100×10 mm were subjected to static compression. The crack evolution and failure mode of specimens were observed during the test. Then, the displacement field and strain distribution over the specimen surfaces were obtained and analyzed by using the digital image correlation (DIC) technique. Based on the results, the failure process and mechanism of GRAC under compression were further investigated. The following conclusions were drawn:

- For all the specimens, cracks mainly initiated near the ITZs, and usually nucleated around NA rather than RA. As observed from the final crack patterns, it was more frequent for the RA that cracks passed through the aggregate particles, in comparison with the NA.
- DIC method can accurately determine the full-field displacement and strain distribution of the test specimens under various stages of stress. Therefore, the DIC technic has the potential to replace the conventional measurement setup and provide rich information data to help understand the deformation behavior.
- At a given global stress level, the specimens with higher RA replacement ratios generally had a higher magnitude for the displacement vectors. Additionally, the differences between the displacement vectors within the crack regions are smaller for the specimens with higher RA replacement ratios.
- The location of the strain concentration region, especially in the maximum principal strain field and maximum shear strain field, is closely consistent with that of the observed micro-cracks. Hence, the DIC technic could effectively provide a warning for the initiation of micro-damage and accurately determine the location and degree of micro-damage.

9.1.4 Mechanical performance of CFRP-confined sustainable GRAC under monotonic and cyclic compression

Mechanical performance of CFRP-confined sustainable GRAC under monotonic compression

In this work, GRAC was confined by CFRP jackets. The major test parameters include (1) coarse aggregate type, (2) number of CFRP layers, and (3) slag content. Special attention was devoted to the stress-strain relationship, dilation behavior, and ultimate condition. The test results were also compared with the predictions by existing stress-strain models proposed for FRP-confined concrete to examine their applicability to CFRP-confined GRAC. Empirical models were developed to predict the ultimate condition of CFRP-confined GRAC. Based on the results and discussions, the following conclusions can be drawn:

- The confinement by CFRP jackets has an enhancement on both compressive strength and ultimate strain for geopolymeric concrete. Moreover, the enhancement is more pronounced with the increase in the thickness of CFRP jackets.

- In addition to the decreased compressive strength, the RA replacement results in the reduced volumetric dilation of CFRP-confined geopolymeric concrete. Besides, the stress-strain relationships of CFRP-confined GRAC show a longer transition zone than the counterpart based on GNAC. On the other hand, the reverse trend was achieved due to the incorporation of slag, including the increased compressive strength and obvious volumetric dilation, as well as, the reduced radius for the transition part of the stress-strain curves.

- The aggregate types and slag content do not have a significant effect on the CFRP confinement performance for geopolymeric concrete in terms of compressive strength. In addition, the existing FRP-confined concrete models could provide a reasonable prediction for the strength enhancement ratio of the test CFRP-confined geopolymeric concrete.

Mechanical performance of CFRP-confined sustainable GRAC under cyclic compression

This work experimentally studied the static and cyclic compression behaviors of CFRP-confined GRAC. The parameters considered in this study included (1) aggregate replacement ratio, (2) thickness of CFRP jackets, and (3) loading scheme (i.e., monotonic compression and cyclic compression). Special attention was devoted to the failure model, compressive stress-strain behavior, and axial-lateral strain relationship. Subsequently, detailed discussions were provided regarding the key shape factors that govern the cyclic stress-strain curves. Meanwhile, the results were compared with the predictions by existing models for evaluating the applicability of these models to CFRP-confined GRAC. Based on the results and discussion, the following conclusions can be drawn up as:

- The envelope hypothesis is valid for CFRP-confined geopolymeric concrete, in which the envelope stress-strain curve of the cyclically loaded specimen closely follows the stress-strain curve of the specimen under monotonic loading. Additionally, the presence of cyclic loading has an insignificant influence on the peak strength and ultimate strain compared with that under monotonic loading.

- The plastic strain increases with the increment of unloading strain, and this relationship is affected slightly by the RA replacement ratios and confinement stiffness. The trend of plastic strain changes with the variations in the RA replacement ratios and confinement stiffness.

- Both the residual modulus and reloading modulus reduce gradually with the increases of unloading strain, which follows a negative exponential trend in the beginning and then approaches a constant. Furthermore, the relationships of residual modulus and reloading modulus against unloading strain are affected significantly by the RA replacement ratios but do not appear to be influenced significantly by the thickness of CFRP jackets.

- For the specimens with different RA replacement ratios and thicknesses of CFRP jackets, the stress deterioration ratio has the same trend, which decreases in the first three unloading/reloading cycles, followed by a slight recovery, and eventually reaches a constant value.

9.2 Recommendations for future works

On the basis of current research outcomes, the following areas of research remain relatively unexplored and could form the basis for the future studies:

- A good understanding of concrete durability is fundamental to establish the service life for new or existing structures. Therefore, an extensive experimental program needs to be conducted to investigate the durability of the GRAC, such as under freeze-thaw cycles, sulfate attack, and high temperature.

- Volumetric changes in hardened concrete may occur in the GRAC when subject to environmental (shrinkage) or mechanical (creep) conditions. Shrinkage and creep of concrete can lead to uncontrolled and undesired cracking, which would eventually affect the structure's safety. Consequently, an experimental program should be conducted to study the long-term behavior of the GRAC, especially the shrinkage and creep behavior.

- Concrete is a quasi-brittle material with the material morphology that is heterogeneous across multiple scales. Failure of concrete due to external loads is characterized by distributed microcracking followed by damage localization, eventually leading to loss of structural integrity. An accurate stimulated model is beneficial for understanding the behavior of concrete materials and further for the structural design. Also, simulations are useful tools when the conditions of interest are difficult to achieve in the laboratory. Therefore, it is suggested to develop a multiscale modeling for GRAC. The multiscale modeling refers to a style of modeling in which multiple models at different scales.

- More experimental work on FRP-confined geopolymeric concrete considering more parameters, including column size, FRP arrangement, type of FRPs, and so on, are required to expand the experimental database and generalize the results. By doing these, an accurate model could also be developed for the safe design and use of this material.

- In order to promote the manufacture and application of GRAC, increased attention should be paid to the further development of comprehensive design method comprised of target strength method, performance-based method and statistical factorial model method. Furthermore, there is an urgent need to establish technical and performance standards to use GRAC for the various applications.

REFERENCES

Abbasnia, R., Ahmadi, R. & Ziaadiny, H. 2012, Effect of confinement level, aspect ratio and concrete strength on the cyclic stress–strain behavior of FRP-confined concrete prisms, Composites Part B: Engineering, 43 (2), pp. 825-831.

Abbasnia, R., Hosseinpour, F., Rostamian, M. & Ziaadiny, H. 2013, Cyclic and monotonic behavior of FRP confined concrete rectangular prisms with different aspect ratios, Construction and Building Materials, 40, pp. 118-125.

Abbasnia, R. & Ziaadiny, H. 2010, Behavior of concrete prisms confined with FRP composites under axial cyclic compression, Engineering Structures, 32 (3), pp. 648-655.

Abdesselam, H., Kassoul, A. & Bouzid, H. 2019, New model for confinement of reinforced concrete columns with an ultra-high strength close to 200 MPa, Engineering Structures, 199.

Abdollahnejad, Z., Luukkonen, T., Mastali, M., Kinnunen, P. & Illikainen, M. 2019, Development of One-Part Alkali-Activated Ceramic/Slag Binders Containing Recycled Ceramic Aggregates, Journal of Materials in Civil Engineering, 31 (2).

Adesanya, E., Ohenoja, K., Luukkonen, T., Kinnunen, P. & Illikainen, M. 2018, One-part geopolymer cement from slag and pretreated paper sludge, Journal of Cleaner Production, 185, pp. 168-175.

Ajayi, S.O., Oyedele, L.O., Bilal, M., Akinade, O.O., Alaka, H.A., Owolabi, H.A. & Kadiri, K.O. 2015, Waste effectiveness of the construction industry: Understanding the impediments and requisites for improvements, Resources, Conservation and Recycling, 102, pp. 101-112.

Akçaoğlu, T. 2017, Determining aggregate size & shape effect on concrete microcracking under compression by means of a degree of reversibility method, Construction and Building Materials, 143, pp. 376-386.

Akçaözoğlu, S. & Ulu, C. 2014, Recycling of waste PET granules as aggregate in alkali-activated blast furnace slag/metakaolin blends, Construction and Building Materials, 58, pp. 31-37.

Aly, A.M., El-Feky, M.S., Kohail, M. & Nasr, E.-S.A.R. 2019, Performance of geopolymer concrete containing recycled rubber, Construction and Building Materials, 207, pp. 136-144.

Aly, S.T., Kanaan, D.M., El-Dieb, A.S. & Abu-Eishah, S.I. 2018, 'Properties of ceramic waste powder-based geopolymer concrete', *International Congress on Polymers in Concrete*, Springer, pp. 429-435.

Amin, S.K., El–Sherbiny, S.A., El–Magd, A.A.M.A., Belal, A. & Abadir, M.F. 2017, Fabrication of geopolymer bricks using ceramic dust waste, Construction and Building Materials, 157, pp. 610-620.

Antunes Boca Santa, R.A., Bernardin, A.M., Riella, H.G. & Kuhnen, N.C. 2013, Geopolymer synthetized from bottom coal ash and calcined paper sludge, Journal of Cleaner Production, 57, pp. 302-307.

Arulrajah, A., Kua, T.-A., Horpibulsuk, S., Mirzababaei, M. & Chinkulkijniwat, A. 2017, Recycled glass as a supplementary filler material in spent coffee grounds geopolymers, Construction and Building Materials, 151, pp. 18-27.

Ashraf, M.S., Ghouleh, Z. & Shao, Y. 2019, Production of eco-cement exclusively from municipal solid waste incineration residues, Resources, Conservation and Recycling, 149, pp. 332-342.

Avirneni, D., Peddinti, P.R.T. & Saride, S. 2016, Durability and long term performance of geopolymer stabilized reclaimed asphalt pavement base courses, Construction and Building Materials, 121, pp. 198-209.

Azmi, A.A., Abdullah, M.M.A.B., Ghazali, C.M.R., Ahmad, R., Musa, L. & Rou, L.S. 2019, 'The effect of different crumb rubber loading on the properties of fly ash-based geopolymer concrete', *IOP Conference Series: Materials Science and Engineering*, vol. 551, IOP Publishing, p. 012079.

Azmi, A.A., Abdullah, M.M.A.B., Ghazali, C.M.R., Sandu, A.V. & Hussin, K. 2016, 'Effect of crumb rubber on compressive strength of fly ash based geopolymer concrete', *MATEC Web of Conferences*, vol. 78, EDP Sciences, p. 01063.

Behera, M., Bhattacharyya, S.K., Minocha, A.K., Deoliya, R. & Maiti, S. 2014, Recycled aggregate from C&D waste & its use in concrete – A breakthrough towards sustainability in construction sector: A review, Construction and Building Materials, 68, pp. 501-516.

Belén, G.-F., Fernando, M.-A., Diego, C.L. & Sindy, S.-P. 2011, Stress–strain relationship in axial compression for concrete using recycled saturated coarse aggregate, Construction and Building Materials, 25 (5), pp. 2335-2342.

Bernal, S., Ball, R., Hussein, O., Heath, A. & Provis, J.L. 2014a, 'Paper sludge ash as a precursor for production of alkali-activated materials', *Proceedings of the Second International Conference on Advances in Chemically-Activated Materials (CAM 2014)*.

Bernal, S.A., Provis, J.L. & Green, D.J. 2014b, Durability of alkali-activated materials: progress and perspectives, Journal of the American Ceramic Society, 97 (4), pp. 997-1008.

Bernal, S.A., Provis, J.L., Rose, V. & Mejía de Gutierrez, R. 2011, Evolution of binder structure in sodium silicate-activated slag-metakaolin blends, Cement and Concrete Composites, 33 (1), pp. 46-54.

Beshr, H., Almusallam, A. & Maslehuddin, M. 2003, Effect of coarse aggregate quality on the mechanical properties of high strength concrete, Construction and building materials, 17 (2), pp. 97-103.

Beygi, M.H.A., Kazemi, M.T., Nikbin, I.M. & Amiri, J.V. 2013, The effect of water to cement ratio on fracture parameters and brittleness of self-compacting concrete, Materials & Design, 50, pp. 267-276.

Bhogayata, A.C. & Arora, N.K. 2019, Utilization of metalized plastic waste of food packaging articles in geopolymer concrete, Journal of Material Cycles and Waste Management, 21 (4), pp. 1014-1026.

Bhutta, A., Borges, P.H.R., Zanotti, C., Farooq, M. & Banthia, N. 2017, Flexural behavior of geopolymer composites reinforced with steel and polypropylene macro fibers, Cement and Concrete Composites, 80, pp. 31-40.

Bischoff, P.H. & Perry, S. 1991, Compressive behaviour of concrete at high strain rates, Materials and structures, 24 (6), pp. 425-450.

Blaber, J., Adair, B. & Antoniou, A. 2015, Ncorr: Open-Source 2D Digital Image Correlation Matlab Software, Experimental Mechanics, 55 (6), pp. 1105-1122.

Bongers, J. & Rutten, H. 1998, Concrete in multiaxial compression-a multilevel analysis, HERON-ENGLISH EDITION-, 43, pp. 159-180.

Burciaga-Díaz, O., Durón-Sifuentes, M., Díaz-Guillén, J.A. & Escalante-García, J.I. 2020, Effect of waste glass incorporation on the properties of geopolymers formulated with low purity metakaolin, Cement and Concrete Composites, 107.

Burciaga-Díaz, O., Magallanes-Rivera, R.X. & Escalante-García, J.I. 2013, Alkali-activated slag-metakaolin pastes: strength, structural, and microstructural characterization, Journal of Sustainable Cement-Based Materials, 2 (2), pp. 111-127.

Casuccio, M., Torrijos, M.C., Giaccio, G. & Zerbino, R. 2008, Failure mechanism of recycled aggregate concrete, Construction and Building Materials, 22 (7), pp. 1500-1506.

Chan, C.W., Yu, T., Zhang, S.S. & Xu, Q.F. 2019, Compressive behaviour of FRP-confined rubber concrete, Construction and Building Materials, 211, pp. 416-426.

Chen, G.M., He, Y.H., Jiang, T. & Lin, C.J. 2016a, Behavior of CFRP-confined recycled aggregate concrete under axial compression, Construction and Building Materials, 111, pp. 85-97.

Chen, Y., Cui, Z., Cui, X., Liu, W., Wang, X., Li, X. & Li, S. 2019, Life cycle assessment of end-of-life treatments of waste plastics in China, Resources, Conservation and Recycling, 146, pp. 348-357.

Chen, Z., Liu, Y., Zhu, W. & Yang, E.-H. 2016b, Incinerator bottom ash (IBA) aerated geopolymer, Construction and Building Materials, 112, pp. 1025-1031.

Chiaia, B., Van Mier, J. & Vervuurt, A. 1998, Crack growth mechanisms in four different concretes: microscopic observations and fractal analysis, Cement and Concrete Research, 28 (1), pp. 103-114.

Choi, E., Jeon, J.-S., Cho, B.-S. & Park, K. 2013, External jacket of FRP wire for confining concrete and its advantages, Engineering Structures, 56, pp. 555-566.

Collins, M.P. & Mitchell, D. 1991, *Prestressed concrete structures*, vol. 9, Prentice Hall Englewood Cliffs, NJ.

Cusatis, G. 2011, Strain-rate effects on concrete behavior, International Journal of Impact Engineering, 38 (4), pp. 162-170.

Dave, S., Bhogayata, A. & Arora, N. 2017, Impact resistance of geopolymer concrete containing recycled plastic aggregates, Kalpa Publications in Civil Engineering, 1, pp. 137-143.

Deb, P.S., Nath, P. & Sarker, P.K. 2014, The effects of ground granulated blast-furnace slag blending with fly ash and activator content on the workability and strength properties of geopolymer concrete cured at ambient temperature, Materials and Design, 62, pp. 32-39.

Dehghanpoor Abyaneh, S., Wong, H.S. & Buenfeld, N.R. 2014, Computational investigation of capillary absorption in concrete using a three-dimensional mesoscale approach, Computational Materials Science, 87, pp. 54-64.

del Rio Merino, M., Izquierdo Gracia, P. & Weis Azevedo, I.S. 2010, Sustainable construction: construction and demolition waste reconsidered, Waste Management and Research, 28 (2), pp. 118-129.

Diaz-Loya, E.I., Allouche, E.N., Eklund, S., Joshi, A.R. & Kupwade-Patil, K. 2012, Toxicity mitigation and solidification of municipal solid waste incinerator fly ash using alkaline activated coal ash, Waste Manag, 32 (8), pp. 1521-1527.

Ding, Y., Dai, J.-G. & Shi, C.-J. 2016, Mechanical properties of alkali-activated concrete: A state-of-the-art review, Construction and Building Materials, 127, pp. 68-79.

Ding, Y., Dai, J.-G. & Shi, C.-J. 2018a, Fracture properties of alkali-activated slag and ordinary Portland cement concrete and mortar, Construction and Building Materials, 165, pp. 310-320.

Ding, Y., Shi, C.-J. & Li, N. 2018b, Fracture properties of slag/fly ash-based geopolymer concrete cured in ambient temperature, Construction and Building Materials, 190, pp. 787-795.

Dong, M., Feng, W., Elchalakani, M., Li, G., Karrech, A. & May, E.F. 2017, Development of a High Strength Geopolymer by Novel Solar Curing, Ceramics International, 43 (14), pp. 11233-11243.

Duxson, P., Fernández-Jiménez, A., Provis, J.L., Lukey, G.C., Palomo, A. & van Deventer, J.S.J. 2006, Geopolymer technology: the current state of the art, Journal of Materials Science, 42 (9), pp. 2917-2933.

El-Hassan, H. & Ismail, N. 2017, Effect of process parameters on the performance of fly ash/GGBS blended geopolymer composites, Journal of Sustainable Cement-Based Materials, 7 (2), pp. 122-140.

Faron, A. & Rombach, G.A. 2020, Simulation of crack growth in reinforced concrete beams using extended finite element method, Engineering Failure Analysis, 116.

Feng, K.N., Ruan, D., Pan, Z., Collins, F., Bai, Y., Wang, C.M. & Duan, W.H. 2015, Mechanical behavior of geopolymer concrete subjected to high strain rate compressive loadings, Materials and Structures, 48 (3), pp. 671-681.

Fernández-Jiménez, A., Palomo, A. & Criado, M. 2005, Microstructure development of alkali-activated fly ash cement: a descriptive model, Cement and Concrete Research, 35 (6), pp. 1204-1209.

Fernandez-Jimenez, A.M., Palomo, A. & Lopez-Hombrados, C. 2006, Engineering properties of alkali-activated fly ash concrete, ACI Materials Journal, 103 (2), p. 106.

Fonseca, N., de Brito, J. & Evangelista, L. 2011, The influence of curing conditions on the mechanical performance of concrete made with recycled concrete waste, Cement and Concrete Composites, 33 (6), pp. 637-643.

Fořt, J., Vejmelková, E., Koňáková, D., Alblová, N., Čáchová, M., Keppert, M., Rovnaníková, P. & Černý, R. 2018, Application of waste brick powder in alkali activated aluminosilicates: Functional and environmental aspects, Journal of Cleaner Production, 194, pp. 714-725.

Gandoman, M. & Kokabi, M. 2015, Sound barrier properties of sustainable waste rubber/geopolymer concretes, Iranian Polymer Journal, 24 (2), pp. 105-112.

Gao, C., Huang, L., Yan, L., Jin, R. & Kasal, B. 2019, Strength and ductility improvement of recycled aggregate concrete by polyester FRP-PVC tube confinement, Composites Part B: Engineering, 162, pp. 178-197.

Gao, C., Huang, L., Yan, L., Kasal, B. & Li, W. 2016, Behavior of glass and carbon FRP tube encased recycled aggregate concrete with recycled clay brick aggregate, Composite Structures, 155, pp. 245-254.

Gao, X., Yuan, B., Yu, Q.L. & Brouwers, H.J.H. 2017, Characterization and application of municipal solid waste incineration (MSWI) bottom ash and waste granite powder in alkali activated slag, Journal of Cleaner Production, 164, pp. 410-419.

Gholampour, A., Ozbakkaloglu, T. & Ng, C.-T. 2019, Ambient- and oven-cured geopolymer concretes under active confinement, Construction and Building Materials, 228.

Giaccio, G. & Zerbino, R. 1998, Failure mechanism of concrete: combined effects of coarse aggregates and strength level, Advanced Cement Based Materials, 7 (2), pp. 41-48.

Gluth, G.J.G., Lehmann, C., Rübner, K. & Kühne, H.-C. 2014, Reaction products and strength development of wastepaper sludge ash and the influence of alkalis, Cement and Concrete Composites, 45, pp. 82-88.

Gray, G.T. 2000, Classic split Hopkinson pressure bar testing, ASM handbook, 8, pp. 462-476.

Gualtieri, A.F., Veratti, L., Tucci, A. & Esposito, L. 2012, Recycling of the product of thermal inertization of cement-asbestos in geopolymers, Construction and Building Materials, 31, pp. 47-51.

Guinea, G., El-Sayed, K., Rocco, C., Elices, M. & Planas, J. 2002, The effect of the bond between the matrix and the aggregates on the cracking mechanism and fracture parameters of concrete, Cement and Concrete Research, 32 (12), pp. 1961-1970.

Gundupalli, S.P., Hait, S. & Thakur, A. 2017, A review on automated sorting of source-separated municipal solid waste for recycling, Waste Manag, 60, pp. 56-74.

Guo, D., Zhang, Z., Zhang, X. & Wang, R. 1982, Experimental Investigation of the Complete Stress-Strain Curve of Concrete, Journal of Building Structures, 1.

Guo, H., Shi, C., Guan, X., Zhu, J., Ding, Y., Ling, T.-C., Zhang, H. & Wang, Y. 2018, Durability of recycled aggregate concrete – A review, Cement and Concrete Composites, 89, pp. 251-259.

Guo, Y.B., Gao, G.F., Jing, L. & Shim, V.P.W. 2017, Response of high-strength concrete to dynamic compressive loading, International Journal of Impact Engineering, 108, pp. 114-135.

Hajimohammadi, A., Ngo, T. & Kashani, A. 2018, Glass waste versus sand as aggregates: The characteristics of the evolving geopolymer binders, Journal of Cleaner Production, 193, pp. 593-603.

Han, B. & Xiang, T.-Y. 2017, Axial compressive stress-strain relation and Poisson effect of structural lightweight aggregate concrete, Construction and Building Materials, 146, pp. 338-343.

Hoornweg, D. & Bhada-Tata, P. 2012, *What a waste: a global review of solid waste management*, vol. 15, World Bank, Washington, DC.

Hoy, M., Horpibulsuk, S. & Arulrajah, A. 2016a, Strength development of Recycled Asphalt Pavement – Fly ash geopolymer as a road construction material, Construction and Building Materials, 117, pp. 209-219.

Hoy, M., Horpibulsuk, S., Arulrajah, A. & Mohajerani, A. 2018, Strength and Microstructural Study of Recycled Asphalt Pavement: Slag Geopolymer as a Pavement Base Material, Journal of Materials in Civil Engineering, 30 (8).

Hoy, M., Horpibulsuk, S., Rachan, R., Chinkulkijniwat, A. & Arulrajah, A. 2016b, Recycled asphalt pavement - fly ash geopolymers as a sustainable pavement base material: Strength and toxic leaching investigations, Sci Total Environ, 573, pp. 19-26.

Hoy, M., Rachan, R., Horpibulsuk, S., Arulrajah, A. & Mirzababaei, M. 2017, Effect of wetting–drying cycles on compressive strength and microstructure of recycled asphalt pavement – Fly ash geopolymer, Construction and Building Materials, 144, pp. 624-634.

Hu, X., Lu, Q., Xu, Z., Zhang, W. & Cheng, S. 2018, Compressive stress-strain relation of recycled aggregate concrete under cyclic loading, Construction and Building Materials, 193, pp. 72-83.

Huang, B., Wang, X., Kua, H., Geng, Y., Bleischwitz, R. & Ren, J. 2018a, Construction and demolition waste management in China through the 3R principle, Resources, Conservation and Recycling, 129, pp. 36-44.

Huang, G., Ji, Y., Li, J., Hou, Z. & Jin, C. 2018b, Use of slaked lime and Portland cement to improve the resistance of MSWI bottom ash-GBFS geopolymer concrete against carbonation, Construction and Building Materials, 166, pp. 290-300.

Huang, G., Ji, Y., Li, J., Zhang, L., Liu, X. & Liu, B. 2019a, Effect of activated silica on polymerization mechanism and strength development of MSWI bottom ash alkali-activated mortars, Construction and Building Materials, 201, pp. 90-99.

Huang, G., Ji, Y., Zhang, L., Hou, Z., Zhang, L. & Wu, S. 2019b, Influence of calcium content on structure and strength of MSWI bottom ash-based geopolymer, Magazine of Concrete Research, 71 (7), pp. 362-372.

Huang, Y., He, X., Wang, Q. & Xiao, J. 2019c, Deformation field and crack analyses of concrete using digital image correlation method, Frontiers of Structural and Civil Engineering, 13 (5), pp. 1183-1199.

Huseien, G.F., Ismail, M., Khalid, N.H.A., Hussin, M.W. & Mirza, J. 2018a, Compressive strength and microstructure of assorted wastes incorporated geopolymer mortars: Effect of solution molarity, Alexandria Engineering Journal, 57 (4), pp. 3375-3386.

Huseien, G.F., Sam, A.R.M., Mirza, J., Tahir, M.M., Asaad, M.A., Ismail, M. & Shah, K.W. 2018b, Waste ceramic powder incorporated alkali activated mortars exposed to elevated Temperatures: Performance evaluation, Construction and Building Materials, 187, pp. 307-317.

Huseien, G.F., Sam, A.R.M., Shah, K.W., Asaad, M.A., Tahir, M.M. & Mirza, J. 2019a, Properties of ceramic tile waste based alkali-activated mortars incorporating GBFS and fly ash, Construction and Building Materials, 214, pp. 355-368.

Huseien, G.F., Sam, A.R.M., Shah, K.W. & Mirza, J. 2020, Effects of ceramic tile powder waste on properties of self-compacted alkali-activated concrete, Construction and Building Materials, 236.

Huseien, G.F., Sam, A.R.M., Shah, K.W., Mirza, J. & Tahir, M.M. 2019b, Evaluation of alkali-activated mortars containing high volume waste ceramic powder and fly ash replacing GBFS, Construction and Building Materials, 210, pp. 78-92.

Hwang, C.-L., Damtie Yehualaw, M., Vo, D.-H. & Huynh, T.-P. 2019a, Development of high-strength alkali-activated pastes containing high volumes of waste brick and ceramic powders, Construction and Building Materials, 218, pp. 519-529.

Hwang, C.-L., Yehualaw, M.D., Vo, D.-H., Huynh, T.-P. & Largo, A. 2019b, Performance evaluation of alkali activated mortar containing high volume of waste brick powder blended with ground granulated blast furnace slag cured at ambient temperature, Construction and Building Materials, 223, pp. 657-667.

Ismail, I., Bernal, S.A., Provis, J.L., San Nicolas, R., Brice, D.G., Kilcullen, A.R., Hamdan, S. & van Deventer, J.S.J. 2013, Influence of fly ash on the water and chloride permeability of alkali-activated slag mortars and concretes, Construction and Building Materials, 48, pp. 1187-1201.

Ji, Z. & Pei, Y. 2019, Bibliographic and visualized analysis of geopolymer research and its application in heavy metal immobilization: A review, J Environ Manage, 231, pp. 256-267.

Jiang, T. & Teng, J.G. 2007, Analysis-oriented stress–strain models for FRP–confined concrete, Engineering Structures, 29 (11), pp. 2968-2986.

Jiang, T., Wang, X.M., Chen, G.M., Zhang, J.J. & Zhang, W.P. 2019, Behavior of recycled brick block concrete-filled FRP tubes under axial compression, Engineering Structures, 198.

Jin, M., Zheng, Z., Sun, Y., Chen, L. & Jin, Z. 2016, Resistance of metakaolin-MSWI fly ash based geopolymer to acid and alkaline environments, Journal of Non-Crystalline Solids, 450, pp. 116-122.

Kaliyavaradhan, S.K. & Ling, T.-C. 2017, Potential of CO 2 sequestration through construction and demolition (C&D) waste—An overview, Journal of CO2 Utilization, 20, pp. 234-242.

Kathirvel, P. & Kaliyaperumal, S.R.M. 2016, Influence of recycled concrete aggregates on the flexural properties of reinforced alkali activated slag concrete, Construction and Building Materials, 102, pp. 51-58.

Kazmi, S.M.S., Munir, M.J., Wu, Y.-F., Patnaikuni, I., Zhou, Y. & Xing, F. 2019, Axial stress-strain behavior of macro-synthetic fiber reinforced recycled aggregate concrete, Cement and Concrete Composites, 97, pp. 341-356.

Keppert, M., Vejmelková, E., Bezdička, P., Doleželová, M., Čáchová, M., Scheinherrová, L., Pokorný, J., Vyšvařil, M., Rovnaníková, P. & Černý, R. 2018, Red-clay ceramic powders as geopolymer precursors: Consideration of amorphous portion and CaO content, Applied Clay Science, 161, pp. 82-89.

Khandelwal, H., Dhar, H., Thalla, A.K. & Kumar, S. 2019, Application of life cycle assessment in municipal solid waste management: A worldwide critical review, Journal of Cleaner Production, 209, pp. 630-654.

Khedmati, M., Kim, Y.-R. & Turner, J.A. 2019, Investigation of the interphase between recycled aggregates and cementitious binding materials using integrated microstructural-nanomechanical-chemical characterization, Composites Part B: Engineering, 158, pp. 218-229.

Khosravani, M.R. & Weinberg, K. 2018, A review on split Hopkinson bar experiments on the dynamic characterisation of concrete, Construction and Building Materials, 190, pp. 1264-1283.

Kinuthia, J. 2018, 'Wastepaper sludge ash', in R. Siddique & P. Cachim (eds), *Waste and Supplementary Cementitious Materials in Concrete*, Woodhead Publishing, pp. 289-321.

Komnitsas, K., Zaharaki, D., Vlachou, A., Bartzas, G. & Galetakis, M. 2015, Effect of synthesis parameters on the quality of construction and demolition wastes (CDW) geopolymers, Advanced Powder Technology, 26 (2), pp. 368-376.

Kua, T.-A., Arulrajah, A., Mohammadinia, A., Horpibulsuk, S. & Mirzababaei, M. 2017, Stiffness and deformation properties of spent coffee grounds based geopolymers, Construction and Building Materials, 138, pp. 79-87.

Kua, T.-A., Imteaz, M.A., Arulrajah, A. & Horpibulsuk, S. 2018, Environmental and economic viability of Alkali Activated Material (AAM) comprising slag, fly ash and spent coffee ground, International Journal of Sustainable Engineering, 12 (4), pp. 223-232.

Kumar, S., Kumar, R. & Mehrotra, S.P. 2010, Influence of granulated blast furnace slag on the reaction, structure and properties of fly ash based geopolymer, Journal of Materials Science, 45 (3), pp. 607-615.

Kurda, R., Silvestre, J.D. & de Brito, J. 2018, Life cycle assessment of concrete made with high volume of recycled concrete aggregates and fly ash, Resources, Conservation and Recycling, 139, pp. 407-417.

Kürklü, G. 2016, The effect of high temperature on the design of blast furnace slag and coarse fly ash-based geopolymer mortar, Composites Part B: Engineering, 92, pp. 9-18.

Łach, M., Kiszka, A., Korniejenko, K. & Mikuła, J. 2018, 'The mechanical properties of waste tire cords reinforced geopolymer concretes', *IOP Conference Series: Materials Science and Engineering*, vol. 416, IOP Publishing, p. 012089.

Lam, L. & Teng, J.G. 2003, Design-oriented stress–strain model for FRP-confined concrete, Construction and Building Materials, 17 (6-7), pp. 471-489.

Lam, L. & Teng, J.G. 2009, Stress–strain model for FRP-confined concrete under cyclic axial compression, Engineering Structures, 31 (2), pp. 308-321.

Lam, L., Teng, J.G., Cheung, C.H. & Xiao, Y. 2006, FRP-confined concrete under axial cyclic compression, Cement and Concrete Composites, 28 (10), pp. 949-958.

Lancellotti, I., Cannio, M., Bollino, F., Catauro, M., Barbieri, L. & Leonelli, C. 2015, Geopolymers: An option for the valorization of incinerator bottom ash derived “end of waste”, Ceramics International, 41 (2), pp. 2116-2123.

Lancellotti, I., Kamseu, E., Michelazzi, M., Barbieri, L., Corradi, A. & Leonelli, C. 2010, Chemical stability of geopolymers containing municipal solid waste incinerator fly ash, Waste Manag, 30 (4), pp. 673-679.

Lancellotti, I., Ponzoni, C., Barbieri, L. & Leonelli, C. 2013, Alkali activation processes for incinerator residues management, Waste Manag, 33 (8), pp. 1740-1749.

Lee, N.K., Kim, E.M. & Lee, H.K. 2016, Mechanical properties and setting characteristics of geopolymer mortar using styrene-butadiene (SB) latex, Construction and Building Materials, 113, pp. 264-272.

Lee, N.K. & Lee, H.K. 2013, Setting and mechanical properties of alkali-activated fly ash/slag concrete manufactured at room temperature, Construction and Building Materials, 47, pp. 1201-1209.

Li, G., Pang, S.-S. & Ibekwe, S.I. 2010, FRP tube encased rubberized concrete cylinders, Materials and Structures, 44 (1), pp. 233-243.

Li, P., Sui, L., Xing, F. & Zhou, Y. 2019a, Static and cyclic response of low-strength recycled aggregate concrete strengthened using fiber-reinforced polymer, Composites Part B: Engineering, 160, pp. 37-49.

Li, P. & Wu, Y.-F. 2015, Stress–strain model of FRP confined concrete under cyclic loading, Composite Structures, 134, pp. 60-71.

Li, P. & Wu, Y.-F. 2016, Stress–strain behavior of actively and passively confined concrete under cyclic axial load, Composite Structures, 149, pp. 369-384.

Li, P., Wu, Y.-F. & Gravina, R. 2016a, Cyclic response of FRP-confined concrete with post-peak strain softening behavior, Construction and Building Materials, 123, pp. 814-828.

Li, P., Wu, Y.-F., Zhou, Y. & Xing, F. 2018, Cyclic stress-strain model for FRP-confined concrete considering post-peak softening, Composite Structures, 201, pp. 902-915.

Li, V.C. & Joan, H. 1990, Relation of concrete fracture toughness to its internal structure, Engineering Fracture Mechanics, 35 (1), pp. 39-46.

Li, W., Luo, Z., Long, C., Wu, C., Duan, W.H. & Shah, S.P. 2016b, Effects of nanoparticle on the dynamic behaviors of recycled aggregate concrete under impact loading, Materials & Design, 112, pp. 58-66.

Li, W., Xiao, J., Sun, Z. & Shah, S.P. 2012, Failure processes of modeled recycled aggregate concrete under uniaxial compression, Cement and Concrete Composites, 34 (10), pp. 1149-1158.

Li, W. & Xu, J. 2009, Mechanical properties of basalt fiber reinforced geopolymeric concrete under impact loading, Materials Science and Engineering: A, 505 (1-2), pp. 178-186.

Li, X. 2009, Recycling and reuse of waste concrete in China, Resources, Conservation and Recycling, 53 (3), pp. 107-112.

Li, Y., Min, X., Ke, Y., Liu, D. & Tang, C. 2019b, Preparation of red mud-based geopolymer materials from MSWI fly ash and red mud by mechanical activation, Waste Manag, 83, pp. 202-208.

Li, Z. & Liu, S. 2007, Influence of slag as additive on compressive strength of fly ash-based geopolymer, Journal of Materials in civil engineering, 19 (6), pp. 470-474.

Lim, J.C. & Ozbakkaloglu, T. 2014, Stress–strain model for normal- and light-weight concretes under uniaxial and triaxial compression, Construction and Building Materials, 71, pp. 492-509.

Lim, J.C. & Ozbakkaloglu, T. 2015, Lateral Strain-to-Axial Strain Relationship of Confined Concrete, Journal of Structural Engineering, 141 (5).

Ling, Y., Wang, K., Li, W., Shi, G. & Lu, P. 2019, Effect of slag on the mechanical properties and bond strength of fly ash-based engineered geopolymer composites, Composites Part B: Engineering, 164, pp. 747-757.

Liu, C., Fan, J., Bai, G., Quan, Z., Fu, G., Zhu, C. & Fan, Z. 2019a, Cyclic load tests and seismic performance of recycled aggregate concrete (RAC) columns, Construction and Building Materials, 195, pp. 682-694.

Liu, D.G., Ke, Y., Min, X.B., Liang, Y.J., Wang, Z.B., Li, Y.C., Fei, J.C., Yao, L.W., Xu, H. & Jiang, G.H. 2019b, Cotreatment of MSWI Fly Ash and Granulated Lead Smelting Slag Using a Geopolymer System, Int J Environ Res Public Health, 16 (1).

Liu, Y., Shi, C., Zhang, Z. & Li, N. 2019c, An overview on the reuse of waste glasses in alkali-activated materials, Resources, Conservation and Recycling, 144, pp. 297-309.

Liu, Z., Cai, C.S., Peng, H. & Fan, F. 2016, Experimental Study of the Geopolymeric Recycled Aggregate Concrete, Journal of Materials in Civil Engineering, 28 (9).

Liu, Z., Peng, H. & Cai, C. 2019d, Nanomechanical Properties of Geopolymer/Cement Matrix in Recycled Aggregate Concrete, J Nanosci Nanotechnol, 19 (1), pp. 251-254.

Lokuge, W. & Karunasena, W. 2015, Ductility enhancement of geopolymer concrete columns using fibre-reinforced polymer confinement, Journal of Composite Materials, 50 (14), pp. 1887-1896.

Long, W.-J., Li, H.-D., Wei, J.-J., Xing, F. & Han, N. 2018, Sustainable use of recycled crumb rubbers in eco-friendly alkali activated slag mortar: Dynamic mechanical properties, Journal of Cleaner Production, 204, pp. 1004-1015.

Lu, J.-X. & Poon, C.S. 2018, Use of waste glass in alkali activated cement mortar, Construction and Building Materials, 160, pp. 399-407.

Lu, S., Xu, J.-Y., Bai, E.-L. & Luo, X. 2017, Effect of particles with different mechanical properties on the energy dissipation properties of concrete, Construction and Building Materials, 144, pp. 502-515.

Lu, Y., Chen, X., Teng, X. & Zhang, S. 2014, Dynamic compressive behavior of recycled aggregate concrete based on split Hopkinson pressure bar tests, Latin American Journal of Solids and Structures, 11 (1), pp. 131-141.

Luhar, S., Chaudhary, S. & Luhar, I. 2018, Thermal resistance of fly ash based rubberized geopolymer concrete, Journal of Building Engineering, 19, pp. 420-428.

Luhar, S., Chaudhary, S. & Luhar, I. 2019a, Development of rubberized geopolymer concrete: Strength and durability studies, Construction and Building Materials, 204, pp. 740-753.

Luhar, S., Cheng, T.-W., Nicolaides, D., Luhar, I., Panias, D. & Sakkas, K. 2019b, Valorisation of glass waste for development of Geopolymer composites – Mechanical properties and rheological characteristics: A review, Construction and Building Materials, 220, pp. 547-564.

Luhar, S., Cheng, T.-W., Nicolaides, D., Luhar, I., Panias, D. & Sakkas, K. 2019c, Valorisation of glass wastes for the development of geopolymer composites – Durability, thermal and microstructural properties: A review, Construction and Building Materials, 222, pp. 673-687.

Luna Galiano, Y., Fernandez Pereira, C. & Vale, J. 2011, Stabilization/solidification of a municipal solid waste incineration residue using fly ash-based geopolymers, J Hazard Mater, 185 (1), pp. 373-381.

Lundberg, B. 1976, A split Hopkinson bar study of energy absorption in dynamic rock fragmentation, International Journal of Rock Mechanics and Mining Sciences & Geomechanics Abstracts, 13 (6), pp. 187-197.

Luo, X., Xu, J., Bai, E. & Li, W. 2013, Research on the dynamic compressive test of highly fluidized geopolymer concrete, Construction and Building Materials, 48, pp. 166-172.

Luo, X., Xu, J., Li, W. & Bai, E. 2014, Effect of alkali-activator types on the dynamic compressive deformation behavior of geopolymer concrete, Materials Letters, 124, pp. 310-312.

Ma, H., Xue, J., Zhang, X. & Luo, D. 2013, Seismic performance of steel-reinforced recycled concrete columns under low cyclic loads, Construction and Building Materials, 48, pp. 229-237.

Ma, L., Li, Z., Liu, J., Duan, L. & Wu, J. 2019, Mechanical properties of coral concrete subjected to uniaxial dynamic compression, Construction and Building Materials, 199, pp. 244-255.

Mamat, N., Kusbiantoro, A. & Rahman, N. 2018, Hydrochloric acid based pre-treatment on paper mill sludge ash as an alternative source material for geopolymer, Materials Today: Proceedings, 5 (10), pp. 21825-21831.

Medina, C., Zhu, W., Howind, T., Sánchez de Rojas, M.I. & Frías, M. 2014, Influence of mixed recycled aggregate on the physical – mechanical properties of recycled concrete, Journal of Cleaner Production, 68, pp. 216-225.

Menegaki, M. & Damigos, D. 2018, A review on current situation and challenges of construction and demolition waste management, Current Opinion in Green and Sustainable Chemistry, 13, pp. 8-15.

Meng, Y., Ling, T.C., Mo, K.H. & Tian, W. 2019, Enhancement of high temperature performance of cement blocks via CO2 curing, Sci Total Environ, 671, pp. 827-837.

Mengel, L., Krauss, H.-W. & Lowke, D. 2020, Water transport through cracks in plain and reinforced concrete – Influencing factors and open questions, Construction and Building Materials, 254.

Moghadam, M.J., Ajalloeian, R. & Hajiannia, A. 2019, Preparation and application of alkali-activated materials based on waste glass and coal gangue: A review, Construction and Building Materials, 221, pp. 84-98.

Mohammadinia, A., Arulrajah, A., Sanjayan, J., Disfani, M.M., Bo, M.W. & Darmawan, S. 2016a, Strength Development and Microfabric Structure of Construction and Demolition Aggregates Stabilized with Fly Ash–Based Geopolymers, Journal of Materials in Civil Engineering, 28 (11).

Mohammadinia, A., Arulrajah, A., Sanjayan, J., Disfani, M.M., Win Bo, M. & Darmawan, S. 2016b, Stabilization of Demolition Materials for Pavement Base/Subbase Applications Using Fly Ash and Slag Geopolymers: Laboratory Investigation, Journal of Materials in Civil Engineering, 28 (7).

Nataraja, M., Dhang, N. & Gupta, A. 1999, Stress–strain curves for steel-fiber reinforced concrete under compression, Cement and concrete composites, 21 (5-6), pp. 383-390.

Nath, P. & Sarker, P.K. 2014, Effect of GGBFS on setting, workability and early strength properties of fly ash geopolymer concrete cured in ambient condition, Construction and Building Materials, 66, pp. 163-171.

Nath, P. & Sarker, P.K. 2017, Flexural strength and elastic modulus of ambient-cured blended low-calcium fly ash geopolymer concrete, Construction and Building Materials, 130, pp. 22-31.

Nematzadeh, M. & Baradaran-Nasiri, A. 2018, Residual Properties of Concrete Containing Recycled Refractory Brick Aggregate at Elevated Temperatures, Journal of Materials in Civil Engineering, 30 (1).

Nematzadeh, M., Salari, A., Ghadami, J. & Naghipour, M. 2016, Stress-strain behavior of freshly compressed concrete under axial compression with a practical equation, Construction and Building Materials, 115, pp. 402-423.

Němeček, J., Šmilauer, V. & Kopecký, L. 2011, Nanoindentation characteristics of alkali-activated aluminosilicate materials, Cement and Concrete Composites, 33 (2), pp. 163-170.

Nidheesh, P.V. & Kumar, M.S. 2019, An overview of environmental sustainability in cement and steel production, Journal of Cleaner Production, 231, pp. 856-871.

Nour, A.I. & Güneyisi, E.M. 2019, Prediction model on compressive strength of recycled aggregate concrete filled steel tube columns, Composites Part B: Engineering, 173.

Noushini, A., Aslani, F., Castel, A., Gilbert, R.I., Uy, B. & Foster, S. 2016, Compressive stress-strain model for low-calcium fly ash-based geopolymer and heat-cured Portland cement concrete, Cement and Concrete Composites, 73, pp. 136-146.

Noushini, A., Hastings, M., Castel, A. & Aslani, F. 2018, Mechanical and flexural performance of synthetic fibre reinforced geopolymer concrete, Construction and Building Materials, 186, pp. 454-475.

Novais, R.M., Saeli, M., Caetano, A.P.F., Seabra, M.P., Labrincha, J.A., Surendran, K.P. & Pullar, R.C. 2019, Pyrolysed cork-geopolymer composites: A novel and sustainable EMI shielding building material, Construction and Building Materials, 229.

Nuaklong, P., Sata, V. & Chindaprasirt, P. 2016, Influence of recycled aggregate on fly ash geopolymer concrete properties, Journal of Cleaner Production, 112, pp. 2300-2307.

Nuaklong, P., Sata, V., Wongsa, A., Srinavin, K. & Chindaprasirt, P. 2018a, Recycled aggregate high calcium fly ash geopolymer concrete with inclusion of OPC and nano-SiO2, Construction and Building Materials, 174, pp. 244-252.

Nuaklong, P., Sata, V., Wongsa, A., Srinavin, K. & Chindaprasirt, P. 2018b, Recycled aggregate high calcium fly ash geopolymer concrete with inclusion of OPC and nano-SiO 2, Construction and Building Materials, 174, pp. 244-252.

Olivia, M. & Nikraz, H. 2012, Properties of fly ash geopolymer concrete designed by Taguchi method, Materials & Design (1980-2015), 36, pp. 191-198.

Onuaguluchi, O., Borges, P.H.R., Bhutta, A. & Banthia, N. 2017, Performance of scrap tire steel fibers in OPC and alkali-activated mortars, Materials and Structures, 50 (2).

Ouda, A.S. & Gharieb, M. 2020, Development the properties of brick geopolymer pastes using concrete waste incorporating dolomite aggregate, Journal of Building Engineering, 27, p. 100919.

Ozbakkaloglu, T. & Akin, E. 2012, Behavior of FRP-Confined Normal- and High-Strength Concrete under Cyclic Axial Compression, Journal of Composites for Construction, 16 (4), pp. 451-463.

Ozbakkaloglu, T. & Lim, J.C. 2013, Axial compressive behavior of FRP-confined concrete: Experimental test database and a new design-oriented model, Composites Part B: Engineering, 55, pp. 607-634.

Ozbakkaloglu, T., Lim, J.C. & Vincent, T. 2013, FRP-confined concrete in circular sections: Review and assessment of stress–strain models, Engineering Structures, 49, pp. 1068-1088.

Ozbakkaloglu, T. & Xie, T. 2016, Geopolymer concrete-filled FRP tubes: Behavior of circular and square columns under axial compression, Composites Part B: Engineering, 96, pp. 215-230.

Pan, B., Qian, K., Xie, H. & Asundi, A. 2009, Two-dimensional digital image correlation for in-plane displacement and strain measurement: a review, Measurement Science and Technology, 20 (6).

Pan, Z., Sanjayan, J.G. & Rangan, B.V. 2011, Fracture properties of geopolymer paste and concrete, Magazine of Concrete Research, 63 (10), pp. 763-771.

Park, Y., Abolmaali, A., Kim, Y.H. & Ghahremannejad, M. 2016, Compressive strength of fly ash-based geopolymer concrete with crumb rubber partially replacing sand, Construction and Building Materials, 118, pp. 43-51.

Parthiban, K. & Saravana Raja Mohan, K. 2017, Influence of recycled concrete aggregates on the engineering and durability properties of alkali activated slag concrete, Construction and Building Materials, 133, pp. 65-72.

Patel, R., Bhogayata, A., Arora, N. & Parmar, K. 2013, Flexural response of geopolymer concrete beam containing metallized plastic waste, International Journal of Advanced Engineering Technology, 72, pp. 72-74.

Peters, W. & Ranson, W. 1982, Digital imaging techniques in experimental stress analysis, Optical engineering, 21 (3), p. 213427.

Peyne, J., Joussein, E., Gautron, J., Doudeau, J. & Rossignol, S. 2017, Feasibility of producing geopolymer binder based on a brick clay mixture, Ceramics International, 43 (13), pp. 9860-9871.

Piasta, W., Góra, J. & Budzyński, W. 2017, Stress-strain relationships and modulus of elasticity of rocks and of ordinary and high performance concretes, Construction and Building Materials, 153, pp. 728-739.

Picandet, V., Khelidj, A. & Bastian, G. 2001, Effect of axial compressive damage on gas permeability of ordinary and high-performance concrete, Cement and Concrete Research, 31 (11), pp. 1525-1532.

Poon, C.-S. & Chan, D. 2007, The use of recycled aggregate in concrete in Hong Kong, Resources, Conservation and Recycling, 50 (3), pp. 293-305.

Poon, C.S., Shui, Z.H., Lam, L., Fok, H. & Kou, S.C. 2004, Influence of moisture states of natural and recycled aggregates on the slump and compressive strength of concrete, Cement and Concrete Research, 34 (1), pp. 31-36.

Posi, P., Ridtirud, C., Ekvong, C., Chammanee, D., Janthowong, K. & Chindaprasirt, P. 2015, Properties of lightweight high calcium fly ash geopolymer concretes containing recycled packaging foam, Construction and Building Materials, 94, pp. 408-413.

Posi, P., Teerachanwit, C., Tanutong, C., Limkamoltip, S., Lertnimoolchai, S., Sata, V. & Chindaprasirt, P. 2013, Lightweight geopolymer concrete containing aggregate from recycle lightweight block, Materials & Design (1980-2015), 52, pp. 580-586.

Prachasaree, W., Limkatanyu, S., Hawa, A. & Samakrattakit, A. 2014, Development of Equivalent Stress Block Parameters for Fly-Ash-Based Geopolymer Concrete, Arabian Journal for Science and Engineering, 39 (12), pp. 8549-8558.

Provis, J.L. 2014, Geopolymers and other alkali activated materials: why, how, and what?, Materials and Structures, 47 (1-2), pp. 11-25.

Provis, J.L., Myers, R.J., White, C.E., Rose, V. & van Deventer, J.S.J. 2012, X-ray microtomography shows pore structure and tortuosity in alkali-activated binders, Cement and Concrete Research, 42 (6), pp. 855-864.

Provis, J.L., Palomo, A. & Shi, C. 2015, Advances in understanding alkali-activated materials, Cement and Concrete Research, 78, pp. 110-125.

Puertas, F., Palacios, M., Manzano, H., Dolado, J., Rico, A. & Rodríguez, J. 2011, A model for the CASH gel formed in alkali-activated slag cements, Journal of the European Ceramic Society, 31 (12), pp. 2043-2056.

Puligilla, S. & Mondal, P. 2013, Role of slag in microstructural development and hardening of fly ash-slag geopolymer, Cement and Concrete Research, 43, pp. 70-80.

Rakhimova, N.R. & Rakhimov, R.Z. 2015, Alkali-activated cements and mortars based on blast furnace slag and red clay brick waste, Materials & Design, 85, pp. 324-331.

Ramos, G.A., Pelisser, F., Paul Gleize, P.J., Bernardin, A.M. & Michel, M.D. 2018, Effect of porcelain tile polishing residue on geopolymer cement, Journal of Cleaner Production, 191, pp. 297-303.

Reddy, M.S., Dinakar, P. & Rao, B.H. 2016, A review of the influence of source material's oxide composition on the compressive strength of geopolymer concrete, Microporous and Mesoporous Materials, 234, pp. 12-23.

Reig, L., Sanz, M.A., Borrachero, M.V., Monzó, J., Soriano, L. & Payá, J. 2017, Compressive strength and microstructure of alkali-activated mortars with high ceramic waste content, Ceramics International, 43 (16), pp. 13622-13634.

Reig, L., Soriano, L., Borrachero, M.V., Monzó, J. & Payá, J. 2016, Influence of calcium aluminate cement (CAC) on alkaline activation of red clay brick waste (RCBW), Cement and Concrete Composites, 65, pp. 177-185.

Reig, L., Tashima, M.M., Borrachero, M.V., Monzó, J., Cheeseman, C.R. & Payá, J. 2013a, Properties and microstructure of alkali-activated red clay brick waste, Construction and Building Materials, 43, pp. 98-106.

Reig, L., Tashima, M.M., Soriano, L., Borrachero, M.V., Monzó, J. & Payá, J. 2013b, Alkaline Activation of Ceramic Waste Materials, Waste and Biomass Valorization, 4 (4), pp. 729-736.

Ren, X. & Zhang, L. 2018, Experimental study of interfacial transition zones between geopolymer binder and recycled aggregate, Construction and Building Materials, 167, pp. 749-756.

Ridzuan, A., Khairulniza, A., Fadzil, M., Nurliza, J., Fauzi, M. & Yusoff, W. 2014a, 'Alkaline activators concentration effect to strength of waste paper sludge ash-based geopolymer mortar', *Proceedings of the International Civil and Infrastructure Engineering Conference 2013*, Springer, pp. 169-175.

Ridzuan, A.R.M., Khairulniza, A.A., Fadzil, M.A. & Nurliza, J. 2014b, Effect of Alkaline Activators Concentration to the Strength and Morphological Properties of Wastepaper-Based Geopolymer Mortars, Materials Science Forum, 803, pp. 88-92.

Robayo, R.A., Mulford, A., Munera, J. & Mejía de Gutiérrez, R. 2016, Alternative cements based on alkali-activated red clay brick waste, Construction and Building Materials, 128, pp. 163-169.

Ross, C.A., Tedesco, J.W. & Kuennen, S.T. 1995, Effects of strain rate on concrete strength, ACI Materials Journal, 92 (1), pp. 37-47.

Rossi, P., Van Mier, J., Boulay, C. & Le Maou, F. 1992, The dynamic behaviour of concrete: influence of free water, Materials and Structures, 25 (9), pp. 509-514.

Rossi, P., Van Mier, J.G., Toutlemonde, F., Le Maou, F. & Boulay, C. 1994, Effect of loading rate on the strength of concrete subjected to uniaxial tension, Materials and structures, 27 (5), pp. 260-264.

Rovnaník, P., Rovnaníková, P., Vyšvařil, M., Grzeszczyk, S. & Janowska-Renkas, E. 2018, Rheological properties and microstructure of binary waste red brick powder/metakaolin geopolymer, Construction and Building Materials, 188, pp. 924-933.

Rqhl, M. & Atkinson, G. 1999, The influence of recycled aggregate concrete on the stress-strain relation of concrete, Darmstadt concrete, 26 (14), pp. 36-52.

S Mohammed, B., Liew, M.S., S Alaloul, W., Al-Fakih, A., Ibrahim, W. & Adamu, M. 2018, Development of rubberized geopolymer interlocking bricks, Case Studies in Construction Materials, 8, pp. 401-408.

Şahmaran, M., Keskin, S.B., Ozerkan, G. & Yaman, I.O. 2008, Self-healing of mechanically-loaded self consolidating concretes with high volumes of fly ash, Cement and Concrete Composites, 30 (10), pp. 872-879.

Saikia, N. & de Brito, J. 2012, Use of plastic waste as aggregate in cement mortar and concrete preparation: A review, Construction and Building Materials, 34, pp. 385-401.

Saride, S., Avirneni, D. & Challapalli, S. 2016, Micro-mechanical interaction of activated fly ash mortar and reclaimed asphalt pavement materials, Construction and Building Materials, 123, pp. 424-435.

Sarmiento, L.M., Clavier, K.A., Paris, J.M., Ferraro, C.C. & Townsend, T.G. 2019, Critical examination of recycled municipal solid waste incineration ash as a mineral source for portland cement manufacture – A case study, Resources, Conservation and Recycling, 148, pp. 1-10.

Sata, V., Wongsa, A. & Chindaprasirt, P. 2013, Properties of pervious geopolymer concrete using recycled aggregates, Construction and Building Materials, 42, pp. 33-39.

Sedira, N., Castro-Gomes, J. & Magrinho, M. 2018, Red clay brick and tungsten mining waste-based alkali-activated binder: Microstructural and mechanical properties, Construction and Building Materials, 190, pp. 1034-1048.

Shaikh, F.U.A. 2016, Mechanical and durability properties of fly ash geopolymer concrete containing recycled coarse aggregates, International Journal of Sustainable Built Environment, 5 (2), pp. 277-287.

Shaikh, F.U.A., Odoh, H. & Than, A.B. 2015, Effect of nano silica on properties of concretes containing recycled coarse aggregates, Proceedings of the Institution of Civil Engineers - Construction Materials, 168 (2), pp. 68-76.

Shang, J., Dai, J.-G., Zhao, T.-J., Guo, S.-Y., Zhang, P. & Mu, B. 2018, Alternation of traditional cement mortars using fly ash-based geopolymer mortars modified by slag, Journal of Cleaner Production, 203, pp. 746-756.

Shi, C., Li, Y., Zhang, J., Li, W., Chong, L. & Xie, Z. 2016, Performance enhancement of recycled concrete aggregate – A review, Journal of Cleaner Production, 112, pp. 466-472.

Shi, X.S., Collins, F.G., Zhao, X.L. & Wang, Q.Y. 2011, 'Experimental study on geopolymeric recycled concrete used as sustainable construction material', *International conference on advances in construction materials through science and engineering, RILEM*, Hong Kong SAR, China.

Shi, X.S., Collins, F.G., Zhao, X.L. & Wang, Q.Y. 2012, Mechanical properties and microstructure analysis of fly ash geopolymeric recycled concrete, J Hazard Mater, 237-238, pp. 20-29.

Shiota, K., Nakamura, T., Takaoka, M., Nitta, K., Oshita, K., Fujimori, T. & Ina, T. 2017, Chemical kinetics of Cs species in an alkali-activated municipal solid waste incineration fly ash and pyrophyllite-based system using Cs K-edge in situ X-ray absorption fine structure analysis, Spectrochimica Acta Part B: Atomic Spectroscopy, 131, pp. 32-39.

Shoaei, P., Musaeei, H.R., Mirlohi, F., Narimani zamanabadi, S., Ameri, F. & Bahrami, N. 2019, Waste ceramic powder-based geopolymer mortars: Effect of curing temperature and alkaline solution-to-binder ratio, Construction and Building Materials, 227, p. 116686.

Si, R., Dai, Q., Guo, S. & Wang, J. 2020, Mechanical property, nanopore structure and drying shrinkage of metakaolin-based geopolymer with waste glass powder, Journal of Cleaner Production, 242, p. 118502.

Siad, H., Lachemi, M., Sahmaran, M., Mesbah, H.A., Anwar Hossain, K.M. & Ozsunar, A. 2017, Potential for using recycled glass sand in engineered cementitious composites, Magazine of Concrete Research, 69 (17), pp. 905-918.

Siddique, R. 2010a, Use of municipal solid waste ash in concrete, Resources, Conservation and Recycling, 55 (2), pp. 83-91.

Siddique, R. 2010b, Utilization of municipal solid waste (MSW) ash in cement and mortar, Resources, Conservation and Recycling, 54 (12), pp. 1037-1047.

Silva, G., Castañeda, D., Kim, S., Castañeda, A., Bertolotti, B., Ortega-San-Martin, L., Nakamatsu, J. & Aguilar, R. 2019, Analysis of the production conditions of geopolymer matrices from natural pozzolana and fired clay brick wastes, Construction and Building Materials, 215, pp. 633-643.

Silva, R.V., de Brito, J. & Dhir, R.K. 2014, Properties and composition of recycled aggregates from construction and demolition waste suitable for concrete production, Construction and Building Materials, 65, pp. 201-217.

Singh, B., Rahman, M.R., Paswan, R. & Bhattacharyya, S.K. 2016, Effect of activator concentration on the strength, ITZ and drying shrinkage of fly ash/slag geopolymer concrete, Construction and Building Materials, 118, pp. 171-179.

Song, W., Zhu, Z., Peng, Y., Wan, Y., Xu, X., Pu, S., Song, S. & Wei, Y. 2019, Effect of steel slag on fresh, hardened and microstructural properties of high-calcium fly ash based geopolymers at standard curing condition, Construction and Building Materials, 229.

Sparks, P.R. & Menzies, J. 1973, The effect of rate of loading upon the static and fatigue strengths of plain concrete in compression, Magazine of Concrete Research, 25 (83), pp. 73-80.

Spasiano, D. & Pirozzi, F. 2017, Treatments of asbestos containing wastes, J Environ Manage, 204 (Pt 1), pp. 82-91.

Stroeven, P., *Some aspects of the micromechanics of concrete*, Delft : Technological university of Delft. Stevin laboratory.

Su, Y., Li, J., Wu, C., Wu, P. & Li, Z.-X. 2016, Influences of nano-particles on dynamic strength of ultra-high performance concrete, Composites Part B: Engineering, 91, pp. 595-609.

Suksiripattanapong, C., Kua, T.-A., Arulrajah, A., Maghool, F. & Horpibulsuk, S. 2017, Strength and microstructure properties of spent coffee grounds stabilized with rice husk ash and slag geopolymers, Construction and Building Materials, 146, pp. 312-320.

Sun, H., Gao, Y., Zheng, X., Chen, Y., Jiang, Z. & Zhang, Z. 2019, Meso-Scale Simulation of Concrete Uniaxial Behavior Based on Numerical Modeling of CT Images, Materials (Basel), 12 (20).

Sun, L., Fujii, M., Tasaki, T., Dong, H. & Ohnishi, S. 2018, Improving waste to energy rate by promoting an integrated municipal solid-waste management system, Resources, Conservation and Recycling, 136, pp. 289-296.

Sun, Z., Cui, H., An, H., Tao, D., Xu, Y., Zhai, J. & Li, Q. 2013, Synthesis and thermal behavior of geopolymer-type material from waste ceramic, Construction and Building Materials, 49, pp. 281-287.

Tam, V.W.Y., Soomro, M. & Evangelista, A.C.J. 2018, A review of recycled aggregate in concrete applications (2000–2017), Construction and Building Materials, 172, pp. 272-292.

Tam, V.W.Y. & Tam, C.M. 2006, A review on the viable technology for construction waste recycling, Resources, Conservation and Recycling, 47 (3), pp. 209-221.

Tang, Y.-C., Li, L.-J., Feng, W.-X., Liu, F. & Zhu, M. 2018, Study of seismic behavior of recycled aggregate concrete-filled steel tubular columns, Journal of Constructional Steel Research, 148, pp. 1-15.

Tang, Z., Hu, Y., Li, W. & Tam, V.W.Y. 2019a, Uniaxial compressive behaviors of fly ash/slag-based geopolymeric concrete with recycled aggregates, Cement and Concrete Composites, 104, p. 103375.

Tang, Z., Hu, Y., Tam, V.W.Y. & Li, W. 2019b, Uniaxial compressive behaviors of fly ash/slag-based geopolymeric concrete with recycled aggregates, Cement and Concrete Composites, 104, p. 103375.

Tasdemir, M.A., Maji, A.K. & Shah, S.P. 1990, Crack Propagation in Concrete under Compression, Journal of Engineering Mechanics, 116 (5), pp. 1058-1076.

Tasdemir, M.A., Tasdemir, C., Akyüz, S., Jefferson, A.D., Lydon, F.D. & Barr, B.I.G. 1998, Evaluation of strains at peak stresses in concrete: a three-phase composite model approach, Cement and Concrete Composites, 20 (4), pp. 301-318.

Teng, J., Huang, Y., Lam, L. & Ye, L. 2007, Theoretical model for fiber-reinforced polymer-confined concrete, Journal of composites for construction, 11 (2), pp. 201-210.

Teng, J., Jiang, T., Lam, L. & Luo, Y. 2009, Refinement of a design-oriented stress–strain model for FRP-confined concrete, Journal of Composites for Construction, 13 (4), pp. 269-278.

Teng, J.G., Zhao, J.L., Yu, T., Li, L.J. & Guo, Y.C. 2016, Behavior of FRP-Confined Compound Concrete Containing Recycled Concrete Lumps, Journal of Composites for Construction, 20 (1).

Thomas, B.S. & Gupta, R.C. 2016, A comprehensive review on the applications of waste tire rubber in cement concrete, Renewable and Sustainable Energy Reviews, 54, pp. 1323-1333.

Thomas, R.J. & Peethamparan, S. 2015, Alkali-activated concrete: Engineering properties and stress–strain behavior, Construction and Building Materials, 93, pp. 49-56.

Tome, S., Etoh, M.-A., Etame, J. & Sanjay, K. 2018, Characterization and Leachability Behaviour of Geopolymer Cement Synthesised from Municipal Solid Waste Incinerator Fly Ash and Volcanic Ash Blends, Recycling, 3 (4).

Tu, T.-Y., Chen, Y.-Y. & Hwang, C.-L. 2006, Properties of HPC with recycled aggregates, Cement and Concrete Research, 36 (5), pp. 943-950.

Tuyan, M., Andiç-Çakir, Ö. & Ramyar, K. 2018, Effect of alkali activator concentration and curing condition on strength and microstructure of waste clay brick powder-based geopolymer, Composites Part B: Engineering, 135, pp. 242-252.

Usha, S., Nair, D.G. & Vishnudas, S. 2016, Feasibility Study of Geopolymer Binder from Terracotta Roof Tile Waste, Procedia Technology, 25, pp. 186-193.

van Oss, H.G. & Padovani, A.C. 2002, Cement Manufacture and the Environment: Part I: Chemistry and Technology, Journal of Industrial Ecology, 6 (1), pp. 89-105.

Vegt, I., Breugel, V. & Weerheijm, J. 2007, Failure mechanisms of concrete under impact loading, Fracture Mechanics of Concrete and Concrete Structures, FraMCoS-6, 1, pp. 579-587.

Vinai, R. & Soutsos, M. 2019, Production of sodium silicate powder from waste glass cullet for alkali activation of alternative binders, Cement and Concrete Research, 116, pp. 45-56.

Wan, X., Shen, C., Wang, P., Zhao, T. & Lu, Y. 2020, A study on fracture toughness of ultra-high toughness geopolymer composites based on Double-K Criterion, Construction and Building Materials, 251.

Wang, W., Wu, C., Liu, Z. & Si, H. 2018, Compressive behavior of ultra-high performance fiber-reinforced concrete (UHPFRC) confined with FRP, Composite Structures, 204, pp. 419-437.

Waste Atlas 2019, D-Waste. <http://www.atlas.d-waste.com/> (accessed 10.21.2019).

Wongkvanklom, A., Posi, P., Homwuttiwong, S., Sata, V., Wongsa, A., Tanangteerapong, D. & Chindaprasirt, P. 2019, Lightweight Geopolymer Concrete Containing Recycled Plastic Beads, Key Engineering Materials, 801, pp. 377-384.

Wongsa, A., Sata, V., Nematollahi, B., Sanjayan, J. & Chindaprasirt, P. 2018a, Mechanical and thermal properties of lightweight geopolymer mortar incorporating crumb rubber, Journal of Cleaner Production, 195, pp. 1069-1080.

Wongsa, A., Sata, V., Nuaklong, P. & Chindaprasirt, P. 2018b, Use of crushed clay brick and pumice aggregates in lightweight geopolymer concrete, Construction and Building Materials, 188, pp. 1025-1034.

Xiao, J., Huang, Y., Yang, J. & Zhang, C. 2012a, Mechanical properties of confined recycled aggregate concrete under axial compression, Construction and Building Materials, 26 (1), pp. 591-603.

Xiao, J., Li, H. & Yang, Z. 2013a, Fatigue behavior of recycled aggregate concrete under compression and bending cyclic loadings, Construction and Building Materials, 38, pp. 681-688.

Xiao, J., Li, J. & Zhang, C. 2005, Mechanical properties of recycled aggregate concrete under uniaxial loading, Cement and Concrete Research, 35 (6), pp. 1187-1194.

Xiao, J., Li, L., Shen, L. & Poon, C.S. 2015, Compressive behaviour of recycled aggregate concrete under impact loading, Cement and Concrete Research, 71, pp. 46-55.

Xiao, J., Li, W., Fan, Y. & Huang, X. 2012b, An overview of study on recycled aggregate concrete in China (1996–2011), Construction and Building Materials, 31, pp. 364-383.

Xiao, J., Li, W., Sun, Z., Lange, D.A. & Shah, S.P. 2013b, Properties of interfacial transition zones in recycled aggregate concrete tested by nanoindentation, Cement and Concrete Composites, 37, pp. 276-292.

Xiao, J., Li, W., Sun, Z. & Shah, S.P. 2012c, Crack Propagation in Recycled Aggregate Concrete under Uniaxial Compressive Loading, Aci Materials Journal, 109 (4), pp. p.451-461.

Xiao, Y. & Wu, H. 2000, Compressive behavior of concrete confined by carbon fiber composite jackets, Journal of materials in civil engineering, 12 (2), pp. 139-146.

Xiao, Y. & Wu, H. 2003, Compressive behavior of concrete confined by various types of FRP composite jackets, Journal of Reinforced Plastics and Composites, 22 (13), pp. 1187-1201.

Xie, J., Wang, J., Rao, R., Wang, C. & Fang, C. 2019a, Effects of combined usage of GGBS and fly ash on workability and mechanical properties of alkali activated geopolymer concrete with recycled aggregate, Composites Part B: Engineering, 164, pp. 179-190.

Xie, J., Wang, J., Zhang, B., Fang, C. & Li, L. 2019b, Physicochemical properties of alkali activated GGBS and fly ash geopolymeric recycled concrete, Construction and Building Materials, 204, pp. 384-398.

Xie, T. & Ozbakkaloglu, T. 2016, Behavior of recycled aggregate concrete-filled basalt and carbon FRP tubes, Construction and Building Materials, 105, pp. 132-143.

Xu, J., Chen, Y., Xie, T., Zhao, X., Xiong, B. & Chen, Z. 2019a, Prediction of triaxial behavior of recycled aggregate concrete using multivariable regression and artificial neural network techniques, Construction and Building Materials, 226, pp. 534-554.

Xu, P., Zhao, Q., Qiu, W., Xue, Y. & Li, N. 2019b, Microstructure and Strength of Alkali-Activated Bricks Containing Municipal Solid Waste Incineration (MSWI) Fly Ash Developed as Construction Materials, Sustainability, 11 (5).

Xuan, D., Tang, P. & Poon, C.S. 2019, MSWIBA-based cellular alkali-activated concrete incorporating waste glass powder, Cement and Concrete Composites, 95, pp. 128-136.

Yahya, Z., Abdullah, M., Ramli, S., Minciuna, M. & Razak, R.A. 2018, 'Durability of fly ash based geopolymer concrete infilled with rubber crumb in seawater exposure', *IOP Conference Series: Materials Science and Engineering*, vol. 374, IOP Publishing, p. 012069.

Yan, B., Huang, L., Yan, L., Gao, C. & Kasal, B. 2017, Behavior of flax FRP tube encased recycled aggregate concrete with clay brick aggregate, Construction and Building Materials, 136, pp. 265-276.

Yan, D. & Lin, G. 2006, Dynamic properties of concrete in direct tension, Cement and Concrete Research, 36 (7), pp. 1371-1378.

Yan, S. & Sagoe-Crentsil, K. 2012, Properties of wastepaper sludge in geopolymer mortars for masonry applications, J Environ Manage, 112, pp. 27-32.

Yan, S. & Sagoe-Crentsil, K. 2016, Evaluation of fly ash geopolymer mortar incorporating calcined wastepaper sludge, Journal of Sustainable Cement-Based Materials, 5 (6), pp. 370-380.

Yang, K.-H., Cho, A.-R. & Song, J.-K. 2012a, Effect of water–binder ratio on the mechanical properties of calcium hydroxide-based alkali-activated slag concrete, Construction and Building Materials, 29, pp. 504-511.

Yang, T., Yao, X., Zhang, Z. & Wang, H. 2012b, Mechanical property and structure of alkali-activated fly ash and slag blends, Journal of Sustainable Cement-Based Materials, 1 (4), pp. 167-178.

Yao, W., Xia, K., Liu, Y., Shi, Y. & Peterson, K. 2019, Dependences of dynamic compressive and tensile strengths of four alkali-activated mortars on the loading rate and curing time, Construction and Building Materials, 202, pp. 891-903.

Ye, N., Chen, Y., Yang, J., Liang, S., Hu, Y., Xiao, B., Huang, Q., Shi, Y., Hu, J. & Wu, X. 2016, Co-disposal of MSWI fly ash and Bayer red mud using an one-part geopolymeric system, J Hazard Mater, 318, pp. 70-78.

Yliniemi, J., Luukkonen, T., Kaiser, A. & Illikainen, M. 2019, 'Mineral wool waste-based geopolymers', *IOP Conference Series: Earth and Environmental Science*, vol. 297, IOP Publishing, p. 012006.

Yoo, D.-Y. & Banthia, N. 2017, Mechanical and structural behaviors of ultra-high-performance fiber-reinforced concrete subjected to impact and blast, Construction and Building Materials, 149, pp. 416-431.

Yu, T. & Teng, J.G. 2011, Design of Concrete-Filled FRP Tubular Columns: Provisions in the Chinese Technical Code for Infrastructure Application of FRP Composites, Journal of Composites for Construction, 15 (3), pp. 451-461.

Yu, T., Zhang, B. & Teng, J.G. 2015, Unified cyclic stress–strain model for normal and high strength concrete confined with FRP, Engineering Structures, 102, pp. 189-201.

Zaumanis, M., Mallick, R.B. & Frank, R. 2014, 100% recycled hot mix asphalt: A review and analysis, Resources, Conservation and Recycling, 92, pp. 230-245.

Zawrah, M.F., Gado, R.A., Feltin, N., Ducourtieux, S. & Devoille, L. 2016, Recycling and utilization assessment of waste fired clay bricks (Grog) with granulated blast-furnace slag for geopolymer production, Process Safety and Environmental Protection, 103, pp. 237-251.

Zeng, L., Li, L., Su, Z. & Liu, F. 2018, Compressive test of GFRP-recycled aggregate concrete-steel tubular long columns, Construction and Building Materials, 176, pp. 295-312.

Zeng, M.-H., Wu, Z.-M. & Wang, Y.-J. 2020, A stochastic model considering heterogeneity and crack propagation in concrete, Construction and Building Materials, 254.

Zhang, J., Shi, C., Zhang, Z. & Ou, Z. 2017, Durability of alkali-activated materials in aggressive environments: A review on recent studies, Construction and Building Materials, 152, pp. 598-613.

Zhang, Z., Provis, J.L., Reid, A. & Wang, H. 2014, Fly ash-based geopolymers: The relationship between composition, pore structure and efflorescence, Cement and Concrete Research, 64, pp. 30-41.

Zhao, J., Yu, T. & Teng, J. 2014, Stress-strain behavior of FRP-confined recycled aggregate concrete, Journal of Composites for Construction, 19 (3), p. 04014054.

Zhao, S., Muhammad, F., Yu, L., Xia, M., Huang, X., Jiao, B., Lu, N. & Li, D. 2019, Solidification/stabilization of municipal solid waste incineration fly ash using uncalcined coal gangue-based alkali-activated cementitious materials, Environ Sci Pollut Res Int, 26 (25), pp. 25609-25620.

Zheng, L., Wang, C., Wang, W., Shi, Y. & Gao, X. 2011, Immobilization of MSWI fly ash through geopolymerization: effects of water-wash, Waste Manag, 31 (2), pp. 311-317.

Zheng, L., Wang, W. & Gao, X. 2016, Solidification and immobilization of MSWI fly ash through aluminate geopolymerization: Based on partial charge model analysis, Waste Manag, 58, pp. 270-279.

Zhong, H., Poon, E.W., Chen, K. & Zhang, M. 2019, Engineering properties of crumb rubber alkali-activated mortar reinforced with recycled steel fibres, Journal of Cleaner Production, 238.

Zhou, Y., Hu, J., Li, M., Sui, L. & Xing, F. 2016, FRP-Confined Recycled Coarse Aggregate Concrete: Experimental Investigation and Model Comparison, Polymers (Basel), 8 (10).

Zhu, W., Chen, X., Struble, L.J. & Yang, E.-H. 2019a, Quantitative characterization of aluminosilicate gels in alkali-activated incineration bottom ash through sequential chemical extractions and deconvoluted nuclear magnetic resonance spectra, Cement and Concrete Composites, 99, pp. 175-180.

Zhu, W., Rao, X.H., Liu, Y. & Yang, E.-H. 2018, Lightweight aerated metakaolin-based geopolymer incorporating municipal solid waste incineration bottom ash as gas-forming agent, Journal of Cleaner Production, 177, pp. 775-781.

Zhu, W., Teoh, P.J., Liu, Y., Chen, Z. & Yang, E.-H. 2019b, Strategic utilization of municipal solid waste incineration bottom ash for the synthesis of lightweight aerated alkali-activated materials, Journal of Cleaner Production, 235, pp. 603-612.